Computational Studies of Linear and Non-linear Optical Properties of Nano-Structured Metamaterials

Claudiu G. Biris

A dissertation submitted in partial fulfillment
of the requirements for the degree of
Doctor of Philosophy
of the
University College of London.

Department of Electronic and Electrical Engineering
University College London

November 10, 2011

I, Claudiu Gheorghe Biris confirm that the work presented in this thesis is my own. Where information has been derived from other sources, I confirm that this has been indicated in the thesis.

Abstract

In this thesis, a comprehensive analytical and numerical study of optical non-linear effects in plasmonic metamaterials is presented. The new results reported and described in this work can potentially have a significant impact on our understanding of electromagnetic phenomena in artificial optical materials, and facilitate the design and fabrication of new active optical devices with new or enhanced functionality. Equally important, these results could lead to deeper physical insights into the fundamental properties of these metamaterials.

To this end, a new analytical formalism based on the multiple scattering theory has been developed, a theoretical framework that allows one to fully characterise the linear and non-linear electromagnetic properties of arbitrary distributions of metallic nanowires. This formalism is unique in allowing readily retrieval of the spatial distribution of the electromagnetic field both at the fundamental frequency (linear analysis) and the second harmonic (non-linear optical response). The formalism also allows for both frequency- and time-domain investigations.

Based on this work, a new software tool with unique features has been implemented and used to achieve a better understanding of the intricate electromagnetic phenomena occurring in nano-structured plasmonic systems. In particular, this tool has been used to design and investigate numerically several new non-linear plasmonic structures and nanodevices with remarkable properties. Amongst them were non-linear plasmonic cavities with high quality factors, plasmonic cavities that support non-linear whispering gallery modes and sub-wavelength non-linear plasmonic sensors with enhanced sensitivity and reduced device volume.

Several other plasmonic systems that show tremendous potential for the development of advanced metamaterials-based devices have also been explored. Specifically, it was demonstrated that nano-patterned metasurfaces can be employed to achieve polarisation controlled electromagnetic response in arrays of cruciform apertures and magnetisation induced second harmonic generation in chiral metallic structures. The numerical investigation of photonic superlattices exhibiting zero effective index of refraction has also been discussed.

It’s still magic, even if you know how it’s done.

Terry Pratchett

Acknowledgements

First and foremost, I would like to thank my supervisor, Nicolae Panoiu. Without his counsel, guidance, insight, patience and understanding I do not think I could have achieved this much. I will be indebted to him for the rest of my professional career.

Second, I would like to extend my gratitude to my secondary supervisor, Anibal Fernandez, for the insightful conversations we have had and the advice he has provided throughout my time as a PhD student.

I would like to also thank my close collaborators at UCL and the LCN, Paul Warburton, Edward Osley and Paul Thompson. The importance of their contribution to the exciting work we have done together cannot be understated, nor can the impact of their ideas, suggestions and advice to the thesis at hand be ignored.

I also thank Ventsilav Valev from the Katholieke Universiteit Leuven and Serdar Kocaman from Columbia University, for their remarkable collaboration and support. It has been a pleasure and a privilege to work alongside them.

I extend the same gratitude to all my other collaborators, colleagues and co-authors with whom I have interacted over these years and whose names are, unfortunately, too many to mention here. Thank you all.

I am also grateful to all the people who have taught me much of what I know today including, among many others, my former mentors and teachers from the West University of Timisoara and the Universite Joseph Fourier.

Of course, a great thank you goes out to the people who have made these past few years an extraordinary experience. My colleagues and friends from the EE department, the CALT and the LCN and my friends both from London and from back home. Many of you have stuck by me and made the difficult times easier and the good times even better.

Finally, I want to thank my family for their support and understanding, and the sacrifices they have sometimes had to make these past few years for me to be here.

I would like to acknowledge my funding agency, the UK Engineering and Physical Sciences Research Council, for supporting this work. I also acknowledge the use of the UCL Legion High Performance Computing Facility, and associated support services, in the completion of this work.

ARTICLES IN PEER REVIEWED JOURNALS

1. S. Kocaman, M. S. Aras, P. -C. Hsieh, J. F. McMillan, **C. G. Biris**, N. C. Panoiu, M. B. Yu, D. L. Kwong, A. Stein and C. W. Wong, *Zero phase delay in negative-index photonic crystal superlattices*, Nature Photonics **5**, 499-505 (2011).

2. **C. G. Biris** and N. C. Panoiu, *Excitation of dark plasmonic cavity modes via nonlinearly induced dipoles: applications to near-infrared plasmonic sensing*, Nanotechnology **22**, 235502 (2011).

3. V. K. Valev, X. Zheng, **C. G. Biris**, A. V. Silhanek, V. Volskiy, B. De Clercq, O. A. Aktsipetrov, M. Ameloot, N. C. Panoiu, G. A. E. Vandenbosch and V. V. Moshchalkov, *The origin of second harmonic generation of hotspots in chiral optical metamaterials*, Opt. Mat. Express **1**, 36-45 (2011).

4. V. K. Valev, A. V. Silhanek, W. Gillijns, Y. Jeyaram, H. Paddubrouskaya, A. Volodin, **C. G. Biris**, N. C. Panoiu, B. De Clercq, M. Ameloot, O. A. Aktsipetrov, V. V. Moshchalkov and T. Verbiest, *Plasmons Reveal the Direction of Magnetization in Nickel Nanostructures*, ACS Nano **5**, 91-96 (2011).

5. **C. G. Biris** and N. C. Panoiu, *Excitation of Linear and Nonlinear Cavity Modes upon Interaction of Femtosecond Pulses with Arrays of Metallic Nanowires*, Appl. Phys. A **103**, 863-867 (2011).

6. **C. G. Biris** and N. C. Panoiu, *Nonlinear pulsed excitation of high-Q optical modes of plasmonic nanocavities*, Opt. Express **18**, 17165-17179 (2010); also in Virt. J. Ultrafast Sci. **9**, No.10, (2010).

7. **C. G. Biris** and N. C. Panoiu, *Surface Second Harmonic Generation in Metamaterials of Nanowires made of Centro-Symmetric Media*, Phys. Rev. B. **81**, 195102 (2010).

8. P. G. Thompson, **C. G. Biris**, E. J. Osley, O. Gatoon, R. M. Osgood, N. C. Panoiu and P. A. Warburton, *Polarization-induced tunability of localized surface plasmon resonances in arrays of sub-wavelength cruciform apertures*, Opt. Express (submitted).

9. **C. G. Biris** and N. C. Panoiu, *Multi-colour Whispering Gallery Modes in Plasmonic Cavities*, (to be submitted).

PEER REVIEWED CONFERENCES

1. N. C. Panoiu and **C. G. Biris**, *Nonlinear modes of plasmonic microcavities: theoretical analysis and device application* [invited], SPIE "Photonics West", San Francisco, USA, 2012.

2. **C. G. Biris** and N. C. Panoiu, *Linear and non-linear dark whispering gallery modes in nanowire plasmonic cavities*, "Metamaterials 2011", Barcelona, Spain, 2011.

3. V. K. Valev, A. V. Silhanek, X. Zheng, **C. G. Biris**, B. De Clercq, V. Volskiy, D. Denkova, N. C. Panoiu, G. A. E. Vandenbosch, O. A. Aktsipetrov, M. Ameloot, V. V. Moshchalkov and T. Verbiest, *Experimental mapping of plasmonic patterns based on second harmonic generation microscopy* [invited], "Metamaterials 2011", Barcelona, Spain, 2011.

4. P. G. Thompson, **C. G. Biris**, E. J. Osley, O. Gaathon, R. M. Osgood, N. C. Panoiu and P. A. Warburton *Polarization-dependent plasmon resonances in sub-wavelength cruciform aperture arrays*, "Metamaterials 2011", Barcelona, Spain, 2011.

5. N. C. Panoiu, **C. G. Biris**, F. Ye, L. Cao and R. M. Osgood, *Nonlinear Optics in Subwavelength Plasmonic Nanostructures* [invited], CLEO/Europe-EQEC, Munich, Germany, 2011.

6. V. K. Valev, A. V. Silhanek, X. Zheng, V. Volskiy, **C. G. Biris**, N. C. Panoiu, B. De Clerq, M. Ameloot, O. A. Aktsipetrov, G. A. E. Vandenbosch, V. V. Moshchalkov and T. Verbiest, *The Origin of Second Harmonic Generation Hotspots in Chiral Optical Metamaterials*, CLEO/Europe-EQEC, Munich, Germany, 2011.

7. P. G. Thompson, **C. G. Biris**, E. J. Osley, R. M. Osgood, N. C. Panoiu and P. A. Warburton, *Polarization-sensitive optical response of plasmonic metasurfaces*, APS March Meeting, Dallas, Texas, USA, 2011.

8. E. J. Osley, P. G. Thompson, **C. G. Biris**, N. C. Panoiu and P. A. Warburton, *Plasmon-mediated polarization-tunable enhancement of optical absorption in a polymer film*, APS March Meeting, Dallas, Texas, USA, 2011.

9. **C. G. Biris** and N. C. Panoiu, *Non-linear active optical devices based on metallic plasmon nano-cavities*, "TIM 2010" Conference, Timisoara, Romania, 2010.

10. N. C. Panoiu, L. Cao, **C. G. Biris**, F. Ye, R. M. Roth and R. M. Osgood, *Computational Modeling of Linear and Nonlinear Optical Properties of Plasmonic Nanostructures* [invited], "28th PIERS", Cambridge, USA, 2010.

11. **C. G. Biris** and N. C. Panoiu, *Localized nonlinear plasmonic cavity modes in two-dimensional distributions of metallic nanowires*, "Metamaterials 2010", Karlsruhe, Germany, 2010.

12. **C. G. Biris** and N. C. Panoiu, *Non-linear Plasmonic Cavities made of Metallic Nanowires: Theoretical Analysis and Applications*, "Nanotechnology and Electronic Materials Symposium", London, UK, 2010.

13. **C. G. Biris** and N. C. Panoiu, *Temporal behaviour of non-linear plasmonic cavity modes excited by ultra-short pulses,* "Photon 10", Southampton, UK, 2010.

14. **C. G. Biris** and N. C. Panoiu, *Linear and Nonlinear Pulse Dynamics in Scattering by Nanowires*, "META '10" 2nd International Conference on Metamaterials, Photonic Crystals and Plasmonics, Cairo, Egypt, 2010.

15. **C. G. Biris** and N. C. Panoiu, *Non-linear Interaction of Femtosecond Pulses with Arrays of Metallic Nanowires*, Nonlinear photonics in micro- and nanostructures, IoP meeting, London, UK, 2009.

16. **C. G. Biris** and N. C. Panoiu, *Numerical Investigations of Second Harmonic Generation in Metamaterials based on Metallic Nanowires*, "Nanotechnology and Electronic Materials Symposium", London, UK, 2009.

17. **C. G. Biris** and N. C. Panoiu, *Surface Second Harmonic Generation in Metamaterials of Nanowires made of Centro-Symmetric Media*, "Metamaterials 2009", London, UK, 2009.

LIST OF NOTATIONS AND ACRONYMS

c	speed of light in vacuum (3×10^8 m/s)
DFG	difference frequency generation
DL	detection limit
ϵ_0	electric permittivity of vacuum (8.854×10^{-12} F/m)
ϵ	electric permittivity
ϵ_r	relative electric permittivity (ϵ/ϵ_0)
FDTD	finite-difference time-domain
FF	fundamental frequency
FWHM	full-width at half-maximum
$H_m^{(1)}(x)$	Hankel function of the first kind
$H_m^{(2)}(x)$	Hankel function of the second kind
$J_m(x)$	Bessel function of the first kind
$\mathbf{k}$	wave vector
λ	wavelength
LSP	localised surface plasmon
MSHG	magnetisation induced second harmonic generation
MSM	multiple scattering matrix
PhC	photonic crystal
PMMA	Poly(methyl methacrylate)
Q	quality factor
RCWA	rigorous coupled wave analysis
RIU	refractive index unit
SERS	surface enhanced Raman scattering
SFG	sum frequency generation
SH	second harmonic
SHG	second harmonic generation
SNR	signal-to-noise ratio
SP	surface plasmon
SPP	surface plasmon polariton
μ_0	magnetic permeability of vacuum (1.256×10^{-6} H/m)
μ	magnetic permeability
μ_r	relative magnetic permeability (μ/μ_0)
ω	angular frequency
WGM	whispering gallery mode
$\chi^{(1)}$	linear susceptibility
$\chi^{(2)}$	second order susceptibility

Contents

List of Figures

List of Tables

Chapter 1

Introduction

Photonics has established itself as one of the leading fields of research in physics and engineering. Nowadays, our ability to manipulate light and matter far surpasses anything that was considered possible only a few years ago. The foundation of these innovations lies in the advances made in nanotechnology and nanofabrication. It is possible today to fabricate structures with characteristic dimensions much smaller than the wavelength at which they operate. As a result, these basic structures can be designed to act as “meta-atoms” leading to effective material properties not available in nature. The end result is a new type of material, a metamaterial, where the properties of the medium can be artificially engineered and controlled at will. The emergence of this new paradigm in materials design has led to the development of materials with remarkable physical properties, including media with negative or zero index of refraction, photonic bandgaps, photonic anisotropy and magnetism at terahertz frequencies. Equally important, metamaterials have been shown to have extraordinary potential applications, such as optical cloaking, superlensing below the diffraction limit, nano-scale sensors, sub-wavelength lasers and perfect absorption. It is thus clear that photonic metamaterials possess the potential needed to tackle some of the main technological requirements of modern society. Major breakthroughs in photonics are already being employed in designing and building new applications in fields as varied as telecommunications, high-performance computing, medicine or renewable energy.

This great potential for innovation, however, brings with it new challenges in photonics research. Understanding the behaviour of the electromagnetic field at the nanoscale becomes a crucial factor in discovering and quantifying the relation between the inner workings of metamaterials and their properties and applications. At sub-wavelength scale, there are a series of intriguing new electromagnetic phenomena that occur in artificial media. Two of them, in particular, will be the main focus of this work. The first is related to the excitation of bound surface waves at metal-dielectric interfaces, known as surface plasmons. The resonant excitation of plasmon modes can lead to very large field enhancement at sub-wavelength scale. The second phenomenon

is the generation of non-linear optical harmonics in arbitrary distributions of metallic nano-particles, and, more specifically, the generation of the second-harmonic. Second harmonic generation is an important optical process, which occurs at half the wavelength (double the frequency) of the input radiation and, being a non-linear process, its intensity depends on the fourth power of the electric field. Consequently, second harmonic generation can, as will be shown in this work, allow for low-power operation of nano-devices and reduced, sub-wavelength device volume. These two characteristics are also directly correlated and the possibility of controlling the former can lead to the ability to manipulate the latter.

The importance of understanding these fundamental electromagnetic phenomena and how they influence the optical properties of metamaterials cannot be understated. In order to be able to employ these effects in enhancing the functionality of current optical devices and designing new ones for advanced applications, a solid, comprehensive, theoretical background of the physical properties of metamaterials is required. Several components of this background are already being investigated by the scientific community with remarkable advances occurring in analytical, numerical simulations and experimental areas. Nevertheless, many unknowns still remain. Specifically, in the context of this work, there is, to the best of my knowledge, little information available on surface second harmonic generation in structured plasmonic materials. It is thus the main objective of this work, to help further understand this non-linear optical process, its properties and how it influences, and can be influenced by, the environment in which it occurs. This information can then be used to design and investigate new non-linear optical devices and extend the range of applications of metamaterials as will be shown in the work at hand. The next section will describe these objectives in more detail.

1.1 Main Objective of the Work

The objectives of this work can be combined in four main vertically integrated thrusts, with each of them building upon and extending the previous one. In this section, these four thrusts will be described in more detail.

The first objective, of analytical nature, is to develop an accurate theoretical model for non-linear optical effects in plasmonic nanostructures. Specifically, I will demonstrate that by employing multiple scattering theory, one can derive a comprehensive model of linear and non-linear light scattering from two dimensional distributions of metallic nanowires. The model will take into account both the surface and bulk contributions to second harmonic generation from arbitrary distributions of metallic objects. This phenomenon has not been, thus far, described, nor have its many potential applications been investigated. I will also show that this theoretical model lends itself well to an efficient numerical implementation and provides the possibility to accurately map

the linear and non-linear electromagnetic field at any given point in the system. Secondly, I will explain how several other important physical parameters can be extracted from this model, including far- and near- field electromagnetic responses.

In the second stage, this analytical model of light scattering in metallic nanowires will be implemented in a new numerical algorithm. The end result of this work is a powerful new software tool, named OPTIMET (OPTIcal METamaterials). This unique tool will be able to efficiently solve the linear and non-linear, frequency domain, scattering problem in arbitrarily distributed, finite arrays of parallel metallic cylinders with arbitrary geometrical and electromagnetic properties. Further to this, I will show how, by extending the mathematical formalism developed in the first step of the project, OPTIMET's capabilities can be augmented to include solving both time-domain problems, as well as the possibility to simulate resonant non-linear modes that possess angular momentum.

Using this tool, in the third phase of this work, I will use advanced numerical simulations to illustrate how resonant non-linear plasmonic structures can be employed to study complex optical effects, such as plasmon coupling, plasmon waveguides, subwavelength light focusing and light localisation. Using the insights into second harmonic generation from metallic structures gained in this step, the focus of the work will shift towards resonant nonlinear plasmonic cavities and their applications. I will investigate plasmonic cavities that can be tailored so as to provide very high quality factors and to support non-linear whispering gallery modes (cavity modes that possess angular momentum). Finally, a new design for a non-linear plasmonic sensor will be proposed, a design based on the previously investigated plasmonic cavities. These devices have sensitivities well in line with currently available plasmon sensor designs, but allow for device volumes up to several orders of magnitude smaller.

In the fourth and final stage of the work, several ideas related to what will have been discussed previously will be considered. The objective at this stage will be to explore other potential areas of interest pertaining to plasmonic metamaterials, so as to better understand how plasmon-enhanced devices can be employed in new applications and how non-linear effects can be effectively integrated into these devices. Specifically, I will be discussing the possibilities offered by nano-patterned metallic surfaces, known as metasurfaces, in polarisation sensitive devices, enhanced surface second harmonic generation in chiral materials and magnetically enhanced non-linear effects. Also, I will demonstrate that, by using photonic crystals, a metamaterial with zero effective refractive index can be achieved. Throughout this part of the work I will be considering several other numerical methods employed in the study of electromagnetic effects. I will discuss how these methods can be used to further expand the understanding of the linear and non-linear optical effects in structured media with focus on plasmon-

enhanced effects. Finally, I will give an overview on the use of numerical methods to help design, tune and validate several experimental findings presented at this stage.

1.2 Outline

In Chapter 2, an overview of the main concepts and ideas which will be used in further chapters is given. This overview is based on both historical and current scientific literature. At the same time, a detailed review of the current state-of-the-art in the field will be given with relevant references to the large body of published work. Throughout the following chapters, this parallel to existing studies will be extended in each case and the need for and contributions of this work will be highlighted.

Chapter 3 consists of a comprehensive description of a new mathematical formalism based on multiple scattering theory, which accurately models second harmonic generation in arbitrary distributions of metallic nanowires. This new method takes into account both the surface and bulk non-linear contribution of the nanowires and allows one to extract accurate linear and non-linear field profiles, as well as total, scattering and absorption cross sections. In this chapter, the extension of this model to allow for time-domain studies will also be presented.

The software implementation of this new formalism as part of the OPTIMET tool will be discussed in Chapter 4. The logical and technical implementation of OPTIMET will be explained in detail. The work flow of the numerical solver will also be linked to the relevant parts of the numerical algorithm so as to give a clear picture of the implementation. The technical presentation will include the various input and output options supported by OPTIMET, details about the architecture it was implemented and used on, as well as its performance as a parallel algorithm.

Following this, in Chapter 5 a detailed analysis of linear and non-linear wave scattering in arrays of metallic nanowires is given. The results in this chapter, obtained using the OPTIMET tool, show how plasmon enhanced surface second harmonic generation leads to exciting new phenomena in a wide array of structures such as single cylindrical scatterers, metallic dimers, nanowire chains and 2D ordered random distributions of metallic cylinders. These phenomena will be thoroughly discussed and the findings put into the wider context of the research area.

In Chapter 6 the design and numerical investigation of non-linear plasmonic cavities will be discussed. To this end, the chapter will contain details on how the time-domain capabilities of OPTIMET can be used to tune these structures, so as to excite modes with very high quality factor. The properties of these modes and their increased sensitivity to geometrical changes will be elaborated upon. Also, the major potential applications of these designs will be analysed and discussed, together with a quantitative characterisation of their performance.

A detailed presentation of how beams carrying angular momentum can be used to excite non-linear whispering gallery modes in plasmonic cavities is given in Chapter 7. Specifically, it will be shown how by analysing the components of the incoming and scattered fields, one can find a close relation between their symmetries and the symmetries of the cavity being excited. This relation can be used to determine whether a given incident beam will couple with a specific whispering gallery mode. The effects of the structural properties of the cavity on the behaviour of the modes will also be discussed in this chapter.

A new design for a non-linear plasmonic sensor will be proposed in Chapter 8. Here, it will be discussed how non-linear plasmon cavity modes can be used to obtain a very high sensor sensitivity, which equals that of current plasmon based devices, but with a much smaller volume. To this end, several of the characteristic properties associated with a sensor, such as sensitivity, detection limit and signal-to-noise ratio, will be analysed and compared with existing designs.

In Chapter 9, the rigorous coupled wave analysis method will be used to investigate nano-patterned metallic surfaces. The results given will illustrate how these metasurfaces can be employed to design plasmonic devices whose optical response is strongly dependent on the polarisation of the incoming light. The physical phenomena leading to this effect will be thoroughly investigated and explained. The findings will also be compared to, and shown to be in very good agreement with, experimental results.

Plasmonic metasurfaces are also the focus of Chapter 10. Here, numerical simulations will be used to validate and further enhance the results of the experimental investigation of metallic metasurfaces with chiral patterns. Specifically, it will be proven that, using surface second harmonic generation, it is possible to accurately map the non-linear field distribution, and that it corresponds to the distribution of the field at the fundamental frequency. Finally, the effects of magnetic fields on second harmonic generation in metasurfaces will also be discussed.

Chapter 11 consists of an analysis of a photonic crystal structure with alternating positive and negative refractive index layers. Numerical simulations using the finite-difference time-domain algorithm will be employed to confirm the experimental findings of a new type of photonic band-gap, which corresponds to a zero refractive index. Also, the same numerical method will be used to show that this remarkable property is not affected by random geometry variations incurred during the fabrication process. The possible applications of this photonic structure will be discussed as well.

Finally, the main conclusions of this work and its contributions to the field are outlined in Chapter 12. Ideas for extending this work and future prospects are also presented in this concluding chapter.

Chapter 2

Background

2.1 Introduction

Electromagnetic effects are closely tied to the internal properties of the materials in which they occur. As was pointed out in the introductory chapter, these properties can now be artificially engineered to produce new types of materials not readily available in the natural world. A common classification scheme for artificial media takes into account the size of their characteristic features relative to the wavelength region in which they operate. Figure 2.1 illustrates this concept. Thus, electromagnetic materials can be split into three broad groups. In the first group, the feature size is much larger than the wavelength of incident light, which is the well known regime of geometrical optics. In the second case, the feature size is comparable to the wavelength and this category of materials is known as *photonic crystals* (PhCs). Finally, in the third group, we have *metamaterials*, materials whose characteristic feature size is much smaller than the wavelength, allowing thus for effective linear and non-linear electromagnetic properties. In this chapter, the latter two types of media will be presented and their fundamental properties analysed.

At the same time, we will look here at the various electromagnetic effects which take place both in natural and artificial media. Specifically, in this chapter, surface plasmon resonances, surface second harmonic generation and magnetisation induced non-linear effects will be presented. The fundamental physical principles behind these phenomena, their properties and the relations between them will be discussed. At the same time, the various influence of these effects on the properties and applications of artificial materials will be considered. Throughout the chapter, the discussion will be accompanied by specific examples from the state-of-the-art research in the field as well as details regarding the historical evolution, current situation and future challenges related to each particular topic.

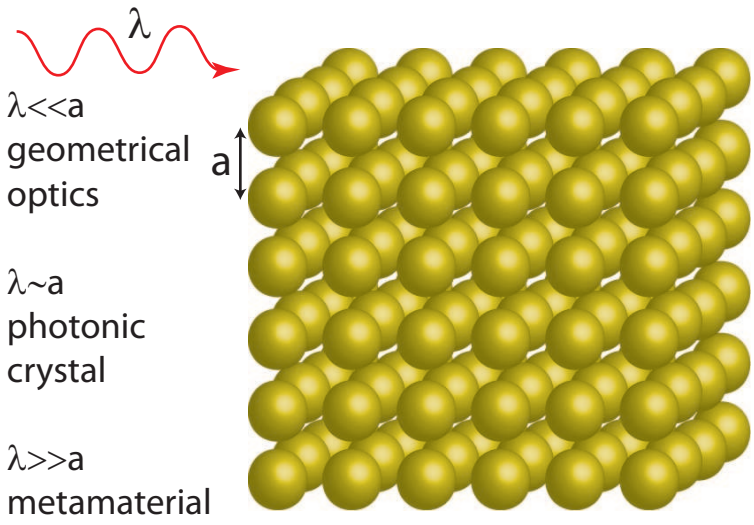

Fig. 2.1: Types of matter categorised by the size of their characteristic feature relative to the operating wavelength.

2.2 Fundamentals of Plasmonics

Several electric and magnetic phenomena have been known since antiquity. However, the modern field of electromagnetism can be said to have begun during the 19^{th} century with the publication of Maxwell's seminal paper *A Dynamical Theory of the Electromagnetic Field*, which first suggested that light is an electromagnetic wave and also laid out the well known Maxwell equations as a mathematical framework to describe the dynamics of the electromagnetic field [1]. Since then, several new areas of research in electromagnetism have emerged which draw upon, and extend, Maxwell's theory of electromagnetism. Among these, one field which has seen remarkable growth in recent years is that of *plasmonics*. Plasmons have been known for some time; however, only in recent years has their great potential application to optics been brought into focus. Before moving on to discuss how plasmons are used in modern optics and photonics and the possibilities they offer for future technologies, it is important to understand the fundamental physical concepts which describe plasmons and their properties. This is the objective of this section. The discussion here will begin by examining Maxwell's equations and showing how, by combining them with the material equations describing the properties of metals, plasmon solutions can be found. At the same time, examples will be given of how plasmons can be practically excited in metallic structures and of some of the state-of-the-art applications of plasmonic devices.

2.2.1 Maxwell's Equations and Electromagnetic Field Dynamics

Due to their nature, most of the physical properties of plasmons can be fully described within the framework of classical electrodynamics. The classical equations of electromagnetism are the well known Maxwell's equations, which in their macroscopic form

are written as [2]:

$$\nabla \cdot \mathbf{D} = \rho, \tag{2.1a}$$

$$\nabla \cdot \mathbf{B} = 0, \tag{2.1b}$$

$$\nabla \times \mathbf{E} = -\frac{\partial \mathbf{B}}{\partial t}, \tag{2.1c}$$

$$\nabla \times \mathbf{H} = \mathbf{J} + \frac{\partial \mathbf{D}}{\partial t}, \tag{2.1d}$$

where $\mathbf{E}$ and $\mathbf{H}$ are the electric and magnetic fields, respectively, $\mathbf{D}$ is the electric displacement, or electric induction, $\mathbf{B}$ is the magnetic induction, and ρ and $\mathbf{J}$ are the charge and current densities, respectively. In the case of a homogeneous isotropic medium, Maxwell's equations are complemented by a set of material equations, which relate the macroscopic fields $\mathbf{E}, \mathbf{H}, \mathbf{D}, \mathbf{B}$ to the electric polarisation $\mathbf{P}$ and magnetisation $\mathbf{M}$ inside the material:

$$\mathbf{D} = \epsilon_0 \mathbf{E} + \mathbf{P} \tag{2.2a}$$

$$\mathbf{H} = \frac{1}{\mu_0}\mathbf{B} - \mathbf{M}, \tag{2.2b}$$

where ϵ_0 is the electric permittivity and μ_0 the magnetic permeability of free space. The polarisation $\mathbf{P}$ can also be related to both the *bound* charge and current density *via*:

$$\nabla \cdot \mathbf{P} = -\rho_p, \tag{2.3a}$$

$$\mathbf{J} = \frac{\partial \mathbf{P}}{\partial t}. \tag{2.3b}$$

The total charge and current density are constrained by the charge conservation, or continuity, equation:

$$\nabla \cdot \mathbf{J} + \frac{\partial \rho}{\partial t} = 0, \tag{2.4}$$

a relation that can be easily derived from Maxwell's equations (2.1). Moreover, in linear and isotropic media, the electric field $\mathbf{E}$ and the magnetic field $\mathbf{H}$ can be related to the electric and magnetic inductions $\mathbf{D}$ and $\mathbf{B}$ by the constitutive relations:

$$\mathbf{D} = \epsilon_0 \epsilon_r \mathbf{E}, \tag{2.5a}$$

$$\mathbf{B} = \mu_0 \mu_r \mathbf{H}, \tag{2.5b}$$

where ϵ_r and μ_r are the relative permittivity and permeability of the medium, respectively. Equations (2.5), in conjunction with the material equations (2.2), also show that the electric polarisation and magnetisation are proportional to the electric and magnetic field, respectively. This can be expressed by introducing the electric and magnetic sus-

ceptibilities χ_e and χ_m, respectively, namely $\mathbf{P} = \epsilon_o \chi_e \mathbf{E}$ and $\mathbf{M} = \mu_0 \chi_m \mathbf{H}$. From Eqs. (2.5), the relative permittivity and permeability can then be related to the susceptibilities by:

$$\epsilon_r = 1 + \chi_e, \tag{2.6a}$$

$$\mu_r = 1 + \chi_m. \tag{2.6b}$$

It is worth noting here that a non-magnetic material, namely a medium in which $\mathbf{M} = 0$, is characterised by $\chi_m = 0$ and $\mu_r = 1$.

One of the most important features of Maxwell's equations is that they allow for travelling wave solutions that carry energy. Consider for simplicity an infinite medium with no sources (*i.e.* $\rho = 0$ and $\mathbf{J} = 0$), which has a constant spatial distribution of the permittivity ϵ and permeability μ. Then, taking the curl of Eq. (2.1c) leads to:

$$\nabla \times \nabla \times \mathbf{E} = -\mu \frac{\partial}{\partial t} \nabla \times \mathbf{H}, \tag{2.7}$$

which according to Eq. (2.1d) without sources can be written:

$$\nabla \times \nabla \times \mathbf{E} = -\mu \epsilon \frac{\partial^2 \mathbf{E}}{\partial t^2}. \tag{2.8}$$

Finally, using the vector relation $\nabla \times (\nabla \times \mathbf{A}) = \nabla(\nabla \cdot \mathbf{A}) - \nabla^2 \mathbf{A}$, where $\mathbf{A}$ is any vector function of $\mathbf{r}$, Eq. (2.8) can now be written:

$$\nabla^2 \mathbf{E} - \mu \epsilon \frac{\partial^2 \mathbf{E}}{\partial t^2} = 0, \tag{2.9}$$

which is the electromagnetic wave equation for the electric field. Here, we have also made use of the fact that the divergence $\nabla \cdot \mathbf{D} = 0$ when no sources are present. For the magnetic field, the same line of reasoning can be followed, the result being that the dynamics of $\mathbf{B}$ can be described by Eq. (2.9), too.

One of the simplest solutions for Eq. (2.9) is the transverse plane wave. Assuming a harmonic spatial and temporal dependence of the fields, $E \sim e^{i(\mathbf{k}\cdot\mathbf{r} + \omega t)}$, Eq. (2.9) can be rewritten as:

$$\nabla^2 \mathbf{E} - \mu \epsilon \omega^2 \mathbf{E} = 0, \tag{2.10}$$

which is the Helmholtz equation. The wave vector $\mathbf{k}$ is related to the frequency ω and properties of the medium by $\mathbf{k}^2 = \mu \epsilon \omega^2$, which implies a phase velocity of $v \equiv \omega/k = 1/\sqrt{\epsilon\mu}$. The phase velocity can also be expressed in terms of the refractive index, n, and the speed of light in vacuum, c, as $v = c/n$, which leads to the expression for the refractive index, $n = \sqrt{\epsilon_r \mu_r}$.

2.2.2 Electrodynamics of Plasma Oscillation

A plasmon is commonly defined as a quanta of plasma oscillations of the free electron gas [3]. The plasmon can thus be viewed as a quasi-particle whose physical properties strongly depend on the electromagnetic characteristics of the medium in which it is excited. It can be described in simpler terms as the oscillation of the electrons in a free electron gas against the positive charge background provided by the fixed ions in a metal. In an ideal metal, *i.e.* a metal with no optical losses (damping), and with no external sources, this oscillation occurs at the plasma frequency associated with the metal.

In *dispersive* media, ϵ and μ are dependent on the frequency ω of the electromagnetic wave propagating in the medium. Assuming the case of non-magnetic metals (*i.e.* $\mu_r = 1$) one can easily derive a general expression for the frequency dispersion $\epsilon(\omega)$. One simple model which explains the behaviour of metals over a broad frequency range is the free electron model. In this model, a metal is viewed as consisting of a classical gas of non-interacting electrons, which exhibit free movement within the confines of the material boundaries. The equation of motion for an electron which is acted upon by an electric field $\mathbf{E}$ can be written as:

$$m\ddot{\mathbf{r}} + m\gamma\dot{\mathbf{r}} = -e\mathbf{E}, \tag{2.11}$$

where $\mathbf{r}$ is the electron displacement, γ is the damping coefficient (frequency) due to electron-ion collisions and e is the electron charge. Assuming an harmonic time dependence for $\mathbf{E}$ and $\mathbf{r}$, $\mathbf{E}(t) = \mathbf{E}_0 e^{i\omega t}$ and $\mathbf{r}(t) = \mathbf{r}_0 e^{i\omega t}$, where $\mathbf{r}_0$ and $\mathbf{E}_0$ are the amplitudes of $\mathbf{E}$ and $\mathbf{r}$, respectively, the solution to Eq. 2.11 is:

$$\mathbf{r}_0 = \frac{e}{m(\omega^2 - i\gamma\omega)}\mathbf{E}_0. \tag{2.12}$$

The displacement of the electrons in the metal will induce a polarisation $\mathbf{P} = -Ne\mathbf{r}$, where N is the electron density. By using this expression for the polarisation, Eq. (2.2a) becomes:

$$\mathbf{D} = \epsilon_0 \left[1 - \frac{Ne^2}{\epsilon_0 m(\omega^2 - i\gamma\omega)}\right]\mathbf{E}, \tag{2.13}$$

where, for simplicity, the subscript of the fields was dropped. By denoting $\omega_p^2 = (Ne^2)/(\epsilon_0 m)$, the plasma frequency, and using Eq. (2.5) it becomes easy to identify in Eq. (2.13) the expression of the dielectric function $\epsilon(\omega)$ of the free electron gas as:

$$\epsilon(\omega) = \epsilon_0 \left(1 - \frac{\omega_p^2}{\omega^2 - i\gamma\omega}\right). \tag{2.14}$$

Expression (2.14) is known as the *Drude model* of the permittivity of metals [4].

Equation (2.14) leads to an interesting observation. The dielectric function $\epsilon(\omega)$ is a complex quantity, which means that an electromagnetic wave interacting with the medium experiences absorption and thus its energy is dissipated into the medium. The attenuation of the wave by an absorbing material can be expressed by using a complex wave vector k:

$$k = \beta + i\frac{\alpha}{2}, \tag{2.15}$$

where α is the absorption coefficient, that is to say, the wave amplitude decreases with the propagation distance, d, as $e^{-\alpha d/2}$, also known as Beer's law. Moreover, β represents the propagation constant of the wave. Assuming a complex dielectric function $\epsilon = \epsilon_1 + i\epsilon_2$, the real and imaginary components can be expressed as a function of the components of k. By taking into account that $k = \sqrt{\epsilon_r \mu_r}(\omega/c)$, these components can be written as:

$$\frac{\epsilon_1}{\epsilon_0} = \frac{c^2}{\omega^2}\left(\beta^2 - \frac{\alpha^2}{4}\right), \tag{2.16a}$$

$$\frac{\epsilon_2}{\epsilon_0} = \frac{c^2}{\omega^2}\beta\alpha. \tag{2.16b}$$

In the same manner, ϵ_1 and ϵ_2 can be related to the complex index of refraction $\tilde{n}$:

$$\frac{\epsilon_1}{\epsilon_0} = n^2 - \kappa^2, \tag{2.17a}$$

$$\frac{\epsilon_2}{\epsilon_0} = 2n\kappa, \tag{2.17b}$$

where $\tilde{n} = n + i\kappa$ and we employed the relation between n and k, $k = n(\omega/c)$.

Equation (2.14) has a series of important consequences. In the very low frequency regime, where $\omega < \omega_p$ and $\omega \ll \gamma$, the imaginary part of the dielectric function is dominant and metals are highly absorbent. In this case, the absorption coefficient can be written as:

$$\alpha = \sqrt{2\sigma_{DC}\omega\mu_0}, \tag{2.18}$$

where $\sigma_{DC} = \omega_p\epsilon_0/\gamma$ is the DC electrical conductivity. From Beer's law it is possible to relate the dc conductivity with the characteristic depth of the penetration of an electromagnetic wave inside a metal, also know as the *skin depth* δ. The definition of the skin depth implies that the field intesity inside the metal is attenuated by $e^{-d/\delta}$, which implies:

$$\delta = \frac{2}{\alpha} = \sqrt{\frac{2}{\sigma_{DC}\omega\mu_0}}. \tag{2.19}$$

As ω approaches ω_p, σ_{DC} is no longer sufficient to describe the electromagnetic response of the metal. Instead, a complex conductivity $\sigma(\omega)$ is required. The method of obtaining the expression for the frequency dependent conductivity is similar to that

used to obtain Eq. (2.14). The frequency dependent expression $\sigma(\omega)$, also know as Drude's law of conductivity [2], can then be cast as:

$$\sigma(\omega) = \frac{\sigma_{DC}}{1 - i\omega\tau}, \tag{2.20}$$

where $\tau = \gamma^{-1}$ is the mean time interval between electron-ion collisions. Equations (2.20) and (2.14) can be used to find the relation between the dielectric function and the complex conductivity:

$$\epsilon(\omega) = 1 + \frac{i\sigma(\omega)}{\omega}. \tag{2.21}$$

For most metals, when ω approaches ω_p, ω becomes much larger than γ and damping effects can be neglected. To give an example, for the case of gold, $\omega_p = 13.72 \times 10^{15}\ \mathrm{rad/s}$ and $\gamma = 4.05 \times 10^{13}\ \mathrm{s}^{-1}$ [5]. Equation (2.14) can then be simplified to:

$$\epsilon(\omega) = 1 - \frac{\omega_p^2}{\omega^2}, \tag{2.22}$$

with the dielectric function becoming purely real. The wave vector can then be written as:

$$k = \frac{\sqrt{\omega_p^2 - \omega^2}}{c}, \tag{2.23}$$

or, alternatively:

$$\omega^2 = \omega_p^2 + k^2 c^2. \tag{2.24}$$

This equation describes the frequency dispersion of travelling waves in a free electron gas. Figure 2.2 plots this dispersion relation. For frequencies $\omega < \omega_p$ the wave number k is purely imaginary and thus no waves can propagate. In the regime where $\omega > \omega_p$, the dispersion relation shows that electromagnetic waves can propagate. The group velocity of these waves, defined as $v_g = d\omega/dk$, is smaller than c and the metal behaves as a transparent dielectric. Finally, when $\omega = \omega_p$, one has $\epsilon(\omega) = 0$. Inserting this expression into Eq. (2.5a) and using Eq. (2.2a), the electric field inside the free electron gas becomes:

$$\mathbf{E} = -\frac{\mathbf{P}}{\epsilon_0}, \tag{2.25}$$

which is a depolarisation field [3]. Physically, this can be understood in terms of the oscillation of the free electrons in the plasma. A static ($\omega = 0$) electric field induces the polarisation of the plasma gas. If the field is turned off, the electrons will feel a restoring force which will lead to the excitation of a collective longitudinal oscillation against the positive background of the fixed ions in the metal. This oscillation will occur at a frequency $\omega = \omega_p$, which is the natural resonant frequency of the plasma gas, the reason for which it is called the plasma frequency. The quanta of oscillations of the plasma gas is known as a plasmon or, to distinguish it from other plasmonic effects

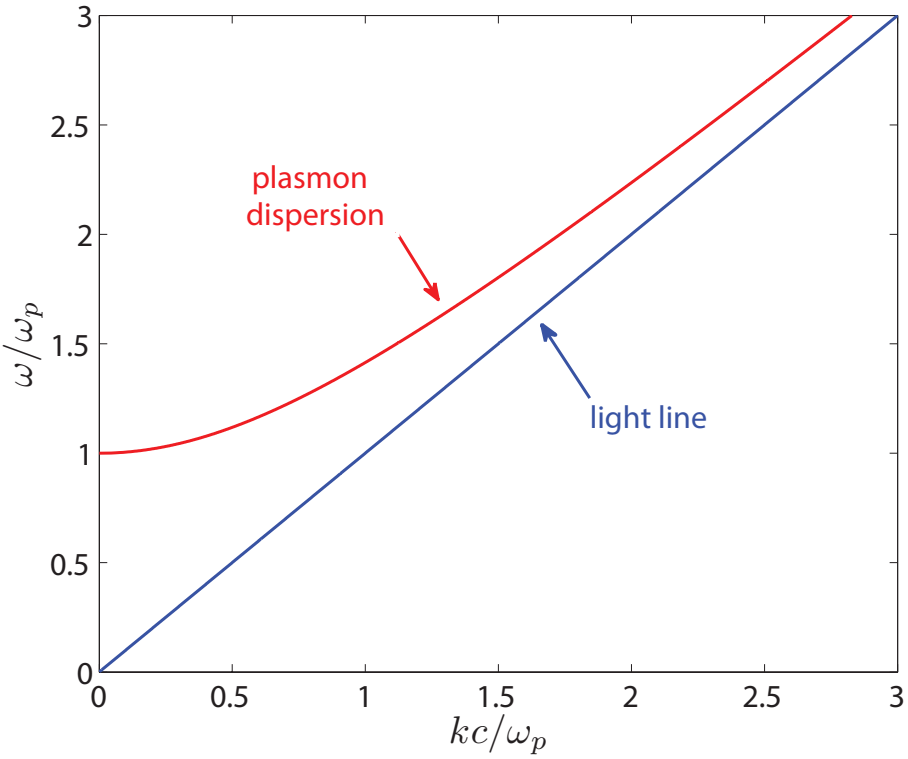

Fig. 2.2: Dispersion of an electromagnetic wave propagating in a free electron gas ("plasmon dispersion") and in free space ("light line").

occurring at the surface of the metal, a *volume plasmon*.

It is worth mentioning that in the case of metals the free electron model becomes less accurate as the frequency approaches the near-infrared. This is especially important in the case of noble metals such as Au and Ag, as they are most widely used in plasmonic applications. The source of this discrepancy is that the free electron model does not take into account the inter-band effects which are the result of the excitation of electrons from the filled bands below the Fermi surface into higher level bands *via* photon absorption. This effect can be modelled by adding to Eq. (2.14) a second term corresponding to bound electrons with specific oscillator strengths and frequencies. Formally, this additional term is expressed by rewriting the dielectric function as:

$$\frac{\epsilon(\omega)}{\epsilon_0} = \epsilon_r^f + \epsilon_r^b. \tag{2.26}$$

Here, ϵ_r^f is the dielectric constant of free electrons, or intra-band contribution described by Eq. (2.14) and can be written as:

$$\epsilon_r^f = 1 - \frac{\Omega_p^2}{\omega^2 - i\omega\gamma}. \tag{2.27}$$

This is the Drude model of the dielectric function with ω_p replaced by the plasma frequency of an oscillator with strength f_0, $\Omega_p = \sqrt{f_0}\omega_p$. The second term in Eq. (2.26)

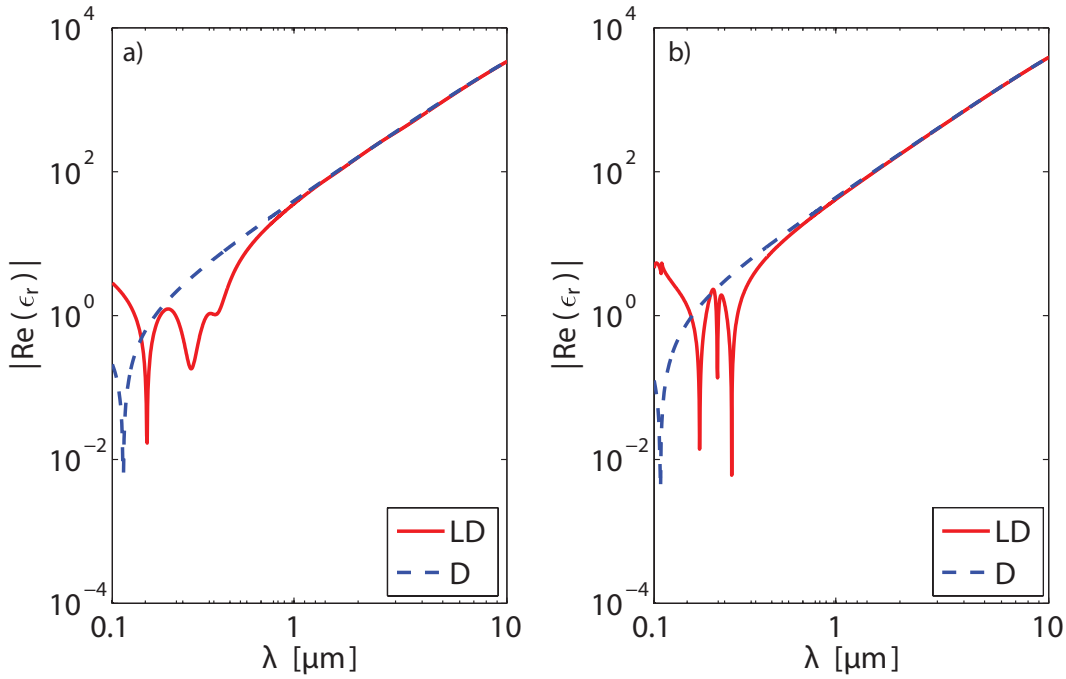

Fig. 2.3: Comparison between the Drude and Lorentz-Drude models for Au (a) and Ag (b).

accounts for the contribution of the bound electrons (or inter-band contribution) and is of the form:

$$\epsilon_r^b = \sum_{j=1}^{N} \frac{f_j \omega_p^2}{(\omega_j^2 - \omega^2) + i\omega\gamma_j}. \tag{2.28}$$

Here N is the number of oscillators with frequency ω_j, strength f_j and damping frequency γ_j where $(j = 1, \cdots, N)$ [6]. This model is also known as the *Lorentz-Drude model*. Figure 2.3 shows a comparison between the Drude and the Lorentz-Drude models for Au and Ag. At the near-infrared and higher frequencies, the Drude model no longer accurately describes the complex behaviour of the dielectric constant of metals. At lower frequencies, however, the Drude and Lorentz-Drude models lead to similar results. Therefore, the Drude dielectric function can be successfully employed to model the various electromagnetic phenomena which can occur in plasmonics, but care must be used, particularly when considering the frequency range in which these phenomena are studied. Throughout this work, both the Drude and the Lorentz-Drude models will be employed depending on the particular application that is investigated. The use of one formalism over the other will be clearly specified in all cases.

This section has given a brief overview of the principal physical concepts used in plasmonics, as well as an explanation of the origin of plasmons in metals. Volume plasmons are not, however,the only possible type of plasmons so that the next section is devoted to the plasmonic effects that are observed at the interface between a metal and a dielectric.

2.2.3 Surface Plasmon Polaritons at Metal-Dielectric Interfaces

Plasmonic effects do not occur solely in bulk metals. First investigated in the late 1950s [7], surface plasmons are a type of electromagnetic waves which propagate at the surface of a conductor embedded in a dielectric. Surface plasmons are evanescent waves which exhibit exponential decay in the direction normal to the metal-dielectric interface, leading to a very high field concentration within sub-wavelength regions [8]. Because surface plasmons are a direct consequence of the coupling of the electromagnetic foeld with the plasma oscillations of a metal, they are highly sensitive to the properties of the background and conductive environment, as well as the shape of the interface at which they occur [9].

To better understand how plasmon surface waves can be described as solutions to Maxwell's equations, consider the simple geometry in Fig. 2.4 consisting of two semi-infinite planar media: a linear, loss-less dielectric with $\epsilon_d > 0$ and a non-magnetic metallic region with $Re[\epsilon_m(\omega)] < 0$. The interface between the two media is assumed to be located at $z = 0$. Assuming as well that there is no spatial variation of the dielectric properties in the x and y direction , the dielectric function of the entire system can now be written as $\epsilon = \epsilon(z)$. With these conventions, a propagating wave in the x direction can be described as $\mathbf{E}(\mathbf{r}) = \mathbf{E}(z)e^{ik_x x}$ where $\mathbf{k} = (k_x, k_y, k_z)$ is the wave vector. Coupled with Eq. (2.10), this leads to the desired form of the wave equation:

$$\frac{\partial^2 \mathbf{E}(z)}{\partial z^2} + \left(k_0^2 \frac{\epsilon}{\epsilon_0} - k_x^2\right)\mathbf{E} = 0, \tag{2.29}$$

where k_0 is the free-space wave vector. A similar expression can be derived for the magnetic field $\mathbf{H}$. The wave equation (2.29) supports two solutions representing waves propagating in the x direction and bound to the metal-dielectric interface (*i.e.* exponentially decaying in the z direction, away from the metal-dielectric interface). The two waves correspond to the TE and TM polarisations [10].

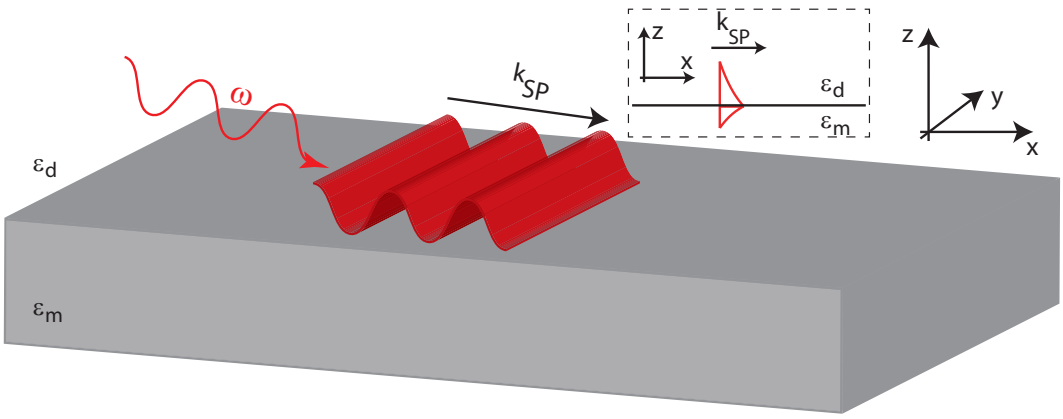

Fig. 2.4: Interface between a dielectric and a conductor. Propagation of surface waves is assumed to be in the x direction. Inset shows 2D view of surface wave propagation.

In the TM polarisation, also called the *p*-polarisation case, the electric field has no components on the y axis and the magnetic field is oriented along the y axis. Then, simple calculations show that, assuming a harmonic temporal dependence of the fields, the field components are given by:

$$H_y^d(z) = A_d e^{ik_x x - k_z^d z} \tag{2.30a}$$

$$E_x^d(z) = -i\frac{A_d}{\omega\epsilon_d} k_z^d e^{ik_x x - k_z^d z} \tag{2.30b}$$

$$E_z^d(z) = \frac{A_d k_x}{\omega\epsilon_d} e^{ik_x x - k_z^d z}, \tag{2.30c}$$

in the dielectric region ($z > 0$) and:

$$H_y^m(z) = A_m e^{ik_x x - k_z^m z} \tag{2.31a}$$

$$E_x^m(z) = i\frac{A_m}{\omega\epsilon_m} k_z^m e^{ik_x x - k_z^m z} \tag{2.31b}$$

$$E_z^m(z) = \frac{A_m k_x}{\omega\epsilon_m} e^{ik_x x - k_z^m z}, \tag{2.31c}$$

in the metallic region ($z < 0$), where A_d and A_m are the field amplitudes in the dielectric and metallic regions, respectively. The continuity conditions of the fields at the metal-dielectric interface are:

$$H_y^d(z) = H_y^m(z) \tag{2.32a}$$

$$E_y^d(z) = E_y^m(z). \tag{2.32b}$$

Equation (2.32a) implies that $A_d = A_m$, while from Eq. (2.32b) it is easy to see that:

$$\frac{A_d}{\epsilon_d} k_z^d = -\frac{A_m}{\epsilon_m} k_z^m. \tag{2.33}$$

In addition, the field components expressed by Eqs. (2.30) and (2.31) must obey the wave equation (2.29), which leads to the following relations:

$$k_z^d = \sqrt{k_x^2 - k_0^2 \epsilon_d/\epsilon_0}, \tag{2.34a}$$

$$k_z^m = \sqrt{k_x^2 - k_0^2 \epsilon_m/\epsilon_0}. \tag{2.34b}$$

Combining the continuity conditions with Eq. (2.34) yields the dispersion relation of the surface waves $k_x = k_x(\omega)$, of the form [11]:

$$k_x(\omega) = \frac{\omega}{c\epsilon_0}\sqrt{\frac{\epsilon_d \epsilon_m}{\epsilon_d + \epsilon_m}}. \tag{2.35}$$

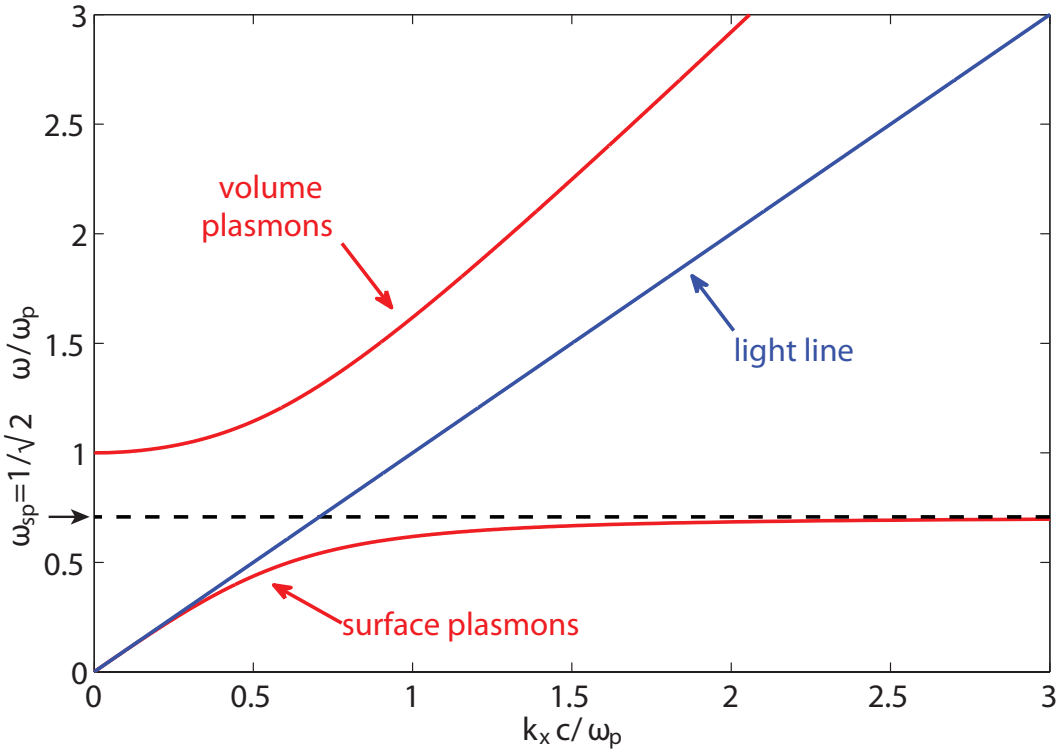

Fig. 2.5: Dispersion relation of a surface plasmon polariton wave at the interface between air and a loss-less metal with plasma frequency ω_p. The dashed line indicates the limiting surface plasmon frequency ω_{sp}.

Before further analysing the properties of *surface plasmon polaritons* (SPPs) it is relevant to point out one important property of these bound surface modes. Equation (2.33) can be satisfied only in the case in which ϵ_d and ϵ_m have opposite signs as surface confinement requires $Re(k_z^d) > 0$ and $Re(k_z^m) > 0$. Assuming $\epsilon_d > 0$, which is true in the case of dielectrics, it becomes necessary that $Re(\epsilon_m) < 0$, that is, the defining property of a metal. In conclusion, SPP waves can only occur at the interface between a metal and an insulator, typically a metal-dielectric interface. Moreover, Eqs. (2.30) and (2.31) describe a surface mode with evanescent decay in both directions normal to the interface. The decay length of the surface wave is defined as the reciprocal value of $k_z^{d,m}$, that is $l_{d,m} = 1/|k_z^{d,m}|$. It should be noted that the decay lengths in the two media are different.

The dispersion relation (2.35) reveals several of the most important characteristics of surface plasmons. Figure 2.5 plots the dispersion of surface plasmon polariton waves at the interface between air and a metal with plasma frequency ω_p. The metal is assumed to be described by the Drude model; with damping frequency $\gamma = 0$. Under these cicumstances, the dielectric constant has real values ($Im[\epsilon_m(\omega)] = 0$). The dispersion curve of SPPs lies to the right side of the light line defined by $\omega = kc\sqrt{\epsilon_o/\epsilon_d}$, which implies that SPPs in this particular configuration cannot directly couple with, nor radiate, a free-space photon.

Figure 2.5 also illustrates that for very low frequencies ($\omega << \omega_p$), the dispersion of SPPs approaches that of a free propagating light wave. In this region, SPPs become indistinguishable from grazing-incidence light waves. At higher frequencies, where ω approaches ω_p, the SPP dispersion curve levels off as $k_x \to \infty$ and the group velocity of the surface wave goes asymptotically to zero. In this regime, SPPs are called *surface plasmons* and are similar to an *electrostatic* surface wave [11]. The electrostatic character of the wave stems from the fact that it can be obtained as a solution to the Laplace equation $\nabla^2\phi = 0$, ϕ being the electric potential ($\mathbf{E} = -\nabla\phi$). The solution of the Laplace equation that describes a wave propagating in the x direction and decaying exponentially in the z direction is [10]:

$$\phi(z)_d = A_d e^{ik_x x - k_z^d z}, \tag{2.36}$$

for $z > 0$ and

$$\phi(z)_m = A_m e^{ik_x x + k_z^m z}, \tag{2.37}$$

when $z < 0$. The boundary conditions at $z = 0$ can now be written as:

$$\phi_d(z) = \phi_m(z), \tag{2.38a}$$

$$\frac{\epsilon_d}{\epsilon_0}\frac{d\phi_d(z)}{dz} = \frac{\epsilon_m}{\epsilon_0}\frac{d\phi_m(z)}{dz}, \tag{2.38b}$$

corresponding to the continuity of the tangential and normal components of the electric field, respectively. Finally, for Eqs. (2.36) and (2.37) to be solutions to a Laplace equation, it is necessary that $\nabla^2\phi_{d,m} = 0$, which requires that $k_z^d = k_z^m = k_x$.

One of the characteristics of surface plasmons in the $k_x \to \infty$ limit is that the evanescent decay length $z = 1/k_z^{d,m}$ is the same in both media. Combining the continuity relations with the Laplace solutions (2.36) and (2.37) and the above conditions yields:

$$A_d = A_m \tag{2.39a}$$

$$\epsilon_d + \epsilon_m = 0. \tag{2.39b}$$

Since in the case of dielectrics, $\epsilon_d > 0$, Eq. (2.39b) can only be satisfied if $\epsilon_m < 0$, which is a characteristic shared with SPPs. Inserting Eq. (2.39b) into Eq. (2.35) leads to the conclusion that a surface plasmon is the limit case of a surface plasmon polariton with $k_x \to \infty$. Assuming a metal described by Eq. (2.22), the limiting surface plasmon frequency ω_{sp} can be expressed in the well-known form:

$$\omega_{sp} = \frac{\omega_p}{\sqrt{\epsilon_d/\epsilon_0 + 1}}. \tag{2.40}$$

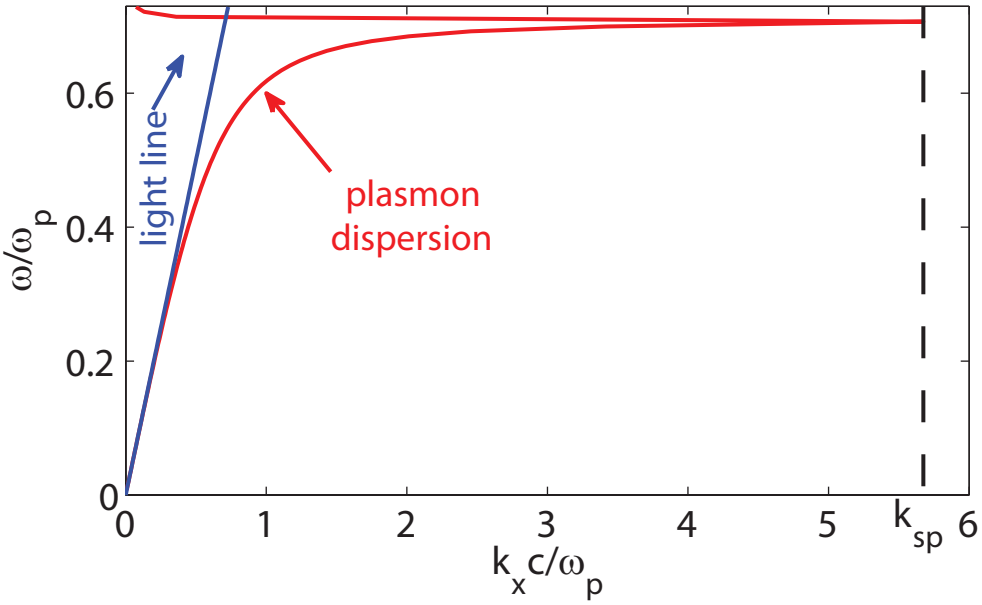

Fig. 2.6: Dispersion relation of a surface plasmon polariton wave at the interface between air and Au in the Drude model. The dashed line indicates the limiting surface plasmon wave vector k_{SP}

The region in which $\omega \to \omega_{sp}$ is also known as the *non-retarted* regime (*i.e.* the speed of light can be considered to be infinite), and it is another method of defining the regime in which surface plasmons exist [10]. Consequently, surface plasmon polaritons are said to exist in the retarted regime, where the finiteness of the speed of light is taken into consideration.

In the case of a real metal with $\gamma \neq 0$ and described by the Drude model (2.14), the dispersion curve of SPPs changes significantly. Figure 2.6 shows the dispersion relation of SPPs at the interface between air and Au. The main difference between this case and a loss-less metal is that the SPP wave vector k_x is now bound by a maximum value, k_{sp}, which occurs as ω approaches ω_p. One important consequence of this fact is that SPPs with a wavelength smaller than $\lambda_{sp} = 2\pi/\mathrm{Re}(k_{sp})$ cannot be excited in real metals.

The decay length of a surface plasmon, on either side of the interface, can be calculated by inserting the dispersion relation (2.35) into Eq. (2.34). The z-component of the wave vector, which is also equal to the decay constant, becomes:

$$k_z^{d,m} = \frac{\omega}{c}\frac{1}{\sqrt{\epsilon_0}}\sqrt{\frac{-\epsilon_{d,m}^2}{\epsilon_d + \epsilon_m}}. \tag{2.41}$$

The decay constant determines the attenuation length, which is defined as $l_{d,m} = 1/k_z^{d,m}$. This is the characteristic length after which the field decreases to $1/e$. In the dielectric medium it is larger than the wavelength of propagating wave, as $l_d > 1/k_x$. In the metallic region the attenuation length (skin depth) is determined by Eq. (2.19). At high frequencies, where the surface plasmon is in the non-retarted regime, the skin

depth becomes $\delta \sim 1/k_x$ so that l_m is comparable to the wavelength of the plasmon [11]. This leads to a very strong localisation of the field at the interface which is one of the most important characteristics of surface plasmon resonances in terms of possible applications.

In the case of the TE polarisation, also called the *s*-polarisation case, the solution of Maxwell's equations are similar to Eqs. (2.30) and (2.31), the non-zero components of the electromagnetic field being given by the following expressions:

$$E_y^d(z) = A_d e^{ik_x x - k_z^d z} \tag{2.42a}$$

$$H_x^d(z) = i\frac{A_d}{\omega\mu_0} k_z^d e^{ik_x x - k_z^d z} \tag{2.42b}$$

$$H_z^d(z) = -\frac{A_d k_x}{\omega\mu_0} e^{ik_x x - k_z^d z}, \tag{2.42c}$$

for $z > 0$, respectively:

$$E_y^m(z) = A_m e^{ik_x x - k_z^m z} \tag{2.43a}$$

$$H_x^m(z) = -i\frac{A_m}{\omega\mu_0} k_z^m e^{ik_x x - k_z^m z} \tag{2.43b}$$

$$H_z^m(z) = -\frac{A_m k_x}{\omega\mu_0} e^{ik_x x - k_z^m z}, \tag{2.43c}$$

for $z < 0$. The continuity conditions for the TM case are:

$$E_y^d(z) = E_y^m(z) \tag{2.44a}$$

$$H_z^d(z) = H_z^m(z). \tag{2.44b}$$

which as before imply that $A_d = A_m$ and:

$$A_d(k_z^d + k_z^m) = 0. \tag{2.45}$$

Because for waves bound to the metal-dielectric surface $Re(k_z^d) > 0$ and $Re(k_z^m) > 0$, Eq. (2.45) can only be satisfied when $A_d = A_m = 0$. Consequently, for this type of geometry, surface plasmon polaritons cannot exist for the TE polarisation.

Finally, a third type of surface plasmon excitations can exist in several other geometries, such as metallic particles. These excitations do not propagate but are bound to the surface of the particle; they are called *localised surface plasmons* (LSPs) [12]. Localised surface plasmons, like SPPs, can only occur at frequencies smaller than a certain threshold frequency ω_{lsp} which can be determined in the electrostatic regime by solving the Laplace equation with appropriate boundary conditions. For example, in the case of a metallic sphere embedded in air and described by a Drude model, the LSP

frequencies can be written [10]:

$$\omega_{lsp}^{m} = \omega_p \sqrt{\frac{m}{2m+1}}, \tag{2.46}$$

where m is the order of the plasmon mode. For small spheres, the only important contribution is that of the dipole mode given by $m = 1$, in which case the LSP frequency approaches the well known value $\omega_{lsp} = \omega_p/\sqrt{3}$. For largerspheres, higher order multipole modes become significant and in the limit $m \to \infty$, relation (2.46) approaches the frequency of surface plasmons at a planar interface, $\omega_{lsp}^{\infty} = \omega_p/\sqrt{2}$.

In the case of a cylindrical geometry, due to the symmetries of the structure, the LSP frequency depends on the polarisation of the electric field [13]. In the high frequency regime, for an electric field normal onto the interface, ω_{lsp} approaches the frequency of surface plasmons at a planar interface, $\omega_{lsp} = \omega_p/\sqrt{2}$. When the system consists of several cylinders with a filling fraction f defined as the ratio between the volume occupied by the metal and the total volume, the LSP frequency becomes the reduced plasmon frequency $\omega = \sqrt{f}\omega_p$ [11]. If the electric field is parallel to the axis of the cylinder, it does not induce surface charges at the interface and the only possible plasmon modes are volume plasmons.

Localised surface plasmons differ from surface plasmon polaritons by being restricted to small objects and having a discrete set of frequencies, which depend on the shape and size of the confining geometry. Unlike propagating SPPs, localised plasmons can be excited by light of appropriate frequency and polarisation. For LSPs with frequencies close to that of an SPP it is also possible for a LSP to decay into, or be excited by, a surface plasmon polariton.

2.2.4 Excitation of Surface Plasmon Polaritons at Metallic Surfaces

The wave vector of a surface plasmon polariton at a flat metal-dielectric interface is larger than that of a photon with the same frequency, which prevents direct coupling between incoming photons and SPPs. Therefore, special techniques are required in order to match the wave vector of the incoming radiation and that of the surface plasmon. These techniques involve coupling through prisms, coupling *via* surface features, as well as coupling using optical near-field effects.

Prism based coupling of light to surface plasmon polariton modes is based on the fact that the wave vector of a beam of light passing through a prism is modified as follows:

$$k_{prism} = \frac{\omega}{c}\sqrt{\frac{\epsilon_{prism}}{\epsilon_0}}\sin\theta, \tag{2.47}$$

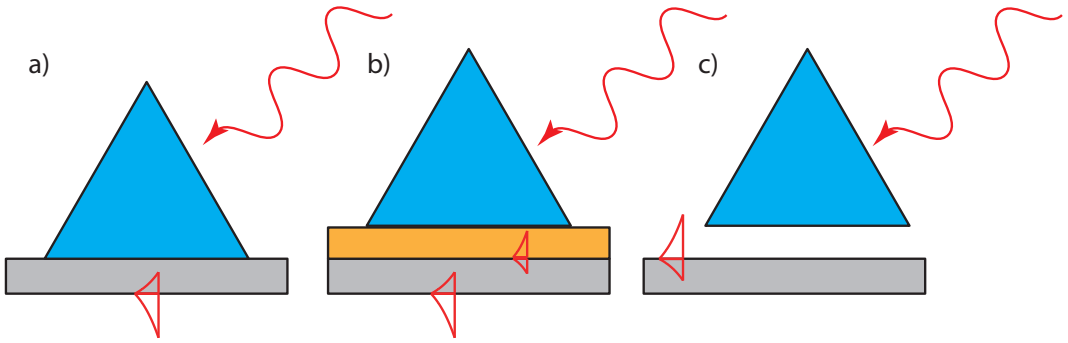

Fig. 2.7: Geometries for prism based coupling of incident light to SPP modes. Panels a) and b) show the Kretschmann configuration and panel c) shows the Otto configuration.

where ϵ_{prism} is the permittivity of the material of the prism and θ is the angle of incidence of light. By carefully adjusting the angle of incidence, it is possible to fulfil the condition for SPP-photon coupling, $k_{prism} = k_{spp}(\omega)$, at a particular frequency ω. The three main configuration for this technique are shown in Fig. 2.7. In the Kretschmann configuration, a dielectric prism is placed on top of a metallic film and illuminated at an angle greater than the angle of internal reflection [14]. If the incidence angle leads to a k_{prism} that obeys the SPP coupling condition, resonant light tunneling in the metal film occurs and a surface plasmon is excited on the opposite side of the film. A dielectric layer of refractive index $n_d > n_{prism}$ placed between the prism and the metal film can lead to the formation of a SPP on the metallic side closer to the prism. In such cases two SPP modes can be achieved, on either side of the metallic strip, by varying the angle of incidence. In the third configuration, known as the Otto configuration [15], the prism is placed at a specific distance above the metal layer. In this case, tunneling occurs through the medium between the prism and the conductor, leading to the excitation of surface modes on the latter.

Diffraction and scattering based coupling mechanisms rely on the fact that light impinging onto a surface can be decomposed into components with varying wave vectors. Some of these components can satisfy the SPP coupling condition and give rise to a surface resonance. Figure 2.8 illustrates the two main techniques used to excite SPPs. In coupling *via* diffraction gratings, a diffraction pattern etched into the surface of the metal can lead to diffracted wave components which can generate a SPP mode on the smooth region of the metal [8]. By tailoring the size and pattern of the diffraction grating, it is possible to achieve SPP coupling at different frequencies. Alternatively, it is well known that in the near-field domain, light scattered from a surface defect contains field components with a broad spectrum of wave vectors [8, 16]. In this case, the components with wave vectors k_{sp} will excite SPP modes at the metal interface. This process, however, cannot be easily controlled and, as expected, has a low conversion efficiency.

Surface plasmon polariton coupling on planar metal interfaces can also be

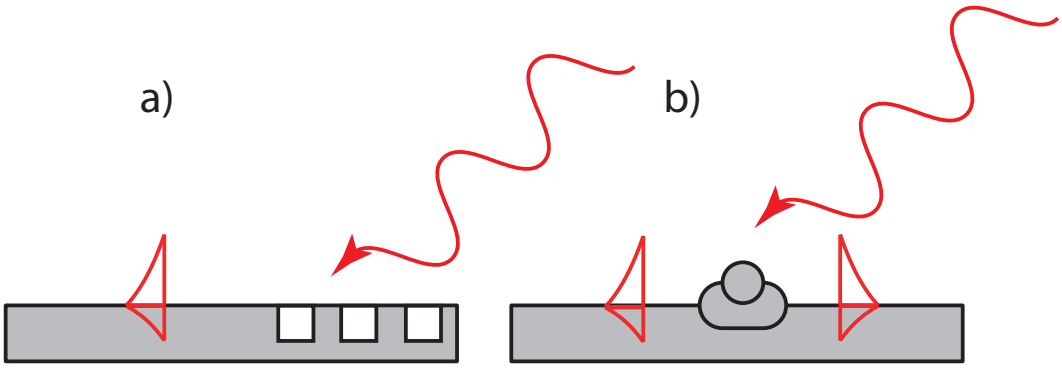

Fig. 2.8: Geometries for surface feature based coupling of incident light to SPP modes. Panel a) shows the surface grating configuration and panel b) shows SPP coupling via scattering from surface defects.

achieved in the near-field domain by optical focusing of the incoming radiation on the metal surface [17] and by using surface near-field optical microscopy (SNOM) [18]. The latter approach is of particular interest as it also allows the probing of the near-field and direct observation of surface plasmon modes.

2.2.5 Applications of Surface Plasmons

Due to their ability to concentrate light on a very small scale and high degree of tunability, structures employing surface plasmon resonances can be used for crucial applications in the fields of optics, telecommunications, electronics, medicine and many others. For example, it is well known that photonic components are superior to electronic ones in terms of usable bandwidth. Optical device design, however, is constrained by the diffraction of light. Through the use of plasmon based devices, this limit has been shown to be surpassable [19]. As a result, several basic devices have been designed and demonstrated, devices which can be employed in on-chip photonic systems. These include sub-wavelength plasmonic waveguides, bent waveguides, splitters and on-chip resonators [20, 21]. The ability to increase the propagation length of SPPs in plasmonic devices, allowing for more efficient on-chip device coupling, has also been investigated [22].

The strong field enhancement associated with plasmon resonances can be used to increase the optical absorption in nano-patterned metallic layers. As a result, plasmons have been shown to have great potential in designing new and more efficient photovoltaic devices [23]. In parallel to this, strong field enhancement can lead to resonant structures with high quality factors, which is the fundamental feature required in order to build sub-wavelength surface plasmon lasers [24–26]. Designs for plasmon structures which act as light-driven motors [27] have also been proposed.

The unique characteristics of resonant excitation associated with the formation of LSPs have also led to many exciting applications. As plasmons are highly sensitive to the medium in which they are excited, several chemical and biomedical sensors based

Fig. 2.9: Applications of surface plasmons: a) SPP design for field focusing [19]; b) waveguide plasmonic ring resonator [19]; c) novel SPP design for photovoltaic cells [23]; d) nano-pillar plasmonic laser [26].

on surface plasmon resonances have been reported [28–30]. In relation to this, it has been shown that surface plasmons can be used in surface-enhanced Raman excitation spectroscopy [31–33], leading to very high detection limits including the possibility to detect single molecules. At the same time, LSPs can be employed to concentrate light around nano-scale structures, with many exciting applications such as metallic nano-tips for near-field optical microscopy [34–36] or optical nano-antennae [37–39].

Moreover, electromagnetic coupling [40–43] induces the hybridisation of LSP resonances of closely-spaced interacting nano-particles [44, 45], leading to complex plasmonic resonance spectra [46–48]. This strong interaction at the nano-scale can have major implications in designing materials with new optical properties. Some of these application are illustrated in Fig. 2.9.

2.3 Non-Linear Optical Effects in Plasmonic Structures

So far, we have considered only electromagnetic phenomena in linear materials, that is to say, materials which have a linear response to the electromagnetic field. The use of such materials that support surface plasmon resonances has been shown to produce enhanced electromagnetic effects with far ranging applications. These phenomena can be further enhanced, and new ones made possible, by employing media with a non-linear optical response to light. These non-linear optical effects, specifically second harmonic generation in metallic structures, are the main topic of this section.

2.3.1 Non-Linear Optical Effects

The electromagnetic phenomena covered in the previous section assumed that ligh interacted with a linear medium. That is to say, the polarisation $\mathbf{P}$ is of the form:

$$\mathbf{P}(\omega) = \epsilon_0 \chi^{(1)} \mathbf{E}(\omega), \tag{2.48}$$

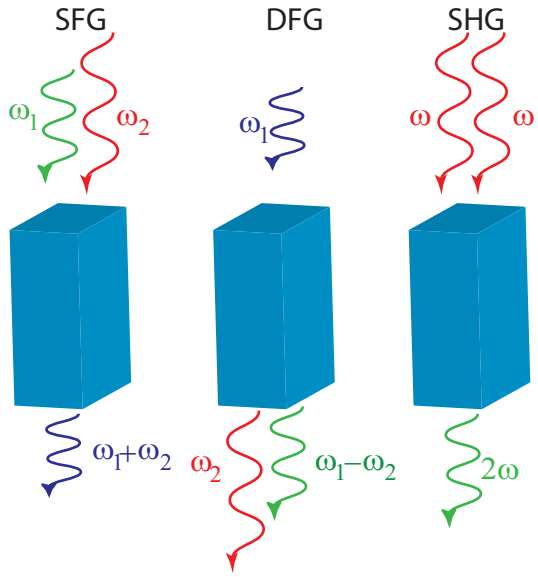

Fig. 2.10: Schematic representation of second-order non-linear effects: a) sum frequency generation , b) difference frequency generation , c) second harmonic generation.

where $\chi^{(1)}$ is the first-order electric susceptibility. Equation (2.48) describes the polarisation induced in a medium where the displacement of electrons is assumed to be small [49]. This model can be extended by considering that the restoring force also has a non-linear component, that is, it depends on the electric field $\mathbf{E}$ in a non-linear fashion. In this model, also known as the *an-harmonic classical oscillator model*, the polarisation can be expanded in a Taylor series in the electric field:

$$\mathbf{P}(\mathbf{r}) = \epsilon_0 \chi^{(1)} \mathbf{E}(\mathbf{r}) + \epsilon_0 \chi^{(2)} : \mathbf{E}(\mathbf{r})\mathbf{E}(\mathbf{r}) + \epsilon_0 \chi^{(3)} \vdots \mathbf{E}(\mathbf{r})\mathbf{E}(\mathbf{r})\mathbf{E}(\mathbf{r}) + \dots . \tag{2.49}$$

Here $\chi^{(2)}$ and $\chi^{(3)}$ are the second- and third- order non-linear susceptibilities, respectively. The non-linear susceptibilities define the corresponding non-linear polarisation components $\mathbf{P}^{(2)} = \chi^{(2)} : \mathbf{EE}$ and $\mathbf{P}^{(3)} = \chi^{(3)} \vdots \mathbf{EEE}$. The polarisations $\mathbf{P}^{(2)}(\mathbf{r})$ and $\mathbf{P}^{(3)}(\mathbf{r})$ are known as the second-order and third-order non-linear polarisations, respectively. The higher-order non-linear polarisations are several orders of magnitude smaller than the linear one, which implies that non-linear optical effects are much weaker than the linear ones. In fact, only with the invention of the laser in the 1960s the observation of non-linear optical effects has become possible. Second harmonic generation was experimentally demonstrated by using a ruby laser beam at $694.3\mathrm{nm}$, which induced the generation of the second harmonic at $347.2\mathrm{nm}$ in a quartz crystal [50]. The laser was required in order to generate a very strong electric field in the crystal of a magnitude which had not been possible before.

Based on the definition of the second-order non-linear polarisation, it is possible to investigate the various non-linear effects that can occur when one or more beams of light interact with a quadratically non-linear medium. Figure 2.10 illustrates some of

these phenomena. Thus, assuming a beam of light with harmonic time dependence of the electric field:

$$\mathbf{E}(t) = \mathbf{E_0} e^{i\omega t} + \text{c.c.}, \tag{2.50}$$

the second-order polarisation becomes:

$$\mathbf{P}^{(2)}(t) = \epsilon_0 \chi^{(2)} \mathbf{E}_0^2 e^{2i\omega t} + \chi^{(2)} E_0^{*2} e^{-2i\omega t} + 2\epsilon_0 \chi^{(2)} \mathbf{E}_0 \mathbf{E}_0^*. \tag{2.51}$$

The first two terms in Eq. (2.51) correspond to a radiated wave at the second-harmonic frequency 2ω and is the source of *second harmonic generation* (SHG) in non-linear media. The third term has no time dependance and thus does not correspond to a wave-like solution. This term is the source of a static electric field generated within the non-linear medium, a process known as *optical rectification* [51].

A more complex case arises when the optical beam interacting with the non-linear medium has two distinct frequency components, ω_1 and ω_2. The electric field in this case can be written as:

$$\mathbf{E} = \mathbf{E_1} e^{i\omega_1 t} + \mathbf{E_2} e^{i\omega_2 t} + \text{c.c.}, \tag{2.52}$$

which leads to a second-order polarisation of the form:

$$\begin{aligned} \mathbf{P}^{(2)}(t) =& \epsilon_0 \chi^{(2)} (\mathbf{E}_1^2 e^{2i\omega_1 t} + \mathbf{E}_2^2 e^{2i\omega_2 t} + \mathbf{E}_1^{*2} e^{-2i\omega_1 t} + \mathbf{E}_2^{*2} e^{-2i\omega_2 t}) \\ &+ 2\epsilon_0 \chi^{(2)} [\mathbf{E}_1 \mathbf{E}_2 e^{i(\omega_1+\omega_2)t} + \mathbf{E}_1^* \mathbf{E}_2 e^{-i(\omega_1-\omega_2)t} + \mathbf{E}_1^* \mathbf{E}_2^* e^{-i(\omega_1+\omega_2)t} \\ &+ \mathbf{E}_1 \mathbf{E}_2^* e^{i(\omega_1-\omega_2)t}] + 2\epsilon_0 \chi^{(2)} (\mathbf{E}_1 \mathbf{E}_1^* + \mathbf{E}_2 \mathbf{E}_2^*). \end{aligned} \tag{2.53}$$

The first term in the r.h.s of Eq. (2.53) corresponds to the SHG at the two second harmonic frequencies, $2\omega_1$ and $2\omega_2$. The second term corresponds to non-linear processes processes known as *sum frequency generation* (SFG) and *difference frequency generation* (DFG). The final term is the optical rectification in the non-linear medium.

Sum frequency generation occurs at $\omega_1 + \omega_2$ and can be viewed as a more general version of the SHG process with $\omega_1 \neq \omega_2$. It can be used to obtain optical signals with finely tuneable frequency, by simply fixing one of the two frequency components and tuning the other one. Moreover, difference frequency generation occurs at the frequency equal to $\omega_1 - \omega_2$. Assuming $\omega_1 > \omega_2$, in this process, the medium absorbs a photon of frequency ω_1 which emits two photons with frequencies ω_2 and $\omega_1 - \omega_2$.

When the third-order optical non-linearity is considered, several other effects are possible. Among these are phenomena such as third-harmonic generation or intensity dependent refractive index. Several other complex non-linear effects such as two-photon absorption and four-wave mixing are also possible [52]. These effects are beyond the scope of this work and will not be discussed further.

2.3.2 Physical Properties of the Non-linear Susceptibility

Optical non-linear effects can be described mathematically by treating the electrons in a medium as an-harmonic oscillators. As such, the strongest non-linear effects should occur in media in which the electrons are tightly bound to the ionic lattice. The most common class of such materials are crystals. The optical properties of crystals are a direct result of their intricate ionic structure. It is then useful to investigate how such a structure can affect the non-linear polarisation and non-linear susceptibility. Specifically, because the second order non-linear susceptibility is a tensor, it becomes necessary to examine its components.

If the total field incident on a non-linear crystal consists of several frequency components, it can be expressed as:

$$\mathbf{E}(\mathbf{r},t) = \sum_n \mathbf{E}(\omega_n) e^{i\omega_n t}, \tag{2.54}$$

where the spatial dependence of the amplitudes $\mathbf{E}(\omega_n)$ has been dropped. The total second-order non-linear polarisation arising from this field can be written:

$$\mathbf{P}(\mathbf{r},t) = \sum_n \mathbf{P}(\omega_n) e^{i\omega_n t}. \tag{2.55}$$

Because of the vector nature of this polarisation, the second-order susceptibility is expressed as a tensor $\chi^{(2)}_{ijk}$ where i,j,k represent the cartesian components. With this notation, the second-order polarisation becomes:

$$P_i(\omega_n + \omega_m = \omega) = \sum_{j,k} \sum_{n,m} \epsilon_0 \chi^{(2)}_{ijk} E_j(\omega_n) E_k(\omega_m), \tag{2.56}$$

where the summation over n and m is performed while keeping $\omega_n + \omega_m$ fixed. Equation (2.56) can be viewed as the general form of the second-order non-linear polarisation. With this definition, for lossy materials, $\chi^{(2)}_{ijk}$ becomes complex, while for dispersive media, $\chi^{(2)}_{ijk}$ is frequency dependent. Because in the general case different components of the electric field have different contributions to the total polarisation, $\chi^{(2)}_{ijk}$ will be a tensor that depends on the symmetry of the crystal lattice.

Another important property of the second-order non-linear polarisation we mention here is its behaviour in centrosymmetric media, that is, media which are invariant to the inversion symmetry transformation, $\mathbf{r} \rightarrow -\mathbf{r}$. One example of materials with inversion symmetry is that of noble metals. In a centrosymmetric medium, one has:

$$\mathbf{P}(2\omega) \rightarrow -\mathbf{P}(2\omega) \Longrightarrow \chi^{(2)} : \mathbf{E}(\omega)\mathbf{E}(\omega) \rightarrow \chi^{(2)} : (-\mathbf{E}(\omega))(-\mathbf{E}(\omega)). \tag{2.57}$$

This implies that:

$$-\mathbf{P}(2\omega) = \mathbf{P}(2\omega), \tag{2.58}$$

which can only hold if $\mathbf{P}(2\omega) = 0$ and, implicitly $\chi^{(2)} = 0$. It thus becomes apparent that for media with inversion symmetry, no second-order non-linear effects can occur in the bulk of the material. From a physical point of view this can be understood by the fact that in a centrosymmetric medium a second-harmonic wave generated at $\mathbf{r}$ will always be accompanied by a wave generated at $-\mathbf{r}$, leading to an overall cancellation of the non-linear field.

2.3.3 Phase Matched Non-linear Optical Wave Interaction

One other important physical mechanism which can lead to effective non-linear wave interaction is phase matching. Thus, in this case, the non-linear optical interaction takes place over many wavelenghts and therefore, in most cases, it is the result of the interaction of propagating waves and not that of local excitations. In particular, one important factor pertaining to the efficiency of non-linear optical effects is that of the mismatch between the wavevectors of the interacting waves. Thus, in the case of SFG, when $\omega_3 = \omega_1 + \omega_2$, the intesity, I, of the non-linear output beam can be expressed as [52]:

$$I = I_{max}\frac{\sin^2(\Delta kL/2)}{(\Delta kL/2)^2}, \tag{2.59}$$

where L is the effective optical path length through the crystal and $\Delta k = k_1 + k_2 - k_3$, is the the mismatch between the wavevectors of the interacting wave. It is easy to see from Eq. (2.59) that maximum intensity occurs only in the case for which $\Delta k = 0$, also known as the *phase matching condition*.

Achieving phase matching in bulk non-linear systems is thus an important step in ehancing non-linear effects. However, it is very difficult to find cases in which $\Delta k = 0$. For example, for isotropic bulk crystals in the normal dispersion regime (*i.e.* the refractive index increases as a function of the frequency), phase matching is impossible. Considering that $\omega_1 \leq \omega_2 \leq \omega_3$, the condition for perfect phase matching can be written:

$$n_1\omega_1 + n_2\omega_2 = n_3\omega_3. \tag{2.60}$$

In the case of SHG, where $\omega_1 = \omega_2$ and $\omega_3 = 2\omega_1$, Eq. (2.60) can be rewritten as:

$$n(\omega_1) = n(2\omega_1). \tag{2.61}$$

It thus becomes clear that under normal dispersion conditions, phase matching cannot occur for second harmonic generation. Similarly, when considering sum frequency

generation, the phase matching condition becomes:

$$n_3 - n_2 = (n_1 - n_2)\frac{\omega_1}{\omega_3}. \tag{2.62}$$

Here, $n_3 > n_2$, but at the same time, $n_2 > n_1$. As a result, no solution can be found for Eq. (2.62) under normal dispersion conditions.

One method of achieving phase matching is to employ the properties of anomalous dispersion (*i.e.* the decrease in refractive index with increasing frequency), which occurs in the spectral regions near strong absorption. However, the most common method for phase matching is the use of crystals which exhibit polarisation dependent refractive indices, also known as *birefringence*. In uniaxial birefrigent materials, the refractive index has two possible values, the ordinary refractive index n_o and the extraordinary refractive index n_e. The actual value of the refractive index depends on whether the polarisation is perpendicular to the plane formed by $\mathbf{k}$ and the optic axis of the crystal(ordinary polarisation), or parallel to this plane (extraordinary polarisation). Several types of phase matching can be achieved depending on how the polarisations of the incident beams, ω_1 and ω_2, are taken relative to each other and the nature of the birefrigence the crystal exhibits. A detailed discussion of these types is outside the scope of this work and will not be elaborated upon further [see Ref. [52] and the references within for a detailed explanation of the phenomena].

We do mention here two methods of achieving phase matching in birefringent crystals. The first makes use of the fact that the refractive index of a birefringent crystal depends on the angle θ between $\mathbf{k}$ and the optic axis. This relation can be expressed mathematically as:

$$\frac{1}{n_e(\theta)^2} = \frac{\sin^2\theta}{\bar{n}_e^2} + \frac{\cos^2\theta}{n_o^2}, \tag{2.63}$$

where $\bar{n}_e$ is the principal value of the refractive index. The value of $n_e(\theta)$ becomes $\bar{n}_e$ for $\theta = 90^\circ$ and n_o for $\theta = 0$. Consequently, by carefully adjusting the value of θ, one can find a situation in which the phase matching condition $\Delta k = 0$ is satisified. The second method of obtaining phase matching relies on the fact that certain crystals exhibit varying amounts of birefrigence, depending on their temperature. Consequently, one can keep the angle θ fixed at a specific value and vary the temperature of the crystals so as to satisfy $\Delta k = 0$.

2.3.4 Second Harmonic Generation at Metal-Dielectric Interfaces

As discussed in a previous section, second harmonic generation cannot occur inside centrosymmetric media, due to the symmetry properties of the material. This statement is only valid, however, for the case in which only the electric dipole contribution to the non-linear field is considered. Shortly after the experimental demonstration of SHG

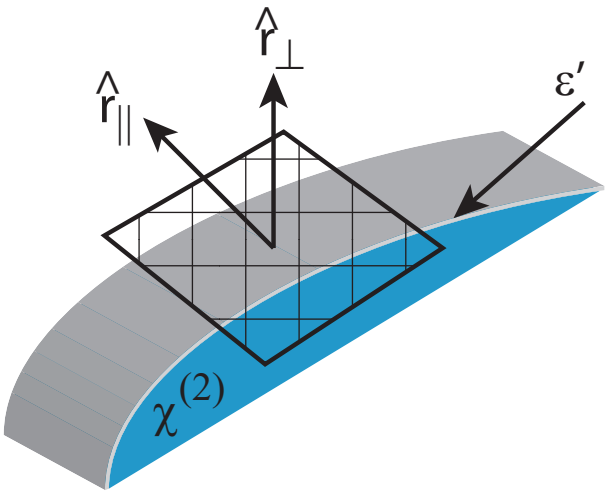

Fig. 2.11: Interface between a dielectric and centrosymmetric material. The thin layer where the second harmonic is generated is represented by the grey area.

in a non-linear crystal, it was shown that a centrosymmetric medium can support a non-vanishing, second-order non-linear polarisation, due to the electric quadrupoles and magnetic dipoles in the bulk of the material [53]. Further, at the interface between two media with inversion symmetry a surface second-order non-linear polarisation can arise owing to the breaking of the inversion symmetry at the boundary between the two materials [54]. These ideas can be expressed formally by writing the total second harmonic polarisation as [55]:

$$\mathbf{P}_{total}(2\omega) = \epsilon_0 \chi_s^{(2)} : \mathbf{E}(\omega)\mathbf{E}(\omega) + \epsilon_0 \chi_b^{(3)} : \mathbf{E}(\omega)\nabla\mathbf{E}. \tag{2.64}$$

Here, $\chi_s^{(2)}$ is the electric-dipole (surface) second-order susceptibility and $\chi_b^{(2)}$ is the bulk susceptibility.

Let us assume now that a 2D metallic (centrosymmetric) region is surrounded by an infinite dielectric and consider that a monochormatic wave with frequency ω impinges on the metal. Then, a second harmonic (SH) field at 2ω will be generated, the source of which being the second-order non-linear polarisation. According to the model that we just described, this non-linear polarisation can be separated in two distinct components. First, the (local) dipole-allowed surface nonlinear polarisation, $\mathbf{P}_s(\mathbf{r}; 2\omega)$, whose support is a surface layer several Ångströms thin [the first term in the r.h.s of Eq. (2.64)] and second, the (nonlocal) bulk nonlinear polarisation, $\mathbf{P}_b(\mathbf{r}; 2\omega)$, which is generated inside the nonlinear medium by electric quadrupoles and magnetic dipoles [the second term in the r.h.s of Eq. (2.64)].

The surface polarisation vector is defined as:

$$\mathbf{P}_s(\mathbf{r}; 2\omega) = \epsilon_0 \chi_s^{(2)} : \mathbf{E}(\mathbf{r}; \omega)\mathbf{E}(\mathbf{r}; \omega)\delta(\mathbf{r} - \mathbf{r}_s), \tag{2.65}$$

where $\mathbf{r}_s$ defines the surface, $\chi_s^{(2)}$ is the surface second-order susceptibility tensor, and the Dirac function shows the surface characteristic of this source non-linear polarization. Unless the surface contains structural features with intrinsic chirality, the metal/background interfaces possess an isotropic mirror-symmetry plane perpendicular to the interface. Under these circumstances, the surface non-linear susceptibility $\chi_s^{(2)}$ has only three independent components, namely, $\chi_{s,\perp\perp\perp}^{(2)}$, $\chi_{s,\perp\parallel\parallel}^{(2)}$, and $\chi_{s,\parallel\parallel\perp}^{(2)} = \chi_{s,\parallel\perp\parallel}^{(2)}$, where the symbols $\perp$ and $\parallel$ refer to the directions normal and tangent to the surface, respectively. The individual components of the non-linear surface susceptibility have been experimentally measured for several metals. As an example, the independent components of $\chi_s^{(2)}$ for Ag are: $\chi_{s,\perp\perp\perp}^{(2)} = 2.79 \times 10^{-18}\ \mathrm{m}^2/\mathrm{V}$, $\chi_{s,\parallel\parallel\perp}^{(2)} = \chi_{s,\parallel\perp\parallel}^{(2)} = 3.98 \times 10^{-20}\ \mathrm{m}^2/\mathrm{V}$, and $\chi_{s,\perp\parallel\parallel}^{(2)} = 0$ [56].

From the symmetry properties of the surface susceptibility tensor $\chi_s^{(2)}$ one can derive the polarisation characteristics of the field at the SH, which is generated by the surface nonlinear polarisation. There are two polarisation cases which need to be considered. In the first, the electric field has no component normal to a plane tangent to the interface. In this case, no surface second harmonic generation can occur for materials with $\chi_{s,\perp\parallel\parallel} = 0$. In the second polarisation case, the electric field at the interface between the metal and the background contains both a normal and a tangent component [see Fig. 2.11]. In this case, the nonlinear surface polarisation has the following components:

$$P_{s,\perp} = \epsilon_0 \chi_{s,\perp\perp\perp}^{(2)} E_\perp^2, \tag{2.66a}$$

$$P_{s,\parallel} = 2\epsilon_0 \chi_{s,\parallel\perp\parallel}^{(2)} E_\perp E_\parallel. \tag{2.66b}$$

The nonlinear bulk polarisation in an isotropic centrosymmetric medium has the following general expression [57]:

$$\mathbf{P}_b(2\omega) = \alpha[\mathbf{E}(\omega)\cdot\nabla]\mathbf{E}(\omega) + \beta\mathbf{E}(\omega)[\nabla\cdot\mathbf{E}(\omega)] + \gamma\nabla[\mathbf{E}(\omega)\cdot\mathbf{E}(\omega)], \tag{2.67}$$

where α, β, and γ are the bulk nonlinear coefficients of the material. For example, if we assume that the electrons in the metal are described by the free-electron model, these parameters are:

$$\alpha = 0, \tag{2.68a}$$

$$\beta = \frac{\epsilon_0 e}{2m_0\omega^2}, \tag{2.68b}$$

$$\gamma = \frac{\beta}{4}[1 - \epsilon_r(\omega)], \tag{2.68c}$$

with e and m_0 being the electron charge and mass, respectively, and $\epsilon_r(\omega) = \epsilon(\omega)/\epsilon_0$

the relative permittivity of the metal. As it will be shown in subsequent chapters, the SHG is dominated by the surface component. Furthermore, it should be noted that the free electrons in the metal also contribute to the nonlinear surface susceptibility (primarily to the component $\chi^{(2)}_{s,\perp\perp\perp}$), but this contribution is accounted for by using the experimentally determined values of the components of the nonlinear surface susceptibility [56].

The nonlinear boundary conditions obeyed by the electromagnetic fields at the SH, are given by [55]:

$$\Delta B_{\perp} = 0 \tag{2.69a}$$

$$\Delta \mathbf{H}_{\parallel} = \frac{\partial \boldsymbol{\mathcal{P}}_s}{\partial t} \times \hat{\mathbf{r}}_{\parallel} \tag{2.69b}$$

$$\Delta D_{\perp} = -\nabla_{\mathbf{r}} \cdot \boldsymbol{\mathcal{P}}_s(\mathbf{r}_{\parallel}) \tag{2.69c}$$

$$\Delta \mathbf{E}_{\parallel} = -\frac{1}{\epsilon'}(\nabla_{\parallel}\mathcal{P}^s_{\perp} - \mathbf{P}^b_{\parallel}). \tag{2.69d}$$

where ϵ' is the permittivity of the thin layer supporting SHG, t is time, $\nabla_r = (\nabla_{\parallel}, \partial_{\perp})$ [see Fig. 2.11], $\Delta B_{\perp} = B_{\perp_2} - B_{\perp_1}$ and the permittivities are evaluated at the SH frequency, $\Omega = 2\omega$. The approach by which Eq. (2.69) can be obtained is given in Appendix A.

It may at first seem counter-intuitive to use metallic surfaces to design and build optical non-linear structures, as in this case only surface effects contribute to the non-linear optical response of the system. However, when considering that metal-dielectric interfaces can support SPPs and LSP modes, the advantages of this design choice become clear. Plasmons have the ability to concentrate the electromagnetic field in a very small region leading to strong local field enhancement. This in turn leads to strong SHG due to the surface component of the non-linear polarisation. At the same time, unlike bulk crystals where the SHG is mostly determined by the properties of the crystal, non-linear plasmonic devices are highly susceptible to both their shape and the surrounding environment. Several important practical applications based on the combination of the two phenomena have been reported including, surface-enhanced Raman scattering [32], enhanced non-linear plasmonic effects at metal-dielectric interfaces [58,59] and in gain media [60], sub-wavelength, optically active, guiding nanostructures [61, 62], high-Q factor optical cavities [63, 64] and sub-wavelength sensors [65].

2.3.5 Second Harmonic Generation in Chiral Materials

Second harmonic generation upon interaction with metallic structures is particularly of interest because of its sensitivity to changes of the surface/interface properties down to the atomic level [66]. More generally speaking, this sensitivity is also present in the case of higher-order harmonics, as long as their order is even and the medium

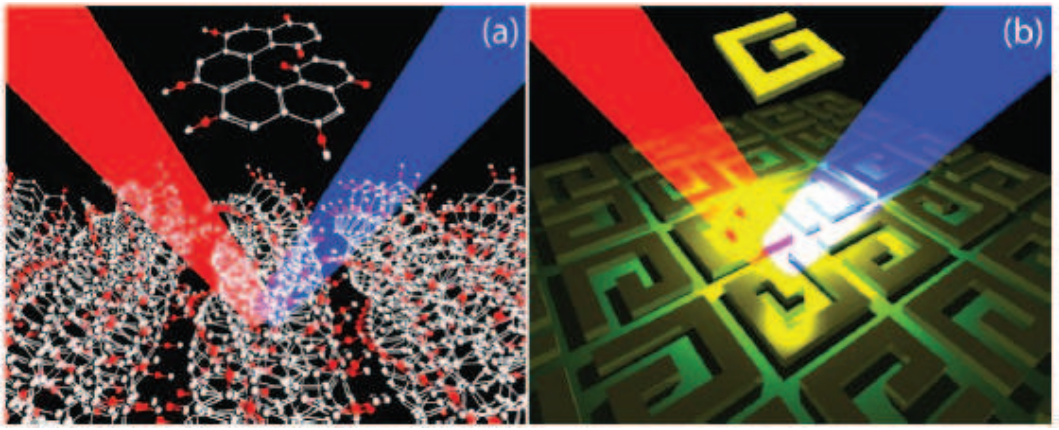

Fig. 2.12: Second harmonic generation methods for studying chirality were developed in organic molecules before being applied to metamaterials. In (a), illustration of SHG from supramolecularly ordered chiral helicenes molecules. In (b), illustration of SHG from G-shaped nanostructures, arranged in a chiral unit cell [74].

is centrosymmetric; this latter condition is satisfied by most metals used in practical applications. Besides its surface/interface sensitivity, SHG is also dependant on the symmetry properties of the crystalline lattice [67], geometric features [68], as well as the presence of externally applied electric [69] and magnetic [70, 71] static fields. More specifically, local or externally applied static electric and magnetic fields can break the symmetry of the material at the interface; consequently, SHG can be used effectively for imaging ferroelectric [72] and ferromagnetic [73] domains. In addition to rotation and time reversal symmetry transformations, surface SHG is also sensitive to mirror symmetry transformations. This effect occurs in a material which lacks an internal plane of symmetry and so it cannot be superimposed on its mirror image. Such materials are known as *chiral materials* and the phenomena associated with them are known as *chiral effects*.

From a historical perspective, SHG studies of chiral symmetry breaking have been chiefly associated with chemistry and biology. Specifically, many organic molecules are chiral and thus their handedness plays an important role in chemical reactions. It has been demonstrated that the SHG equivalent of optical rotatory dispersion (ORD) and circular dichroism (CD), designated as SHG-ORD [75] and SHG-CD [76], respectively, is typically several orders of magnitude more sensitive than their linear counterpart. Consequently, SHG techniques constitute particularly valuable spectroscopic tools for investigating the physical properties of thin layers, including molecular monolayers, fibres, surfaces, and membranes [77]. In such structures, supramolecular ordering can further increase the SHG signal; Fig. 2.12a illustrates this concept. The role of supramolecular ordering has been demonstrated in chiral helicene molecules [78], where the SHG-ORD and SHG-CD spectra yield very large signals [79]. Viewing chiral plasmonic resonators (meta-molecules) as the macroscopic counterpart of chiral

molecules (see Fig. 2.12b) [80], it is expected that the SHG would be significantly enhanced upon distributing chiral plasmonic structures so as to form a supramolecular chiral patterned surface, which are also called chiral *metasurfaces*.

2.3.6 Non-linear Magneto-optic Effects

In the preceeding section we have assumed that the material in which the second harmonic is generated is a non-magnetic medium ($\mu = \mu_0$). However, a series of new phenomena occur when non-linear optical effects are considered in a material with non-zero magnetisation $\mathbf{M}$. These effects are further ehanced when coupled with the excitation of propagating or localised surface plasmons. The influence of magnetic fields on surface plasmons combines aspects of photonics and electromagnetism at the nanoscale [81]. Because surface plasmons are collective excitations of electrons under the influence of an external electromagnetic field, in magnetic materials these electrons can experience the effects induced by externally applied magnetic fields. Recently, this area of research has attracted intense interest as it was shown that plasmons can be controlled *via* externally applied magnetic fields [82]. In order to better understand the behavior of surface plasmons in magnetic media it is important to consider surface-specific non-linear magneto-optic phenomenona known as *magnetization-induced second harmonic generation* (MSHG) [70, 83, 84].

As previously shown, in the dipole approximation, in centrosymmetric materials second harmonic can originate only from regions where the inversion symmetry is broken, for example, at surfaces and interfaces. Due to symmetry considerations, MSHG has the same requirements for structural symmetry breaking. Consequently, MSHG can be used to probe the magnetisation at surfaces and interfaces down to an atomic monolayer [66]. More specifically, a contrast in the MSHG intensity is recorded upon switching the sign of the magnetisation in the material. In this connection, it has also been demonstrated that this reversal can be achieved in the presence of surface plasmons [85, 86]. The latter could also cause a general enhancement of the MSHG signal. Additionally, such enhancements were reported in ferromagnetic gratings [87] and granular films [71, 88].

In the presence of the magnetisation, the second order non-linear polarisation $\mathbf{P}(2\omega)$ includes an additional term [70, 83, 89], such that:

$$\mathbf{P}(2\omega) = \epsilon_0 \chi^{(2),e} : \mathbf{E}(\omega)\mathbf{E}(\omega) + \epsilon_0 \chi^{(2),m)} : \mathbf{E}(\omega)\mathbf{E}(\omega)\mathbf{M}, \tag{2.70}$$

where $\chi^{(2),m}$ is the third rank (polar) non-linear susceptibility of a non-magnetic medium, while $\chi^{(2),e}$ is a fourth rank axial tensor associated with the magnetisation of the medium. This additional term gives rise to magnetisation-induced SHG. Because the direction of $\mathbf{M}$ can be fixed by an external magnetic field, Eq. (2.70) reduces to a

third rank polar tensor and $\mathbf{P}(2\omega)$ can be written in the compact form:

$$\mathbf{P}(2\omega) = \epsilon_0 \chi^{(2)}_{eff} : \mathbf{E}(\omega)\mathbf{E}(\omega), \tag{2.71}$$

where $\chi^{(2)}_{eff}$ is an effective non-linear susceptibility. Its components at an isotropic interface with incidence plane xz are given by [70]:

$$\chi^{(2)}_{eff} = \begin{pmatrix} \chi^{(2),m}_{xxx}(M_y) & \chi^{(2),m}_{xyy}(M_y) & \chi^{(2),m}_{xzz}(M_y) & \chi^{(2),m}_{xzy}(M_z) & \chi^{(2),e}_{xzx} & \chi^{(2),m}_{xxy}(M_x) \\ \chi^{(2),m}_{yxx}(M_x) & \chi^{(2),m}_{yyy}(M_x) & \chi^{(2),m}_{xzz}(M_x) & \chi^{(2),e}_{yzy} & \chi^{(2),m}_{yzx}(M_z) & \chi^{(2),m}_{yxy}(M_y) \\ \chi^{(2),e}_{zxx} & \chi^{(2),e}_{zyy} & \chi^{(2),e}_{zzz} & \chi^{(2),m}_{zzy}(M_x) & \chi^{(2),m}_{zzx}(M_y) & \chi^{(2),m}_{zxy}(M_z) \end{pmatrix}.$$

In the above it can be seen that the $\chi^{(2),e}_{ijk}$ components have an *even* contribution to the effective susceptibility with respect to the the magnetisation, M_l. On the other hand, $\chi^{(2),m}_{ijk}(M_l)$ is *odd* with respect to the magnetisation. As a result, the generated second harmonic produced will depend on the magnetisation $\mathbf{M}$ and can consequently be tuned using an external magnetic field.

For example, assuming that the magnetisation has been set so that only the M_y component is non-zero and that the the electric field is given by $|\mathbf{E}| = E_y$, the only non-zero contribution to the second harmonic field will be given by $\chi^{(2),e}_{zyy}$ and $\chi^{(2),m}_{xyy}(M_y)$. The intensity of the MHSG wave, or the period averaged energy flux, then becomes:

$$I^{2\omega}(\pm\mathbf{M}) \approx E_y^4[\chi^{(2),e}_{zyy} \pm \chi^{(2),m}_{xyy}(M_y)]^2, \tag{2.72}$$

leading to a change in the MHSG intensity due to the change in direction of $\mathbf{M}$. Alternatively, when the magnetisation is such that M_x is the only non-zero component, the odd component $\chi^{(2),m}_{yyy}(M_x)$ will produce a y-polarised output wave, which combined with the even contribution $\chi^{(2),e}_{zyy}$ will lead to an overall non-linear polarisation that again depends on the direction of $\mathbf{M}$.

It is worth noting that the direction of the magnetisation is not the only externally controllable parameter which can influence MHSG. As mentioned earlier, the presence of surface plasmons, which can also be controlled by external magnetic fields, can have a strong effect on the generation of surface second harmonic in metals. Moreover, when normal incidence is no longer assumed, the angle of incidence upon the surface of a magnetic material will have a direct influence on the MSHG at that surface [85, 86]. Equally important, extending the MSHG model to include the bulk non-linear contributions of the metal can also lead to additional complex non-linear phenomena [70].

2.4 Introduction to Metamaterials and Metasurfaces

Electromagnetic phenomena in readily available natural materials lead to a large number of optical effects with several interesting applications, as it was illustrated in the previous sections. Nevertheless, there are certain limits which, natural media impose on photonic devices. With the recent tremendous advances in nano-fabrication, it has now become possible to overcome these limitations. In this chapter, it will be shown how artificially engineered materials can be used to alter the electromagnetic properties of matter and design effective parameters which go beyond what the natural world offers. At the same time the applications of such artificial media will be discussed.

2.4.1 Effective Properties of Electromagnetic Media

Maxwell's equations (2.1), coupled with the constitutive relations (2.5) fully describe the interaction of electromagnetic waves and matter. It is interesting to note that these equations do not impose any restrictions on the electromagnetic properties of the medium characterised by the parameters, ϵ, μ and the higher-order susceptibilities. There is, for example, no physical reason why a material with both negative ϵ and μ would not exist. In such a material, the refractive index $n = \pm\sqrt{(\epsilon\mu)/(\epsilon_0\mu_0)}$ would become negative [90]. A *negative index material* (NIM) was first theoretically studied in the late 1960s by Veselago [91]. Maxwell's equations in a medium with negative index of refraction lead to some intriguing phenomena, including negative refraction, inverse Doppler-shift and perfect lensing. Nevertheless, these effects were not validated experimentally for a long time, primarily due to the lack of natural materials with both negative ϵ and μ.

In recent years, however, major advances in micro- and nano-scale fabrication technologies have brought about the possibility of artificially engineering materials with optical properties not readily available in nature. The principle behind this concept is the fact that the material optical constants are of a macroscopic nature. For example, in naturally occurring materials, as well as some artificially engineered ones, the index of refraction is given by the distribution of the atoms at the microscopic level, molecules and the way they interact with electromagnetic waves. In other words, the refractive index characterises the overall (effective) response of the medium. Because, in most applications at optical frequencies the wavelength of light is much larger than the characteristic inter-atomic distances, the light samples locally a homogeneous medium whose response is characterised by a permittivity and a permeability. Extending this reasononing to artificially engineered materials whose building blocks are much smaller than the operating wavelength, one can introduce the concept of *metamaterials*. These are materials whose primary , predesigned, constituents are much smaller than the wavelength, their electromagnetic properties being described by effective parameters determined by field averaging over the basic unit cell of the metamaterial and not at microscopic level

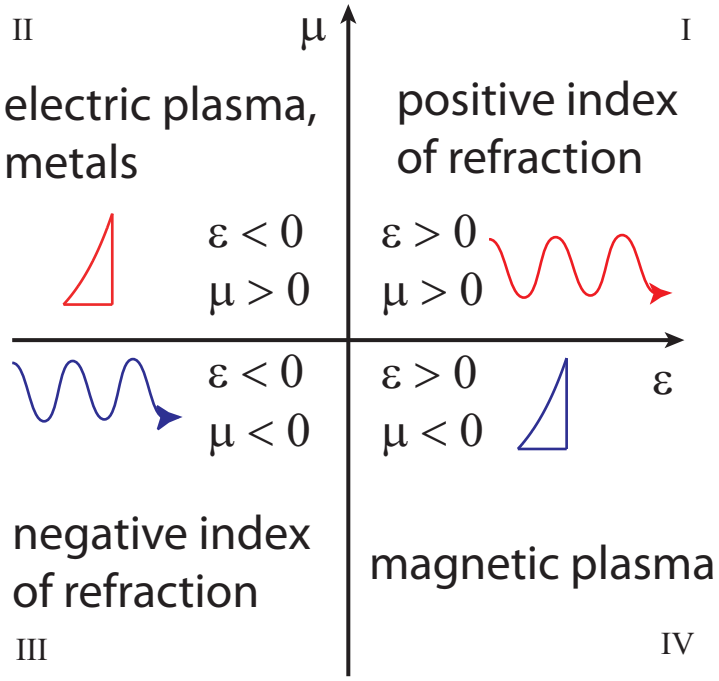

Fig. 2.13: Parameter space for ϵ and μ in electromagnetic media.

as is the case with regular materials. The first experimental demonstration of such a metamaterial employed interspersed split-ring resonator and metallic wires, to obtain an effective medium with negative index of refraction [92].

This new class of materials is known in the literature as metamaterials [93], mainly because they are seen as materials with properties "beyond" those available in nature. Metamaterials can be viewed as structures with internal components much smaller than the operating wavelength. This concept was illustrated in Fig. 2.1.

Another type of classification which can be applied to optical media is based on their electromagnetic properties, specifically, the sign of μ and ϵ. This classification is illustrated in Fig. 2.13. Quadrants I and III consist of materials that allow propagating waves (*i.e.* have a real index of refraction) either in the "normal" right-handed configuration, where the Poynting vector $\mathbf{S}$ and the wave-vector $\mathbf{k}$ are in the same direction, or the left-handed region in which the two vectors are opposite, corresponding to a negative refractive index medium. The remaining quadrants correspond to media where no propagating waves can exist, the index of refraction being purely imaginary. Metals are the best known example of materials with $\epsilon < 0$ and $\mu > 0$, while examples of matter with negative μ have only been found in some ferromagnetic substances at resonance [94].

2.4.2 Applications of Electromagnetic Metamaterials

Because of their properties not readily achievable in nature, metamaterials have been proposed and successfully demonstrated for a broad array of applications. For example, by a proper design of the primary unit cell of metamaterials it has been pos-

Fig. 2.14: Metamaterial designs: a)NIM metamaterial based on split-ring resonators [92], b) frequency-agile terahertz metamaterial [120], c) 3D metamaterial [101], d) polarisation tunable metasurface [121]

sible to demonstrate, theoretically and experimentally, metamaterials that are magnetically active at terahertz and optical frequencies [95–97], 3D [98–101] and 2D [102, 103] materials with negative index of refraction, frequency-selective surfaces [104], transformation-optics electromagnetic media [105–107], low-index of refraction materials [108–111], optical cloaks [112, 113] or super-lenses [114]. It has also been demonstrated that the "meta-toms", which are the primary building blocks of metamaterials, can be designed so as not only to emulate linear physical properties of regular atoms, such as magnetic moment [115] or electric polarisability [116] but also to possess nonlinear optical properties, such as second-order [58, 59, 117] and third-order [118, 119] nonlinear optical response. Some of these applications are illustrated in Figure 2.14.

One important property of many metamaterial designs is that they employ only classical electromagnetic phenomena. The most important of these in terms of metamaterial applications are surface plasmon effects. For example, in recent years much attention has been focused on optical properties of nano-patterned metallic films. One particularly intriguing characteristic of these plasmonic nanostructures is their ability to resonantly trap and tightly confine light in spatial domains comparable or smaller than the optical wavelength, leading thus to the formation of localised surface plasmon resonances. Because the frequencies of LSPs are strongly dependent on the shape and size of the plasmonic nano-particles, as well as the properties of the dielectric environment, they can be tuned over the entire visible and infrared domains [12, 122]. Plasmonic nanoparticles can be assembled in one-dimensional (1D), 2D, or 3D periodic structures, the corresponding interacting LSPs leading to plasmonic chains, metasurfaces, or metamaterials with remarkable properties. For example, it has been demonstrated that chains of resonantly interacting LSPs can be used to control the flow of optical power at deep-subwavelength scale, [123] whereas, in the nonlinear regime, these same structures can be used for all-optical signal processing at the nano-scale [61]. Furthermore, by engineering the optical response of LSPs one can provide an efficient mechanism to enhance the optical transmission of metallic films [124], as well as achieve plasmonic metasurfaces with large surface chirality [125] and optical non-linearity which

Fig. 2.15: Photonic crystal designs: a)2D photonic crystal waveguides [127], b) 3D layered photonic crystal structure (wood pile geometry) [128].

could have major applications in designing integrated optoelectronic devices for optical signal processing [117].

2.5 Photonic Crystals: Definition and Basic Properties

Another class of artificial material which has attracted significant interest in recent years are *photonic crystals* (PhCs). Photonic crystals are periodically structured media, wherein the characteristic spatial period is comparable to the operating wavelength [126] [also see Fig. 2.1]. Owing to their periodical structure, photonic crystals can be used to manipulate the propagation of light and give rise to optical effects not possible in natural materials. In this section, an introduction to photonic crystals will be given and some of the optical phenomena associated with PhCs will be analysed.

2.5.1 Wave Propagation in Periodically Structured Media

In many respects, photons propagating in photonic crystals have similar properties with those of electrons in crystalline materials. In particular, this similarity between PhCs and regular crystals extends to properties such as the existance of Bloch modes and energy (frequency) bands whose properties are determined by the group symmetries of the lattice [126].

Photonic crystal designs vary greatly according to their intended applications. Possible structures can be periodic in either one, two or three dimensions. One-dimensional (1D) PhCs have been known for a few decades and are employed in many optoelectronic devices such as optical filters or isolators [129]. Photonic crystals are relatively easy to fabricate in the microwave domain but this becomes much more difficult as the wavelength approaches the optical spectrum, primarily because of the small size of the required lattice constant. Although the majority of PhCs are based on dielectrics and semiconductors, there has also been extensive research into photonic crystals made of metallic structures [130], also called *plasmonic crystals*. Two examples of practical implementations of these designs are presented in Fig. 2.15.

One of the main reasons photonic crystals have garnered so much interest in recent years is the high degree to which the dispersion of waves propagating in a periodic structure can be engineered. Unlike the case of a bulk dielectric, PhCs exhibit an intricate photonic band-structure which can be tuned by simply changing the structure of

the PhC. To better understand this phenomenon, consider for simplicity the 1D structure in Fig. 2.16a. Assuming a linear, non-magnetic, non-dispersive dielectric medium, the permittivity of the systems is $\epsilon = \epsilon(x)$. According to the definition of a photonic crystal, the dielectric function is periodic with period d, $\epsilon(x) = \epsilon(x+d)$. The dielectric function can then be expanded in a Fourier series:

$$\epsilon(x) = \sum_{m=-\infty}^{\infty} a_m e^{i\frac{2\pi m}{d}x}, \tag{2.73}$$

where a_m are the Fourier coefficients of the series expansion. From this relation, one can infer that $a_{-m} = a_m^*$ as $\epsilon(x)$ is real for all values of x. In a structure with a periodic dielectric function, a propagating electromagnetic wave can be considered to be a photonic eigenmode which experiences a periodic "potential", due to the periodically modulated dielectric function. This implies that one can use Bloch's theorem to describe the photonic eigenmodes [131]. The solution for the electromagnetic wave equation (2.9) in one dimension can then be written as a Bloch solution:

$$E_k(x,t) = u_k e^{ikx+i\omega_k t}, \tag{2.74}$$

where k is the Bloch wave vector of the eigenmode at the eigen-frequency ω_k and $u_k(x+d) = u_k(x)$ is a periodic function. Expanding in Fourier series the function $u_k(x)$, Eq. (2.74) can be rewritten:

$$E_k(x,t) = \sum_{m=-\infty}^{\infty} A_m e^{i\left(k+\frac{2\pi m}{a}\right)x+i\omega_k t}, \tag{2.75}$$

where A_m are Fourier coefficients. Combining Eqs. (2.73) and (2.75) and inserting them into the wave equation (2.9) leads to the dispersion relation for the 1D photonic crystal structure in Fig. 2.16a. In the limit of small modulation of ϵ, this dispersion relation can be written as:

$$\omega_\pm \approx \frac{\pi c}{d}\sqrt{a_0 \pm |a_1|} \pm \frac{dc}{\pi|a_1|\sqrt{a_0}}\left(a_o^2 - \frac{|a_1|^2}{4}\right)h^2, \tag{2.76}$$

where c is the speed of light in vacuum and $h = k - \pi/d$ [126]. This solution is valid for $|h| \ll \pi/d$ and if only the $m = 0, \pm 1$ contributions to (2.73) and (2.75) are considered.

Figure 2.16b plots the dispersion relation (2.76). The dispersion lines for the photonic crystals are folded into the first Brillouin zone $k \in [-\pi/d, \pi/d]$ as outside of this region, they differ only by a multiple of $2\pi/d$. For a weekly modulated crystal, in most regions, the mode dispersion approaches the dispersion of light in a material with uniform ϵ. However, when two dispersion lines cross each other, a photonic band-gap

Fig. 2.16: Geometry of a 1D photonic crystal (a) and the corresponding band diagram (solid lines) (b). The dashed lines in (b) correspond to the light lines in a uniform material while the two solid vertical lines show the boundaries of the first Brillouin zone [126].

opens up and light can no longer propagate through the photonic crystal (such as the Bragg gap in the 1D case).

2.5.2 Photonic Band Structure of 2D and 3D Photonic Crystals

The concept of calculating the band structures of a 1D photonic crystal introduced in the previous section can be expanded to two and three dimensional structures. In a periodic three dimensional, non-dispersive and isotropic system, the dielectric function depends on the position vector $\mathbf{r}$ as $\epsilon(\mathbf{r}) = \epsilon(\mathbf{r} + \mathbf{d}_i)$, where $\{\mathbf{d}_i\},\ (i = 1, 2, 3)$ are the elementary lattice vectors of the photonic crystal. By introducing the elementary reciprocal lattice vectors $\{\mathbf{e}_i\}$ and the reciprocal lattice vectors $\{\mathbf{G}\}$:

$$\mathbf{d}_i \cdot \mathbf{e}_j = 2\pi\delta_{ij}, \tag{2.77a}$$

$$\mathbf{G} = l_1\mathbf{e}_1 + l_2\mathbf{e}_2 + l_3\mathbf{e}_3, \tag{2.77b}$$

where l_i are integers, the dielectric function can be expressed as a Fourier expansion [126]:

$$\epsilon(\mathbf{r}) = \sum_{\mathbf{G}} a(\mathbf{G})e^{i\mathbf{G}\cdot\mathbf{r}}, \tag{2.78}$$

where the Fourier coefficients have the property $a(-\mathbf{G}) = a^*(\mathbf{G})$, due to $\epsilon(\mathbf{r})$ being real. The expansion coefficients for a given geometry can be found by using the inverse Fourier transform of Eq. (2.78):

$$a(\mathbf{G}) = \epsilon_0 \frac{1}{V} \int_V d\mathbf{r}\epsilon(\mathbf{r})e^{-i\mathbf{G}\cdot\mathbf{r}}, \tag{2.79}$$

where V is the volume of the unit cell. The integral (2.79) is usually evaluated numerically, although analytical solutions exist for simple geometries.

Using Maxwell's equations (2.1) and the dielectric function in Eq. (2.78), we can

write, as before, a double curl expression for the electric field, namely:

$$\frac{1}{\epsilon(\mathbf{r})}\nabla \times [\nabla \times \mathbf{E}(\mathbf{r},t)] = -\frac{1}{c^2}\frac{\partial^2}{\partial t^2}\mathbf{E}(\mathbf{r},t). \tag{2.80}$$

The equation above can now be re-written as an eigenvalue equation [132]:

$$\Theta_E \mathbf{E}(\mathbf{r}) = \frac{\omega^2}{c^2}\mathbf{E}(\mathbf{r}), \tag{2.81}$$

where the differential operator Θ_E is:

$$\Theta_E \equiv \frac{1}{\epsilon_r}\nabla \times [\nabla \times \mathbf{E}(\mathbf{r})]. \tag{2.82}$$

Equation (2.80) supports time harmonic solutions of the type $\mathbf{E}(\mathbf{r},t) = \mathbf{E}(\mathbf{r})e^{i\omega t}$, where ω is the eigen-frequency and $\mathbf{E}(\mathbf{r})$ are the eigen-functions.

As before, the plane-wave solutions to the wave equation in the photonic crystal are described by eigenfunctions of the type

$$\mathbf{E}_{\mathbf{k}n}(\mathbf{r}) = \mathbf{u}_{\mathbf{k}n}(\mathbf{r})e^{i\mathbf{k}\cdot\mathbf{r}}, \tag{2.83}$$

where $\mathbf{u}_{\mathbf{k}n}(\mathbf{r}) = \mathbf{u}_{\mathbf{k}n}(\mathbf{r}+\mathbf{d}_i)$ is a vectorial periodic function, n is known as the band index, k and ω are the eigenvector and eigen-frequency, respectively, and the time dependence is assumed to be harmonic, $\mathbf{E}(\mathbf{r},t) = \mathbf{E}(\mathbf{r})e^{i\omega t}$. The same line of reasoning can also be applied to the magnetic field $\mathbf{H}$. Equation (2.83) can be expanded into a Fourier series, which leads to:

$$\mathbf{E}_{\mathbf{k}n}(\mathbf{r}) = \sum_{\mathbf{G}} \mathbf{E}_{\mathbf{k}n}(\mathbf{G})e^{i(\mathbf{k}+\mathbf{G})\cdot\mathbf{r}}. \tag{2.84}$$

Introducing (2.78) and (2.84) into the wave equation (2.9) results in an eigenvalue equation for the Fourier coefficients $\{\mathbf{E}_{\mathbf{k}n}(\mathbf{G})\}$. This equation needs to be solved numerically [133]. The same reasoning can be applied to obtain the Fourier coefficients for the magnetic field $\{\mathbf{H}_{\mathbf{k}n}(\mathbf{G})\}$. With one of the two sets of Fourier components known, the photonic band structure (dispersion relation of the eigenmodes), can be calculated.

An example of a simple 2D photonic crystal structure, consisting of dielectric rods embedded in a dielectric medium, is given in Fig. 2.17. Even though the geometry of the PhC is relatively simple, it presents a complex photonic band structure with several band-gaps present. The band-gaps can also be identified by examining the photon density of states, $D(\omega)$, in the crystal. The density of states is defined as $D(\omega) = \omega^2 V/\pi^2 v_g^3$ where V is the volume of the unit cell and v_g is the group velocity. It is important to note that these band-gaps are not *complete* in the sense that the dispersion relation in

Fig. 2.17: 2D photonic crystal geometry consisting of infinite rods: a) schematic of the structure, b) photonic band structure and density of states [134].

Fig. 2.17 considers only the TE polarisation; eigenmodes can exist in the TE band-gap regions for the TM polarisation or for waves with off-plane wave vectors [134]. The dispersion relation also shows another interesting phenomenon which can occur in photonic crystals. The slope of the third or fourth lowest bands in the ΓX region, for example, is very small, which translates into a very small group velocity $\mathbf{v}_g$, defined as:

$$\mathbf{v}_g = \frac{\partial \omega}{\partial \mathbf{k}}. \tag{2.85}$$

Physically, a very low group velocity translates into an increased optical path length and a longer time of interaction between the radiation and the medium of propagation. This leads to increased coupling between the two and can result in the enhancement of several optical effects [135, 136] including optical non-linearities [137]. Note also that, similar to the case of electrons in a crystalline medium, the density of states becomes infinite at frequencies at which $v_g = 0$. This effect is the optical equivalent of the Van Hove singularities, which are discontinuities in the electron density of states of solids [4].

Bibliography

[1] J. C. Maxwell. A Dynamical Theory of the Electromagnetic Field. *Philos. T. Roy. Soc. A*, 155:459–512, January 1865.

[2] J. D. Jackson. *Classical Electrodynamics*. John Wiley & Sons, Hoboken, 3rd edition, 1999.

[3] S. A. Maier. *Plasmonics: Fundamentals and Applications*. Springer-Verlag, New York, 2007.

[4] N. W. Ashcroft and N. D. Mermin. *Solid State Physics*. Brooks/Cole, Belmont, 1976.

[5] M. A. Ordal, R. J. Bell, R. W. Alexander, L. L. Long, and M. R. Querry. Optical properties of fourteen metals in the infrared and far infrared: Al, Co, Cu, Au, Fe, Pb, Mo, Ni, Pd, Pt, Ag, Ti, V, and W. *Appl. Optics*, 24(24):4493–4499, December 1985.

[6] A. D. Rakic, A. B. Djurisic, J. M. Elazar, and M. L. Majewski. Optical properties of metallic films for vertical-cavity optoelectronic devices. *Appl. Optics*, 37(22):5271–5283, 1998.

[7] R. H. Ritchie. Plasma losses by fast electrons in thin films. *Phys. Rev.*, 106(5):874–881, 1957.

[8] H. Raether. *Surface Plasmons on Smooth and Rough Surfaces and on Gratings*. Springer-Verlag, Berlin, 1986.

[9] W. L. Barnes, A. Dereux, and T. W. Ebbesen. Surface plasmon subwavelength optics. *Nature*, 424(6950):824–830, 2003.

[10] A. Zayats, I. I. Smolyaninov, and A. A. Maradudin. Nano-optics of surface plasmon polaritons. *Phys. Rep.*, 408(3-4):131–314, 2005.

[11] J. M. Pitarke, V. M. Silkin, E. V. Chulkov, and P. M. Echenique. Theory of surface plasmons and surface-plasmon polaritons. *Rep. Prog. Phys.*, 70(1):1–87, January 2007.

[12] U. Kreibig and M. Vollmer. *Optical Properties of Metal Clusters*. Springer-Verlag, Berlin, 1995.

[13] M. Schmeits. Surface-plasmon coupling in cylindrical pores. *Phys. Rev. B.*, 39(11):7567–7577, 1989.

[14] E. Kretschmann and H. Raether. Radiative Decay of Non-radiative Surface Plasmons Excited by Light. *Z. Naturforsch. A*, 23a:2135, 1968.

[15] A. Otto. Excitation of Nonradiative Surface Plasma Waves in Silver by the Method of Frustrated Total Reflection. *Z. Phys.*, 216(4):398–410, 1968.

[16] C. F. Bohren and D. R. Huffman. *Absorption and Scattering of Light by Small Particles*. John Wiley & Sons, New York, 1998.

[17] R. Mueckstein and O. Mitrofanov. Imaging of terahertz surface plasmon waves excited on a gold surface by a focused beam. *Opt. Express*, 19(4):3212–3217, 2011.

[18] B. Hecht, H. Bielefeldt, L. Novotny, Y. Inouye, and D. W. Pohl. Local excitation, scattering, and interference of surface plasmons. *Phys. Rev. Lett.*, 77(9):1889–1892, 1996.

[19] D. K. Gramotnev and S. I. Bozhevolnyi. Plasmonics beyond the diffraction limit. *Nature Photon.*, 4(2):83–91, 2010.

[20] G. Veronis and S. Fan. Bends and splitters in metal-dielectric-metal subwavelength plasmonic waveguides. *Appl. Phys. Lett.*, 87(13):131102, 2005.

[21] S. I. Bozhevolnyi, V. S. Volkov, E. Devaux, J.-Y. Laluet, and T. W. Ebbesen. Channel plasmon subwavelength waveguide components including interferometers and ring resonators. *Nature*, 440(7083):508–511, 2006.

[22] P. M. Bolger, W. Dickson, A. V. Krasavin, L. Liebscher, S. G. Hickey, D. V. Skryabin, and A. V. Zayats. Amplified spontaneous emission of surface plasmon polaritons and limitations on the increase of their propagation length. *Opt. Lett.*, 35(8):1197–1199, April 2010.

[23] H. A. Atwater and A. Polman. Plasmonics for improved photovoltaic devices. *Nature Mater.*, 9(3):205–213, 2010.

[24] M. A. Noginov, G. Zhu, A. M. Belgrave, R. Bakker, V. M. Shalaev, E. E. Narimanov, S. Stout, E. Herz, T. Suteewong, and U. Wiesner. Demonstration of a spaser-based nanolaser. *Nature*, 460(7259):1110–1113, 2009.

[25] K. Yu, A. Lakhani, and M. C. Wu. Subwavelength metal-optic semiconductor nanopatch lasers. *Opt. Express*, 18(9):8790–8799, 2010.

[26] M. P. Nezhad, A. Simic, O. Bondarenko, B. Slutsky, A. Mizrahi, L. Feng, V. Lomakin, and Y. Fainman. Room-temperature subwavelength metallo-dielectric lasers. *Nature Photon.*, 4(6):395–399, 2010.

[27] M. Liu, T. Zentgraf, Y. Liu, G. Bartal, and X. Zhang. Light-driven nanoscale plasmonic motors. *Nature Nanotech.*, 5(8):570–573, July 2010.

[28] J. L. West and N. J. Halas. Engineered nanomaterials for biophotonics applications: improving sensing, imaging, and therapeutics. *Annu. Rev. Biomed. Eng.*, 5:285–292, January 2003.

[29] C. Sönnichsen and P. A. Alivisatos. Gold nanorods as novel nonbleaching plasmon-based orientation sensors for polarized single-particle microscopy. *Nano Lett.*, 5(2):301–4, February 2005.

[30] N. Liu, M. Mesch, T. Weiss, M. Hentschel, and H. Giessen. Infrared Perfect Absorber and Its Application As Plasmonic Sensor. *Nano letters*, 10(7):2342–2348, June 2010.

[31] S. Nie and S. R. Emory. Probing Single Molecules and Single Nanoparticles by Surface-Enhanced Raman Scattering. *Science*, 275(5303):1102–1106, February 1997.

[32] K. Kneipp, Y. Wang, H. Kneipp, L. T. Perelman, I. Itzkan, R R Dasari, and M S Feld. Single molecule detection using surface-enhanced Raman scattering (SERS). *Phys. Rev. Lett.*, 78(9):1667–1670, 1997.

[33] C. L. Haynes and R. P. Van Duyne. Plasmon-Sampled Surface-Enhanced Raman Excitation Spectroscopy. *J. Phys. Chem.-US*, 107(30):7426–7433, July 2003.

[34] B. Knoll and F. Keilmann. Near-field probing of vibrational absorption for chemical microscopy. *Nature*, 399(6732):134–137, 1999.

[35] T. Ichimura, N. Hayazawa, M. Hashimoto, Y. Inouye, and S. Kawata. Tip-Enhanced Coherent Anti-Stokes Raman Scattering for Vibrational Nanoimaging. *Phys. Rev. Lett.*, 92(22):20–23, June 2004.

[36] R. M. Roth, N. C. Panoiu, M. M. Adams, R. M. Osgood, C. C. Neacsu, and M. B. Raschke. Resonant-plasmon field enhancement from asymmetrically illuminated conical metallic-probe tips. *Opt. Express*, 14(7):2921–2931, April 2006.

[37] P. Mühlschlegel, H.-J. Eisler, O. J. F. Martin, B. Hecht, and D. W. Pohl. Resonant optical antennas. *Science*, 308(5728):1607–1609, June 2005.

[38] P. J. Schuck, D. P. Fromm, A. Sundaramurthy, G. S. Kino, and W. E. Moerner. Improving the Mismatch between Light and Nanoscale Objects with Gold Bowtie Nanoantennas. *Phys. Rev. Lett.*, 94(1):14–17, January 2005.

[39] T. H. Taminiau, R. J. Moerland, F. B. Segerink, L. Kuipers, and N. F. van Hulst. $\lambda/4$ Resonance of an Optical Monopole Antenna Probed by Single Molecule Fluorescence. *Nano Lett.*, 7(1):28–33, 2007.

[40] V. M. Shalaev. Electromagnetic properties of small-particle composites. *Phys. Rep.*, 272(2):61–137, 1996.

[41] J. R. Krenn, J. C. Weeber, A. Dereux, E. Bourillot, J. P. Goudonnet, and C. Girard. Direct observation of localized surface plasmon coupling. *Phys. Rev. B.*, 60(7):5029–5033, August 1999.

[42] S. Sheikholeslami, Yo.-W. Jun, P. K. Jain, and A. P. Alivisatos. Coupling of Optical Resonances in a Compositionally Asymmetric Plasmonic Nanoparticle Dimer. *Nano Lett.*, 10(7):2655–2660, June 2010.

[43] J. P. Kottmann and O. J. F. Martin. Plasmon resonant coupling in metallic nanowires. *Opt. Express*, 8(12):655–63, June 2001.

[44] E. Prodan, C. Radloff, N. J. Halas, and P. Nordlander. A hybridization model for the plasmon response of complex nanostructures. *Science*, 302(5644):419–22, October 2003.

[45] T. J. Davis, D. E. Gomez, and K. C. Vernon. Simple Model for the Hybridization of Surface Plasmon Resonances in Metallic Nanoparticles. *Nano Lett.*, 10(7):2618–2625, June 2010.

[46] J. M. McMahon, S. K. Gray, and G. C. Schatz. Optical Properties of Nanowire Dimers with a Spatially Nonlocal Dielectric Function. *Nano Lett.*, 10(9):3473–3481, August 2010.

[47] M. Liu, T.-W. Lee, S. Gray, P. Guyot-Sionnest, and M. Pelton. Excitation of Dark Plasmons in Metal Nanoparticles by a Localized Emitter. *Phys. Rev. Lett.*, 102(10):107401, March 2009.

[48] C. G. Biris and N. C. Panoiu. Second harmonic generation in metamaterials based on homogeneous centrosymmetric nanowires. *Phys. Rev. B.*, 81(19):195102, May 2010.

[49] Y. R. Shen. *Nonlinear Optics*. John Wiley & Sons, Hoboken, 1984.

[50] P. A. Franken, A. E. Hill, C. W. Peters, and G. Weinreich. Generation of optical harmonics. *Phys. Rev. Lett.*, 7(4):118–119, 1961.

[51] M. Bass, P. A. Franken, J. F. Ward, and G. Weinreich. Optical Rectification. *Phys. Rev. Lett.*, 9(11):28–31, 1962.

[52] R. W. Boyd. *Nonlinear Optics*. Elsevier, San Diego, 2nd edition, 2003.

[53] P. S. Pershan. Nonlinear optical properties of solids: energy considerations. *Phys. Rev.*, 130(3):919–929, 1963.

[54] N. Bloembergen and P. S. Pershan. Light Waves at the Boundary of Nonlinear Media. *Phys. Rev.*, 128(2):606–622, October 1962.

[55] T. F. Heinz. Second-order nonlinear optical effects at surfaces and interfaces. In *Nonlinear Surface Electromagnetic Phenomena*, chapter 5, pages 353–416. Elsevier, 1991.

[56] D. Krause, C. W. Teplin, and C. T. Rogers. Optical surface second harmonic measurements of isotropic thin-film metals: Gold, silver, copper, aluminum, and tantalum. *J. Appl. Phys.*, 96(7):3626–3634, 2004.

[57] N. Bloembergen, R. K. Chang, S. S. Jha, and C. H. Lee. Optical second-harmonic generation in reflection from media with inversion symmetry. *Phys. Rev.*, 174(3):813–822, 1968.

[58] L. Cao, N. C. Panoiu, R. D. R. Bhat, and R. M. Osgood. Surface second-harmonic generation from scattering of surface plasmon polaritons from radially symmetric nanostructures. *Phys. Rev. B.*, 79(23):235416, June 2009.

[59] J van Nieuwstadt, M Sandtke, R Harmsen, F Segerink, J Prangsma, S Enoch, and L Kuipers. Strong Modification of the Nonlinear Optical Response of Metallic Subwavelength Hole Arrays. *Physical Review Letters*, 97(14):1–4, 2006.

[60] A. Marini, A. V. Gorbach, D. V. Skryabin, and A. V. Zayats. Amplification of surface plasmon polaritons in the presence of nonlinearity and spectral signatures of threshold crossover. *Opt. Lett.*, 34(18):2864–2866, September 2009.

[61] N. C. Panoiu and R. M. Osgood. Subwavelength Nonlinear Plasmonic Nanowire. *Nano Lett.*, 4(12):2427–2430, December 2004.

[62] D. V. Skryabin, A. V. Gorbach, and A. Marini. Surface-induced nonlinearity enhancement of TM modes in planar subwavelength waveguides. *J. Opt. Soc. Am. B*, 28(1):109–114, 2011.

[63] C. G. Biris and N. C. Panoiu. Nonlinear pulsed excitation of high-Q optical modes of plasmonic nanocavities. *Opt. Express*, 18(16):17165–17179, August 2010.

[64] C. G. Biris and N. C. Panoiu. Excitation of linear and nonlinear cavity modes upon interaction of femtosecond pulses with arrays of metallic nanowires. *Appl. Phys. A-Mater.*, 103(3):863–867, January 2011.

[65] C. G. Biris and N. C. Panoiu. Excitation of dark plasmonic cavity modes via nonlinearly induced dipoles: applications to near-infrared plasmonic sensing. *Nanotechnology*, 22(23):235502, April 2011.

[66] V. K. Valev, A. Kirilyuk, F. Dalla Longa, J. Kohlhepp, B. Koopmans, and Th. Rasing. Observation of periodic oscillations in magnetization-induced second harmonic generation at the MnCo interface. *Phys. Rev. B.*, 75(1):012401, January 2007.

[67] H. W. K. Tom, T. F. Heinz, and Y. R. Shen. Second-Harmonic Reflection from Silicon Surfaces and Its Relation to Structural Symmetry. *Phys. Rev. Lett.*, 51(21):1983–1985, 1983.

[68] O. A. Aktsipetrov, I. M. Baranova, E. D. Mishina, and A. V. Petukhov. Lightning rod effect in surface-enhanced second harmonic generation. *JETP Lett.*, 40(6):1012–1015, 1984.

[69] C. H. Lee, R. K. Chang, and N. Bloembergen. Nonlinear electroreflectance in Silicon and Silver. *Phys. Rev. Lett.*, 18(5):167–169, 1967.

[70] A. Kirilyuk and Th. Rasing. Magnetization-induced-second-harmonic generation from surfaces and interfaces. *J. Opt. Soc. Am. B*, 22(1):148–167, 2005.

[71] O. A. Aktsipetrov, T. V. Murzina, E. M. Kim, R. V. Kapra, A. A. Fedyanin, M. Inoue, A. F. Kravets, S. V. Kuznetsova, M. V. Ivanchenko, and V. G. Lifshits. Magnetization-induced second-and third-harmonic generation in magnetic thin films and nanoparticles. *J. Opt. Soc. Am. B*, 22(1):138–147, 2005.

[72] Y. Sheng, A. Best, H.-J. Butt, W. Krolikowski, A. Arie, and K. Koynov. Three-dimensional ferroelectric domain visualization by Cerenkov-type second harmonic generation. *Opt. Express*, 18(16):409–413, 2010.

[73] V. V. Pavlov, J. Ferré, P. Meyer, G. Tessier, P. Georges, A. Brun, P. Beauvillain, and V. Mathet. Linear and non-linear magneto-optical studies of Pt/Co/Pt thin films. *J. Phys.-Condens. Mat.*, 13(44):9867–9878, 2001.

[74] V. K. Valev, X. Zheng, C. G. Biris, A. V. Silhanek, V. Volskiy, B. De Clercq, O. A. Aktsipetrov, M. Ameloot, N. C. Panoiu, and G. A. E. Vandenbosch. The origin of second harmonic generation hotspots in chiral optical metamaterials. *Opt. Mater. Express*, 1(1):36–45, 2011.

[75] J. D Byers and H. I. Yee. A second harmonic generation analog of optical rotatory dispersion for the study of chiral monolayers. *J. Chem. Phys.*, 101(7):6233–6241, 1994.

[76] T. Petralli-Malow, T. M. Wong, J. D. Byers, H. I. Yee, and J. M. Hicks. Circular Dichroism Spectroscopy at Interfaces: A Surface Second Harmonic Generation Study. *J. Phys. Chem.-US*, 97(7):1383–1388, 1993.

[77] P. Fischer and F. Hache. Nonlinear optical spectroscopy of chiral molecules. *Chirality*, 17(8):421–437, 2005.

[78] T. Verbiest, S. Van Elshocht, M. Kauranen, L. Hellemans, J. Snauwaert, C. Nuckolls, T. J. Katz, and A. Persoons. Strong Enhancement of Nonlinear Optical Properties Through Supramolecular Chirality. *Science*, 282(5390):913–915, October 1998.

[79] S. Foerier, I. A. Kolmychek, O. A. Aktsipetrov, T. Verbiest, and V. K. Valev. Optical second harmonic generation chiral spectroscopy. *ChemPhysChem*, 10(9-10):1431–1434, 2009.

[80] Y. Tang and A. E. Cohen. Optical Chirality and Its Interaction with Matter. *Phys. Rev. Lett.*, 104(16):1–4, April 2010.

[81] V. K. Valev, A. V. Silhanek, W. Gillijns, Y. Jeyaram, H. Paddubrouskaya, A. Volodin, C. G. Biris, N. C. Panoiu, B. De Clercq, M. Ameloot, O. A. Aktsipetrov, V. V. Moshchalkov, and T. Verbiest. Plasmons reveal the direction of magnetization in nickel nanostructures. *ACS Nano*, 5(1):91–6, January 2011.

[82] V. V. Temnov, G. Armelles, U. Woggon, D. Guzatov, A. Cebollada, A. Garcia-Martin, J. M. Garcia-Martin, Ti. Thomay, A. Leitenstorfer, and R. Bratschitsch. Active magneto-plasmonics in hybrid metalferromagnet structures. *Nature Photon.*, 4(2):107–111, 2010.

[83] M. Fiebig, V. V. Pavlov, and R. V. Pisarev. Second-harmonic generation as a tool for studying electronic and magnetic structures of crystals : review. *J. Opt. Soc. Am. B*, 22(1):96–118, 2005.

[84] J. F. McGilp, L. Carroll, K. Fleischer, J. P. Cunniffe, and S. Ryan. Magnetic second-harmonic generation from interfaces and nanostructures. *J. Magn. Magn. Mater.*, 322(9-12):1488–1493, May 2010.

[85] G. Tessier, C. Malouin, P. Georges, A. Brun, D. Renard, V. V. Pavlov, P. Meyer, J. Ferré, and P. Beauvillain. Magnetization-induced second-harmonic generation enhanced by surface plasmons in ultrathin Au/Co/Au metallic films. *Appl. Phys. B-Lasers O.*, 68(3):545–548, March 1999.

[86] V. V. Pavlov, G. Tessier, C. Malouin, P. Georges, A. Brun, D. Renard, P. Meyer, J. Ferré, and P. Beauvillain. Observation of magneto-optical second-harmonic generation with surface plasmon excitation in ultrathin Au/Co/Au films. *Appl. Phys. Lett.*, 75(2):190–192, 1999.

[87] D. M. Newman, M. L. Wears, R. J. Matelon, and I. R. Hooper. Magneto-optic behaviour in the presence of surface plasmons. *J. Phys.-Condens. Mat.*, 20(34):345230, August 2008.

[88] T. V. Murzina, T. V. Misuryaev, A. F. Kravets, J. Gudde, D. Schuhmacher, G. Marowsky, A. A. Nikulin, and O. A. Aktsipetrov. Nonlinear Magneto-optical Kerr Effect and Plasmon-Assisted SHG in Magnetic Nanomaterials Exhibiting Giant Magnetoresistance. *Surf. Sci.*, 482-485:1101–1106, 2001.

[89] Th. Rasing. Nonlinear magneto-optics. *J. Magn. Magn. Mater.*, 175(1-2):35–50, November 1997.

[90] S. A. Ramakrishna. Physics of negative refractive index materials. *Rep. Prog. Phys.*, 68(2):449–521, February 2005.

[91] V. G. Veselago. The Electrodynamics of Substances with Simultaneously Negative Values of ϵ and μ. *Phys.-Uspekhi*, 10(4):509–514, 1968.

[92] R. A. Shelby, D. R. Smith, and S. Schultz. Experimental verification of a negative index of refraction. *Science*, 292(5514):77–79, April 2001.

[93] W. Cai and V. M. Shalaev. *Optical Metamaterials: Fundamentals and Applications*. Springer-Verlag, New York, 2010.

[94] G. H. B. Thompson. Unusual waveguide characteristics associated with the apparent negative permeability obtainable in ferrites. *Nature*, 175(4469):1135–1136, 1955.

[95] S. Linden, C. Enkrich, M. Wegener, J. Zhou, T. Koschny, and C. M. Soukoulis. Magnetic response of metamaterials at 100 terahertz. *Science*, 306(5700):1351–1353, November 2004.

[96] S. Zhang, W. Fan, B. K. Minhas, A. Frauenglass, K. J. Malloy, and S. R. J. Brueck. Midinfrared Resonant Magnetic Nanostructures Exhibiting a Negative Permeability. *Phys. Rev. Lett.*, 94(3):037402, January 2005.

[97] W. Cai, U. K. Chettiar, H.-K. Yuan, V. C. de Silva, A. V. Kildishev, V. P. Drachev, and V. M. Shalaev. Metamagnetics with rainbow colors. *Opt. Express*, 15(6):3333–3341, 2007.

[98] N. C. Panoiu and R. M. Osgood. Influence of the dispersive properties of metals on the transmission characteristics of left-handed materials. *Phys. Rev. E*, 68(1):016611, July 2003.

[99] S. Zhang, W. Fan, N. C. Panoiu, K. J. Malloy, R. M. Osgood, and S. R. J. Brueck. Experimental Demonstration of Near-Infrared Negative-Index Metamaterials. *Phys. Rev. Lett.*, 95(13):137404, 2005.

[100] V. M. Shalaev, W. Cai, U. K. Chettiar, H.-K. Yuan, A. K. Sarychev, V. P. Drachev, and A. V. Kildishev. Negative index of refraction in optical metamaterials. *Opt. Lett.*, 30(24):3356–3358, December 2005.

[101] N. Liu, H. Guo, L. Fu, S. Kaiser, H. Schweizer, and H. Giessen. Three-dimensional photonic metamaterials at optical frequencies. *Nature Mater.*, 7(1):31–38, 2008.

[102] G. V. Eleftheriades, A. K. Iyer, and P. C. Kremer. Planar negative refractive index media using periodically LC loaded transmission lines. *IEEE Trans. Microw. Theory*, 50(12):2702–2712, 2002.

[103] C. Caloz, A. Sanada, and T. Itoh. A novel composite right-/left-handed coupled-line directional coupler with arbitrary coupling level and broad bandwidth. *IEEE Trans. Microw. Theory*, 52(3):980–992, 2004.

[104] D. Sievenpiper, R. F. J. Broas, N. G. Alexopolous, and E. Yablonovitch. High-impedance electromagnetic surfaces with a forbidden frequency band. *IEEE Trans. Microw. Theory*, 47(11):2059–2074, 1999.

[105] A. Alù and N. Engheta. Achieving transparency with plasmonic and metamaterial coatings. *Phys. Rev. E*, 72(1):016623, 2005.

[106] U. Leonhardt. Optical conformal mapping. *Science*, 312(5781):1777–1780, June 2006.

[107] J. B. Pendry, D. Schurig, and D. R. Smith. Controlling electromagnetic fields. *Science*, 312(5781):1780–1782, June 2006.

[108] J. Li, L. Zhou, C. T. Chan, and P. Sheng. Photonic Band Gap from a Stack of Positive and Negative Index Materials. *Phys. Rev. Lett.*, 90(8):083901, 2003.

[109] R. Ziolkowski. Propagation in and scattering from a matched metamaterial having a zero index of refraction. *Phys. Rev. E*, 70(4):046608, 2004.

[110] N. C. Panoiu, R. M. Osgood, S. Zhang, and S. R. J. Brueck. Zero-$\bar{n}$ bandgap in photonic crystal superlattices. *J. Opt. Soc. Am. B*, 23(3):506–513, 2006.

[111] S. Kocaman, R. Chatterjee, N. C. Panoiu, J. F. McMillan, M. B. Yu, R. M. Osgood, D. L. Kwong, and C. W. Wong. Observation of Zeroth-Order Band Gaps in Negative-Refraction Photonic Crystal Superlattices at Near-Infrared Frequencies. *Phys. Rev. Lett.*, 102(20):203905, 2009.

[112] R. D. Kekatpure, E. S. Barnard, W. Cai, and M. L. Brongersma. Phase-Coupled Plasmon-Induced Transparency. *Phys. Rev. Lett.*, 104(24):243902, 2010.

[113] T. Ergin, N. Stenger, P. Brenner, J. B. Pendry, and M. Wegener. Three-dimensional invisibility cloak at optical wavelengths. *Science*, 328(5976):337–339, April 2010.

[114] J. B. Pendry. Negative refraction makes a perfect lens. *Phys. Rev. Lett.*, 85(18):3966–3969, 2000.

[115] J.B. Pendry, A.J. Holden, D.J. Robbins, and W.J. Stewart. Magnetism from conductors and enhanced nonlinear phenomena. *IEEE Trans. Microw. Theory*, 47(11):2075–2084, 1999.

[116] R. M. Roth, N. C. Panoiu, M. M. Adams, J. I. Dadap, and R. M. Osgood. Polarization-tunable plasmon-enhanced extraordinary transmission through metallic films using asymmetric cruciform apertures. *Opt. Lett.*, 32(23):3414–3416, 2007.

[117] W. Fan, S. Zhang, N. C. Panoiu, A. Abdenour, S. Krishna, R. M. Osgood, K. J. Malloy, and S. R. J. Brueck. Second Harmonic Generation from a Nanopatterned Isotropic Nonlinear Material. *Nano Lett.*, 6(5):1027–1030, May 2006.

[118] I. I. Smolyaninov, A. V. Zayats, A. Gungor, and C. C. Davis. Single-Photon Tunneling via Localized Surface Plasmons. *Phys. Rev. Lett.*, 88(18):187402, 2002.

[119] X. W. Wang, G. C. Schatz, and S. K. Gray. Ultrafast pulse excitation of a metallic nanosystem containing a Kerr nonlinear material. *Phys. Rev. B.*, 74(19):195439, 2006.

[120] H.-T. Chen, J. F. O'Hara, A. K. Azad, A. J. Taylor, R. D. Averitt, D. B. Shrekenhamer, and W. J. Padilla. Experimental demonstration of frequency-agile terahertz metamaterials. *Nature Photon.*, 2(5):295–298, April 2008.

[121] P. G. Thompson, C. G. Biris, E. J. Osley, O. Gaathon, R. M. Osgood, N. C. Panoiu, and P. A. Warburton. Polarization-induced tunability of localized surface plasmon resonances in arrays of sub-wavelength cruciform appertures. *Opt. Express*, xx(xxxx):(to be submitted), 2011.

[122] S. J. Oldenburg, R. D. Averitt, S. L. Westcott, and N. J. Halas. Nanoengineering of optical resonances. *Chem. Phys. Lett.*, 288(2-4):243–247, 1998.

[123] S. A. Maier, M. L. Brongersma, P. G. Kik, S. Meltzer, A. A. G. Requicha, and H. a. Atwater. Plasmonics - A Route to Nanoscale Optical Devices. *Adv. Mater.*, 13(19):1501–1505, September 2001.

[124] F. J. Garcia-Vidal, T. W. Ebbesen, and L. Kuipers. Light passing through subwavelength apertures. *Rev. Mod. Phys.*, 82(1):729–787, March 2010.

[125] A. Papakostas, A. Potts, D. M. Bagnall, S. L. Prosvirnin, H. J. Coles, and N. I. Zheludev. Optical Manifestations of Planar Chirality. *Phys. Rev. Lett.*, 90(10):107404, March 2003.

[126] K. Sakoda. *Optical Properties of Photonic Crystals*. Springer-Verlag, Heidelberg, 2nd edition, 2005.

[127] A. Birner, R. B. Wehrspohn, U. M. Gösele, and K. Busch. Silicon-Based Photonic Crystals. *Adv. Mater.*, 13(6):377–388, March 2001.

[128] J. G. Fleming, S. Y. Lin, R. Biswas, and K. M. Ho. All-metallic three-dimensional photonic crystals with a large infrared bandgap. *Nature*, 417:1548–1551, 2002.

[129] C. R. Giles. Lightwave applications of fiber Bragg gratings. *J. Lightwave Technol.*, 15(8):1391–1404, 1997.

[130] V. Kuzmiak, A. A. Maradudin, and F. Pincemin. Photonic band structures of two-dimensional systems containing metallic components. *Phys. Rev. B.*, 50(23):16835–16844, 1994.

[131] Z. Zhang and S. Satpathy. Electromagnetic Wave Propagation in Periodic Structures: Bloch Wave Solution of Maxwell's Equations. *Phys. Rev. Lett.*, 65(21):2650–2663, 1990.

[132] J. D. Joannopoulos, S. G. Johnson, J. N. Winn, and R. D. Meade. *Photonic Crystals: Molding the Flow of Light*. Princeton Univesrity Press, Princeton, 2008.

[133] K. M. Ho, C. T. Chan, and C. M. Soukoulis. Existence of a Photonic Gap in Periodic Dielectric Structures. *Phys. Rev. Lett.*, 65(25):3152–3155, 1990.

[134] K. Sakoda and H. Shiroma. Numerical method for localized defect modes in photonic lattices. *Phys. Rev. B.*, 56(8):4830–4835, August 1997.

[135] J. P. Dowling, M. Scalora, M. J. Bloemer, and C. M. Bowden. The photonic band edge laser: A new approach to gain enhancement. *J. Appl. Phys.*, 75(4):1896, 1994.

[136] R. W. Boyd and D. J. Gauthier. Controlling the Velocity of Light Pulses. *Science*, 326:1074–1077, 2009.

[137] M Soljacic and J D Joannopoulos. Enhancement of nonlinear effects using photonic crystals. *Nature materials*, 3(4):211–220, 2004.

Chapter 3

Theory of Linear and Non-Linear Scattering of Electromagnetic Waves from Two-dimensional Systems

3.1 Introduction

As discussed in the previous chapter, one of the main consequences of the plasmon-induced resonant enhancement of the electromagnetic field is that strong non-linear optical effects can be achieved at relatively small optical power. In particular, the strength of second-order non-linear optical effects, such as the second-harmonic generation, is proportional to $|E|^4$, and therefore an enhancement of $\sim$10–100 of the local field at the fundamental frequency, easily achievable by using metallic nanoparticles, leads to an increase of up to 10^8 of the intensity of the light generated at the second harmonic [1–3]. It should therefore be clear that in order to achieve a comprehensive characterisation of the SHG in metallo-dielectric structures one has to employ theoretical methods and/or numerical simulations that enable one to accurately determine the spatial distribution of the electromagnetic field at the FF.

Since most metals are centrosymmetric media, it is of particular interest to develop robust theoretical models that describe the generation of the SH upon the scattering of light from ensembles of nanoparticles made of centrosymmetric materials. Recently, significant progress towards this goal has been made, with some notable examples being the theory of SHG from spherical [4] and cylindrical [5] particles of low-index contrast centrosymmetric materials or, more generally, SHG from a metallic cylinder [6]. It should be noted that in the former case the theoretical approach is valid only within the Rayleigh-Gans-Debye approximation, *i.e.*, it is assumed that the field at the FF is not perturbed during the scattering process, whereas the latter approach only applies to a single scatterer.

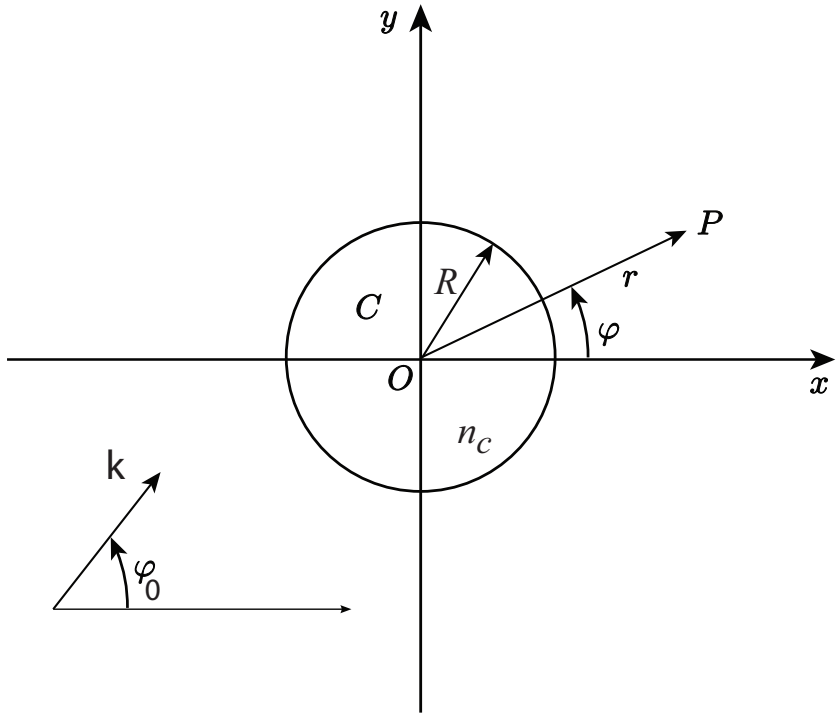

Fig. 3.1: Geometry of a single cylindrical scatterer. The cylinder is assumed to have radius R and permitivitty ϵ_c.

This chapter will present a theoretical formalism based on the *multiple scattering matrix* (MSM) algorithm, which can rigorously describe the general case, namely, the SHG from a collection of cylinders with arbitrary electric permittivity, which are made of centrosymmetric materials. Importantly, this theoretical approach enables one to account for the contribution to the SH field of both the surface and the bulk non-linear polarisations. Using this formalism, it is possible to retrieve the full linear and non-linear field distribution, as well as the linear and non-linear total, scattering and absorption cross sections.

3.2 Formulation of the Scattering Problem for Two-dimensional Geometries

The scattering of electromagnetic waves by materials is a well known problem in electromagnetism. Given an object or system of objects that is illuminated by an electromagnetic wave, the question arises as to how the system will interact with the incoming light and what are the effects of this interaction, both in the near- and the far- field. The focus of this chapter will be on introducing a new numerical method which allows one to study both the liner and non-linear scattering from an array of arbitrarily distributed parallel cylinders. Nevertheless, it is useful to begin with a simpler case, that is, finding the analytical solution to the scattering problem from a single, linear, non-magnetic, infinite cylinder in air.

To begin with, we define the geometry and the physical conditions of the system. For simplicity, we assume an infinite cylinder centred at the origin of a system of cylindrical coordinates (ρ, ϕ, z), with $(0, 0, z)$ being the cylinder axis. The cylinder is illuminated by a monochromatic wave, normal onto its surface. This setup is illustrated in Fig. 3.1. In this configuration, two polarisation cases can be identified. In one case, the electric field is parallel to the z-axis, thus it has a single non-zero component E_z, and the magnetic field is perpendicular to the axis of the cylinder. We call this the TM polarisation. In the second case, the TE polarisation, the magnetic field is parallel to the z-axis and the electric field has two non-zero components, E_r and E_φ. In what follows, the TM case will be considered in detail with the extensions to the TE polarisation being given at the end of the analysis.

In the free space around the cylinder, the z-component of the incoming plane wave can be expanded in a Fourier-Bessel series as [7]:

$$E_z^{inc}(r, \varphi) = \sum_{m=-\infty}^{\infty} a_m J_m(kr) e^{im\varphi}, \tag{3.1}$$

where k is the transverse component of the wave vector, a_m are the Fourier-Bessel coefficients of the incoming wave and J_m is Bessel function of the first kind. Equation (3.1) is evaluated at a point $P(r, \varphi)$. In the case considered here, of normal incidence and TE polarisation, the Fourier coefficients can be written as:

$$a_m = E_0 e^{-im(\varphi_0 + \pi/2)}, \tag{3.2}$$

where E_0 is the wave amplitude and φ_0 is the angle between the x-axis and the wave vector of the incoming wave.

To understand the origin of Eq. (3.1), let us now consider the Helmholtz equation (2.10) in cylindrical coordinates:

$$\frac{\partial^2 U}{\partial r^2} + \frac{1}{r}\frac{\partial U}{\partial r} + \frac{1}{r^2}\frac{\partial^2 U}{\partial \varphi^2} + \frac{\partial^2 U}{\partial z^2} - \mu\epsilon\omega^2 U = 0, \tag{3.3}$$

where U can be any of the electromagnetic field components. It can be separated as $U(r, \varphi, z) = R(r)Q(\varphi)Z(z)$. This leads to three separate differential equations [8]:

$$\frac{d^2 Z}{dz^2} - l^2 Z = 0 \tag{3.4a}$$

$$\frac{d^2 Q}{d\varphi^2} + m^2 Q = 0 \tag{3.4b}$$

$$\frac{d^2 R}{dr^2} + \frac{1}{r}\frac{dR}{dr} + \left(n^2 - \frac{m^2}{r^2}\right) R = 0. \tag{3.4c}$$

Here m and l are integers, $k = \sqrt{\epsilon\mu\omega^2}$ is the wave vector, and we have used the notation $n^2 = l^2 + k^2$. The solutions to Eqs. (3.4a) and (3.4b) are of the form:

$$Z(z) = e^{\pm lz} \tag{3.5a}$$

$$Q(\varphi) = e^{\pm im\varphi} \tag{3.5b}$$

Of particular interest, however, in the case of a cylindrical geometry, is the radial equation (3.4c). In the case of normal incidence at $z = 0$, we can set $l = 0$. Then, using the notation $\kappa = kr$, Eq. (3.4c) becomes:

$$\frac{d^2R}{d\kappa^2} + \frac{1}{\kappa}\frac{dR}{d\kappa} + \left(1 - \frac{m^2}{\kappa^2}\right) R = 0, \tag{3.6}$$

which is the well known Bessel equation. Equation (3.6) supports solutions of the form [8]:

$$J_m(\kappa) = \left(\frac{\kappa}{2}\right)^m \sum_{j=0}^{\infty} \frac{(-1)^j}{j!\,\Gamma(j+m+1)} \left(\frac{\kappa}{2}\right)^{2j} \tag{3.7a}$$

$$J_{-m}(\kappa) = \left(\frac{\kappa}{2}\right)^{-m} \sum_{j=0}^{\infty} \frac{(-1)^j}{j!\,\Gamma(j-m+1)} \left(\frac{\kappa}{2}\right)^{2j}, \tag{3.7b}$$

which are the Bessel functions of the first kind. When m is an integer, it is easy to see from Eqs. (3.7) that:

$$J_{-m}(\kappa) = (-1)^m J_m(\kappa). \tag{3.8}$$

Another set of useful Bessel functions, are the Bessel functions of the third kind, or Hankel functions. The common definition for the Hankel functions is:

$$H_m^{(1)}(\kappa) = J_m(\kappa) + iN_m(\kappa) \tag{3.9a}$$

$$H_m^{(2)}(\kappa) = J_m(\kappa) - iN_m(\kappa), \tag{3.9b}$$

where $N_m(\kappa) = [J_m(\kappa)\cos(m\pi) - J_{-m}(\kappa)]/\sin(m\pi)$ are the Neumann functions (or Bessel functions of the second kind) and $H_m^{(1)}$ and $H_m^{(2)}$ are usually reffered to as the Hankel functions of the first and second kind, respectively.

Finally, all Bessel functions and their derivatives obey the recursion relation:

$$\frac{d\Omega_m(\kappa)}{d\kappa} = \frac{\Omega_{m-1}(\kappa) - \Omega_{m+1}(\kappa)}{2}, \tag{3.10}$$

where $\Omega_m(\kappa)$ can be any of the $J_m, N_m, H_m^{(1)}$ and $H_m^{(2)}$ functions.

We now search for the most general solution to the Helmoltz equation (3.3). With

the previous assumption of $l = 0$, this solution will be of the form:

$$U(r, \varphi) = \sum_m A_m R_m(r) Q_m(m), \tag{3.11}$$

where A_m are Bessel expansion coefficients. It is easy to see now that by using Eq. (3.5b) and the Bessel equation solutions (3.7), Eq. (3.11) becomes the expansion in Eq. (3.1). Here, we have identified $A_m = a_m$ as the incoming field Bessel expansion coefficients and $U(r, \varphi) = E_z^{inc}(r, \varphi)$ as the z component of the incoming electric field.

Inside the cylinder, the fields are expressed in terms of Bessel functions, too. However, one also has to take into account the material properties of the cylinder. Thus, the electric field inside the cylinder can be written as:

$$E_z^{int} = \sum_{m=-\infty}^{\infty} c_m J_m(\kappa_c) e^{im\phi}, \tag{3.12}$$

where c_m are the internal Fourier-Bessel expansion coefficients and $\kappa_c = k n_c r$ is the wave number of the field inside the cylinder, with n_c being the refractive index of the cylinder.

The field scattered by the cylinders also obeys Eq. (3.3). In this case, however, the field needs to be expanded using the Hankel functions, as they describe outgoing waves. Thus, the scattered electric field becomes:

$$E_z^{sca} = \sum_{m=-\infty}^{\infty} b_m H_m^{(2)}(\kappa) e^{im\varphi}, \tag{3.13}$$

where b_m are the scattered field coefficients.

The scattering problem is now reduced to finding the coefficients b_m and c_m. This can be achieved by imposing the boundary conditions of the electromagnetic field at the interface between the cylinder and the background (*i.e.*, for $r = R$, where R is the radius of the cylinder). For the case of a system with no internal sources, the electromagnetic boundary conditions imply the continuity of the tangent field components, $E_z^{ext} = E_z^{int}$ and $H_\varphi^{ext} = H_\varphi^{int}$, where:

$$E_z^{ext} = E_z^{inc} + E_z^{sca} \tag{3.14a}$$

$$H_\varphi^{ext} = H_\varphi^{inc} + H_\varphi^{sca} \tag{3.14b}$$

are the total fields outside the cylinder. The H_φ components can be determined from Maxwell's equations [8]. Imposing the boundary conditions and eliminating the c_m components between the two resulting equations, leads to the following solution for

the b_m coefficients [for the detailed steps required, see Appendix B]:

$$b_m = a_m \frac{\alpha J_m(kn_cR)J'_m(kR) - J_m(kR)J'_m(kn_cR)}{H^{(2)}(kR)J'_m(kn_cR) - \alpha J_m(kn_cR)H^{(2)\prime}_m(kR)}, \tag{3.15}$$

where the prime denotes a derivative with respect to the argument and $\alpha = (k_c\epsilon)/(k\epsilon_c)$. The coefficients b_m can now be found as all the terms in the r.h.s of Eq. (3.15) are known. Consequently, the internal field coefficients can also be determined as:

$$c_m = \frac{a_m J_m(kR) + b_m H^{(2)}(kR)}{J_m(kn_cR)}. \tag{3.16}$$

To complete the discussion, the TE case must also be taken into account. In this case, the z component of the electromagnetic field is H_z. The incoming field coefficients for this polarisation can be written:

$$a_m = H_0 e^{-im(\pi/2+\varphi_0)}, \tag{3.17}$$

where $H_0 = E_0/Z$ with $Z = \sqrt{\mu/\epsilon}$ the impedance of the background. The same line of reasoning can be followed as for the TM problem. The boundary conditions at the surface of the cylinder now require that $H_z^{ext} = H_z^{int}$ and $E_\varphi^{ext} = E_\varphi^{int}$. The scattering field coefficients can be found to be:

$$b_m = a_m \frac{\beta J_m(kn_cR)J'_m(kR) - J_m(kR)J'_m(kn_cR)}{H^{(2)}(kR)J'_m(kn_cR) - \beta J_m(kn_cR)H^{(2)\prime}_m(kR)}, \tag{3.18}$$

where $\beta = k_c/k$. The internal field coefficients can still be found using Eq. (3.16).

With both the TM and TE cases treated, the scattering problem of a single, infinite, cylinder can be considered solved. In the next section, this method will be extended to an arbitrary distribution of cylinders. At the same time, the solution of the scattering problem for such a geometry will be shown in the non-linear case, too, namely when the surface second harmonic generation is considered.

3.3 Scattering Problem for an Ensemble of Cylinders

The numerical method used in our analysis of the linear and non-linear scattering problem from an ensemble of cylinders is based on a recently introduced numerical algorithm that describes the SHG in photonic systems made of non-centrosymmetric quadratically non-linear optical materials [9]. In this case, the dominant non-linear optical interaction is described by the dipole (local) contribution of the second-order non-linear bulk polarization. However, this dipole contribution to the non-linear polarization vanishes in the case of centrosymmetric materials and therefore the numerical

method introduced in Ref. [9] can not be used to study the SHG in this important class of materials.

In the approach introduced in this chapter the calculation of the scattered field at the SH is performed in two stages. First, by using a standard *multiple scattering matrix* (MSM) algorithm the electromagnetic field at the fundamental frequency is calculated, and this field is subsequently used to determine the non-linear polarisation at the SH. In a second stage, this non-linear polarisation, which plays the role of the source of the field at the second harmonic, is used to calculate the spatial distribution of the scattered field at the SH. Note that this two-stage approach implies that no energy is transferred back from the SH to the FF and therefore the numerical method presented here is valid only within the so-called undepleted pump approximation, *i.e.*, when the energy at the SH dissipates only through linear optical losses. Due to the reduced conversion efficiency of the SHG interaction and the small size of the nanostructures involved in the non-linear scattering process, the undepleted pump approximation is valid in all cases considered.

3.3.1 Description of the System Geometry

The non-linear scattering problem is schematically illustrated in Fig. 3.2. Thus, an ensemble of N parallel, infinitely long cylinders, C_j, $j = 1, 2, \ldots, N$, embedded in a background medium with electric permittivity ϵ_b and magnetic permeability μ_b is considered. The cylinders are assumed to be oriented along the z-axis. The j-th cylinder has radius R_j and is characterized by the permittivity $\epsilon_j(\omega)$, which, for the sake of generality, is assumed to be dependent on the frequency ω, and the magnetic permeability μ_j; here and in what follows it is considered that $\mu_j = \mu_b \equiv \mu_0$, $j = 1, 2, \ldots, N$, where μ_0 is the magnetic permeability of the vacuum. In addition, each cylinder is characterised by a surface second-order susceptibility, $\hat{\chi}^{(2)}_{s,j}$. The position of the center O_j of the j-th cylinder is specified by the polar coordinates (r_j, φ_j), which are defined with respect to a coordinate system with the origin in O. Moreover, as per fig. 3.2, the position of the center of the k-th cylinder, specified in a coordinate system with the origin in O_j, is defined by the polar coordinates (r^j_k, φ^j_k), whereas the position of an arbitrary point P, defined with respect to the coordinate systems with the origin in O and O_j, is specified by the polar coordinates (r_P, φ_P) and (r^j_P, φ^j_P), respectively.

An incident monochromatic electromagnetic plane wave impinging onto the system of cylinders is fully described by its conicity angles ϕ_0, θ_0, and δ_0, where ϕ_0 is the angle between the projection onto the xy-plane of the wave vector of the incident wave and the x-axis, θ_0 is the angle between the wave vector of the incident wave and the z-axis, and δ_0 is the angle between the electric field of the incident wave and the plane defined by the z-axis and the wave vector. Moreover, while this analysis can be applied

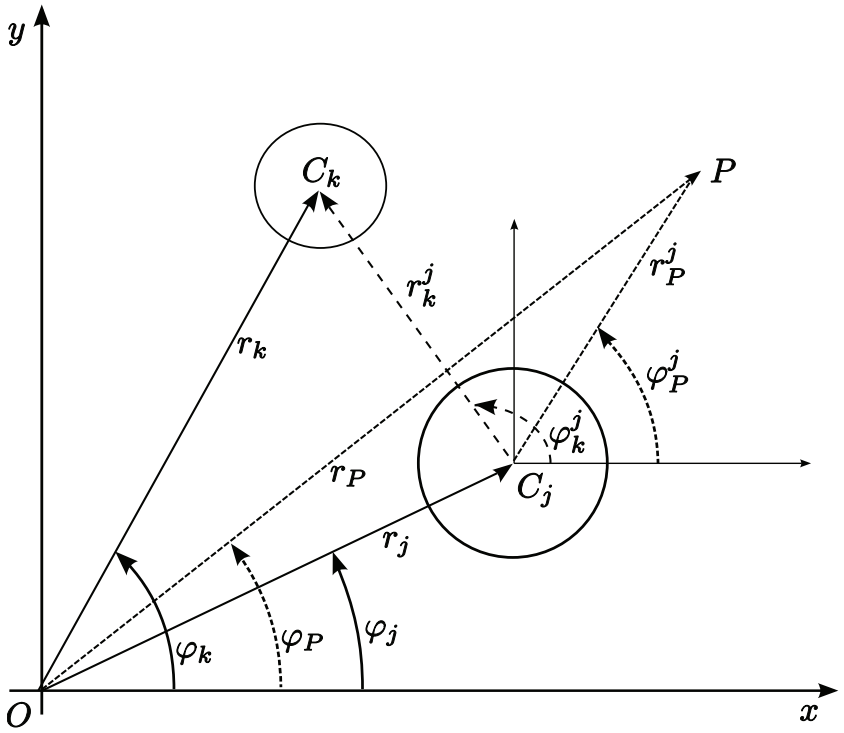

Fig. 3.2: Schematics of the system geometry. The scattering system consists of N cylinders embedded in a background medium with electric permittivity ϵ_b and magnetic permeability μ_b. The j-th cylinder has radius R_j, permittivity ϵ_j, permeability μ_j, and surface second-order susceptibility $\hat{\chi}^{(2)}_{s,j}$.

to the general case of oblique incidence, for the sake of simplicity only the case of normal incidence is considered here, *i.e.*, $\theta_0 = \pi/2$. Then, under these circumstances, two independent cases can be considered: in the first case, which corresponds to the transverse electric (TE) polarisation, the electric field of the incident wave is perpendicular to the axis of the cylinders ($\delta_0 = \pi/2$), whereas in the case of the transverse magnetic (TM) polarization ($\delta_0 = 0$), the magnetic field of the incident wave is perpendicular to the axis of the cylinders.

3.3.2 Calculation of the Electromagnetic Fields at the Fundamental Frequency

In order to calculate the fields at both the FF and SH we have employed a method based on the MSM algorithm [10]. This formalism has been successfully used, *e.g.*, to solve the linear scattering problem in the case of oblique incidence of light onto a 2D photonic crystal [11] [for a comprehensive review of the MSM method and its applications see Ref. [12] and the references therein].

Due to the 2D nature of the linear scattering problem considered here, the electromagnetic field at the FF is fully determined once one knows the longitudinal (z) component of either the electric or the magnetic field. To be more specific, for the TM (TE) polarization this longitudinal component is E_z (H_z). Then, using Maxwell's equa-

tions, it can be easily shown that for harmonic fields that depend on time as $e^{i\omega t}$, the transverse components are given by:

$$H_\varphi = -\frac{i}{\kappa^2}\epsilon\omega\frac{\partial E_z}{\partial r}, \tag{3.19a}$$

$$H_r = \frac{i}{\kappa^2}\epsilon\omega\frac{1}{r}\frac{\partial E_z}{\partial \varphi}, \tag{3.19b}$$

for the TM polarisation, and:

$$E_\varphi = \frac{i}{\kappa^2}\mu_0\omega\frac{\partial H_z}{\partial r}, \tag{3.20a}$$

$$E_r = -\frac{i}{\kappa^2}\mu_0\omega\frac{1}{r}\frac{\partial H_z}{\partial \varphi}, \tag{3.20b}$$

for the TE polarisation (see for example Ref. [8]). In these relations, the transverse component of the wave vector, κ, is defined as:

$$\kappa^2(\mathbf{r}) = k^2(\mathbf{r}) - k^2\cos^2\theta_0 \tag{3.21}$$

where $k = \sqrt{\mu_0\epsilon(\mathbf{r})}\omega$ is the wave vector. Depending on the position $\mathbf{r}$ in the transverse plane, $\epsilon(\mathbf{r})$ is equal to either the permittivity of one of the cylinders or to ϵ_b. Also, note that for normal incidence $\kappa = k$, as in this case $\theta_0 = \pi/2$.

In order to simplify the presentation of the numerical method, all cylinders are assumed to be made of the same material. In particular, considering the case of metallic cylinders, their permittivity is described by the Drude or the Lorentz-Drude model, the latter one being more accurate in the visible region of the spectrum.

Although the technical details can be somewhat complicated, the MSM formalism consists of two simple steps. First, the incident and the scattered electromagnetic fields are expanded in Fourier-Bessel series. Then, the boundary conditions at the surface of the scatterers are used to construct a system of linear equations whose solution determines the Fourier coefficients of the Fourier-Bessel series expansion of the scattered field. Once these coefficients are determined, by solving the corresponding system of linear equations, the electromagnetic field can be found at any point in space. Thus, given an incident plane wave, the longitudinal component of the incoming field, U_z^{inc}, which depending on the polarisation of the incoming wave is $U_z^{\text{inc}} = E_z^{\text{inc}}$ ($U_z^{\text{inc}} = H_z^{\text{inc}}$) for TM (TE) polarised waves, can be written as:

$$U_z^{\text{inc}}(r,\varphi) = \sum_{m=-\infty}^{\infty} a_m J_m(\kappa_b r)e^{im\varphi}, \tag{3.22}$$

where J_m denotes the Bessel functions of the first kind. Note that in Eq. (3.22), the har-

monic time dependence of the incident field has been dropped. The Fourier coefficients a_m depend solely on the type of the incoming wave, for a plane wave being given by the following formulae:

$$a_m = \begin{cases} E_0 \sin\delta_0 \sin\theta_0 e^{-im(\pi/2+\phi_0)}, & U_z = E_z \\ \dfrac{E_0}{Z_b} \cos\delta_0 \sin\theta_0 e^{-im(\pi/2+\phi_0)}, & U_z = H_z \end{cases} \tag{3.23}$$

where $Z_b = \sqrt{\mu_b/\epsilon_b}$ is the impedance of the background medium.

The field scattered by the cylinder C_j can be expanded, too, in a Fourier-Bessel series, but since at $r \to \infty$ the scattered field must contain only outgoing waves, the basis of expansion functions consists of Hankel functions of the second kind, $H_m^{(2)}$. Hence, at a point $P(r, \varphi)$, the field scattered by the cylinder C_j is written as:

$$U_{z,j}^{\rm sc}(r,\varphi) = \sum_{m=-\infty}^{\infty} b_{mj} H_m^{(2)}(\kappa_b r_P^j) e^{im\varphi_P^j}, \tag{3.24}$$

where b_{mj} are the expansion coefficients and represent the main quantities that are to be determined numerically. It is easy to see now that once the coefficients b_{mj} are computed, the total field at a point P can be readily found. Thus, the field $U_z^{\rm tot}(P)$ is given by the sum between the incoming field and the fields scattered by all the cylinders:

$$\begin{aligned} U_z^{\rm tot}(P) = &\sum_{m=-\infty}^{\infty} a_m J_m(\kappa_b r_P) e^{im\varphi_P} \\ &+ \sum_{j=1}^{N} \sum_{m=-\infty}^{\infty} b_{mj} H_m^{(2)}(\kappa_b r_P^j) e^{im\varphi_P^j}. \end{aligned} \tag{3.25}$$

To find the scattered field the source of the field around a cylinder C_j is investigated. Thus, this field can be viewed as being generated *via* scattering off this cylinder of an incoming local field, $U_{z,j}^{\rm loc}$, which consists of the incoming plane wave and the sum of the fields scattered by all cylinders, except the cylinder C_j. This local field can be written as:

$$\begin{aligned} U_{z,j}^{\rm loc}(P) = Q_j &\sum_{m=-\infty}^{\infty} a_m J_m(\kappa_b r_P^j) e^{im\varphi_P^j} \\ &+ \sum_{\substack{k=1 \\ k\neq j}}^{N} \sum_{m,q=-\infty}^{\infty} \mathbf{T}_{jk,mq} b_{qk} J_m(\kappa_b r_P^j) e^{im\varphi_P^j}, \end{aligned} \tag{3.26}$$

where Q_j are phase factors that transform the incoming field from the system with the origin in O to the system with the origin in O_j and $\mathbf{T}_{jk}$ is the electromagnetic coupling

matrix between the cylinders j and k. These parameters are defined as [11]:

$$Q_j = e^{-i\kappa_b r_j \cos(\varphi_j - \phi_0)}, \tag{3.27a}$$

$$\mathbf{T}_{jk,mq} = e^{i(q-m)\varphi_k^j} H_{m-q}^{(2)}(\kappa_b r_k^j). \tag{3.27b}$$

One important observation, which must be made here, is that the scattered component of the local field accounts for all the scattering processes in the system (except that off the cylinder C_j). This property of the MSM formalism is also apparent in its actual implementation, wherein no iterative processes are needed. As a result, the only numerical approximation present in the formalism is related to the number of expansion terms kept in the Fourier-Bessel series, as it will be discussed in the next chapter. Therefore, in this respect, the field in Eq. (3.25) is an exact self-consistent solution to Maxwell's equations.

Equation (3.26) can be easily derived by inserting in Eq. (3.25) the Graf formula [13]:

$$H_m^{(2)}(\kappa_b r_P^k) e^{im\varphi_P^k} = \sum_{q=-\infty}^{\infty} e^{i(m-q)\varphi_k^j} H_{q-m}^{(2)}(\kappa_b r_k^j) J_q(\kappa_b r_P^j) e^{iq\varphi_P^j}. \tag{3.28}$$

Now, the local field $U_{z,j}^{\mathrm{loc}}(P)$ can itself be expanded in a Fourier-Bessel series:

$$U_{z,j}^{\mathrm{loc}}(P) = \sum_{m=-\infty}^{\infty} d_{mj} J_m(\kappa_b r_P^j) e^{im\varphi_P^j}. \tag{3.29}$$

The total field around a cylinder C_j can therefore be written as the sum between this local field and the field scattered by the cylinder [the index j here signifies that $U_z^{\mathrm{tot}}(P)$ is calculated in the system with the origin in O_j]:

$$U_{z,j}^{\mathrm{tot}}(P) = \sum_{m=-\infty}^{\infty} \left[d_{mj} J_m(\kappa_b r_P^j) + b_{mj} H_m^{(2)}(\kappa_b r_P^j) \right] e^{im\varphi_P^j}. \tag{3.30}$$

Now let us introduce the column vectors $\mathbf{a}_j = \{Q_j a_m\}$, $\mathbf{b}_j = \{b_{mj}\}$, and $\mathbf{d}_j = \{d_{mj}\}$, contain the Fourier coefficients of the incoming plane wave, the scattered field, and the local field associated to the cylinder C_j, respectively. Furthermore, the scattered field and the local field associated to the cylinder C_j are related by the scattering matrix $\mathbf{S}_j$ of the cylinder C_j, and thus the relation between the vectors $\mathbf{b}_j$ and $\mathbf{d}_j$ is given by:

$$\mathbf{b}_j = \mathbf{S}_j \mathbf{d}_j. \tag{3.31}$$

Combining Eqs. (3.26), (3.30), and (3.31) yields the following linear system of matrix

equations:

$$\sum_{k=1}^{N} \left[\delta_{kj}\mathbf{I} - (1-\delta_{kj})\mathbf{S}_j\mathbf{T}_{jk}\right]\mathbf{b}_k = \mathbf{S}_j\mathbf{a}_j,\ j = 1, 2, \ldots, N, \tag{3.32}$$

where δ_{ij} is the Kronecker symbol and $\mathbf{I}$ is the identity matrix. This system of equations can be reduced to a single matrix equation. For this, the column vectors $\mathbf{b}_j$ and $\mathbf{S}_j\mathbf{a}_j$ are stacked into the single column vectors, $\mathbf{B} = \{\mathbf{b}_j\}$ and $\mathbf{G} = \{\mathbf{S}_j\mathbf{a}_j\}$, respectively, and the scattering matrix, $\mathbf{S}_\omega$, of the entire system of cylinders can be defined as:

$$\mathbf{S}_\omega = \begin{pmatrix} \mathbf{I} & -\mathbf{S}_1\mathbf{T}_{12} & -\mathbf{S}_1\mathbf{T}_{13} & \ldots \\ -\mathbf{S}_2\mathbf{T}_{21} & \mathbf{I} & -\mathbf{S}_2\mathbf{T}_{23} & \ldots \\ -\mathbf{S}_3\mathbf{T}_{31} & -\mathbf{S}_3\mathbf{T}_{32} & \mathbf{I} & \ldots \\ \vdots & \vdots & \vdots & \ddots \end{pmatrix}. \tag{3.33}$$

With these definitions, Eq. (3.32) becomes:

$$\mathbf{S}_\omega\mathbf{B} = \mathbf{G}. \tag{3.34}$$

Since the vector $\mathbf{G}$ is known, the linear scattering problem has been reduced to finding the scattering matrix of the system, $\mathbf{S}_\omega$, and then solving the system (3.34). More exactly, once $\mathbf{S}_\omega$ is determined, the Fourier coefficients $\mathbf{B}$ of the scattered field are calculated by simply solving the linear system (3.34), the total field at a point P being subsequently determined from Eq. (3.25). To this end, computing $\mathbf{S}_\omega$ amounts to finding the matrices $\mathbf{S}_j$ of the cylinders C_j, which can be easily determined by using the continuity of the tangent component of the fields across the boundary of the cylinder C_j.

In the case of the TE polarisation, the boundary conditions can be expressed as:

$$H_{z,j}^{\text{ext}}(R_j, \varphi) = H_{z,j}^{\text{int}}(R_j, \varphi), \tag{3.35a}$$

$$E_{\varphi,j}^{\text{ext}}(R_j, \varphi) = E_{\varphi,j}^{\text{int}}(R_j, \varphi). \tag{3.35b}$$

The magnetic field inside the cylinder C_j, $H_{z,j}^{\text{int}}$, can be written as:

$$H_{z,j}^{\text{int}}(P) = \sum_{m=-\infty}^{\infty} c_{mj} J_m(\kappa_j r_P^j) e^{im\varphi_P^j}, \tag{3.36}$$

whereas the tangent component of the electric field, $E_{\varphi,j}^{\text{int}}$, is determined from the Eq. (3.20a).

Using Eq. (3.30), imposing the continuity conditions (3.35), and eliminating the

coefficients c_{mj} from the resulting system of equations, one obtains the following relation between the b_{mj} and d_{mj} coefficients:

$$\frac{b_{mj}}{d_{mj}} = \frac{\beta_j J'_m(\kappa_b R_j) J_m(\kappa_j R_j) - J_m(\kappa_b R_j) J'_m(\kappa_j R_j)}{H_m^{(2)}(\kappa_b R_j) J'_m(\kappa_j R_j) - \beta_j H_m^{(2)\prime}(\kappa_b R_j) J_m(\kappa_j R_j)}. \tag{3.37}$$

Here, the prime symbol denotes the derivative with respect to the argument and $\beta_j = \kappa_j/\kappa_b$. These calculations can be repeated for the case of the TM polarisation, the result being that Eq. (3.37) becomes:

$$\frac{b_{mj}}{d_{mj}} = \frac{\alpha_j J'_m(\kappa_b R_j) J_m(\kappa_j R_j) - J_m(\kappa_b R_j) J'_m(\kappa_j R_j)}{H_m^{(2)}(\kappa_b R_j) J'_m(\kappa_j R_j) - \alpha_j H_m^{(2)\prime}(\kappa_b R_j) J_m(\kappa_j R_j)}, \tag{3.38}$$

where $\alpha_j = (\epsilon_b \kappa_j)/(\epsilon_j \kappa_b)$. Now, Eq. (3.31) shows that $S_{j,mn} = (b_{mj}/d_{mj})\delta_{mn}$, which means that for cylinders, in the case of a TE or TM polarised incident wave, the scattering matrix is diagonal. As in the case of the one cylinder geometry, a relation can now be found between b_{mj} and c_{mj}. The internal field coefficients can thus be expressed as:

$$c_{mj} = \frac{a_{mj} J_m(\kappa_b R_j) + b_{mj} H^{(2)}(\kappa_b R_j)}{J_m(\kappa_j R_j)}. \tag{3.39}$$

It is worth noting that Eq. (3.39) is valid for both polarisations. With the Fourier coefficients now known, the field inside the cylinders can be determined by using Eq. (3.36). Note that this formalism can be easily extended to the case of scatterers of arbitrary shape, the main difference being that in this case, the scattering matrices $\mathbf{S}_j$ are no longer diagonal [14].

3.3.3 Calculation of the Electromagnetic Fields at the Second Harmonic

The second step of the numerical method consists in the calculation of the electromagnetic field at the SH. To this end, the source of the field at the SH, namely, the non-linear polarisation induced by the field at the FF, must be determined. The two contributions to the non-linear polarisation are given by Eqs. (2.65) and (2.67) for the surface and bulk contributions, respectively. Equations (2.66) show that the surface contribution exists only in the case in which the $E_\perp$ and $E_\parallel$ components are non-zero which here corresponds to the TE polarisation. As a result, in what follows, only this case will be considered.

In the particular case of a cylinder, Eqs. (2.69), describing the non-linear boundary

conditions at the metal-dielectric interface, can be rewritten as:

$$H_z^{\rm int}(\Omega) - H_z^{\rm ext}(\Omega) = i\Omega P_{s,\varphi}, \tag{3.40a}$$

$$\frac{1}{\epsilon_j} D_\varphi^{\rm int}(\Omega) - \frac{1}{\epsilon_b} D_\varphi^{\rm ext}(\Omega) = -\frac{1}{\epsilon_j R_j} \frac{\partial P_{s,r}}{\partial \varphi} + \frac{P_{b,\varphi}}{\epsilon_j}, \tag{3.40b}$$

where the TE polarisation was assumed. Note that due to the presence of the non-linear polarisation sheet at the surface of the metal the non-linear boundary conditions are different from the linear ones, which are given by the Eqs. (3.35).

Similar to the linear scattering problem, the total SH field at a point P can be viewed as consisting of two distinct components: a source field, $H_z^{\rm src}(P,\Omega)$, which reaches the point P without being scattered by any of the cylinders, and the scattered field, $H_z^{\rm sc}(P,\Omega)$, which arrives at P after it was scattered by at least one of the cylinders:

$$H_z^{\rm tot}(P,\Omega) = H_z^{\rm src}(P,\Omega) + H_z^{\rm sc}(P,\Omega). \tag{3.41}$$

The source field satisfies the Helmholtz equation:

$$\nabla^2 H_z^{\rm src}(\mathbf{r};\Omega) + \kappa_b^2(\Omega) H_z^{\rm src}(\mathbf{r},\Omega) = -i\Omega(\nabla \times \mathbf{P}_{\rm nl}) \cdot \mathbf{e}_z, \tag{3.42}$$

where $\mathbf{e}_z$ is the unit vector along the z-axis and $\mathbf{P}_{\rm nl} = \mathbf{P}_s + \mathbf{P}_b$ is the total non-linear polarisation. Since the source polarisation $\mathbf{P}_{\rm nl}$ is known once the electric field at the FF is determined, this source field can easily be calculated by using the Green function of the Helmholtz equation in 2D, $G_{2D}(r) = -(i/4)H_0^{(2)}(r)$:

$$H_z^{\rm src}(P,\Omega) = -\frac{\Omega}{4} H_0^{(2)}(\kappa_b r_P) \otimes [(\nabla \times \mathbf{P}_{\rm nl}) \cdot \mathbf{e}_z]. \tag{3.43}$$

In this equation the symbol $\otimes$ represents the convolution operator, which is defined as $f \otimes g = \int f(\mathbf{r} - \mathbf{r}') g(\mathbf{r}') d\mathbf{r}'$. Because of the particular characteristics of the surface and bulk polarisations, Eq. (3.43) represents the sum between a line integral over the boundaries of all cylinders and a surface integral over their transverse cross sections. Moreover, the field $H_z^{\rm src}(P,\Omega)$ consists of a linear superposition of fields $H_{z,j}^{\rm src}(P,\Omega)$, each such field being generated by the corresponding cylinder C_j. Inserting in the Eq. (3.43), the Graf formula [13] for the Bessel function $H_0^{(2)}(r)$,

$$H_0^{(2)}(\kappa_b|\mathbf{r}_P - \mathbf{r}_M|) = \sum_{m=-\infty}^{\infty} e^{-im\varphi_M^j} J_m(\kappa_b r_M^j) \times H_m^{(2)}(\kappa_b r_P^j) e^{im\varphi_P^j}, \tag{3.44}$$

one can easily show that the Fourier-Bessel expansion of the field $H_{z,j}^{\rm src}(P,\Omega)$, around

the cylinder C_j, can be written as:

$$H_{z,j}^{\rm src}(P) = \sum_{m=-\infty}^{\infty} a_{\Omega,mj} H_m^{(2)}(\kappa_b r_P^j) e^{im\varphi_P^j}, \tag{3.45}$$

where,

$$a_{\Omega,mj} = -\frac{\Omega}{4} \int_{\Gamma_j} e^{-im\varphi_M^j} J_m(\kappa_b r_M^j) [(\nabla_{\mathbf{r}_M^j} \times \mathbf{P}_{\rm nl}) \cdot \mathbf{e}_z] d\mathbf{r}_M^j. \tag{3.46}$$

In this relation, the domain of integration Γ_j is either the boundary of the cylinder C_j, in the case of the surface polarisation, or its transverse cross section, when the bulk polarisation is integrated. Similar to the analysis of the scattering process at the FF, the scattered field at the SH can be written as [see also the Eq. (3.25)]:

$$H_z^{\rm sc}(P,\Omega) = \sum_{j=1}^{N} \sum_{m=-\infty}^{\infty} b_{\Omega,mj} H_m^{(2)}(\kappa_b r_P^j) e^{im\varphi_P^j}, \tag{3.47}$$

where $b_{\Omega,mj}$ are the scattering coefficients at the SH. Combining Eqs. (3.45) and (3.47) leads to the formula for the total field $H_z^{\rm tot}(P,\Omega)$:

$$H_z^{\rm tot}(P,\Omega) = \sum_{j=1}^{N} \sum_{m=-\infty}^{\infty} (a_{\Omega,mj} + b_{\Omega,mj}) H_m^{(2)}(\kappa_b r_P^j) e^{im\varphi_P^j}, \tag{3.48}$$

where the two series containing the $a_{\Omega,mj}$ and $b_{\Omega,mj}$ coefficients correspond to the source and scattered fields, respectively. By inserting in this equation the Graf formula (3.28), the total field outside the cylinder C_j, at a point P, can be written in the following form:

$$\begin{aligned} H_{z,j}^{\rm tot}(P,\Omega) = & \sum_{m=-\infty}^{\infty} (a_{\Omega,mj} + b_{\Omega,mj}) H_m^{(2)}(\kappa_b r_P^j) e^{im\varphi_P^j} \\ & + \sum_{\substack{k=1 \\ k\neq j}}^{N} \sum_{m,q=-\infty}^{\infty} T_{jk,mq} (a_{\Omega,qk} + b_{\Omega,qk}) J_m(\kappa_b r_P^j) e^{im\varphi_P^j}, \end{aligned} \tag{3.49}$$

where the index j signifies that $H_z^{\rm tot}(P,\Omega)$ is calculated in the coordinate system with the origin in O_j. This equation shows that the total field consists of the sum between the field generated and scattered by the cylinder C_j [the first term in the Eq. (3.49)] and the total field incident onto this cylinder [the second term in the Eq. (3.49)]. This latter field, in turn, is given by the sum between the fields generated by all the other cylinders and the fields scattered by these cylinders.

The total field can also be decomposed in an alternative way, namely, it can be

written as the sum of a source field generated by the cylinder C_j, $H_{z,j}^{\mathrm{self}}(P,\Omega)$, a local field, $H_{z,j}^{\mathrm{loc}}(P,\Omega)$, which is the field incident onto C_j, and the corresponding scattered field, $H_{z,j}^{\mathrm{sc}}(P,\Omega)$. Furthermore, the source field must satisfy the non-linear boundary conditions (3.40), whereas the field involved in the scattering process:

$$H_{z,j}^{\mathrm{lin}}(P,\Omega) = H_{z,j}^{\mathrm{loc}}(P,\Omega) + H_{z,j}^{\mathrm{sc}}(P,\Omega), \tag{3.50}$$

satisfies the linear boundary conditions corresponding to the TE polarisation, *i.e.*, Eqs. (3.35). It should be noted that if the non-linear bulk polarisation is given by the Eq. (2.67) then the source term in the Helmholtz equation (3.42) cancels everywhere except on the boundaries of the cylinders and therefore the fields $H_{z,j}^{\mathrm{self}}(P,\Omega)$ and $H_{z,j}^{\mathrm{lin}}(P,\Omega)$ satisfy the homogeneous part of this equation.

Now, the source field can be expanded in Fourier-Bessel series as:

$$H_{z,j}^{\mathrm{self}}(P,\Omega) = \sum_{m=-\infty}^{\infty} c_{\Omega,mj}^{\mathrm{self}} J_m(\kappa_j r_P^j) e^{im\varphi_P^j}, \tag{3.51}$$

for $r_P^j < R_j$ and

$$H_{z,j}^{\mathrm{self}}(P,\Omega) = \sum_{m=-\infty}^{\infty} g_{\Omega,mj}^{\mathrm{self}} H_m^{(2)}(\kappa_b r_P^j) e^{im\varphi_P^j}, \tag{3.52}$$

for $r_P^j > R_j$. By imposing the non-linear boundary conditions (3.40) at $r_P^j = R_j$, one obtains the following system of linear equations for the coefficients $c_{\Omega,mj}^{\mathrm{self}}$ and $g_{\Omega,mj}^{\mathrm{self}}$:

$$c_{\Omega,mj}^{\mathrm{self}} J_m(\kappa_j R_j) - g_{\Omega,mj}^{\mathrm{self}} H_m^{(2)}(\kappa_b R_j) = i\Omega \bar{P}_{\varphi,m}, \tag{3.53a}$$

$$\frac{i\kappa_j}{\epsilon_j \Omega} c_{\Omega,mj}^{\mathrm{self}} J_m'(\kappa_j R_j) - \frac{i\kappa_b}{\epsilon_b \Omega} g_{\Omega,mj}^{\mathrm{self}} H_m^{(2)\prime}(\kappa_b R_j) = \bar{P}_{r,m}. \tag{3.53b}$$

In these relations,

$$\bar{P}_{\varphi,m} = P_{s\varphi,m}, \tag{3.54a}$$

$$\bar{P}_{r,m} = -\frac{1}{\epsilon_j R_j} \left.\frac{\partial P_{sr,m}}{\partial \varphi}\right|_{r_P^j = R_j} + \frac{P_{b\varphi,m}}{\epsilon_j}. \tag{3.54b}$$

are the m-th order coefficients of the expansion in Fourier-Bessel series of the corresponding non-linear polarisation. Their exact expressions can be found in Appendix C. The solution of the linear system (3.53), which completely determines the source field

$H^{\text{self}}_{z,j}(P,\Omega)$, is found as:

$$c^{\text{self}}_{\Omega,mj} = i\frac{H^{(2)}_m(k_bR_j)\bar{P}_{r,m} + Z_bH^{(2)\prime}_m(k_bR_j)\Omega\bar{P}_{\varphi,m}}{Z_bJ_m(\kappa_jR_j)H^{(2)\prime}_m(\kappa_bR_j) - Z_jH^{(2)}_m(\kappa_bR_j)J'_m(\kappa_jR_j)}, \tag{3.55a}$$

$$g^{\text{self}}_{\Omega,mj} = i\frac{J_m(\kappa_jR_j)\bar{P}_{r,m} + Z_jJ'_m(\kappa_jR_j)\Omega\bar{P}_{\varphi,m}}{Z_bJ_m(\kappa_jR_j)H^{(2)\prime}_m(\kappa_bR_j) - Z_jH^{(2)}_m(\kappa_bR_j)J'_m(\kappa_jR_j)}, \tag{3.55b}$$

where $Z_j = (\mu_j/\epsilon_j)^{1/2}$. Note that these coefficients can be easily calculated once the field at the FF is determined.

Based on Eq. (3.50), the field $H^{\text{lin}}_{z,j}(P,\Omega)$ can be written as:

$$H^{\text{lin}}_{z,j}(P,\Omega) = \sum_{m=-\infty}^{\infty} c^{\text{lin}}_{\Omega,mj}J_m(\kappa_jr^j_P)e^{im\varphi^j_P}, \tag{3.56}$$

for $r^j_P < R_j$ and:

$$\begin{aligned} H^{\text{lin}}_{z,j}(P,\Omega) = &\sum_{m=-\infty}^{\infty} f^{\text{loc}}_{\Omega,mj}J_m(\kappa_br^j_P)e^{im\varphi^j_P} \\ &+ \sum_{m=-\infty}^{\infty} g^{\text{sc}}_{\Omega,mj}H^{(2)}_m(\kappa_br^j_P)e^{im\varphi^j_P}, \end{aligned} \tag{3.57}$$

for $r^j_P > R_j$.

Now, by combining Eqs. (3.52) and (3.57) one can cast the total field $H^{\text{tot}}_{z,j}(P,\Omega)$ outside the cylinder C_j in the following form:

$$\begin{aligned} H^{\text{tot}}_{z,j}(P,\Omega) = &\sum_{m=-\infty}^{\infty} f^{\text{loc}}_{\Omega,mj}J_m(\kappa_br^j_P)e^{im\varphi^j_P} \\ &+ \sum_{m=-\infty}^{\infty} (g^{\text{self}}_{\Omega,mj} + g^{\text{sc}}_{\Omega,mj})H^{(2)}_m(\kappa_br^j_P)e^{im\varphi^j_P}, \end{aligned} \tag{3.58}$$

By introducing the vectors $\mathbf{a}_{\Omega,j} = \{a_{\Omega,mj}\}$, $\mathbf{b}_{\Omega,j} = \{b_{\Omega,mj}\}$, $\mathbf{g}^{\text{self}}_{\Omega,j} = \{g^{\text{self}}_{\Omega,mj}\}$, $\mathbf{g}^{\text{sc}}_{\Omega,j} = \{g^{\text{sc}}_{\Omega,mj}\}$, and $\mathbf{f}_{\Omega,j} = \{f^{\text{loc}}_{\Omega,mj}\}$, then, comparing Eqs. (3.49) and (3.58), one can see that these vectors satisfy the following relations:

$$\mathbf{a}_{\Omega,j} + \mathbf{b}_{\Omega,j} = \mathbf{g}^{\text{self}}_{\Omega,j} + \mathbf{g}^{\text{sc}}_{\Omega,j}, \tag{3.59a}$$

$$\sum_{\substack{k=1\\k\neq j}}^{N} \mathbf{T}_{jk}(\mathbf{a}_{\Omega,k} + \mathbf{b}_{\Omega,k}) = \mathbf{f}_{\Omega,j}. \tag{3.59b}$$

Furthermore, the scattered and the incident (local) fields are related *via* the scattering

matrix $\mathbf{S}_{\Omega,j}$,

$$\mathbf{g}^{\mathrm{sc}}_{\Omega,j} = \mathbf{S}_{\Omega,j}\mathbf{f}_{\Omega,j}, \tag{3.60}$$

where the index Ω means that the scattering matrix is evaluated at the frequency of the SH, $\Omega = 2\omega$. From this equation and Eqs. (3.59) one can derive the relation:

$$\sum_{\substack{k=1 \\ k\neq j}}^{N} \mathbf{S}_{\Omega,j}\mathbf{T}_{jk}(\mathbf{a}_{\Omega,k} + \mathbf{b}_{\Omega,k}) = (\mathbf{a}_{\Omega,j} + \mathbf{b}_{\Omega,j}) - \mathbf{g}^{\mathrm{self}}_{\Omega,j}, \tag{3.61}$$

which holds for $j = 1, \ldots, N$. This linear system of matrix equations can be written in a more compact form using the vectors $\mathbf{A}_\Omega = \{\mathbf{a}_{\Omega,j}\}$, $\mathbf{B}_\Omega = \{\mathbf{b}_{\Omega,j}\}$, and $\mathbf{G}^{\mathrm{self}}_\Omega = \{\mathbf{g}^{\mathrm{self}}_{\Omega,j}\}$. With these notations, Eq. (3.61) becomes:

$$\mathbf{S}_\Omega\mathbf{B}_\Omega = \mathbf{G}_\Omega, \tag{3.62}$$

where $\mathbf{S}_\Omega$ is given by Eq. (3.33), with all matrix components evaluated at the frequency Ω, and

$$\mathbf{G}_\Omega = -\mathbf{S}_\Omega\mathbf{A}_\Omega + \mathbf{G}^{\mathrm{self}}_\Omega. \tag{3.63}$$

The vector coefficients $\mathbf{A}_\Omega$ and $\mathbf{G}^{\mathrm{self}}_\Omega$ are completely determined once the field at the FF is calculated. As a result, the scattering vector coefficients $\mathbf{B}_\Omega$ can be found by solving the system (3.62), and subsequently the field at a point P outside the cylinders is determined from Eq. (3.48).

Finally, it can be seen from Eqs. (3.51) and (3.56) that the total field inside the cylinder C_j is given by:

$$H^{\mathrm{tot}}_{z,j}(P,\Omega) = \sum_{m=-\infty}^{\infty} (c^{\mathrm{self}}_{\Omega,mj} + c^{\mathrm{lin}}_{\Omega,mj})J_m(\kappa_j r^j_P)e^{im\varphi^j_P}. \tag{3.64}$$

As in the case of the linear scattering problem, the coefficients $c^{\mathrm{lin}}_{\Omega,mj}$ are calculated by imposing on the field $H^{\mathrm{lin}}_{z,j}(P,\Omega)$ the linear boundary conditions (3.35).

3.3.4 Calculation of the Scattering Cross Sections

The MSM formalism allows one to determine not only the spatial distribution of the electromagnetic field but also a series of important physical quantities, such as the total cross section, the absorption cross section, and the scattering cross section. Whereas the field distribution provides essential information regarding the properties of the optical near field, the scattering cross sections characterize the process of energy transfer from the incident wave into the far field. The total scattering cross section, $Q_s(\omega)$, for the

field at the FF is defined as:

$$Q_s(\omega) \equiv \frac{P^{\text{sc}}(\omega)}{P^{\text{inc}}} = \int_0^{2\pi} q_s(\varphi;\omega)d\varphi, \tag{3.65}$$

where P^{sc} and P^{inc} are the total scattered power per unit length and the power per unit length of the incident wave, respectively, and $q_s(\varphi;\omega)$ is the differential cross section.

In order to calculate the total scattered power consider a cylinder of radius R, which contains all the scatterers. Then, the total power of the scattered field that flows through the boundary of this cylinder can be computed and subsequently the limit $R \to \infty$. This procedure is expressed mathematically as follows:

$$P^{\text{sc}}(\omega) = \lim_{R\to\infty}\left[R\int_0^{2\pi}\frac{1}{2}\mathfrak{Re}\left(\mathbf{E}^{\text{sc}}\times\mathbf{H}^{\text{sc}*}\right)_r d\varphi\right]. \tag{3.66}$$

Using the asymptotic expressions at $x \to \infty$, of the Hankel functions $H_m^{(2)}(x)$ and their derivatives, leads to:

$$P^{\text{sc}}(\omega) = \frac{\mu_b\omega}{\pi\kappa_b^2}\int_0^{2\pi}\left|\sum_{m=-\infty}^{\infty}\tilde{b}_m e^{im\varphi}\right|^2 d\varphi = 2\frac{\mu_b\omega}{\kappa_b^2}\sum_m |b_m|^2, \tag{3.67}$$

where $\tilde{b}_m$ are the scattering coefficients in the coordinate system with the origin in O. Using the Graf addition formula (3.28), these coefficients can be written as:

$$\tilde{b}_m = \sum_{j=0}^{N}\sum_{n=-\infty}^{\infty} b_{mj}e^{i(n-m)\varphi_j}J_{m-n}(\kappa_b r_j). \tag{3.68}$$

Furthermore, the power per unit length of the incident plane wave is given by:

$$P^{\text{inc}} = \frac{1}{2}R_s v\epsilon_b|E_0|^2, \tag{3.69}$$

where R_s is the radius of the smallest cylinder that would contain the entire set of scatterers and v is the phase-velocity of the incident plane wave.

Note that since the amplitude of the scattered field depends linearly on the amplitude E_0 of the incident plane wave, the total and the differential scattering cross sections do not depend on E_0. In order to have this condition satisfied at the SH, too, the scattering cross sections at Ω can be defined as:

$$Q_s(\Omega) \equiv \frac{P^{\text{sc}}(\Omega)}{|P^{\text{inc}}|^2} = \int_0^{2\pi} q_s(\varphi;\Omega)d\varphi = 2\frac{\mu_b\omega}{\kappa_b^2}\frac{\sum_{m=-\infty}^{\infty}|\tilde{b}_m|^2}{\left|\frac{1}{2}R_s v\epsilon_b|E_0|^2\right|^2}. \tag{3.70}$$

Here, $q_s(\varphi;\Omega)$ is the second harmonic differential cross section. The scattering power

in the case of the non-linear field, $P^{sc}(\Omega)$, can also be calculated using Eq. (3.67) with $\Omega = 2\omega$ and the scattering coefficients $\tilde{b_m}$, corresponding to the SH scattering case. A detailed description of how these formulae can be obtained is given in Appendix D.

3.3.5 Calculation of the Absorption Cross Section

The scattering cross section characterizes the strength of the interaction between incoming plane waves and the objects that scatter these waves. Another physical quantity that provides insightful information about the scattering process is the absorption cross section. In particular, the absorption cross section quantifies the rate at which the scattering system absorbs energy from the incident wave, and as such it can be instrumental in characterizing the strength of the coupling between the near field and the system of scatterers. At the FF, the absorption cross section can be determined by separating the total power flow out of the scattering region, $P^{\rm tot}$, which sometimes is also referred to as the *extinction* power, into the absorbed and scattered power,

$$P^{\rm tot} = P^{\rm abs} + P^{\rm sc}. \tag{3.71}$$

In this equation, $P^{\rm tot}$ is defined as:

$$P^{\rm tot}(\omega) = \lim_{R\to\infty}\left[R\int_0^{2\pi}\frac{1}{2}{\rm Re}\left(\mathbf{E}^{\rm tot}\times\mathbf{H}^{\rm tot*}\right)_r d\varphi\right]. \tag{3.72}$$

Taking into account that $\mathbf{E}^{\rm tot} = \mathbf{E}^{\rm inc} + \mathbf{E}^{\rm sc}$ and $\mathbf{H}^{\rm tot} = \mathbf{H}^{\rm inc} + \mathbf{H}^{\rm sc}$, Eq. (3.72), in conjunction with Eq. (3.66), leads to the following expression for the total power [8]:

$$P^{\rm tot} = -\lim_{R\to\infty}\left[R\int_0^{2\pi}\frac{1}{2}{\rm Re}\left(E_\varphi^{\rm sc}H_z^{\rm inc*} + E_\varphi^{\rm inc}H_z^{\rm sc*}\right)d\varphi\right]. \tag{3.73}$$

Using again the asymptotic forms for the Bessel and Hankel functions, the total power can be expressed as:

$$P^{\rm tot} = -\frac{2\mu_b\omega}{\kappa_b^2 Z_b}\sum_{m=-\infty}^{\infty}|\tilde{b}_m|\cos\left(\arg\tilde{b}_m + \frac{m\pi}{2} + m\varphi_0\right). \tag{3.74}$$

This total power is used to define the total (or extinction) cross section:

$$Q_t(\omega) = \frac{P^{\rm tot}(\omega)}{P^{\rm inc}} = -\frac{2\mu_b\omega}{\kappa_b^2 Z_b}\frac{\sum_{m=-\infty}^{\infty}|\tilde{b}_m|\cos\left(\arg\tilde{b}_m + \frac{m\pi}{2} + m\varphi_0\right)}{\frac{1}{2}R_s v\epsilon_b|E_0|^2}. \tag{3.75}$$

Finally, by using Eq. (3.71), the absorption cross section is simply given by:

$$Q_a(\omega) = Q_t(\omega) - Q_s(\omega). \tag{3.76}$$

Similarly, the absorption cross section can also be defined as:

$$Q_a(\omega) = \frac{P^{\text{abs}}(\omega)}{P^{\text{inc}}}. \tag{3.77}$$

It should be noted that when the scatterers exhibit no absorption, *i.e.* when $\nu = 0$, the absorption cross section vanishes, in which case Eq. (3.76) represents the well known optical theorem. A detailed approach to these calculations can be found in Appendix D.

At the SH, as there is no incoming field, the power loss per unit length, is determined by integrating over the transverse cross section of all cylinders the Joule thermal power loss, $P^{\text{abs}} = \frac{1}{2}\mathfrak{Re}(\mathbf{J} \cdot \mathbf{E}^*)$, with $\mathbf{J} = \sigma_j \mathbf{E}$ being the conduction current density and σ_j the conductivity of the cylinder C_j [for the Drude model, $\sigma = (\epsilon_0 \omega_p^2)/(\nu - i\omega)$].

3.4 Description of the Time Domain Linear and Non-linear Wave Scattering by Ensembles of Cylinders

The MSM formalism is an efficient and versatile method for solving the linear and non-linear scattering problem for arbitrary distributions of cylinders. Nevertheless, it is limited to the frequency domain in that it can only provide the solution to the scattering problem for a monochromatic wave excitation. This implies that more general light-matter interactions, namely, interaction with an optical pulse, can not be directly described by the MSM. To overcome this limitation, we have extended the MSM formalism to the time domain [15].

To better understand the approach we have used, consider the Fourier transform between the field in the time and frequency domains:

$$H(\omega) = \int_{-\infty}^{+\infty} h(t) e^{i\omega t} dt, \tag{3.78}$$

for the direct Fourier transform and

$$h(t) = \frac{1}{2\pi} \int_{-\infty}^{+\infty} e^{-i\omega t} d\omega, \tag{3.79}$$

for the inverse Fourier transform. Here $H(\omega)$ and $h(t)$ are the fields in the frequency and time domain, respectively. In the case of our scattering problem, a time varying electromagnetic field $U(t)$ can be written as:

$$U(t) = F(t) e^{i(\mathbf{k}_0 \cdot \mathbf{r} + \omega t)}, \tag{3.80}$$

where, according to Eq. (3.79), $F(t)$ is of the form:

$$F(t) = \frac{1}{2\pi}\int_{-\infty}^{+\infty} \tilde{F}(\omega)e^{-i\omega t}d\omega. \tag{3.81}$$

For example, for a temporal Gaussian pulse with maximum amplitude E_0, temporal duration T_0, full-width at half-maximum $T_{FWHM} = \sqrt{2\ln 2}T_0$, which has its peak amplitude spatially centred in $\mathbf{r} = 0$ at $t = 0$, $\tilde{F}(\omega)$ can be expressed as:

$$\tilde{U}_0(\omega) = E_0\int_{-\infty}^{+\infty} e^{\frac{t^2}{T_0^2}}e^{-i\omega t}dt = E_0 e^{-\frac{\omega^2}{2W_0^2}}e^{i\omega\tau}, \tag{3.82}$$

where $W_0 = 1/T_0$ defines the full-width at half-maximum in the frequency domain, $W_{FWHM} = \sqrt{2\ln 2}W_0$.

A plane wave at a fixed frequency ω of amplitude $\tilde{U}_0(\omega)$ will be given by:

$$U(\omega) = \tilde{U}_0(\omega)e^{i\omega t - i\mathbf{k}\cdot\mathbf{r}}. \tag{3.83}$$

Equation (3.83) can be expanded in a Fourier Bessel series according to Eq. (3.1). This expansion can be written:

$$U(\omega, r, \varphi) = \tilde{U}_0(\omega)\sum_{m=-\infty}^{m=+\infty} a_m^i J(kr)e^{im\varphi}. \tag{3.84}$$

Equation (3.84) summarises how the MSM algorithm can be extended to include the time domain. The values of $\tilde{U}_0(\omega)$ can be found *via* a Fourier transform of the input pulse. By using the MSM approach to solve the scattering problem for each monochromatic wave of the form (3.84), the field distributions for each Fourier frequency can be found. Calculating the time domain evolution of the total field can then be simply done by computing the inverse Fourier transform of the field in the frequency domain.

One final point to note is that, due to the finite nature of the discrete Fourier transform used in the computer implementation of this algorithm, an important parameter to be considered is the number of sampling points, F_N, in the calculations, that is, the number of frequency components one has to consider. At the same time, the input pulse needs to be limited to a time interval T, which is typically given as $T = aT_0$, where a is the padding factor.

3.5 Conclusions

In conclusion, this chapter has introduced a new numerical method, based on the MSM algorithm, for studying the linear and non-linear scattering effects in a metamaterial made of centrosymmetric nanowires (cylinders). In this approach, both the surface and

bulk contributions to the non-linear polarisation have been considered. This chapter has also presented how a series of physical quantities, such as the total cross section, the scattering cross section, the absorption cross section, and the differential scattering cross section, can be calculated and used to characterize the wave scattering process. The MSM formalism introduced here proves to be a robust and powerful method for analyzing the linear and non-linear wave scattering, while at the same time providing a high degree of versatility in choosing the scattering geometries that can be investigated. At the same time, we have described how the MSM formalism can be extended to allow for time-domain numerical simulations.

While this chapter has covered the mathematical formalism used in our analysis of non-linear effects in plasmonic systems, the next chapter will deal with its implementation as part of the OPTIMET, an *ab-initio* solver, developed as part of the project.

Bibliography

[1] S. Bozhevolnyi, J. Beermann, and V. Coello. Direct Observation of Localized Second-Harmonic Enhancement in Random Metal Nanostructures. *Phys. Rev. Lett.*, 90(19):197403, 2003.

[2] M. Breit, V. A. Podolskiy, S. Grésillon, G. von Plessen, J. Feldmann, J. C. Rivoal, P. Gadenne, A. Ak. Sarychev, and V. M. Shalaev. Experimental observation of percolation-enhanced nonlinear light scattering from semicontinuous metal films. *Phys. Rev. B.*, 64(12):125106, September 2001.

[3] C. Anceau, S. Brasselet, J. Zyss, and P. Gadenne. Local second-harmonic generation enhancement on gold nanostructures probed by two-photon microscopy. *Opt. Lett.*, 28(9):713–715, May 2003.

[4] J. I. Dadap, J. Shan, K. B. Eisenthal, and T. F. Heinz. Second-Harmonic Rayleigh Scattering from a Sphere of Centrosymmetric Material. *Phys. Rev. Lett.*, 83(20):4045–4048, November 1999.

[5] J. I. Dadap. Optical second-harmonic scattering from cylindrical particles. *Phys. Rev. B.*, 78(20):205332, 2008.

[6] C. I. Valencia, E. R. Mendez, and B. S. Mendoza. Second-harmonic generation in the scattering of light by an infinite cylinder. *J. Opt. Soc. Am. B*, 21(1):36–44, 2004.

[7] C. F. Bohren and D. R. Huffman. *Absorption and Scattering of Light by Small Particles*. John Wiley & Sons, New York, 1998.

[8] J. D. Jackson. *Classical Electrodynamics*. John Wiley & Sons, Hoboken, 3rd edition, 1999.

[9] E. Centeno and D. Felbacq. Second-harmonic emission in two-dimensional photonic crystals. *J. Opt. Soc. Am. B*, 23(10):2257–2264, 2006.

[10] C. G. Biris and N. C. Panoiu. Second harmonic generation in metamaterials based on homogeneous centrosymmetric nanowires. *Phys. Rev. B.*, 81(19):195102, May 2010.

[11] E. Centeno and D. Felbacq. Rigorous vector diffraction of electromagnetic waves by bidimensional photonic crystals. *J. Opt. Soc. Am. A*, 17(2):320–327, February 2000.

[12] D. Felbacq, G. Tayeb, and D. Maystre. Scattering by a random set of parallel cylinders. *J. Opt. Soc. Am. A*, 11(9):2526–2538, 1994.

[13] M. Abramovitz and I. Stegun. *Handbook of Mathematical Functions*. Dover Publications, New York, 1972.

[14] J. M. Jin. *The Finite Element Method in Electromagnetics*. John Wiley & Sons, Hoboken, 2002.

[15] C. G. Biris and N. C. Panoiu. Nonlinear pulsed excitation of high-Q optical modes of plasmonic nanocavities. *Opt. Express*, 18(16):17165–17179, August 2010.

Chapter 4

OPTIMET: Implementation of the Multiple Scattering Matrix Solver

4.1 Introduction

OPTIMET (OPTIcal METamaterials) is a highly parallel custom implementation of the non-linear MSM algorithm, developed in C++ [1]. Currently, OPTIMET can support geometries of parallel cylinders of arbitrary distribution, size and material properties using Drude, Lorentz-Drude, or more general models for material properties, as well as magnetic materials. OPTIMET allows for continuous-wave regime simulations, using either plane waves or Fourier-Bessel waves, as well as temporal pulses using the fully integrated time domain solver. Output options include full spatial field profiles for both the linear and non-linear (second harmonic) fields, linear and non-linear scattering, absorption and extinction cross sections, and time-dependent field evolution. In this chapter, an overview will be given of both the logical and technical implementation of OPTIMET, as well as its various capabilities. Benchmarks of the parallel efficiency of the code will also be given.

4.2 Logical Implementation of OPTIMET

In this section, the logical structure of OPTIMET will be discussed. To this end, the workflow of the three types of simulations that OPTIMET can perform will be presented together with their respective input and output options. The different steps taken by the numerical solver will also be related to the mathematical formalism. Finally, the numerical parameters used by OPTIMET will also be presented and their influence on numerical stability discussed.

4.2.1 Input Options and Simulation Types

OPTIMET uses a simple and intuitive text-based input system consisting of an easy to edit ASCII file referred to in what follows as the `case` file and an automatically generated, `input` file which is fed directly to the solver. This two-step process ensures

Name of variable	Role	C++ Type
geometry	geometry type	*int*
polarisation	TE or TM polarisation	*int*
simulation_params	simulation type and parameters (based on type)	*int *int|*double*
wave_type	choose between plane wave or various non-zero components of a Fourier-Bessel expansion	**int*
wave_params	parameters of the incoming wave including incidence angles and wavelength	**double*
bground_params	electromagnetic properties of the background including dielectric constant and magnetic constant	**double*
fourier_order	number of Fourier-Bessel components to be included in the simulation	*int*
geometry_size	specify the number of scatterers on one or both axis (not required for some geometries)	**int*
geometry_params	geometrical parameters of the scatterers (varies between different geometry types)	**double*
material_params	Drude model parameters for metal cylinders or dielectric constants for dielectric cylinders	**double|*double*
lorentz_params	parameters for intra-band contributions to the Drude model (can be set to zero for pure Drude models)	**double*
sh_susceptibility	second order non-linear susceptibilities (only non-zero components required)	**double*

Table 4.1: Input variables used by OPTIMET.

that most simulations of often used geometries can be easily implemented by providing only the basic geometrical and numerical parameters needed. The `input` file, which contains the full specifications of the geometry and simulation, can then be created by OPTIMET's input functions using the `case` file. When more control is required, the input system allows for direct modification of the `input` file.

The `case` file contains several parameters that define both the simulation type and output as well as the geometry of the structure being investigated. Based on the type of simulation and geometry required, the case file contains a series of variables. Table 4.1 lists the main variables that can be set using an OPTIMET `case` file.

OPTIMET supports several predefined geometries including, a single cylinder, pairs of cylinders (dimers), 1D nanowire arrays, rectangle and triangle shaped distribu-

tions, regular polygonal distributions up to octagons, with or without a central cylindrical inclusion, elliptical hexagonal and octagonal distributions and random distributions of scatterers. A special type of "geometry" is the predefined `input` file type. When *geometry_type* is set to predefined, the input system bypasses the geometrical parameters of the case file and reads the geometry directly from the input file. The input file contains an ordered list of all the scatterers in the geometry with their respective geometrical and material parameters. This allows for the manual customisation of the simulation when the predefined geometries are not sufficient.

OPTIMET has three distinct types of simulations, or *runs*, which can be employed. In the basic case, a single geometry is illuminated by a single monochromatic wave and the scattering problem needs to be solved only once. This type of simulations are commonly used to retrieve the field profiles of a specific geometry. Here, only the geometry and the wavelength of light are required as input variables, while simulation parameters can include the output quantities needed (such as fields, linear and nonlinear cross sections or differential cross-sections).

In the second type of simulation, one or more variables in the simulation are "scanned". More specifically, this implies that one or more parameters of the simulation are varied to find the response of the system, *e.g.* in several configurations and at several wavelengths. Consequently, the varied parameters usually include the wavelength of the incoming field, one of the geometrical parameters of the structure and/or the incoming angle of incidence. These simulations are extremely useful for finding scattering and absorption spectra as well as geometrical dispersion graphs, while not being as computationally intensive as, for example, finding the field profiles at each single step. In terms of input, this type of simulation requires that the varied parameters be specified with their initial value, final value and the number of steps over which they will be iterated. The current version of OPTIMET only supports a maximum of two variables to be scanned over at the same time. Support for a larger number of scanning parameters can be easily implemented externally using shell scripting.

The third and final type of simulation supported in OPTIMET is the time domain regime. As will be explained in the next section, computationally, this type of run is similar to a wavelength scan. From the point of view of the case file, a time domain run requires that the initial temporal pulse be specified in terms of FWHM and central frequency, as well as the number of Fourier components (F_N) that will be used to Fourier transform the pulse in the frequency domain. This number is important also because the time domain run always outputs the field profiles of each step and F_N will in the end determine the size of the final output files which, for a very fine spatial computational grid, can become large in terms of storage. At the same time, a large enough padding factor a must be chosen to ensure that the pulse has decayed to near

zero as t approaches $T/2$ and $-T/2$, respectively. There is also an important interplay between the number of sampling points, the size of T and the time and frequency steps. For the discrete Fourier transform, the time step is $\delta t = T/F_N$, while the frequency step is given by $\delta\omega = 2\pi F_N/T$. $\delta\omega$ must be small enough to ensure that resonances with very small spectral width are resolved, yet this implies a large T. To ensure that even for a large T, the actual pulse width T_0 is small enough to cover a broad frequency spectrum, the padding factor a needs to be large enough. Finally, this implies that the number of sampling points F_N must be sufficient to cover the T_0 interval but not so large as to require a vast amount of computational power. There is thus a delicate balance that must be maintained between this factors, which must take into account the application in question and the available resources.

Finally, the input system checks the automatically or manually generated `input` file for consistency. This includes making sure that all needed variables are defined and that the scatterers do not intersect each other, which is not allowed by the MSM formalism. This final check can be toggled off by a flag in the input file for testing purposes. If the input file passes this final check, it is sent by the input system to the numerical solver.

4.2.2 The Numerical Engine Solver

OPTIMET's numerical solver is responsible for implements the MSM algorithm to solve the linear and non-linear scattering problems within the physical and geometrical parameters provided by the input system. As such, it closely follows the mathematical formalism presented in Chapter 3. Once the solutions are found, the solver passes them to the output system. Figure 4.1 summarises the implementation of OPTIMET, including the input system, the solver and the output system.

Because of the nature of the MSM method, the numerical algorithm lends itself to a very efficient, parallel implementation, as many of the major computational steps are independent of each other. The main steps in the simulation are as follows. First, the scattering matrices, $\mathbf{S}_j$, of single cylinders are calculated and subsequently the scattering matrix at the FF, $\mathbf{S}_\omega$, is determined using Eq. (3.33). The scattering coefficients at the FF are then found by solving the linear system given by Eq. (3.34). These coefficients are used to determine the fields at the FF, *via* Eq. (3.25) on the boundary of the cylinders, which are then used to compute by means of Eq. (2.65) and Eq. (2.67) the total nonlinear polarization at the SH. Note that in these calculations all the components of the nonlinear surface susceptibility tensor are used (not only the dominant one, $\hat{\chi}^{(2)}_{s,\perp\perp\perp}$) whereas for the bulk nonlinear polarization the free electron model given by Eqs. (2.68) is used.

Furthermore, once one knows the total nonlinear polarization at the SH one can determine the source coefficients, $\mathbf{A}_\Omega$, and the vector $\mathbf{G}^{\mathrm{self}}_\Omega$, and, implicitly, the vector

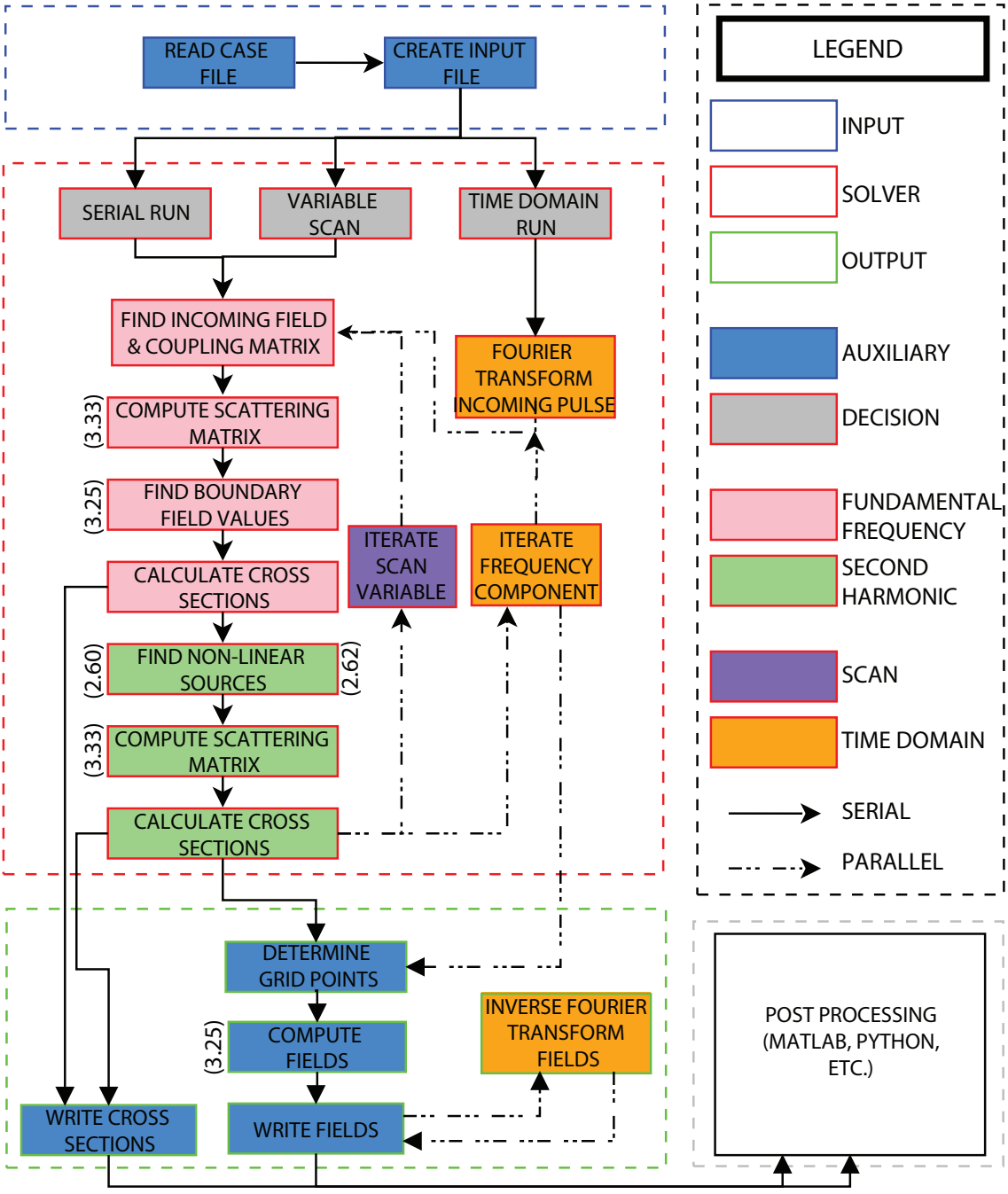

Fig. 4.1: OPTIMET work flow. Numbers in parentheses refer to equations used to compute the corresponding quantity.

$\mathbf{G}_\Omega$. Then, the scattering coefficients at the SH are determined from Eq. (3.62). If the total, absorption and scattering cross sections are requested in the case file, these are calculated before the fields are, at both the FF and the SH. Specifically, at the FF, these cross sections are given by Eqs. (3.75), (3.77) and (3.65), respectively. At the SH, only the scattering cross section has an analytical formula in Eq. (3.70. In order to find the total and absorption cross section at the SH, the total Joule losses are integrated numerically over the total transverse area of the cylinders. All the final values are then sent to the output system for storage until final output.

As discussed in the previous section, OPTIMET supports three main types of simulations. The most basic type involves a single run which can retrieve either the cross sections, the differential cross section, the spatial field profile, or, more commonly, a combination of the three. In this case, only one single run of the solver is required before the final output. In the second case, a scan of several of the variables is needed. In this case, the results of a single run are passed to the output system for storage and the variables over which the scan occurs are iterated to their next values. The solver now finds the solutions to the new scattering problem going through the same process as before. Once all requested iterations are completed, the execution moves on to the final output. For a time domain run, a similar process occurs but the only iterated variable is the wavelength. Specifically, an incoming Gaussian pulse specified at the input is Fourier transformed from the timed domain to the frequency domain. Each frequency will now have an associated incoming field amplitude and will constitute a single scattering case with an incoming monochromatic beam. The solver iterates through all these single frequency simulations, passing the required data for each step to the output system where the fields will be calculated for each frequency and subsequently inverse Fourier transformed into the time domain.

There is a series of numerical parameters that need to be determined so as to obtain convergence of the numerical process. The most important of these parameters is the number M of Bessel and Hankel functions used in the Fourier-Bessel expansions. Due to the technical limitations imposed by the 64 bit data storage, the order, m, of the Bessel functions is limited to 120, leading to a maximum of $M = 241$ expansion terms. Nevertheless, numerical tests have shown that, for example, for a one cylinder ($R = 500\ \mathrm{nm}$) geometry case, convergence can be achieved by employing $M \approx 41$ expansion terms. On the other hand, for the most complex of the scattering geometries studied here convergence is reached at $M \approx 91$. The second limitation has to do with the algorithm that computes the Bessel and Hankel functions. Because the parameter passed to these function is proportional to kr, where k is the wave vector and r a spatial dimension, instabilities can occur if this product is either to small (the case of small geometries and/or large wavelengths) or very large (large geometries

and/or small wavelengths). Fortunately, while these limitations do exist, they are not an impediment to study numerically nano- or micrometre-sized structures in the visible, near-infrared and infrared domains, which is the main purpose of OPTIMET. Other parameters required for the implementation of the MSM method are related to the numerical integrations needed to determine the nonlinear source coefficients, $\mathbf{A}_\Omega$, and the absorption cross section. Thus, the numerical integration is performed by uniformly dividing the $[0, 2\pi]$ domain into 360 intervals and the $[0, R_j]$ domains into 20 intervals. Integration is performed using a fourth-order Simpson formula. Finally, the number of Fourier sampling points F_N u can be set at the input phase and is typically $F_N = 8192$.

4.2.3 The Output System

The final component of OPTIMET is the output system. This module retrieves the scattering problem solutions from the solver and writes the required data to external storage. The output system uses only ASCII files as this allows easy transfer between OPTIMET and several post processing tools, such as MATLAB, Mathematica or Python. The type of output depends again on the type of simulation and the parameters set by the user at the input phase.

For a single geometry, single wavelength, run the output consists of writing the linear and non-linear cross sections (already calculated by the solver) as well as the differential cross-sections (if required) to a set of output files. In most cases, a single run also requires that a spatial field profile be produced. For this, the output system reads a separate "grid" file containing details about the computational grid on which the field is to be calculated. Currently, OPTIMET supports only 2D regular grids, however, independent grid limits and steps can be specified along each spatial direction. It is worth noting here that this grid is simply a visualisation tool. Once the grid is read, with the linear and non-linear scattering coefficients already calculated by the solver, finding a field profile outside the cylinders consists simply in using Eqs. (3.25) and (3.48) for the FF and SH fields, respectively. Inside the cylinders, the fields can be found using Eqs. (3.36) and (3.56). The final field profiles are then stored using a series of individual files. For increased versatility, these files separate the real and imaginary components of each of the three electromagnetic field components at both the FF and SH. This is done so that all the information contained the fields can be extracted in the post-processing phase, including phase information and polarisation. If needed, the actual scattering coefficients at both the FF and SH can also stored. This is useful for investigating cases in which the coefficients have no symmetry, such as, for example, the case of plasmonic cavity modes with angular momentum.

As expected, for the two other types of simulations, the output system does not differ significantly from the single run case. If a variable scan is requested, the output system is called at each iteration to output the needed data. This is to ensure that data

which is irrelevant to the solver (such as the solution found in the previous iterations) does not occupy memory. The output system can write these results either to separate files or, commonly done for cross-section spectra and dispersions, to a single file which is appended at each step with the new data. The time domain case is similar, but an extra step is needed in this type of simulation. The fields for each wavelength step are calculated on the grid and then stored in memory (usually distributed across a series of computational nodes when parallel processing is used) until all the F_N steps have been completed. The output system then inverse Fourier transforms the fields, which are in the frequency domain, back to the time domain and writes the results in either a single master file or in a series of files for each step. At this point, the user can determine whether or not the frequency domain data is also required, in which case it will be written to external storage.

The final step in the OPTIMET work flow consists in post-processing the data calculated by the algorithm. This can be done in a series of numerical analysis packages and is left to the discretion of the user. For the purposes of this work, post-processing was done using the Mathworks MATLAB software package [2].

4.3 Software Implementation of OPTIMET

OPTIMET was developed using the C++ programming language and designed to allow for a modular build and portability across various computer architectures. OPTIMET makes use of a series of performance enhancing numerical libraries for its core numerical engine. As such, all vector and matrix algebra is done using the parallel implementations of BLAS and LAPACK packages, which are part of the Intel®Math Kernel Library (MKL) [3]. MKL also provides the means for direct and inverse discrete Fourier transforms using the FFTW library. The choice of MKL was a result of the target architecture for which OPTIMET was planned as part of this project. Nevertheless, the solver module can be easily linked with the freely available, open source implementations of the three numerical packages. All the corresponding libraries are dynamically linked to the solver. To compute the Bessel and Hankel functions of complex arguments, the Amos Algorithm 644 is used [4]. A version of this algorithm is freely available in the netlib repository [5]. OPTIMET does not link to Algorithm 644 but instead contains a fully working, FORTRAN to C translation of the netlib files, which are compiled and statically linked into the solver.

OPTIMET was designed and built on the Legion High Performance Cluster of the University College of London. Legion consists of 5680 processing cores based on the Intel®Xeon architecture. Each core has exclusive access to either 2 or 4 GB of memory and all cores can write to a 192 TB, RAID level 6 storage area which uses the Lustre Cluster File System. Parallelisation is achieved using the Q Logic MPI implementation

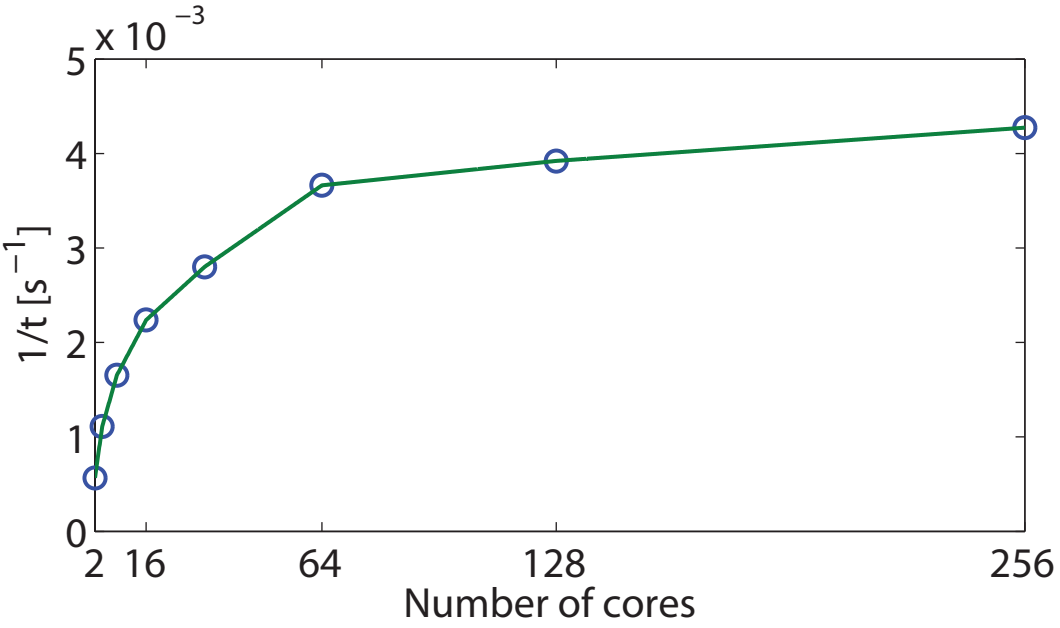

Fig. 4.2: OPTIMET parallel execution times versus the number of cores used. The test simulation consists of a time domain simulation with $F_N = 16384$ Fourier sampling points for a single cylinder with output of a single field point.

of the MPI-1 standard, however, OPTIMET can be linked to any MPI library, including OpenMPI. To optimise the final executable for this specific architecture, OPTIMET was compiled using the Intel®C++ Compiler, version 11.

As discussed in Sec. 4.2, the MSM algorithm lends itself to efficient parallel implementation, as many of the numerical processes involved are independent of each another. In the current version of OPTIMET, parallelism is used only for scan runs and time domain runs. Specifically, a subset of the solver iterations over the scan variables, or the wavelength in the case of time domain simulations, is assigned to a core and executed independently of the other cores. The size of the subset depends on the number of iterations required as well as the number of cores requested. The parallel portions of the OPTIMET work flow are shown in Fig. 4.1 using dashed arrows. The output system is parallelised for the initial output of the data from each core but executes the final data processing and output in the head node in a serial fashion.

Figure 4.2 shows the parallel performance of OPTIMET for a simple time domain simulation. As expected with parallel code, as the number of cores increases, the execution time decreases asymptotically to a certain fixed value due to the fact that the execution time on each core becomes much smaller than the variable initialisation and intra-core communication times. The exact number of cores for which this plateau is reached depends of course on the number of iterations required for the simulation. It is worth noting here that further parallelisation can be achieved in the solver for the one wavelength, one geometry case itself using either MPI or an OpenMP implementation. This parallelisation, however, does not provide a significant improvement to the

execution times.

Finally, the OPTIMET code was designed to be easily documented, with each function and variable being described in the context of the code and allowing for easy porting to an automated code documentation system such as Doxygen. Compilation of the code is done using a system of GNU makefiles, which include the possibility of test cases and convergence checks for predefined geometries. Debugging was done using both the GNU Debugger (`gdb`) and the Data Display Debugger (DDT) running in MPI mode. Debugging is also aided by OPTIMET's runtime output system, which consists of writing the runtime status to `stdout`, and `stderr` in case of non-halt errors.

4.4 Conclusions

To conclude, in this chapter, a logical and technical description of the OPTIMET software package was provided. OPTIMET was specifically built to implement the MSM method described in Chapter 3. To the best of our knowledge, this is the only available implementation of the MSM algorithm that includes bulk and surface second harmonic generation from metals. OPTIMET was designed in a bottom-up approach so as to be modular, portable, easy to implement in parallel fashion and easy to use.

At the time of writing, OPTIMET has been successfully used to study several types of non-linear plasmonic geometries and their applications. Specifically, OPTIMET has been used to show enhanced linear and non-linear plasmonic interactions in regular and random structures made of metallic nanowires [1]. To this end, it was shown that these structures exhibit strong field enhancement, surface plasmon coupling, tight beam focusing, plasmon wave guiding and strong light localisation. The time domain capabilities of OPTIMET was used to show that non-linear plasmon cavities have high quality factors and can become crucial to the developement of sub-wavelength lasers [6, 7]. Non-linear plasmonic cavities were also investigated using OPTIMET to show their potential use as sub-wavelength sensors [8]. Finally, OPTIMET was also employed to study plasmonic cavity modes which possess angular momentum. In the next few chapters, the use of OPTIMET to study these and other problems will be detailed, which will further outline its versatility and usefulness in numerical studies of non-linear metamaterials and devices.

Bibliography

[1] C. G. Biris and N. C. Panoiu. Second harmonic generation in metamaterials based on homogeneous centrosymmetric nanowires. *Phys. Rev. B.*, 81(19):195102, May 2010.

[2] MATLAB product page. `http://www.mathworks.com/products/matlab/`.

[3] MKL product page. `http://software.intel.com/en-us/articles/intel-mkl/`.

[4] D. E. Amos. ALGORITHM 644: a portable package for Bessel functions of a complex argument and nonnegative order. *ACM T. Math. Software*, 12(3):265–273, January 1987.

[5] netlib repository. `http://www.netlib.org/amos/`.

[6] C. G. Biris and N. C. Panoiu. Nonlinear pulsed excitation of high-Q optical modes of plasmonic nanocavities. *Opt. Express*, 18(16):17165–17179, August 2010.

[7] C. G. Biris and N. C. Panoiu. Excitation of linear and nonlinear cavity modes upon interaction of femtosecond pulses with arrays of metallic nanowires. *Appl. Phys. A-Mater.*, 103(3):863–867, January 2011.

[8] C. G. Biris and N. C. Panoiu. Excitation of dark plasmonic cavity modes via nonlinearly induced dipoles: applications to near-infrared plasmonic sensing. *Nanotechnology*, 22(23):235502, April 2011.

Chapter 5

Linear and Non-linear Scattering of Electromagnetic Waves from Two-dimensional Distributions of Metallic Cylinders

5.1 Introduction

In this chapter, the numerical method described in Chapter 3 will be used to investigate the linear and non-linear wave scattering from a set of homogeneous centrosymmetric (metallic) cylinders. Several cases of particular practical interest will be considered from the point of view of the linear and non-linear field distribution and near- and far- field response. The analysis will also focus on the effects of structural changes to the properties of the structures, so as to highlight the high degree of tuneability of the designs and the versatility of the MSM method [1].

The cases that will be discussed here include scattering by one (where a comparison with analytical results is possible) and two cylinder (dimer) structures, and 1D chains of cylinders which will be shown to support plasmon waveguiding. The case of wave scattering by 2D distributions of cylinders will also be considered. Here, it will be shown how beam focusing and high field enhancement can be achieved in triangle- and square-like structures. Finally, the problem of second harmonic generation in random distributions of nanowires will be presented.

5.2 Second Harmonic Generation from a Single Metallic Cylinder

To begin with, consider the linear and non-linear wave scattering by a single metallic cylinder whose dielectric function is given by the Drude model. This is an important

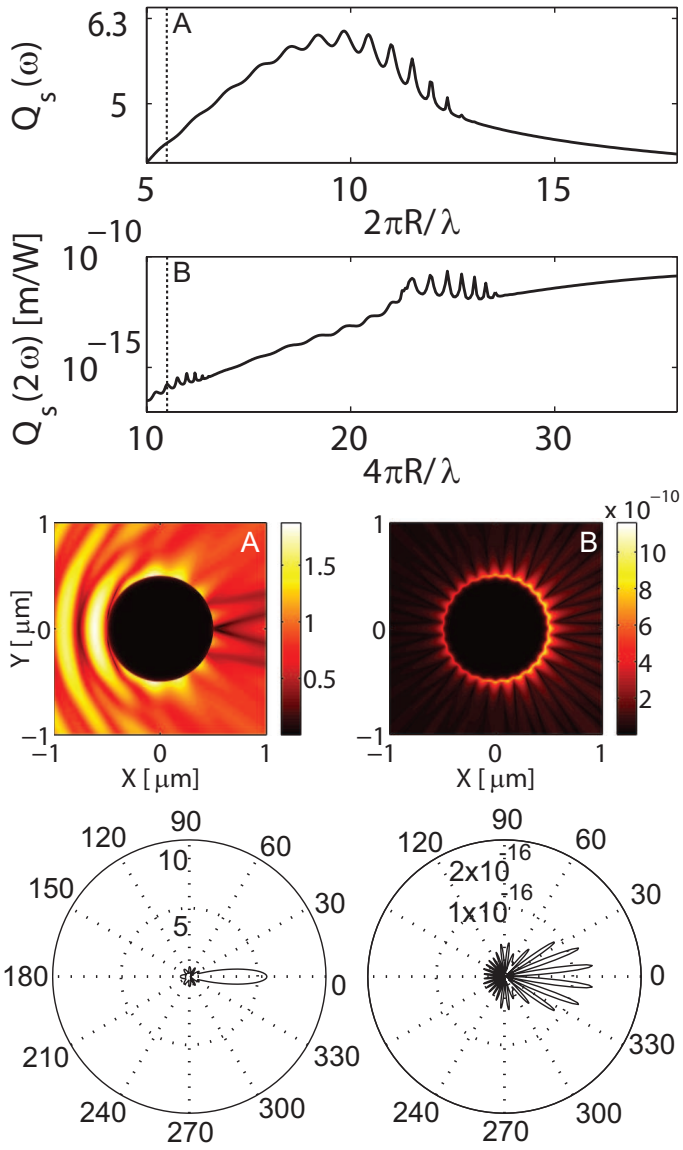

Fig. 5.1: The top two panels show the logarithmic plot of the total scattering cross sections corresponding to a single cylinder with radius $R = 500$ nm. The panels in the middle show the spatial distribution of the electric field amplitude calculated at $\lambda = 570$ nm and correspond to the dashed vertical lines in the top two panels. The bottom panels present the polar representation of the differential scattering cross sections, calculated at the same wavelength $\lambda = 570$ nm. Left and right panels correspond to the FF and SH, respectively.

case because it has an analytical solution [2], which allows the validation of the numerical method. We have therefore considered the wave scattering by a cylinder with radius $R = 500$ nm and calculated the scattering cross section, at both the FF and at the SH. As mentioned in Chapter 2, owing to the symmetries of the $\chi_s^{(2)}$ tensor, only the TE polarisation leads to surface second harmonic generation and, therefore, only this polarisation will be considered here and in subsequent chapters. The results of these calculations, which are presented in Fig. 5.1, show that the scattering cross section at the FF has a global maximum at the wavelength $\lambda \sim 300$ nm, whereas the scattering cross section at the SH decreases with the wavelength. In addition, it can be seen that

the scattering cross sections at the FF and SH present a series of spectral peaks. Note that at the FF there is only one set of such spectral resonances; however, at the SH there are two spectral regions in which the scattering cross section presents a series of spectral peaks. As it will be explained in more detail later, the physical origin of these two sets of spectral peaks at the SH can be traced to different physical effects.

The properties of the maxima in Fig. 5.1 are revealed, in part, by the spatial distribution of the amplitude of the electric field, calculated at the wavelength of these spectral peaks. Thus, Fig. 5.1 shows that at $\lambda = 570\ \mathrm{nm}$, which corresponds to one of the maxima of $Q_s(\Omega)$, the amplitude of the electric field around the cylinder, at the SH, presents a series of local maxima (see panel B in Fig. 5.1). This is the signature of the excitation of localized surface plasmon modes [3]. These are TE modes of the metallic cylinder, at their cut-off wavelength. To be more specific, since the wave vector of the incident wave is perpendicular to the axis of the cylinder, the propagation constant of the waveguide modes of the cylinder must be zero, *i.e.*, it satisfies the cut-off condition. Note that for this wavelength no SPPs are excited at the FF.

There is also an obvious relation between the spatial distribution of the near field at the SH and the scattering pattern showed by the differential scattering cross section, $q_s(\varphi;\Omega)$. Thus, the polar representation of $q_s(\varphi;\Omega)$, shown in Fig. 5.1, reveals that the SH is radiated primarily along a series of specific directions, the number of these angular maxima being equal to the number of maxima of the spatial distribution of the near field. As a general characteristic of the scattering pattern at the SH, most of the radiation is emitted in the forward direction. At the FF most of the radiation is primarily emitted in the forward direction, too, although there are several other secondary directions in which a much smaller amount of radiation is emitted. It should be noted that these results obtained by numerical simulations fully agree with the analytical solution of the linear and non-linear scattering problem, which is presented in Ref. [2].

The same scattering process is also considered for a cylinder with $R = 200\ \mathrm{nm}$. The main results obtained in this case are summarized in Fig. 5.2. It can be seen in this figure that by decreasing the radius of the cylinder the number of SPP modes of the cylinder decreases and their resonance wavelength is blue shifted. Figure 5.2 also provides additional physical insight into the nature of the two different types of SPP resonances excited at the SH. The origin of the first type of such SPP resonances, which are excited al lower wavelengths (at $\lambda = 257\ \mathrm{nm}$ in Fig. 5.2), is the SPP-induced field enhancement at the FF. Thus, as can be seen in Fig. 5.2, at the wavelengths corresponding to these resonances the amplitude of the field at the FF is enhanced near the surface of the cylinder and, as a consequence, the induced non-linear effects are also stronger. On the other hand, the SPP resonances at longer wavelengths (at $\lambda = 480\ \mathrm{nm}$ in Fig. 5.2), are due to the excitation of SPPs at the SH, with no such localized modes being excited

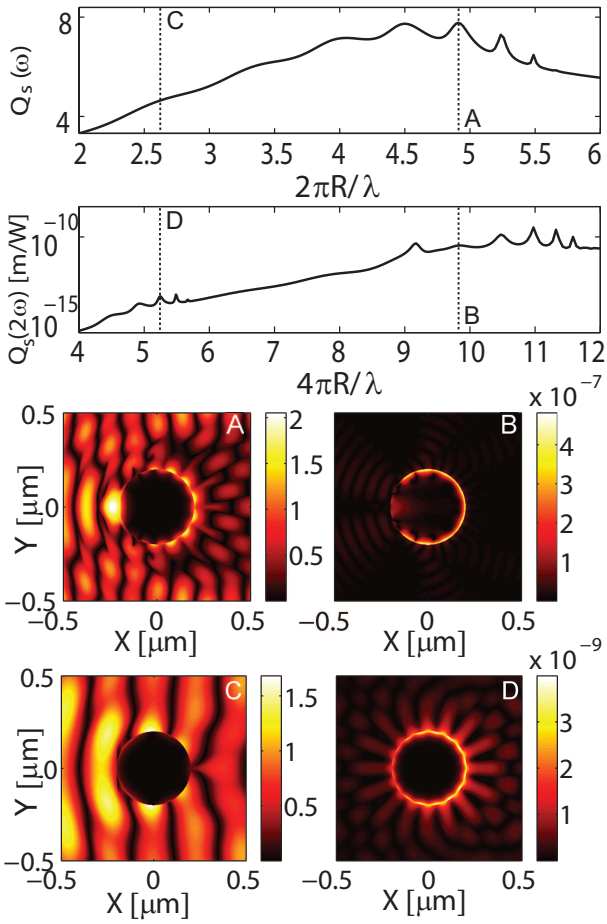

Fig. 5.2: The top panels show the logarithmic spectra of the scattering cross sections. The spatial profile of the amplitude of the electric field, calculated at the wavelength $\lambda = 257$ nm (A and B) and $\lambda = 480$ nm (C and D), are plotted in the bottom panels. The radius of the cylinder is $R = 200$ nm. Left and right panels correspond to the FF and SH, respectively.

at the FF. Inasmuch as, mathematically, the SPP resonances are given by the poles of the scattering matrix in the Eq. (3.37), the latter type of resonances should occur when the operating wavelength is about twice as large as the wavelength at which the former type of resonances occur. This conclusion fully agrees with the results presented in Fig. 5.2. This distinction between the two types of SPP resonances will appear in more complex scattering geometries as well. Importantly, a further increase in the strength of the non-linear interaction can be achieved by tuning the parameters of the cylinder, so as the two types of resonances are excited at the same wavelength. This effect has been recently observed in the case of wave scattering by dielectric cylinders [4].

5.3 Linear and Non-Linear Wave Scattering by a Metallic Dimer

In this section we analyse the wave scattering by a metallic nano-dimer, which has a series of important technological applications that rely on the enhancement of the electric field at the surface of metals. Specifically, by using metallic nanodimers one

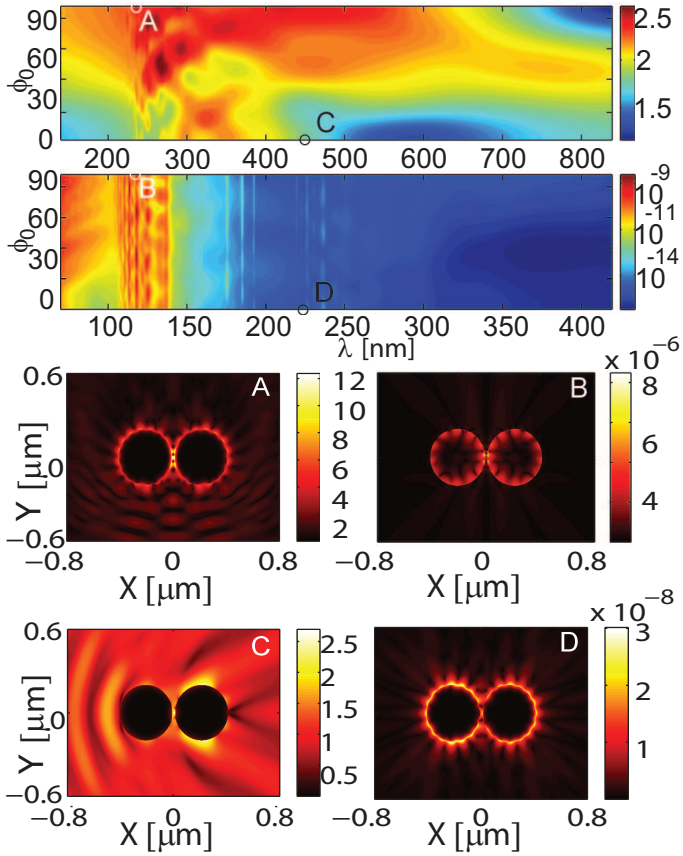

Fig. 5.3: The top two panels present the scattering cross section at the FF (upper panel) and the SH (lower panel) vs. the angle of incidence and wavelength. The radius of the cylinders is $R = 200$ nm *and the separation distance is* $d = 20$ nm*. The spatial profile of the amplitude of the electric field, calculated at* $\lambda = 237$ nm *and* $\phi_0 = 90°$ *(A and B) and* $\lambda = 473$ nm *and* $\phi_0 = 0°$ *(C and D), are plotted in the bottom panels. Left and right panels correspond to the FF and SH, respectively.*

can generate large electric fields, especially in the space between the metallic cylinders forming the dimer. As a result, because non-linear optical effects at metal/dielectric interfaces, such as SHG and SERS, are strongly dependent on the physical properties of the interface, metallic nanodimers can be used efficiently in sensing applications or surface optical microscopy. Importantly, in the linear case there is an analytical solution to the problem of wave scattering by two cylinders [5]; however, in the non-linear case no analytic solution is known yet. Therefore, numerical simulations play an important role in understanding the non-linear wave scattering by these and other more complex nanostructures.

In our analysis, we have considered a dimer consisting of two cylinders with radius $R = 200$ nm, separated by a distance d. The results of the numerical study are summarized in Fig. 5.3 and Fig. 5.4, which correspond to the separation distance $d = 20$ nm and $d = 100$ nm, respectively. The dispersion plots presented in these figures show that, similar to the case of a single cylinder, the scattering cross section of a metallic dimer presents a series of spectral peaks (SPP bands), at both the FF and the SH. These bands

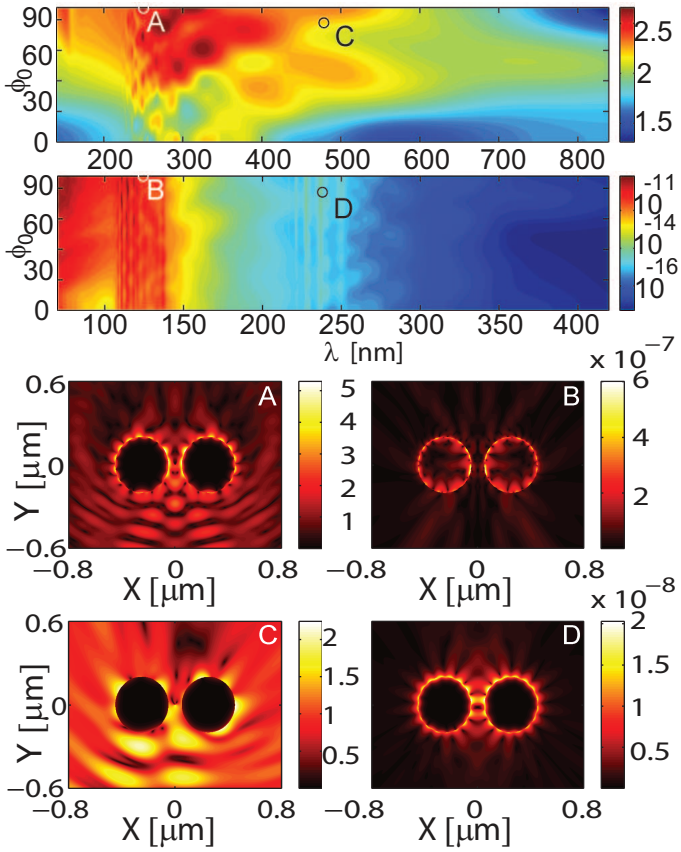

Fig. 5.4: The same as in Fig. 5.3, but for $d = 100$ nm. *The field profiles correspond to* $\lambda = 243$ nm *and* $\phi_0 = 90°$ *(A and B) and* $\lambda = 475$ nm *and* $\phi_0 = 78°$ *(C and D).*

are located in the same spectral regions as in the case of a single cylinder, although the wavelength of the peaks is slightly blue shifted. This shift of the frequency of the SPP resonances is induced by the interaction between the SPPs excited on each cylinder, a physical effect that resembles the hybridization of atomic orbitals. As expected, this blue shift of the wavelength of the SPP resonances decreases as the separation distance d increases. The strength of the coupling between the SPP modes of single cylinders is also illustrated by the field profiles presented in panels D in Fig. 5.3 and Fig. 5.4. Thus, these field profiles are almost independent on the angle of incidence ϕ_0 (the angle made by the incident wave with the longitudinal axis of the dimer), which proves that this field is chiefly the result of near field interactions. This same strong SPP coupling explains the fact that the spectral location of the SPP bands in Fig. 5.3 and Fig. 5.4 does not depend on the angle ϕ_0. On the other hand, the scattering cross sections at both the FF and SH increase with the angle ϕ_0, which is due to a more efficient coupling between the incident wave and the dimer at larger ϕ_0. Furthermore, similar to the case of a single cylinder, the SPP resonances at the SH can be divided into two types, those induced by the resonant excitation of SPP modes at the FF and those that are associated with the excitation of SPP modes solely at the SH. Additional physical insights into the properties of the wave scattering by a metallic dimer are revealed by

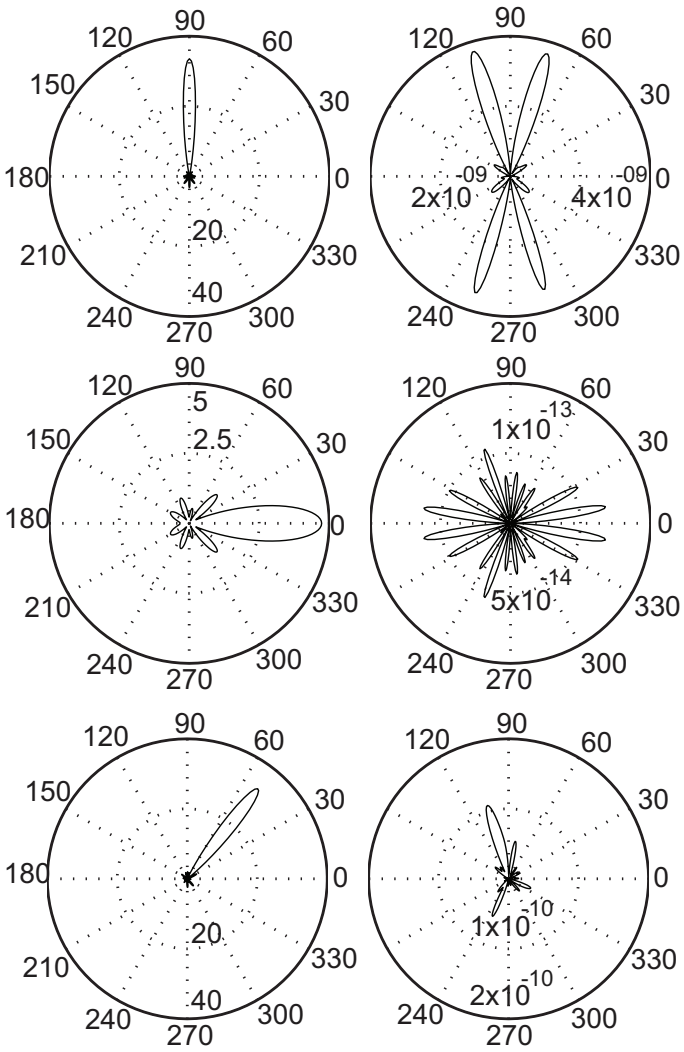

Fig. 5.5: Polar representation of the differential scattering cross section for a metallic dimer with $R = 200\ \mathrm{nm}$ and $d = 20\ \mathrm{nm}$. The plots correspond to $\lambda = 237\ \mathrm{nm}$ and $\phi_0 = 90^\circ$ (upper panels); $\lambda = 437\ \mathrm{nm}$ and $\phi_0 = 0^\circ$ (middle panels); and $\lambda = 266\ \mathrm{nm}$ and $\phi_0 = 62^\circ$ (bottom panels). Left and right panels correspond to the FF and SH, respectively.

the differential scattering cross sections presented in Fig. 5.5 and Fig. 5.6, the plots in these figures corresponding to a separation distance of $d = 20\ \mathrm{nm}$ and $d = 100\ \mathrm{nm}$, respectively. As expected, when the direction of the incoming wave vector coincides with one of the symmetry axes of the dimer, the spatial pattern of the far-field response is also symmetric with respect to this axis; however, at an oblique angle of incidence the scattering pattern is no longer symmetric. In addition, the angular dependence of the differential scattering cross-section shows that at the FF most of the scattered field is emitted in the forward direction. On the other hand, because of the intricate distribution of the sources of the SH (the surface and bulk non-linear polarisations), the scattering pattern of $q_s(\varphi;\Omega)$ presents a much more complex dependence on the polar coordinate φ. Moreover, since the distribution of the sources of the SH depends strongly on the separation distance between the cylinders, the scattering pattern at the SH also changes

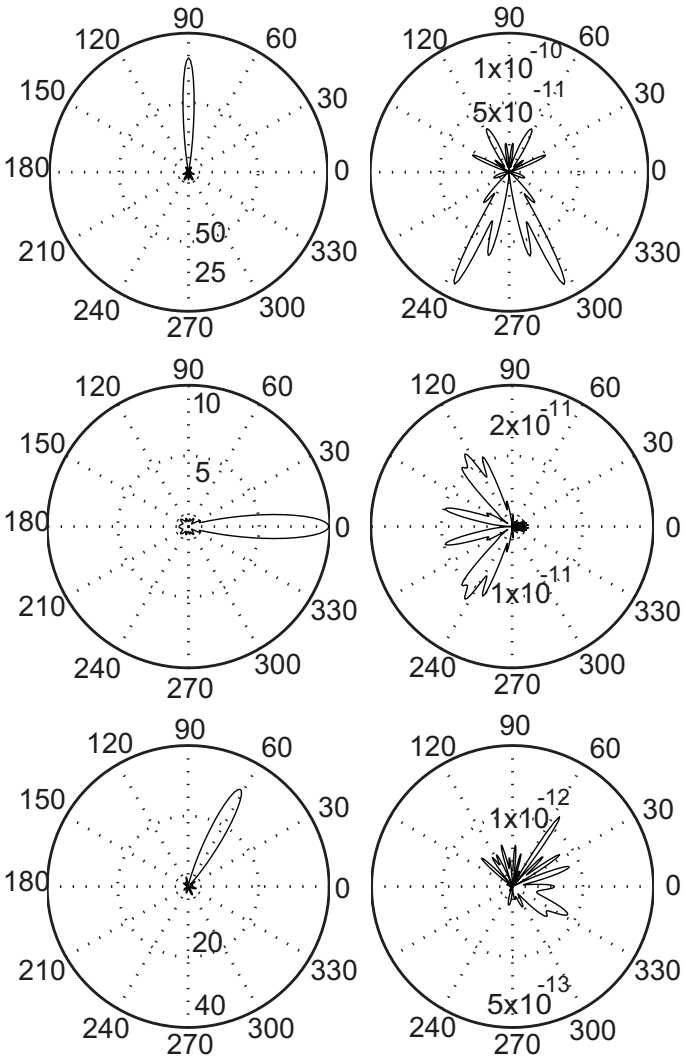

Fig. 5.6: The same as in Fig. 5.5, but for $d = 100\ \mathrm{nm}$. *The plots correspond to* $\lambda = 243\ \mathrm{nm}$ *and* $\phi_0 = 90^\circ$ *(upper panels);* $\lambda = 232\ \mathrm{nm}$ *and* $\phi_0 = 0^\circ$ *(middle panels); and* $\lambda = 328\ \mathrm{nm}$ *and* $\phi_0 = 62^\circ$ *(bottom panels). Left and right panels correspond to the FF and SH, respectively.*

significantly with this distance [see Fig. 5.5 and Fig. 5.6].

The spectral characteristics of the scattering cross sections provide us with insightful information about the transfer of energy from the incident wave to the far-field. In turn, the spectra of the absorption cross sections reveal important properties of the fundamental and second harmonic near-fields. In order to illustrate this idea, we present in Fig. 5.7 the scattering and absorption cross sections for a metallic dimer, as well as the field profiles corresponding to certain resonance wavelengths. This figure reveals several notable dependencies between the spatial profile of the fundamental and second harmonic near-fields and the spectra of the scattering and absorption cross sections. Firstly, at both the FF and the SH the spectral resonances of the absorption and scattering cross sections do not always coincide, which proves that they have different physical origins. Moreover, the spectral peaks in the absorption cross section at the FF correspond to a significant increase of the near-field, at the wavelength of the largest

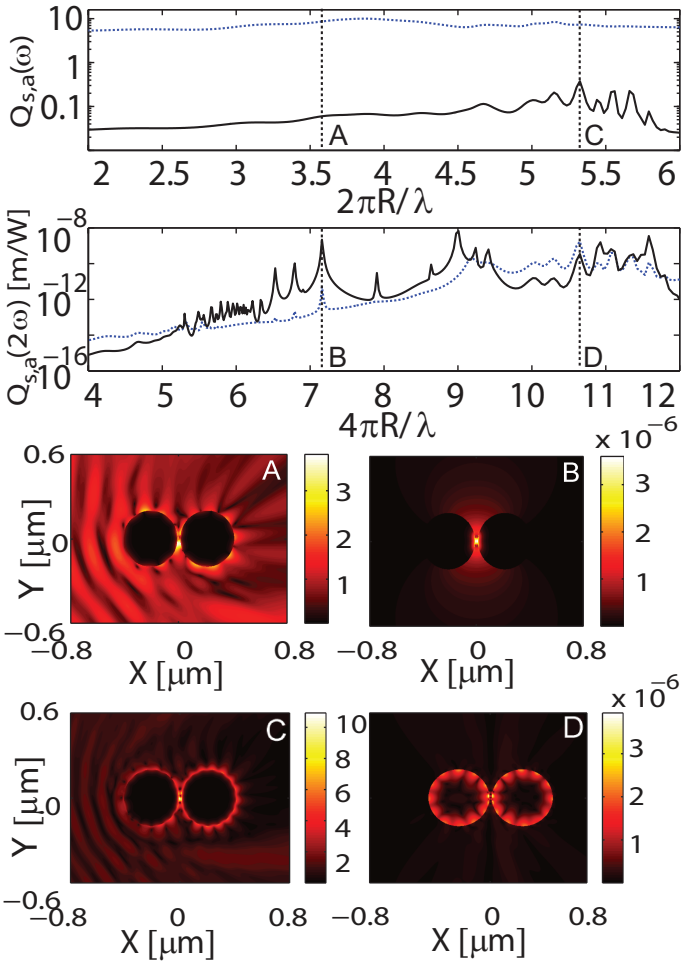

Fig. 5.7: The top panels show the logarithmic absorption (solid line) and scattering (dashed line) cross sections. The radius is $R = 200$ nm and the separation distance $d = 20$ nm. The spatial profile of the amplitude of the electric field for $\lambda = 350$ nm and $\phi_0 = 20^\circ$ (A and B) and $\lambda = 236$ nm and $\phi_0 = 20^\circ$ (C and D) is presented in the bottom panels. Left and right panels correspond to the FF and SH, respectively.

peak the field being enhanced by more than an order of magnitude (compare panels A and C in Fig. 5.7). Furthermore, the spectral resonances seen in the SH spectrum have different origins, too. Thus, the excitation within a small spatial domain in-between the cylinders of a strong field, a so-called "hot spot", is directly related to the resonance at $\lambda = 350$ nm. On the other hand, the resonance at $\lambda = 236$ nm is due to the excitation of a localized mode than penetrates into the cylinders up to a considerable depth. Interestingly enough, the panels C and D in Fig. 5.7 show that at $\lambda = 236$ nm the field at the FF penetrates into the cylinders only a very small distance while at the SH the penetration depth is considerably larger. This effect is explained by the fact that at the SH the wavelength is smaller than the plasma wavelength ($\lambda_p = 139.6$ nm), and therefore at this wavelength the cylinders have dielectric properties, namely, the real part of the permittivity is positive. At the FF, however, $\lambda > \lambda_p$, which means that the permittivity has the optical properties of a metal. Finally, note that whereas at the FF the scattering

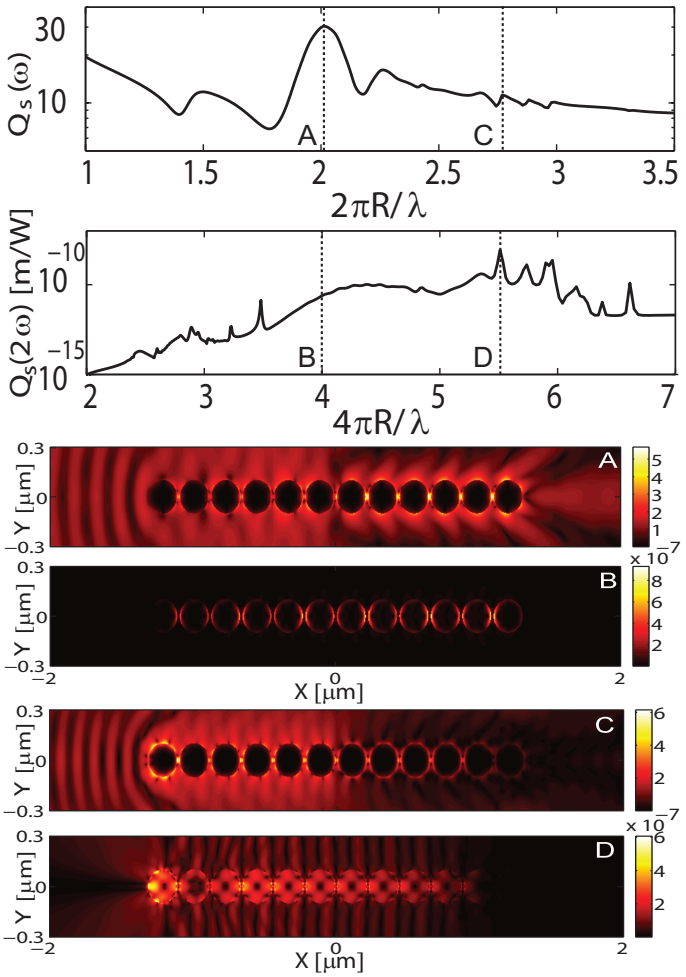

Fig. 5.8: The top two panels show the logarithmic spectra of the scattering cross section corresponding to a chain of $N = 12$ metallic cylinders. The radius is $R = 200$ nm, the angle of incidence is $\phi_0 = 0°$, and the separation distance is $d = 20$ nm. The spatial profile of the amplitude of the electric field, calculated at $\lambda = 313$ nm (A and B) and $\lambda = 229$ nm (C and D), is presented in the bottom panels. The panels A and C correspond to the FF, whereas the panels B and D correspond to the SH.

cross section is more than two orders of magnitude larger than the absorption cross section, at the SH the absorption cross section is larger than the scattering cross section in almost the entire spectral domain considered in our calculations.

5.4 Wave Scattering from 1D Chains of Metallic Cylinders

The MSM numerical method has also been employed to study the SHG in more complex scattering geometries, namely, chains of coupled metallic cylinders. Such nanostructures can find important technological applications to subwavelength active optical waveguides, optical nanoantennae, or light focussing at subwavelength scale.

The geometry considered in our study consists of $N = 12$ metallic cylinders arranged in a linear chain, the radius of the cylinders and the separation distance being

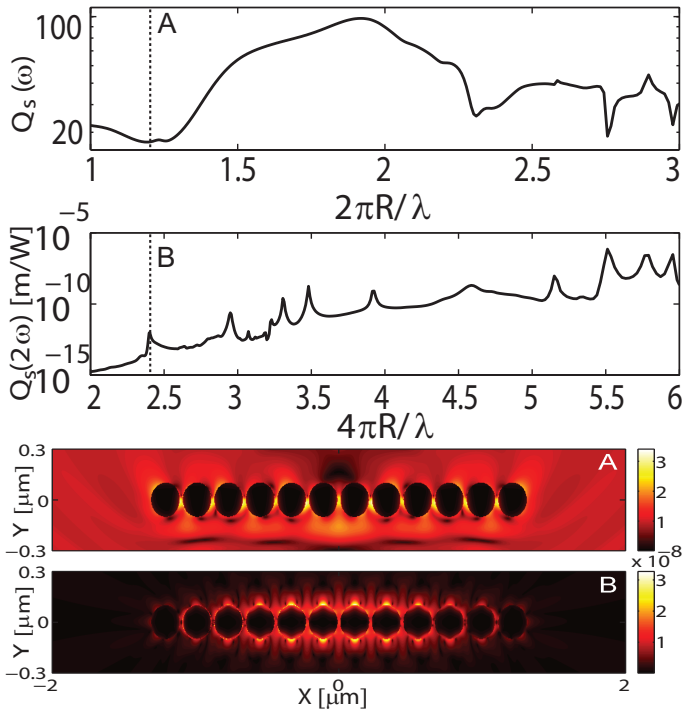

Fig. 5.9: The same as in Fig. 5.8, but for $\phi_0 = 90°$ *and* $\lambda = 525$ nm.

$R = 200$ nm and $d = 20$ nm, respectively. The main results pertaining to this scattering geometry are summarized in Fig. 5.8 and Fig. 5.9, the angle of incidence corresponding to these figures being $\phi_0 = 0°$ and $\phi_0 = 90°$, respectively (ϕ_0 is the angle between the direction of the incident wave and the axis of the chain of cylinders). One of the main conclusions illustrated by these figures is that, for both angles of incidence, the complexity of the scattering spectra increases with the number of scatters. This fact suggests that as the number of scatterers increases, the long-range interactions among the scatterers becomes stronger and therefore they play an increasingly important role in determining the global optical response of the structure. This coherent response of the scatterers is illustrated by the top two panels in Fig. 5.8, which show that although the spectrum of the scattering cross section at the FF has a large peak at $\lambda = 313$ nm, no spectral resonance exists at the SH. To be more specific, it can be seen that at this wavelength most of the SH field (and consequently the non-linear polarisation) is localized in the region in-between adjacent cylinders (see panels A and B in Fig. 5.8), leading to a destructive interference in the far-field of the radiated light. As will be shown in the next section, this coherent optical response of the scatterers is even more evident in the case of 2D ordered distributions of cylinders.

Figures 5.8 and 5.9 demonstrate that the wave scattering by the chain of cylinders is strongly dependent both on the wavelength as well as the angle of incidence. In particular, Fig. 5.8 shows that, depending on the excitation frequency, the chain of metallic cylinders supports either modes that propagate only at the FF (panels A and B) or propagating modes at both the FF and SH (panels C and D). Importantly, the latter

ones can find important applications to subwavelength active nanodevices [6], which can be used to generate and transport optical power at subwavelength scale. Another notable effect illustrated in the panel A in Fig. 5.8 is the formation at the end of the chain of cylinders of an optical beam with width of about $\lambda/3$, a so-called optical nanojet, an effect that can be employed to achieve subwavelength light focusing. On the other hand, one can see in Fig. 5.9 that, as expected, an incoming wave that is normally incident onto the axis of the chain ($\phi_0 = 90°$) leads to the excitation of of standing waves in the chain of cylinders. Indeed, since in this case the projection of the wave vector of the incoming wave onto the longitudinal axis of the chain of cylinders cancels, no propagating modes can be excited.

5.5 Wave Scattering by Ordered 2D Distributions of Metallic Cylinders

As stated before, the versatility of the MSM algorithm allows one to study the linear and non-linear wave scattering in cases in which the scatterers are characterized by a complex spatial distribution. As examples of such complex geometries, in this section we consider 2D hexagonal and square distributions of metallic cylinders. The main results regarding these scattering structures are summarized in Fig. 5.10 and Fig. 5.11 and correspond to hexagonal and square distributions, respectively. Similar to the case of 1D chains of metallic cylinders, both these geometries show a significant increase in the number of resonances in the spectrum of the scattering cross section, at both the FF and the SH. As discussed in the previous section, this effect is the result of the coherent response of the ensemble of cylinders. In addition, in the case of 2D distributions SPPs excited on more than two cylinders can couple, leading to a more intricate interaction among these SPP modes. Moreover, note that as the wavelength decreases the scattering cross section at the SH increases. This dependence is a direct consequence of the fact that at shorter wavelengths the incident field penetrates deeper into the distribution of scatterers and therefore it induces a larger non-linear polarisation.

As can be seen in Fig. 5.10 and Fig. 5.11, the spatial field distribution inside the ensemble of cylinders changes significantly with the layout of the scatterers, a property that can be used to tune the linear and non-linear optical response of metamaterials based on such primary building blocks. Alternative potential technological applications are suggested by the field profiles in Fig. 5.10. Thus, as can be seen in this figure, the hexagonal distribution of cylinders concentrates the incident field towards the tip of the set of scatterers, especially at the SH. Therefore, such a scattering geometry can be used to efficiently focus and couple the optical near-field in guiding nanostructures, such as the chain of nanowires studied in the preceding section. Interestingly enough, Fig. 5.11 shows that in the case of the square distribution of cylinders the field gener-

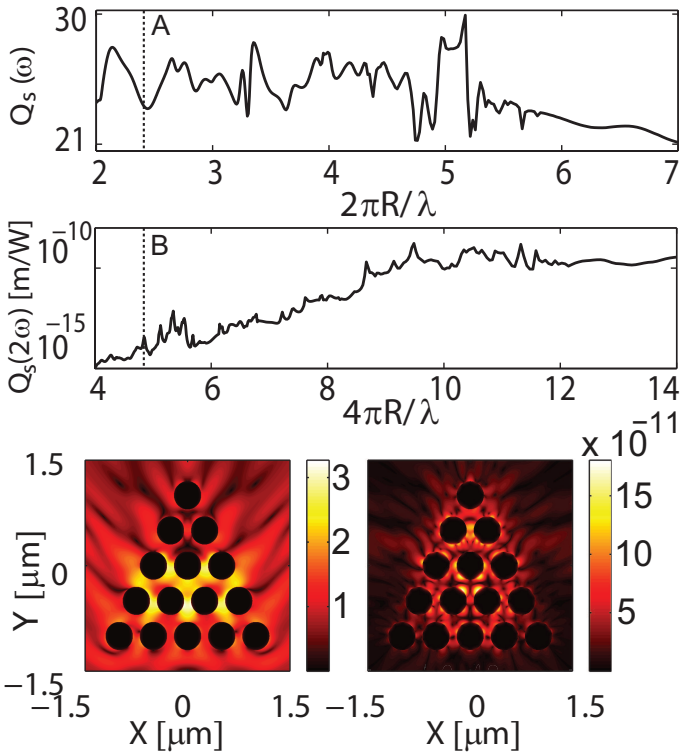

Fig. 5.10: The top two panels show the logarithmic spectra of the scattering cross section corresponding to a hexagonal distribution of $N = 15$ metallic cylinders. The radius is $R = 200$ nm, the angle of incidence is $\phi_0 = 90°$, and the separation distance is $d = 100$ nm. The spatial profile of the amplitude of the electric field, calculated at $\lambda = 471$ nm, is presented in the bottom panels. Left and right panels correspond to the FF and SH, respectively.

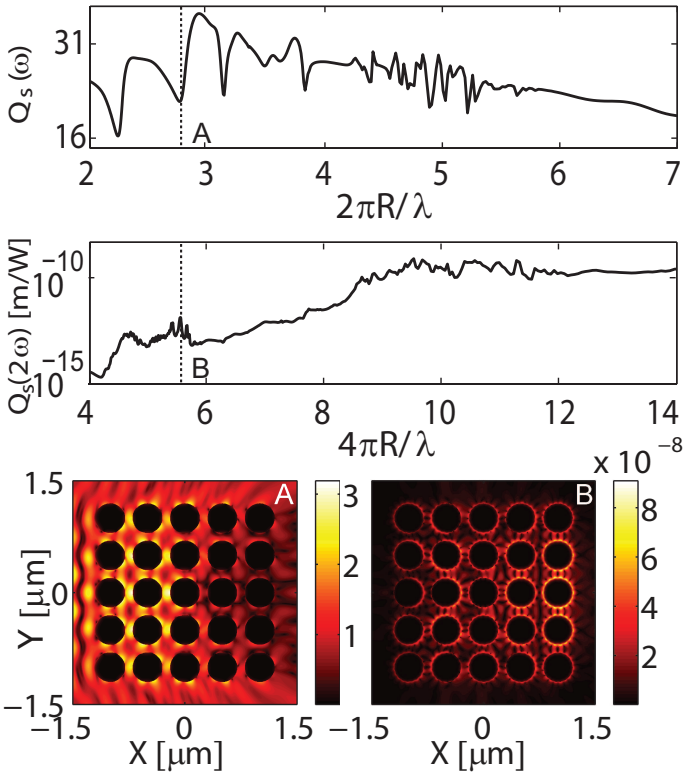

Fig. 5.11: The same as in Fig. 5.10, but for a square distribution of $N = 25$ metallic cylinders. In the bottom panels the wavelength is $\lambda = 454$ nm and the angle of incidence is $\phi_0 = 0°$.

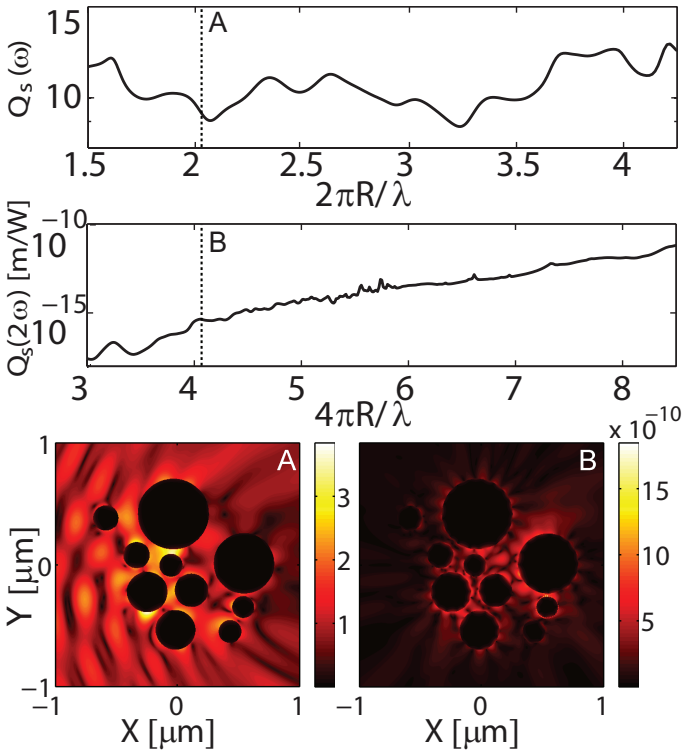

Fig. 5.12: The top two panels show the logarithmic spectra of the scattering cross section corresponding to a random distribution of metallic cylinders. The spatial profile of the amplitude of the electric field, calculated at $\lambda = 600$ nm and $\phi_0 = 0°$, is presented in the bottom panels. Left and right panels correspond to the FF and SH, respectively.

ated at the SH is stronger at the back side of the ensemble of scatterers. This surprising result can be explained by the fact that at the front side of the ensemble of cylinders the phase of the electric field is rather uniform along a plane that is parallel to the first row of cylinders, whereas deeper into the distribution of cylinders the spatial profile of the phase of the electric field becomes strongly inhomogeneous. As a result, the non-linear polarisation induced on the surface of adjacent cylinders at the front side of the ensemble of cylinders would cancel and therefore the amplitude of the generated field at the SH is small. As the field at the FF penetrates further into the distribution of cylinders it becomes strongly inhomogeneous and therefore a considerably larger amount of surface non-linear polarisation is generated. This phenomenon can be compared to that of phase matching in bulk non-linear crystals. This is an important observation, as the presence, in metamaterials, of physical effects commonly attributed to bulk materials, is one of the prerequisites of artificial media with effective non-linear optical properties.

5.6 Second Harmonic Generation in 2D Random Distributions of Metallic Cylinders

The last geometry investigated is that of a 2D random distribution of metallic cylinders. In this case, both the location of the cylinders as well as their radius are random vari-

ables, the only imposed constraint being that the cylinders do not overlap. The results corresponding to one such random ensemble of cylinders are presented in Fig. 5.12. It can be seen in this figure that, as in the case of ordered distributions of cylinders, the scattering cross section at the SH increases as the wavelength decreases. Again, this effect is explained by a stronger non-linear interaction at shorter wavelengths. In addition, the scattering spectra show fewer spectral features as compared to those corresponding to ordered distributions of cylinders, which is a direct consequence of the inhomogenous spectral broadening of the scattering resonances corresponding to single cylinders. It can, in fact, be argued that most of the spectral peaks seen in Fig. 5.12 are due to resonances associated to individual cylinders (or cylinders of similar size), the coherent contribution to the scattering spectra being smaller in this case as compared to the case of ordered distributions. Nonetheless, the interaction among the cylinders is evident in this case, too, leading to a field enhancement in the spaces between the cylinders (cavity effect) at both the FF and SH. Consequently, these structures can prove important for applications such as light localisation.

5.7 Conclusions

To conclude, in this chapter, the MSM numerical method has been used to study the properties of the electromagnetic field generated by the wave scattering by distributions of metallic cylinders, at both the FF and SH. One of the main conclusions of our analysis is that the linear and non-linear optical response of different ensembles of metallic cylinders considered in the work is strongly influenced by the excitation of SPP resonances. The physical origin of these SPP modes has also been elucidated and discussed.

The relation between the geometry and spatial distribution of the scatterers, on one hand, and, on the other hand, the overall response of the ensemble of metallic cylinders has also been analyzed. We have demonstrated that small variations in either the shape of the primary scatterers or the intrinsic structure (spatial distribution) of the ensemble of scatterers can lead to significant changes in both the far-field optical response as well as in the spatial profile of the near-field. It has been revealed that this dependency of the optical response of the ensemble of scatterers on its material and geometrical parameters is especially enhanced when SPPs are excited. A complete characterization of this relationship would represent an important step forward towards developing a comprehensive theoretical description of the effective non-linear optical properties of metamaterials. Importantly, it should be noted that the results reported in this chapter apply not only to metallic cylinders but also to other deeply scaled down nanostructures whose optical properties are similar to those of metals, such as metallic carbon nanotubes [7, 8].

Bibliography

[1] C. G. Biris and N. C. Panoiu. Second harmonic generation in metamaterials based on homogeneous centrosymmetric nanowires. *Phys. Rev. B.*, 81(19):195102, May 2010.

[2] C. I. Valencia, E. R. Mendez, and B. S. Mendoza. Second-harmonic generation in the scattering of light by an infinite cylinder. *J. Opt. Soc. Am. B*, 21(1):36–44, 2004.

[3] V. Kuzmiak, A. A. Maradudin, and F. Pincemin. Photonic band structures of two-dimensional systems containing metallic components. *Phys. Rev. B.*, 50(23):16835–16844, 1994.

[4] D. C. Marinica, A. G. Borisov, and S. V. Shabanov. Second harmonic generation from arrays of subwavelength cylinders. *Phys. Rev. B.*, 76(8):085311, August 2007.

[5] H. A. Yousif and S. Köhler. Scattering by two penetrable cylinders at oblique incidence. I. The analytical solution. *J. Opt. Soc. Am. A*, 5(7):1085–1096, July 1988.

[6] N. C. Panoiu and R. M. Osgood. Subwavelength Nonlinear Plasmonic Nanowire. *Nano Lett.*, 4(12):2427–2430, December 2004.

[7] S. A. Maksimenko, A. Lakhtakia, O. Yevtushenko, and A. V. Gusakov. Electrodynamics of carbon nanotubes: Dynamic conductivity, impedance boundary conditions, and surface wave propagation. *Phys. Rev. B.*, 60(24):17136–17149, December 1999.

[8] M. Y. Sfeir, F. Wang, L. Huang, C.-C. Chuang, J. Hone, S. P. O'brien, T. F. Heinz, and L. E. Brus. Probing electronic transitions in individual carbon nanotubes by Rayleigh scattering. *Science*, 306(5701):1540–1543, November 2004.

Chapter 6

Computational Analysis of Linear and Non-linear Optical Modes of Plasmonic Cavities

6.1 Introduction

Amongst the applications of localised SPPs discussed in the previous chapters, several were related to the strong field enhancement that is generated when SPPs are resonantly excited. For example, previous work has shown that plasmonic nanostructures can be used to significantly enhance the optical absorption (efficiency) of solar cells, detectors, and other photovoltaic devices [1–5], as well as subwavelength, all-optical control of the optical power flow in active nanodevices [6, 7]. Moreover, because of the evanescent character of localized SPPs, they are ideal tools for achieving subwavelength confinement of the optical field, and as such, SPPs can be instrumental in designing ultra-compact devices, such as nanolasers or laser arrays [8–11] and optical microcavities [12–15]. In this connection, a central issue is to design plasmonic structures which support localized SPPs with low optical losses (modes with large Q factor). A promising approach to address this challenge, described in this chapter, is to reduce the radiative losses by employing cavity-shaped plasmonic structures rather than plasmonic nanoparticles.

In this chapter the characteristics of linear and non-linear localised SPPs excited upon the interaction of optical pulses with plasmonic structures made of two-dimensional (2D) distributions of metallic nanowires will be presented. As before, this investigation is based on the multiple scattering matrix algorithm for calculating the field dynamics and the spectral characteristics of the optical field, at both the FF and the SH. In particular, the dependence of the main parameter characterizing the localized SPP modes, namely, the Q factor, on the structure and shape of the plasmonic cavity is investigated. Unlike the previous chapter, in which we described the spectral opti-

cal response of plasmonic nanostructures, in this chapter we analyze *via* time-domain techniques the optical properties of plasmonic cavities. This study reveals the existence at the SH of two markedly different types of plasmon resonances, namely, geometry independent multipole plasmon modes, which correspond to the excitation of weakly interacting modes of single cylinders, and geometry dependent plasmonic cavity modes. In addition, we will show that the main parameter characterizing the cavity modes, namely, the Q factor, strongly depends on the structure and shape of the cavity. The results suggest that by carefully designing the system geometry, specifically, the separation distance between the scatterers, the radiative losses can be greatly reduced, thus being possible to design plasmonic cavities with extremely large Q factor [16, 17].

6.2 Optical Modes of Plasmonic Cavities

In this section we describe how the MSM method can be applied to investigate the physical characteristics of linear and non-linear localized SPP modes excited by sub-picosecond pulses upon their interaction with plasmonic nanocavities. In particular, we explore the relation between the geometry and material parameters of the plasmonic cavities and the main optical properties of the localized SPP modes. The presentation of the main results will focus on the optical properties of the localized modes excited at the SH, as the main conclusions derived in this case also apply to the modes observed at the FF. In addition, since there is no incoming pulse at the SH, some physical quantities characterizing the localized SPP modes, such as their Q factor, can be much easier calculated if the optical field at the SH is analyzed. This approach can also be relevant for a series of potential technological applications, such as sensing or optical detection, as the optical signal generated at the SH is spectrally well separated from the incoming and scattered fields at the FF.

To begin with, in Fig. 6.1 we illustrate the generic characteristics of the linear and non-linear interaction between an incoming optical pulse and a plasmonic cavity. One convenient approach for identifying the modes of the cavity relies on the spectra of the absorption cross-section at the FF, $\sigma_a(\omega)$, and the corresponding absorption spectra at the SH, $\Sigma_a(2\omega)$. To be more specific, it is expected that at the resonance frequency of the localized SPP modes the spectra of the optical absorption presents resonances, as at these specific frequencies the interaction of the optical near-field with the metallic nanowires is enhanced.

The top panels in Fig. 6.1, which corresponds to a plasmonic cavity made of 6 Ag nanowires, whose electromagnetic properties are described by the Drude model, show that the spectra of the absorption cross sections at the FF and SH contain a series of spectral peaks. In addition, the spectral location of these peaks changes with the separation distance between adjacent nanowires, d, a variation of d of less than $100\ \mathrm{nm}$

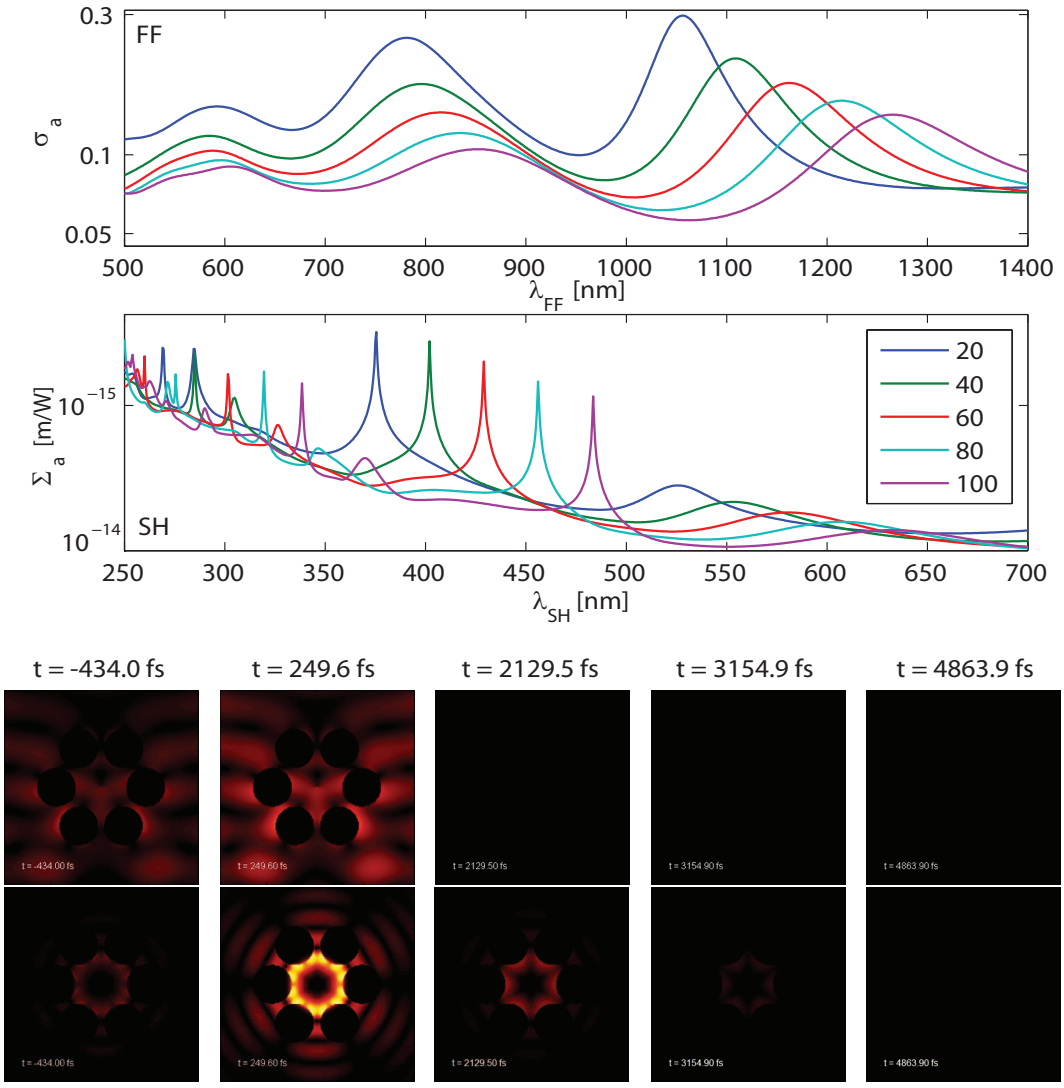

Fig. 6.1: Top panels show logarithmic plots of the absorption cross sections, calculated for a plasmonic cavity containing 6 nanowires. The legend indicates the separation distance, in nanometres. Bottom panels show snapshots of the temporal evolution of the intensity of the electric field at the FF (top) and the SH (bottom). The plasmonic cavity consists of Ag cylinders with $R = 200\ \mathrm{nm}$ *and* $d = 60\ \mathrm{nm}$*. The wavelength at the FF is* $\lambda_{FF} = 858\ \mathrm{nm}$ *and the angle of incidence is* $\phi_0 = 90°$.

leading to a spectral shift of the resonances at the FF of almost $300\ \mathrm{nm}$. Additional information pertaining to the optical properties of plasmonic cavity modes is revealed by the temporal dynamics of the optical near-field. Thus, the bottom panels in Fig. 6.1 reveal that the field at the SH remains trapped in the cavity long after the initial pulsed excitation at the FF has passed through the cavity. Since the non-linear response of the metal is assumed to be instantaneous, it can be inferred that a non-linear cavity mode with a significant lifetime and, implicitly, large Q factor, is formed in the cavity. In addition, the plasmonic character of this mode is evident from the spatial distribution of the near-field, namely, the field has large values at the metal surfaces and decays steeply towards the center of the plasmonic cavity. In what follows, a more detailed

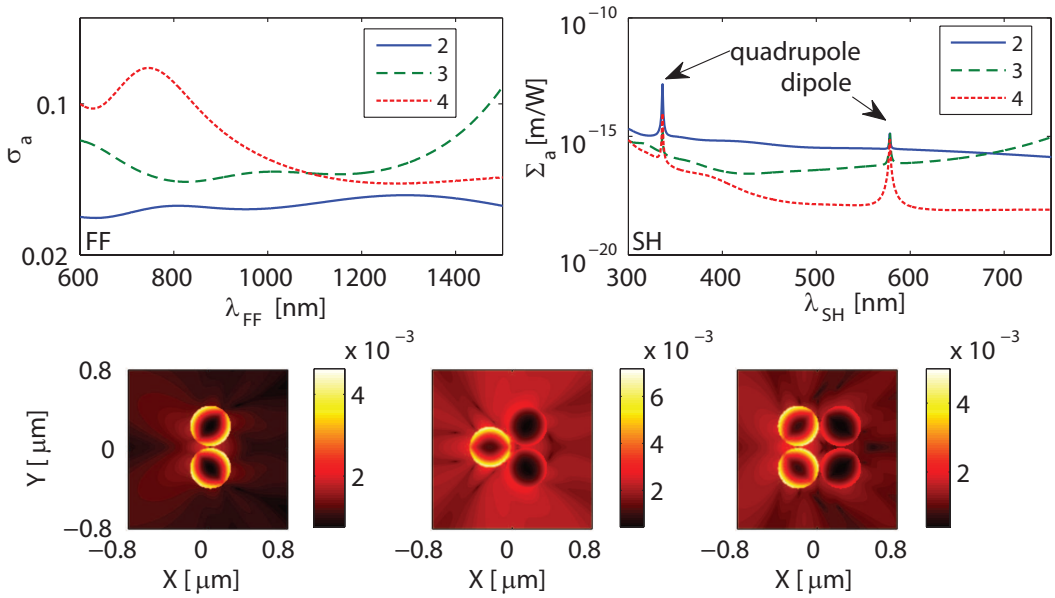

Fig. 6.2: Top panels show logarithmic plots of the absorption cross sections. The legends indicate the number of cylinders. Bottom panels present the amplitude of the electric field at the SH, for Ag cylinders with $R = 200$ nm and $d = 20$ nm, at $\lambda_{SH} = 578$ nm and $\phi_0 = 0$ (for better visualization, the fourth-order square root of the field amplitude is plotted).

analysis of these plasmonic cavity modes, as well as modes of a different physical nature, namely, multipole plasmon modes will be given.

6.2.1 Localized Plasmon Modes in Coupled Cylindrical Nanowires

To begin with, consider a series of different cavity geometries, namely, cylinder distributions containing 2, 3, and 4 cylinders. Figure 6.2 summarizes the main results pertaining to these three geometries. As in the previous case, the spectra of the absorption cross section at the SH show a series of sharp peaks, which suggests the existence of SPP modes. Importantly, the resonance frequency of these modes does not depend on the number of cylinders in the distribution of scatterers, which means that these modes are formed primarily due to the excitation of optical modes in each of the metallic nanowires. This conclusion is supported by the field distributions presented in the bottom panels of Fig. 6.2. Thus, these plots clearly show that the modes at $\lambda_{SH} = 578$ nm correspond to dipole (cut-off) modes of the nanowires. Similar field distributions, shown in Fig. 6.3, demonstrate that the resonances at smaller wavelength ($\lambda_{SH} = 336$ nm) correspond to quadrupole modes of the nanowires. Figure 6.3 also shows that, as expected, multipole resonances are not only excited in plasmonic structures containing a small number of scatterers but that in fact their existance is a generic phenomenon. However, when the number of scatterers increases the amplitude of the optical modes excited in each nanowire varies with its location in the 2D nanowire assembly, especially when the wavelength becomes comparable to the size of the plasmonic structure. It should be noted that similar resonant modes are excited at the FF,

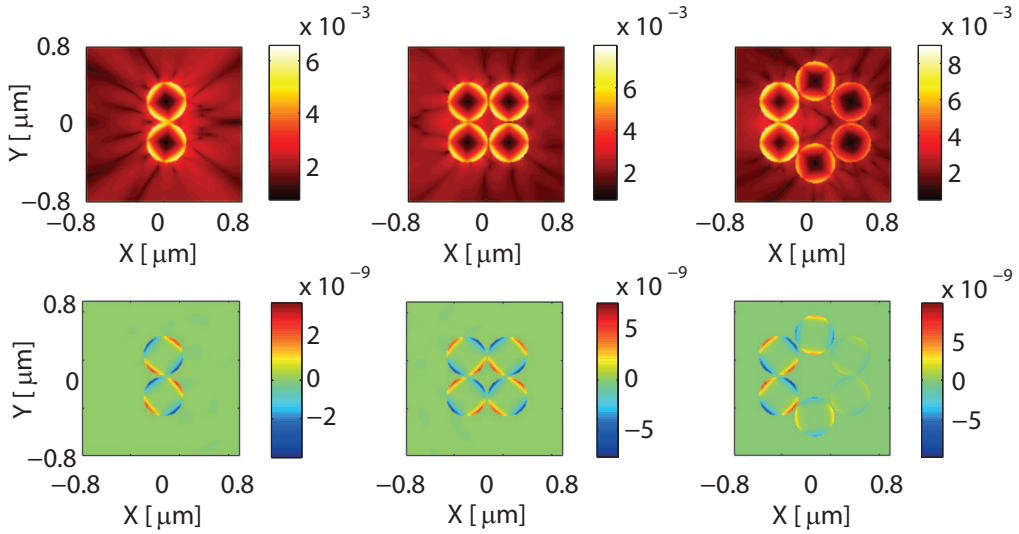

Fig. 6.3: Distribution of the amplitude of the electric field (top panels) and the real part of the magnetic field (botom panels) at the SH, calculated for three different plasmonic cavities made of Ag cylinders with $R = 200$ nm and separation distance $d = 20$ nm. The wavelength at the SH is $\lambda_{SH} = 336$ nm and $\phi_0 = 0$ (for better visualization, in the case of the electric field, the fourth-order square root of the field amplitude is plotted).

too, but they do not appear in the absorption spectra since they are "buried" in the background generated due to the absorption of the input pulse. These modes, however, can be identified as resonance peaks in the spectra of the scattering cross section [18]. Moreover, note that the SH field in the region in-between adjacent cylinders is small, which means that for this separation distance the "hybridization" effects due to the interaction between the optical modes excited in adjacent cylinders are weak.

To characterize the influence of the system geometry on the resonance frequencies of the multipole plasmon modes the absorption spectra for different values of the angle of incidence ϕ_0 and separation distance d have been determined. The dispersion plots corresponding to the absorption spectra at the SH are presented in the Fig. 6.4. These absorption spectra clearly indicate that the resonance frequencies of the multipole plasmon modes are almost independent of the system parameters, supporting therefore the conclusion that they correspond to optical modes excited in each of the metallic nanowires. More specifically, the resonance frequencies of these modes remain unchanged even if the distance between the adjacent metallic nanowires is decreased to a value as small as 1 nm. On the other hand, a significant increase of the optical absorption occurs when the separation distance becomes smaller than a few nanometers, an effect explained by the field enhancement observed in the region separating adjacent nanowires. Figure 6.4 also shows that the spectral width of the resonances varies with the angle of incidence ϕ_0. This dependence suggests that, as expected, the strength of the interaction between the input wave and the plasmonic structure and, consequently, the magnitude of the field generated at the SH, changes with the angle of incidence.

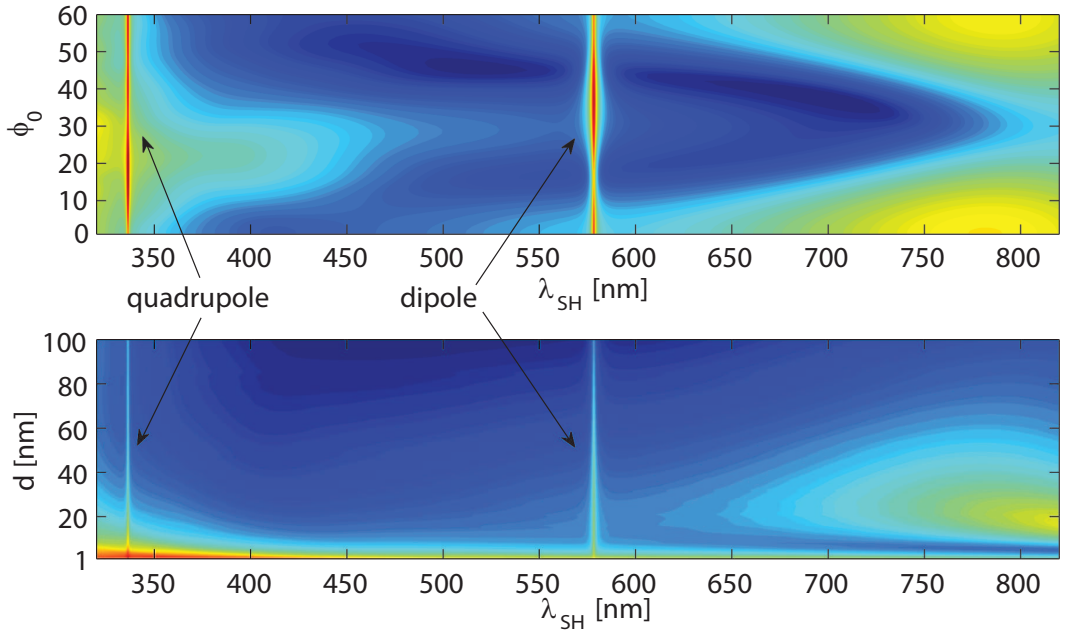

Fig. 6.4: Logarithmic plots of absorption cross section spectra at the SH vs. the angle of incidence ϕ_0 (top) and separation distance d (bottom), determined for a three-cylinder geometry. The top and bottom panels correspond to $d = 60$ nm and $\phi_0 = 0$, respectively.

In addition, it can be seen from Fig. 6.4 that as the separation distance between the nanowires increases the width of the spectral resonances decreases, and effect that is explained by the fact that the strength of the coupling between the modes excited in adjacent nanowires decreases with the separation distance.

6.2.2 Plasmonic Cavity Modes

While the analysis of localized multipole plasmon modes can provide a valuable insight into the contribution of each individual scatterer to the overall optical response of the plasmonic structure, it does not reveal the complete picture of the interaction between optical pulses and plasmonic cavities. To be more specific, our analysis reveals that plasmonic structures containing a larger number of metallic nanowires support additional plasmonic modes, which have a different physical origin as compared to that of the multipole plasmon modes. In order to illustrate this conclusion, Fig. 6.5 presents the absorption spectra, at both the FF and the SH, of cavity-shaped plasmonic structures containing 4, 6, and 8 metallic nanowires. As in the previous cases these spectra present a series of spectral peaks, which correspond to resonances of the plasmonic system. By inspecting the field profiles corresponding to these spectral peaks we found that besides the multipole plasmon modes similar to those supported by plasmonic structures with a smaller number of metallic nanowires there are additional, markedly different type of modes, which are called plasmonic cavity modes. These localized plasmon modes are formed due to the coherent response of the whole cavity. For example, as expected, in the case of the four-cylinder cavity the absorption spectrum at the SH presents two

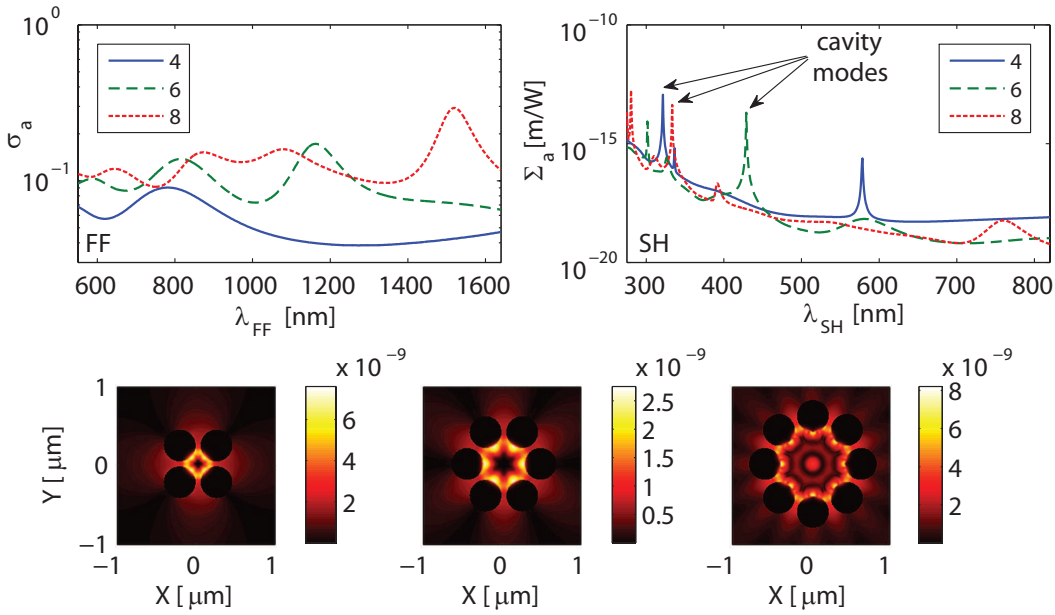

Fig. 6.5: Top panels show logarithmic plots of the absorption cross section at the FF and the SH. The legend indicates the number of cylinders forming the plasmonic cavity. Bottom panels present the distribution of the amplitude of the electric field at the SH, for Ag cylinders with $R = 200$ nm *and separation distance* $d = 60$ nm*. From left to right, the wavelength at the SH is* $\lambda_{SH} = 321$ nm, $\lambda_{SH} = 429$ nm, *and* $\lambda_{SH} = 333$ nm.

resonance peaks at $\lambda_{SH} = 578$ nm and $\lambda_{SH} = 336$ nm, spectral peaks that correspond to the dipole and quadrupole plasmon modes, respectively. The absorption spectra at the SH have, however, additional resonance peaks at $\lambda_{SH} = 321$ nm, $\lambda_{SH} = 429$ nm, and $\lambda_{SH} = 333$ nm. Since the resonance wavelength changes significantly with the number of nanowires forming the plasmonic cavity, it can be concluded that these optical modes are determined by the coherent response of the whole structure. The field profiles presented in Fig. 6.5 further support this conclusion, by showing that at the corresponding resonance wavelengths the optical field is not confined only to the region surrounding each nanowire but spreads inside the plasmonic cavity.

It is important to point out that the plasmonic cavity modes investigated here are similar to whispering-gallery modes recently observed in plasmonic structures with a different geometry [8], the main difference being that in this case, the angular momentum of the plasmonic cavity modes is equal to zero. Indeed, the angular momentum of the incident beam is zero and therefore the angular momentum of the excited modes must be zero, too. One additional important feature of the plasmonic cavity modes presented in Fig. 6.5 is that they do not appear as resonances in the scattering cross section spectra. Therefore, they are *dark-plasmon modes* that do not couple with the radiation continuum [19], and as a result the corresponding radiative losses are suppressed. Nevertheless, in the case presented here, these modes are excited *via* the non-linear polarisation generated at the SH, which acts as localized dipole sources. These results suggest that the non-linear polarisation at the SH can be used to excite subradiant (low

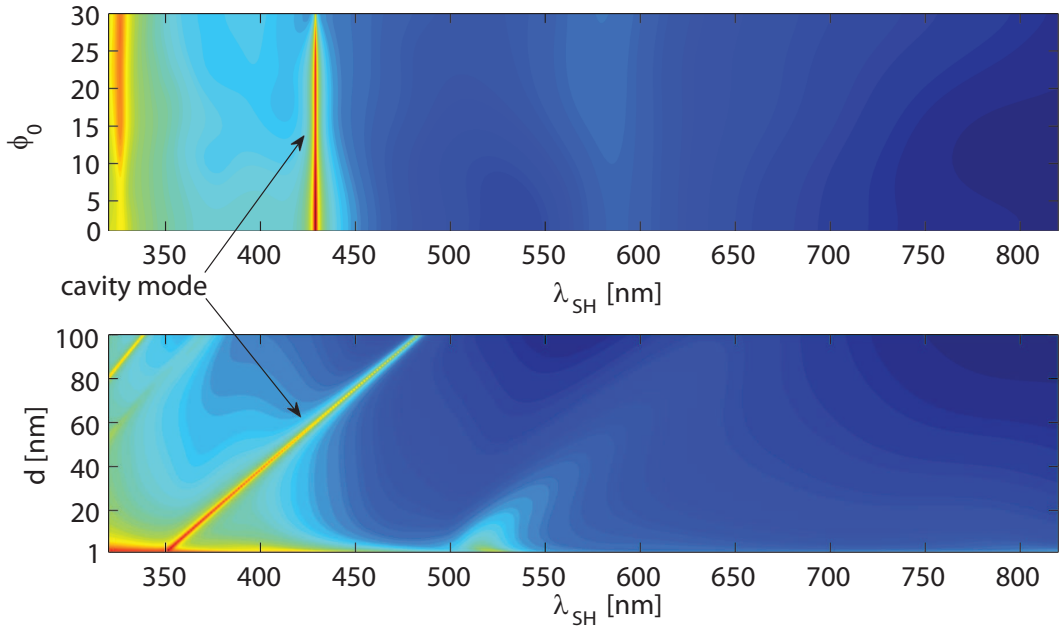

Fig. 6.6: Logarithmic plots of absorption cross section spectra at the SH vs. the angle of incidence ϕ_0 (top) and separation distance d (bottom), determined for a hexagonal geometry. The top and bottom panels correspond to $d = 60$ nm and $\phi_0 = 0$, respectively.

loss) propagating modes formed in chains of metallic nanoparticles, *via* the near-field resonant coupling of single-particle dark-plasmon modes. As will be shown in the next section, the suppression of the radiative losses also leads to a considerable increase of the lifetime of the plasmonic cavity modes and, consequently, makes it possible to design plasmonic cavities with very large Q factor.

As can be seen in Fig. 6.2, for a separation distance of $d = 20$ nm the four-cylinder cavity does not have a plasmonic cavity mode but such a mode exists for $d = 60$ nm. This observation provides further evidence that the characteristics of the plasmonic cavity modes are strongly influenced by the geometry of the cavity. In order to explore this dependence in more detail, we focus in what follows on the optical properties of the plasmonic cavity modes formed by placing metallic nanowires at the corners of a hexagon. In making this choice we were primarily guided by the fact that the cavity modes of this structure are very well defined and, as will be shown in the next section, they have a very large Q factor.

Because the dispersion spectra of the absorption cross section represent a powerful tool for investigating the properties of localized SPP modes, these spectra have been calculated for the hexagonal plasmonic cavity. The results, plotted in Fig. 6.6, provide further insight into the specific properties of plasmonic cavity modes. As expected, because these modes do not depend on the optical coupling between the incoming wave and the plasmonic cavity, they are independent on the angle of incidence ϕ_0. On the other hand, the separation distance between adjacent cylinders does have a notable effect on the spectral location of the resonance wavelength of the plasmonic cavity

modes. Thus, the resonance wavelength of the cavity mode increases almost linearly with the separation distance, a wavelength shift of almost $150\ \mathrm{nm}$ being observed when the separation distance changes by about $100\ \mathrm{nm}$. In addition, it can be seen that, as in the case of multipole plasmon modes, the spectral width of the resonance decreases as d increases; however, as will be demonstrated later, in the case of plasmonic cavity modes this behavior is determined by the interplay between the radiative and absorption losses. As the next section will show, other parameters characterizing the plasmonic cavity modes, such as the Q factor, have a more intricate dependence on the geometry of the cavity. A general feature, however, of these modes is that their optical properties can be easily tailored by modifying the shape of the cavity. Moreover, similar to the case of plasmonic cavities containing a smaller number of metallic nanowires, high optical absorption is observed for a separation distance approaching $1\ \mathrm{nm}$. Again, this effect is attributable to the strong electromagnetic field generated at the surface of the nanowires for small inter-cylinder separation distance.

The strong dependence of the resonance frequency of the plasmonic cavity modes on the separation distance between cylinders or other geometrical and material parameters can have important applications to sensing or photovoltaic devices. To be more specific, the plasmonic cavity can be viewed as playing the role of an optical antenna that collects and concentrates into a reduced volume the signal carried by the input pulse , making it possible to increase the signal-to-noise ratio and/or the speed of a detector. These plasmonic cavities can also be employed in the design of lasers with subwavelength size, as has in fact been recently demonstrated [10, 11]. In particular, the Q factor of plasmonic cavities employed in laser applications plays a crucial role in determining the performance of such nanolasers. Consequently, in what follows the dependence of the Q factor of plasmonic cavity modes on the parameters defining the plasmonic structure will be examined in more detail.

6.2.3 Time Domain Analysis of Plasmonic Cavities

The main physical quantity that describes the temporal response of an optical mode is the Q factor or, equivalently, its lifetime. In order to calculate this important parameter that characterizes a plasmonic cavity mode, the following procedure was employed. First, the cavity is illuminated with an optical pulse of sub-picosecond duration and subsequently the optical field, at both the FF and SH, at an arbitrary location inside the cavity is recorded. If the carrier frequency of the input optical pulse is close to a resonance frequency of a plasmonic cavity mode the asymptotic temporal evolution of the optical field can be represented by an exponential dependence,

$$E(t) = E_0 e^{-\frac{\omega_r t}{Q}}, \tag{6.1}$$

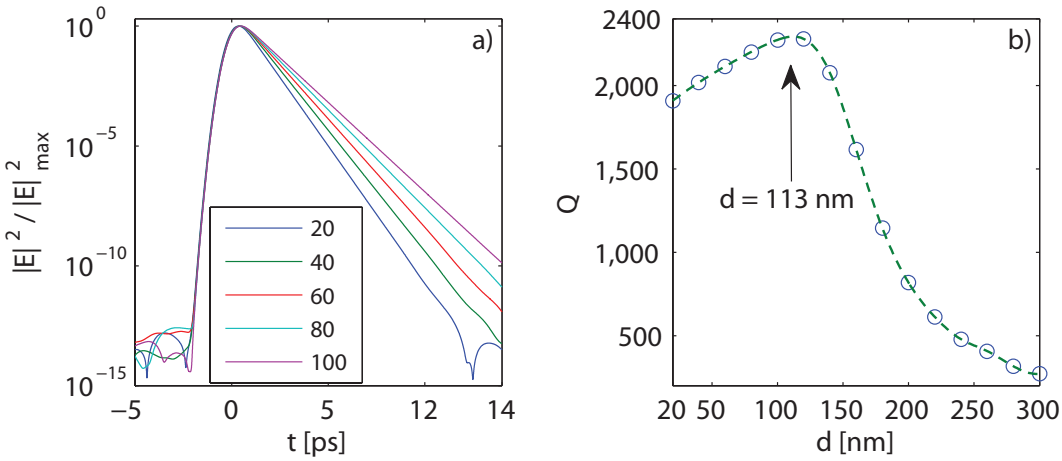

Fig. 6.7: a) Normalized electric field inside the cavity vs. time. The numbers in the legend refer to the separation distance in nanometers. b) The dependence of the Q factor on the separation distance d: circles represent simulation results whereas the dotted line is provided as a guide to the eye. The cavity consists of Ag cylinders with $R = 200$ nm and the incoming pulse has $T_0 = 283$ fs.

where ω_r is the resonance frequency of the plasmonic cavity mode. It should be noted that the relation (6.1) is independent of the location of the point in the cavity where the field is measured, the value of the carrier frequency of the input optical pulse (as long as it is close to ω_r), and the duration of the incident optical pulse, a conclusion that is fully verified by the numerical simulations. Therefore, the Q factor of the optical mode can be easily determined by calculating the slope of the line representing the linear fit of the semi-logarithmic temporal dependence of the computed field inside the cavity.

We have used this procedure and calculated the Q factor of the plasmonic cavity mode of the the hexagonal plasmonic cavity and the main results are summarized in Fig. 6.7. As expected, when the carrier frequency of the input optical pulse is close to the resonance frequency of the cavity mode the temporal evolution of the normalized field inside the cavity follows the exponential decay described by Eq. (6.1). From this asymptotic dependence the value of the Q factor of the cavity mode and the corresponding lifetime, $\tau = Q/\omega_r$ have been derived.

The calculations show that the lifetime of the plasmonic cavity mode increases from $\tau = 380.23$ fs at $d = 20$ nm to $\tau = 582.2$ fs at $d = 100$ nm. If the separation distance is further increased, the lifetime begins to decrease. Moreover, the Q factor of the optical mode follows the same dependence on the separation distance, its maximum value, $Q_{max} = 2294$, being reached for $d = 113$ nm. Note that this extremely large value is more than twice as large as the Q factor of recently observed plasmonic whispering-gallery modes [8] (although it should be mentioned that these modes were observed in three-dimensional plasmonic cavities) and more than an order of magnitude larger than the Q factor of metallic nano-particles. This dependence of the Q factor on the separation distance between the metallic nanowires is somewhat surprising be-

cause one would expect that the radiative losses increase with the separation distance and therefore the Q factor should monotonously decrease as d increases. In order to explain this apparent contradiction, it is useful to decompose the Q factor as:

$$\frac{1}{Q} = \frac{1}{Q_{abs}} + \frac{1}{Q_{rad}}, \tag{6.2}$$

where Q_{abs} is determined by the absorption in the metallic nanowires and Q_{rad} is due to radiative losses. The Q_{abs} factor can be calculated from the absorption spectra by fitting with a Lorentzian the region the spectrum corresponding to the resonance peak. Thus, $Q_{abs} = \omega_r/\Delta\omega$, where $\Delta\omega$ is the spectral width of the Lorentzian. By using this procedure we found that for small values of the separation distance, $Q_{abs} \approx Q$, which means that the losses of the plasmonic cavity mode are primarily due to the absorption loss in the metal. This result also supports the conclusion that the plasmonic cavity mode is a dark-plasmon mode, whose radiative losses are suppressed. As d increases, the field confinement decreases, and therefore the absorption losses decrease. Consequently, the Q factor of the optical mode increases. If the separation distance is further increased, the optical field begins to leak more easily out of the cavity, the cavity effects become weaker, and consequently the radiative losses start to dominate. As a result, the Q factor of the mode begins to decrease. This scenario predicts that there is a separation distance for which the Q factor reaches a maximum value, a prediction which is fully verified by the results presented in Fig. 6.7b. This analysis also suggests that by minimizing the optical losses associated with plasmonic cavity modes it is possible to optimize considerably the efficiency of these plasmonic cavities, a property that can have important implications to the development of efficient subwavelength nanolasers.

6.3 Conclusions

In conclusion, in this chapter, the main optical properties of linear and non-linear localized SPP modes excited upon the interaction between ultra-short optical pulses and nanocavities made of metallic nanowires were presented. The numerical analysis, based on the MSM formalism, has revealed that plasmonic cavities support two distinct types of localized SPP modes, namely, multipole plasmon modes that are the result of the hybridization of coupled plasmon modes supported by each metallic nanowire of the plasmonic cavity, and plasmonic cavity modes, which can be viewed as the coherent optical response of the entire assembly of metallic nanowires. We have also demonstrated that this dichotomy in the physical origin of these optical modes is responsible for their markedly different optical properties. For example, whereas the properties of the multipole plasmon modes depend almost exclusively on the size of the individual nanowires, the geometrical and material parameters of the plasmonic cavity strongly influence the characteristics of the plasmonic cavity modes. In particular, this feature

has been shown to be efective in designing plasmonic cavities with extremely large Q factors.

Large Q factors are important in applications which require the trapping of the electromagnetic field in a small volume such as, for example, in laser cavities. This is easilly achieved in our cavities due to the formation of dark-plasmon modes which do not radiate into the far field and thus lead to field enhancement inside the cavity. This effect also has potential applications in various imaging and detection techniques, as the plasmonic cavities can be used as probing devices. Moreover, the properties of these cavity modes are influenced by the background environment, due to their plasmonic nature. It thus becomes clear that this design can also be employed as a small scale sensor. In this connection, in Chapter 8, the discussion on non-linear dark-plasmon cavity modes will be extended to include their application to sub-wavelength bio-chemical sensors.

Bibliography

[1] T. Ishi, J. Fujikata, K. Makita, T. Baba, and K. Ohashi. Si Nano-Photodiode with a Surface Plasmon Antenna. *Jpn. J. Appl. Phys.*, 44(12):364–366, March 2005.

[2] Z. Yu, G. Veronis, S. Fan, and M. L. Brongersma. Design of midinfrared photodetectors enhanced by surface plasmons on grating structures. *Appl. Phys. Lett.*, 89(15):151116, 2006.

[3] R. D. Bhat, N. C. Panoiu, S. R. Brueck, and R. M. Osgood. Enhancing the signal-to-noise ratio of an infrared photodetector with a circular metal grating. *Opt. Express*, 16(7):4588–4596, March 2008.

[4] D. M. Schaadt, B. Feng, and E. T. Yu. Enhanced semiconductor optical absorption via surface plasmon excitation in metal nanoparticles. *Appl. Phys. Lett.*, 86(6):063106, 2005.

[5] N. C. Panoiu and R. M. Osgood. Enhanced optical absorption for photovoltaics via excitation of waveguide and plasmon-polariton modes. *Opt. Lett.*, 32(19):2825–2827, October 2007.

[6] N. C. Panoiu and R. M. Osgood. Subwavelength Nonlinear Plasmonic Nanowire. *Nano Lett.*, 4(12):2427–2430, December 2004.

[7] F. Ye, D. Mihalache, B. Hu, and N. C. Panoiu. Subwavelength vortical plasmonic lattice solitons. *Opt. Lett.*, 36(7):1179–1181, 2011.

[8] B. Min, E. Ostby, V. Sorger, E. Ulin-Avila, L. Yang, X. Zhang, and K. Vahala. High-Q surface-plasmon-polariton whispering-gallery microcavity. *Nature*, 457(7228):455–458, January 2009.

[9] M. A. Noginov, G. Zhu, A. M. Belgrave, R. Bakker, V. M. Shalaev, E. E. Narimanov, S. Stout, E. Herz, T. Suteewong, and U. Wiesner. Demonstration of a spaser-based nanolaser. *Nature*, 460(7259):1110–1113, 2009.

[10] M. P. Nezhad, A. Simic, O. Bondarenko, B. Slutsky, A. Mizrahi, L. Feng, V. Lomakin, and Y. Fainman. Room-temperature subwavelength metallo-dielectric lasers. *Nature Photon.*, 4(6):395–399, 2010.

[11] K. Yu, A. Lakhani, and M. C. Wu. Subwavelength metal-optic semiconductor nanopatch lasers. *Opt. Express*, 18(9):8790–8799, 2010.

[12] V. Berger. Second-harmonic generation in monolithic cavities. *J. Opt. Soc. Am. B*, 14(6):1351–1360, 1997.

[13] D. Gusev, I. Soboleva, M. Martemyanov, T. Dolgova, a. Fedyanin, and O. Aktsipetrov. Enhanced second-harmonic generation in coupled microcavities based on all-silicon photonic crystals. *Phys. Rev. B.*, 68(23):1–4, December 2003.

[14] G. Kozyreff, J. L. Dominguez Juarez, and J. Martorell. Whispering-gallery-mode phase matching for surface second-order nonlinear optical processes in spherical microresonators. *Phys. Rev. A*, 77(4):043817, April 2008.

[15] Y. Xu, M. Han, A. Wang, Z. Liu, and J. Heflin. Second Order Parametric Processes in Nonlinear Silica Microspheres. *Phys. Rev. Lett.*, 100(16):1–4, April 2008.

[16] C. G. Biris and N. C. Panoiu. Nonlinear pulsed excitation of high-Q optical modes of plasmonic nanocavities. *Opt. Express*, 18(16):17165–17179, August 2010.

[17] C. G. Biris and N. C. Panoiu. Excitation of linear and nonlinear cavity modes upon interaction of femtosecond pulses with arrays of metallic nanowires. *Appl. Phys. A-Mater.*, 103(3):863–867, January 2011.

[18] C. G. Biris and N. C. Panoiu. Second harmonic generation in metamaterials based on homogeneous centrosymmetric nanowires. *Phys. Rev. B.*, 81(19):195102, May 2010.

[19] M. Liu, T.-W. Lee, S. Gray, P. Guyot-Sionnest, and M. Pelton. Excitation of Dark Plasmons in Metal Nanoparticles by a Localized Emitter. *Phys. Rev. Lett.*, 102(10):107401, March 2009.

Chapter 7

Non-linear Whispering Gallery Modes in Plasmonic Cavities

7.1 Introduction

Unlike the electromagnetic modes investigated in Chapter 6, there is a different type of optical modes supported by plasmonic cavities known as *whispering gallery modes* (WGMs). Whispering gallery modes are closed circular beams which carry angular momentum. Specifically, these cavity modes possess a non-zero component of the electromagnetic angular momentum vector and, as a result, can propagate along curved surfaces. Whispering gallery modes were first observed in the propagation of sound over a curved gallery surface (where the term "whispering gallery" stems from). It soon became clear that the same physical effect can also occur in electromagnetic waves and, today, several resonator designs exhibiting WGMs have been proposed [1]. These designs include dielectric resonators [2, 3], plasmonic devices [4, 5] and non-linear structures [6], among others. Several methods for coupling WGMs in optical structures have been investigated including free-beam coupling (which is not efficient in the case of low device volumes), coupling using prisms and waveguides or directional coupling via asymmetries and defects in the cavity design [1]. Also, as will be shown in this chapter, WGM coupling can be achieved in plasmonic cavities by using multipole Bessel excitations which carry angular momentum.

Whispering gallery modes have several important properties such as complex scattering and absorption spectra, tuneable electromagnetic response, low mode volume and very high Q factors (*e.g.* up to $Q = 10^{10}$ in some crystalline resonators) [1, 7]. Consequently, WGMs can be employed to the design of efficient lasing cavities [8–10], optical filters [11], spectroscopic and mechanical sensors [12] or slow-light devices [13]. Whispering gallery modes can also be used to transfer angular momentum to nanoscale objects, which has tremendous potential applications in optical manipulation at sub-wavelength scales [14]. Furthermore, in connection to the idea of effective proper-

ties in metamaterials, the mode orders of WGMs can be thought as the optical equivalent of the classical atomic orbitals [15]. Thus, WGM supporting structures could be used to develop photonic meta-atoms and meta-molecules [16]. Finally, because of the high Q factors and high field enhancement observed in WGM cavities, such devices are ideal candidates for non-linear optics as they can support strong non-linear effects at low input power.

To better understand the properties of WGMs, let us consider the relation between the energy of the electromagnetic field and its angular momentum. It is well known that for a given electromagnetic field distribution, the electromagnetic field momentum density $\mathbf{p}$ can be written as:

$$\mathbf{p} = \frac{1}{c^2}\mathbf{E} \times \mathbf{H}. \tag{7.1}$$

Based on Eq. (7.1) we can define the angular momentum density $\mathbf{l}$ of the fields as:

$$\mathbf{l} = \mathbf{r} \times \mathbf{p}, \tag{7.2}$$

which becomes:

$$\mathbf{l} = \frac{1}{c^2}\mathbf{r} \times (\mathbf{E} \times \mathbf{H}). \tag{7.3}$$

Integrating Eq. (7.3) over all space yields the total angular momentum of an electromagnetic field, $\mathbf{L}$:

$$\mathbf{L} = \frac{1}{c^2}\int \mathbf{r} \times (\mathbf{E} \times \mathbf{H}) d\mathbf{r}. \tag{7.4}$$

It is worth noting here that the angular momentum density in Eq. (7.3) can also be expressed in terms of the Poynting vector $\mathbf{S}$ as:

$$\mathbf{l} = \frac{1}{c^2}\mathbf{r} \times \mathbf{S}, \tag{7.5}$$

given that $\mathbf{S} = \mathbf{E} \times \mathbf{H}$. Equation (7.5) has an important consequence in the plane wave regime. For any given plane wave propagating in an homogeneous isotropic medium, the energy flux $\mathbf{S}$ is always oriented along the direction of propagation, so that the vector product in Eq. (7.5) will always be zero. In other words, a plane wave does not carry angular momentum [17]. Consequently, in order to form WGMs in plasmonic cavities, a plane wave excitation is not sufficient.

In this chapter it will be demonstrated that linear and non-linear whispering gallery modes can be excited in cavities made of metallic cylinders by using a multipole excitation which can couple to modes carrying angular momentum [18]. The intricate phenomena which lead to the coupling of the linear and non-linear components of WGMs will be discussed in detail and the effects of the geometry on the properties of the WGMs and their Q-factors will be presented.

7.2 Excitation of Whispering Gallery Modes

The structures investigated in this chapter are geometrically similar to the ones described in Chapter 6. They consist of an array of parallel cylindrical scatterers arranged in a hexagonal cavity pattern. The cylinders are assumed to be made of Au and their electromagnetic properties are described by the Lorentz-Drude model. According to the MSM formalism, the incoming wave scattered by a system can be written as a Fourier-Bessel expansion [see Eq. (3.22)]:

$$U_z^{inc}(r,\varphi) = \sum_{m=-\infty}^{\infty} a_m J_m(\kappa r) e^{im\varphi}, \tag{7.6}$$

where the coefficients a_m are determined by the particular form of U_z^{inc}. In order to obtain an excitation carrying angular momentum, one component of the incoming field, denoted by $m = m_0$, is chosen as the only non-zero term in expansion (7.6). In what follows, the notation $m_0 = \infty$ denotes a plane wave which includes all of the terms in Eq. (7.6).

This choice of excitation can be explained by considering the angular momentum density given by Eq. (7.3). Thus, the longitudinal (z)-component, l_z, of the angular momentum density can be written as:

$$l_z = -\frac{1}{c^2} r(\mathbf{E} \times \mathbf{H}^*)_\varphi. \tag{7.7}$$

Assuming the case of TE polarisation, the angular momentum corresponding to a term with $m = m_0$ in Eq. (7.6) can be written as:

$$L_z = -\frac{1}{2}\frac{1}{c^2} \int\int (r E_r H_z^*)\, r\, dr\, d\varphi, \tag{7.8}$$

which becomes [see Appendix B for the expressions of the electric and magnetic field components]:

$$L_z = -\pi m_0 \mu_0 \frac{1}{\omega} |a_{m_0}|^2 \int r |J_{m_0}(\kappa r)|^2 dr. \tag{7.9}$$

Due to the asymptotic properties of the Bessel function [see Appendix D], the angular momentum, L_z, becomes infinite as $r \to \infty$.

Now, the total energy of the electromagnetic field can be found from:

$$U = \frac{1}{2}\int_V \mu_0 |H_z|^2 d\mathbf{r} = \pi \mu_0 |a_{m_0}|^2 \int r |J_{m_0}(\kappa r)|^2 dr. \tag{7.10}$$

As for the case of the angular momentum, the total energy, U, becomes infinite in the far field, as $r \to \infty$, which is a property shared with plane waves. From Eqs. (7.9) and

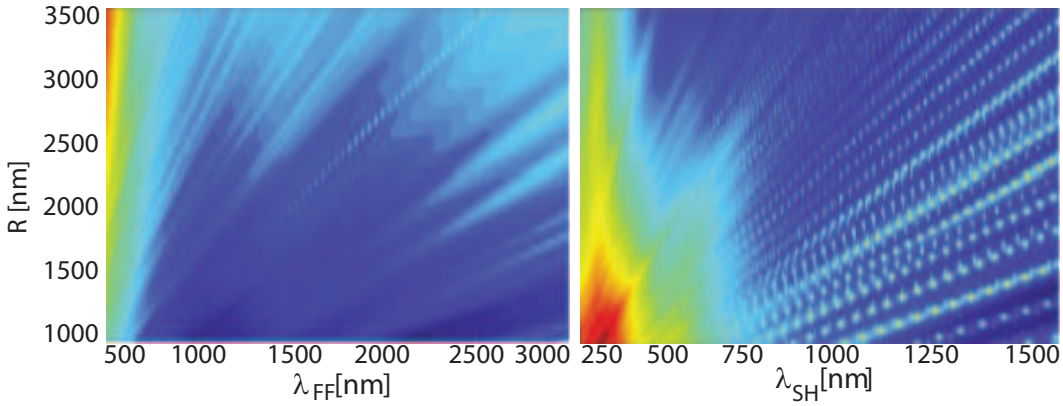

Fig. 7.1: Absorption cross section as a function of radius R and wavelength for a six cylinder cavity. The cylinder are considered to be made of Au and separated by $d = 10$ nm. The cavity is illuminated by a plane wave.

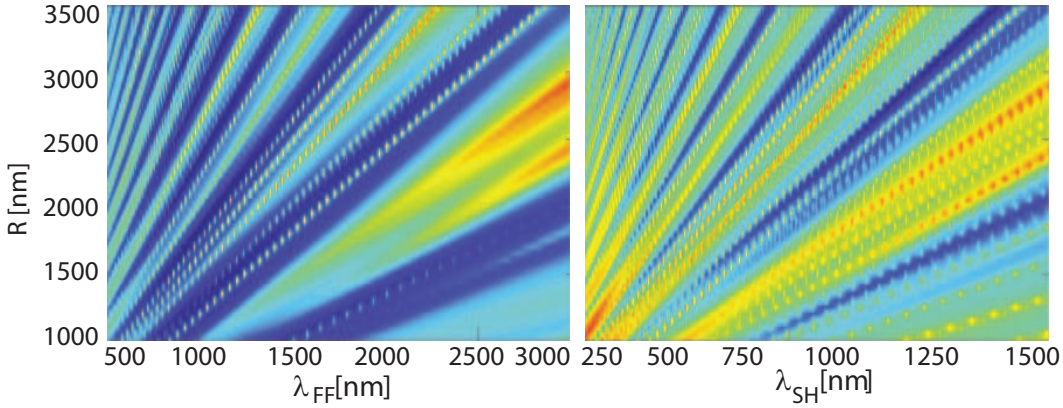

Fig. 7.2: Absorption cross section as a function of radius R and wavelength for a six cylinder cavity. The cylinder are considered to be made of Au and separated by $d = 10$ nm. The cavity is excited by a field with $m_0 = 3$.

(7.10) we can now write:

$$\frac{L_z}{U} = -\frac{m_0}{\omega}. \tag{7.11}$$

Equation (7.11) shows that the angular momentum, L_z, is proportional to the total energy, U, for a given frequency ω, with the proportionality constant being equal to m_0. Here, m_0 can be identified as the *azimuthal index* of a vortex beam of order $n = m_0$ [19]. This particular type of excitation is the equivalent of a multipole Bessel excitation located at the centre of the scattering geometry. One practical way of implementing this type of multipole excitation consists in inserting in the cavity resonant chiral molecules, which can give rise in the system to a field carrying angular momentum and, as a result, couple with whispering gallery modes.

In Chapter 6 it was shown that dark plasmon modes can form in plasmon cavities made of metallic cylinders. Because these modes do not radiate into free space, one needs to consider the absorption cross section of such structures when searching for dark plasmon resonances. Figures 7.1 and 7.2 show the absorption cross section of a cavity consisting of six Au cylinders with varying radii and separation distance $d =$

$10\ \mathrm{nm}$ for the plane wave ($m_0 = \infty$) case and the $m_0 = 3$ case, respectively. These figures illustrate a striking difference between the plane wave regime and the case of $m_0 = 3$. At the fundamental frequency, in the case of the plane wave excitation, only a few resonances are observed; however, for an excitation with $m = m_0$, several new modes are apparent in the absorption spectrum. It thus becomes clear that a multipole excitation carrying angular momentum can in fact excite new cavity modes which are not otherwise excited by a plane wave.

In the remaining part of this chapter, we will further analyse and quantify the properties of this new type of modes, show how they can be coupled to the exciting radiation and how the geometry affects their properties.

7.3 Physical Properties of Plasmonic Whispering Gallery Modes

Let us consider first, the case of a hexagonal cavity with cylinders of radius $R = 1500\ \mathrm{nm}$. Figure 7.3 shows the absorption cross section spectra of such a cavity, calculated for a plane wave case and for $m_0 = 1$ through $m_0 = 5$. As before, the TE polarisation is considered so as to include the surface second harmonic contribution of the metal. The absorption spectra confirm the findings discussed in the previous section. At the fundamental frequency there are only a few resonances in the plane wave regime; however, strong absorption peaks can be identified in the case of a multipole excitation. It is also important to note that even in this latter case, the resonances do not appear for all values of m_0, indicating that there is a complex interplay between the geometry of the cavity and the scattering effects which lead to the formation of a cavity mode. In the case of the second harmonic, there is a direct correspondence between the resonances at the FF and the peaks in the non-linear absorption spectra. This result indicates that the formation of non-linear cavity modes is a direct consequence of the strong field enhancement at the fundamental frequency. Consequently, no directly excited whispering gallery modes exist, in this spectral domain, at the SH. It can thus be said that the modes at the SH are indirectly coupled *via* the contribution of the scattered field at the FF. There are also several resonances in the non-linear absorption spectra which have no equivalent in the fundamental regime. These modes are also present in the plane wave case and will be shown to represent multipole resonances of the individual cylinders, identical to the ones discussed in Chapter 6.

To better understand the physical phenomena behind the formation of WGMs, let us consider the distribution of the total electric field inside the cavities. In addition, in order to determine the characteristics of whispering gallery modes, the profile of the phase of the electromagnetic field is also required. Because in the case of the TE polarisation, the magnetic field has only one component H_z, the phase of this component

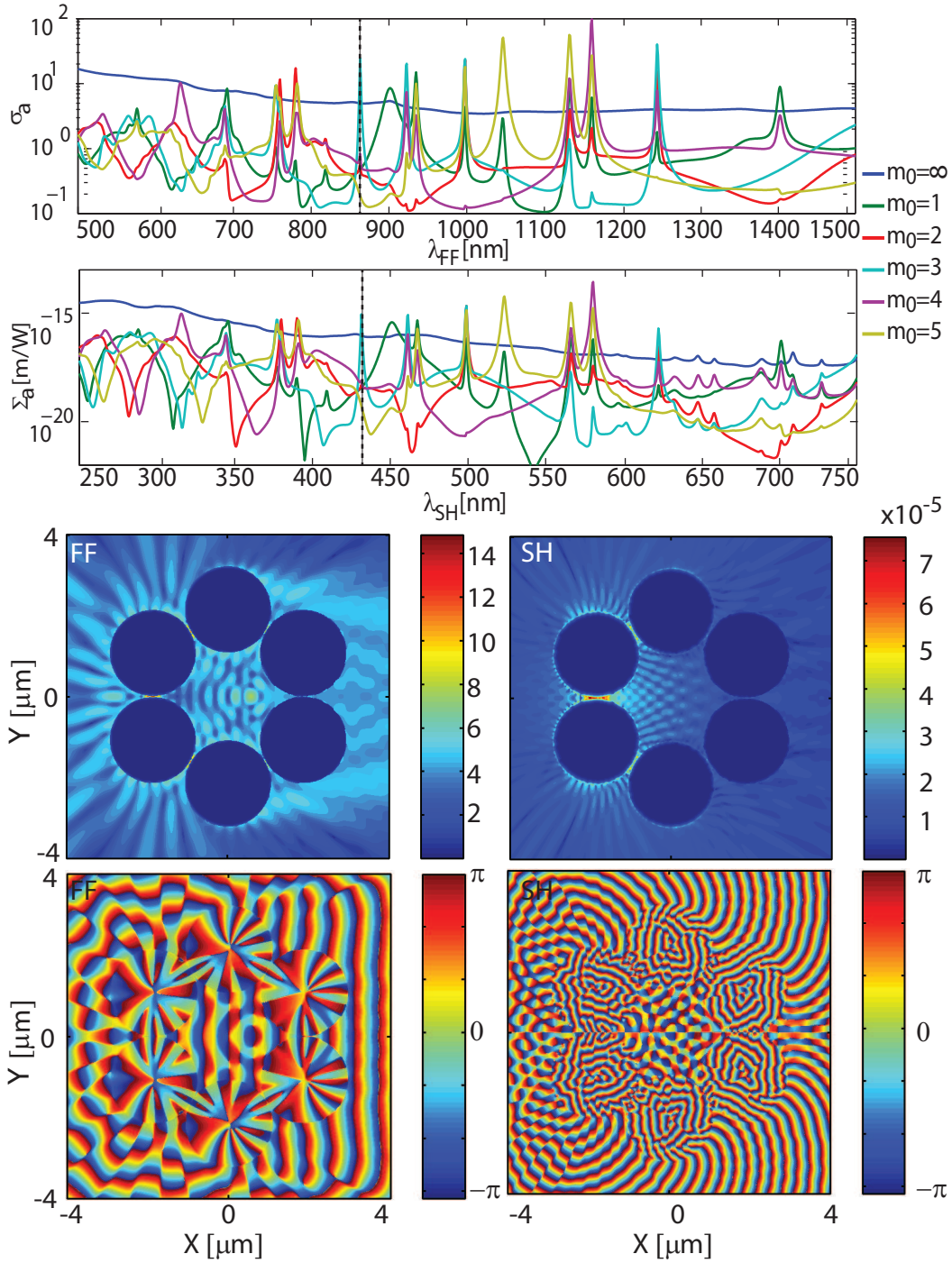

Fig. 7.3: Top panels show the logarithmic absorption cross section spectra for a hexagonal cavity with $R = 1500$ nm and $d = 10$ nm at the FF (top) and SH (botoom). Bottom panels show the spatial distribution of the second order square root of the total electric field (middle panels) and the phase of the magnetic field component H_z (bottom panels) for $m_0 = \infty$. The field profiles are calculated at $\lambda_{FF} = 863$ nm (this values is also marked by the dashed line in the top panels).

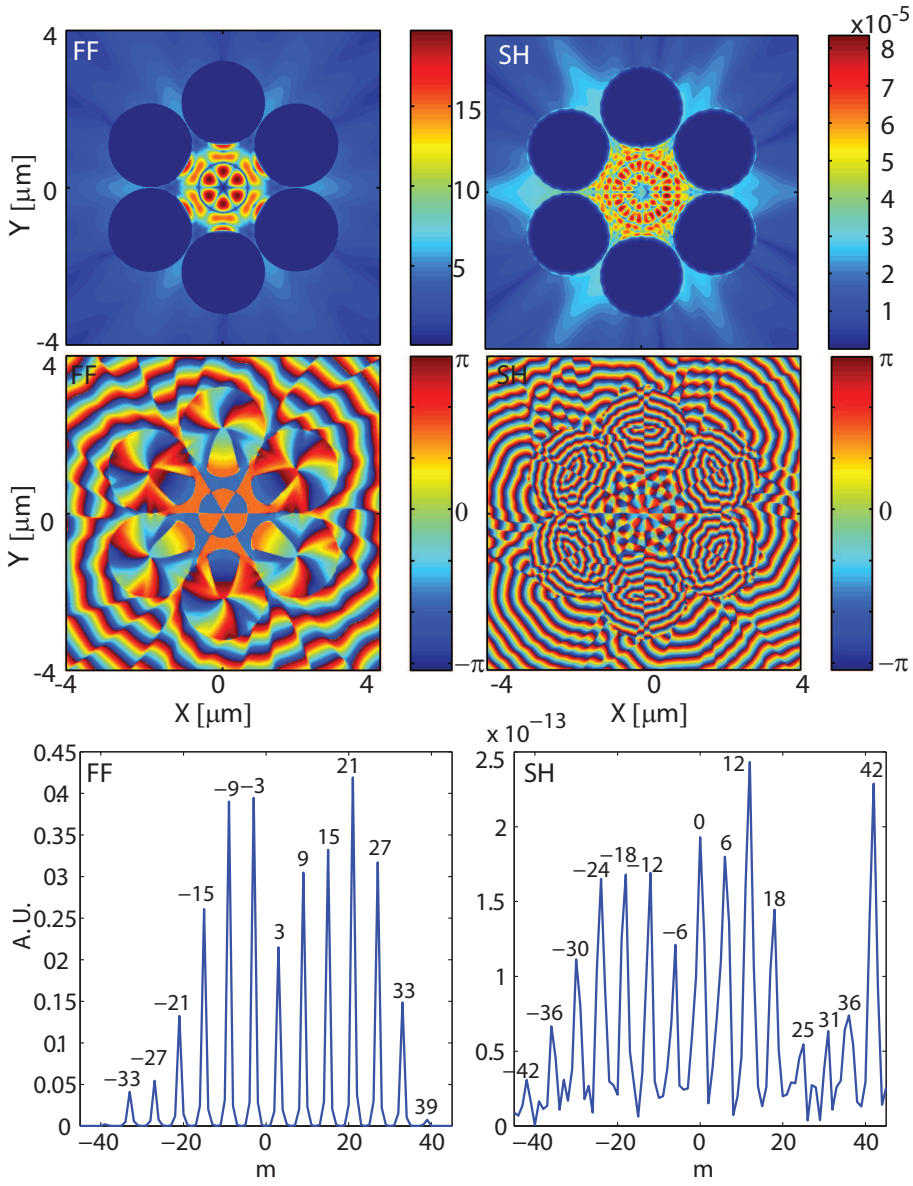

Fig. 7.4: Spatial distribution of the second order square root of the total electric field (top panels) and the phase of the magnetic field component H_z (middle panels) for $m_0 = 3$. The field profiles are calculated at $\lambda_{FF} = 863$ nm. Bottom panels show the dependence of the scattering field coefficients at the FF and the SH on the order m.

is considered. In Fig. 7.3 we plot the field profiles for a plane wave excitation with $\lambda_{FF} = 863$ nm. As suggested by the lack of an absorption peak in the absorption spectra for $m_0 = \infty$, the field profiles show no field confinement, more exactly, no cavity mode is present. This no longer holds true when the $m_0 = 3$ case is considered, at the same wavelength [see Fig. 7.4].

For $m_0 = 3$, the absorption spectrum has a strong resonance at $\lambda_{FF} = 863$ nm. The field profiles at this wavelength, presented in Fig. 7.4, reveal the nature of this resonance. Thus, the electric field clearly shows the formation of a cavity mode at both the FF and the SH. Further, the phase of the magnetic field demonstrates the formation of a

vortex-like field distribution with a central *phase singularity* in the centre of the cavity. This is a strong indication that these modes are in fact whispering gallery modes and thus carry angular momentum. Also, the phase profile exhibits six *phase dislocation lines* (*i.e.* lines across which the phase is discontinous) at the FF and twelve at the SH. The mode at the FF is of order $n = 3$ while, as expected, at the SH, $n = 6$. This is easily explained by the fact that $\lambda_{SH} = \lambda_{FF}/2$. Finally, an important question is why this mode only couples with a $m_0 = 3$ excitation and not, for example, with a plane wave. The answer to this question can be ascertained by considering the expansion coefficients of the scattered field, $\bar{b}_m$ (see Fig. 7.4). Here, $\bar{b}_m = \sum_{j=1}^{N} \bar{b}_{m,j}$ where N is the number of the cylinders and $\bar{b}_{m,j}$ are the scattering coefficients of cylinder j considered in a coordinate system centred in O. The distribution of the scattering coefficients is asymmetric, as opposed to the plane wave case, where, due to the definition of the scattering matrix $\mathbf{S}(\Omega)$, these same coefficients obey the symmetry relation given by $\bar{b}_{m,j} = \bar{b}^*_{-m,j}$. Also, the dominant terms in the distribution are all multiples of 3 at the FF and 6 at the SH. Since the order at the FF is $n = 3$, the first dominant scattering coefficient is $m = 3$ and all other subsequent dominant terms are obtained by changing the order by 6. It is also important to note that, the WGM, being a localised mode, must have the same symmetry as that of the cavity. As the cavity being investigated has hexagonal symmetry, the separation between the dominant scattering coefficients must therefore be equal to 6.

To further expand on these ideas, Fig. 7.5 present the field profiles, phase of the magnetic field and the scattering coefficients for the case $m_0 = 5$. In this case, the absorption cross section does not show a strong resonance at $\lambda_{FF} = 863\ \mathrm{nm}$, which is confirmed by the field distribution. The cavity mode that was present for $m_0 = 3$ no longer forms and the phase profile no longer has the vortex-like features. This can be easily explained by the fact that the incoming field no longer has the right symmetry needed to couple with the WGM.

As illustrated in Fig. 7.2 whispering gallery modes are affected by the system geometry, specifically, the radius of the cylinders. Nevertheless, as discussed in Chapter 6, other types of modes have similar signatures in the dispersion of the absorption spectra. To separate these resonances we now investigate the effect of the separation distance on the absorption spectra when the radius of the cylinders is kept constant. The main results of this analysis are summarised in Fig. 7.6. These absorption spectra indicate that at the FF, the modes vary with the separation distance between the nanowires. This proves that the modes in question are indeed cavity modes and are not multipole modes of the individual cylinders. In the non-linear regime, the presence of the fundamental frequency modes leads to resonances in the second harmonic absorption. However, several other modes can be observed, which are not influenced by the separation dis-

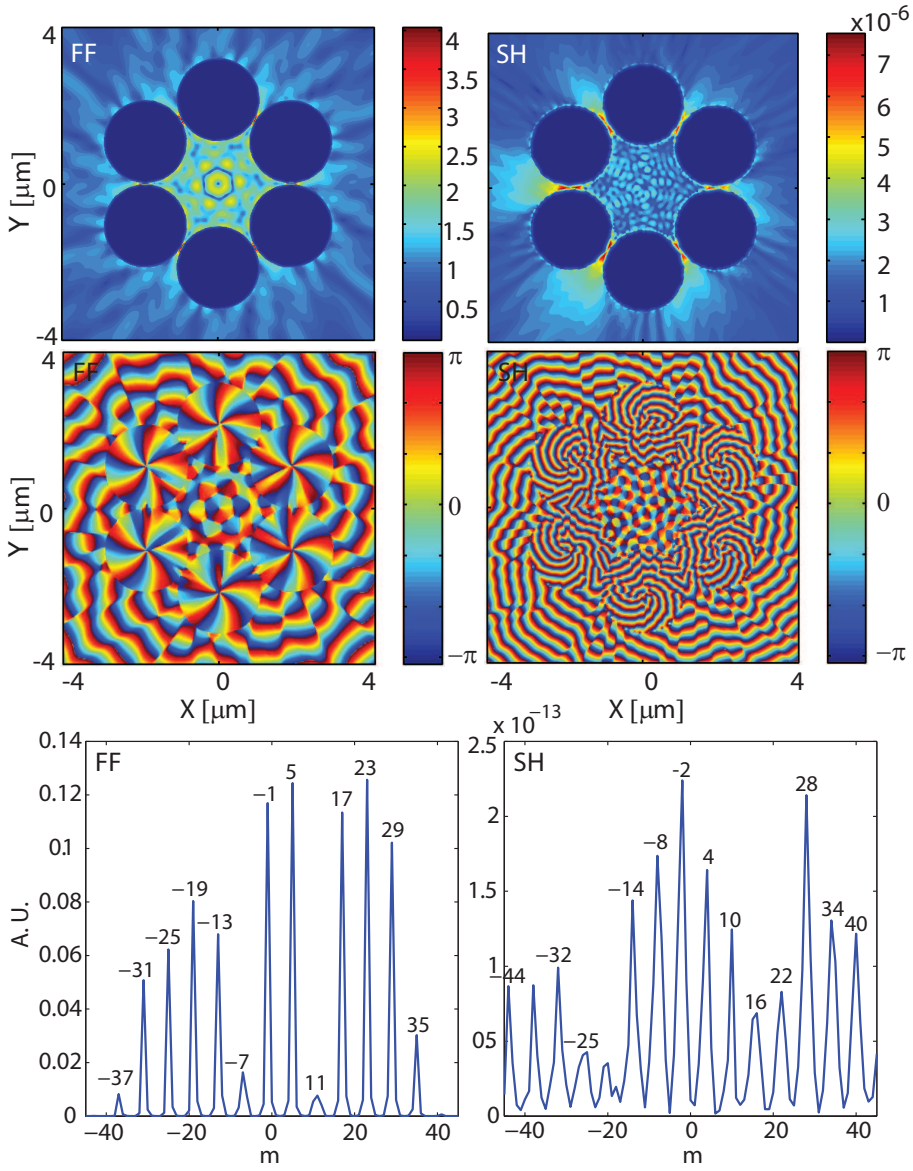

Fig. 7.5: Spatial distribution of the second order square root of the total electric field (top panels) and the phase of the magnetic field component H_z (middle panels) for $m_0 = 5$. The field profiles are calculated at $\lambda_{FF} = 863$ nm. Bottom panels show the dependence of the scattering field coefficients at the FF and the SH on the order m.

tance. It can be concluded that these resonances correspond to multipole modes and are a characteristic of the scatterers rather than the cavity. These modes can be seen in the case of plane wave excitation and since we already discussed them in Chapter 6 we no longer describe them here. Nevertheless, one can observe that for $d = 65$ nm, one of the multipole resonance occurs at the same wavelength, $\lambda_{FF} = 2304$ nm, as a non-linear whispering gallery mode.

Figure 7.7 plots the dispersion of the absorption spectra in the region of the crossing. The results show that, as expected, there is a strong resonance in the absorption spectra associated with the intersection between the two modes. The field profiles in Fig. 7.7 help to clarify the origin of this phenomena. Here, the profile of the non-linear

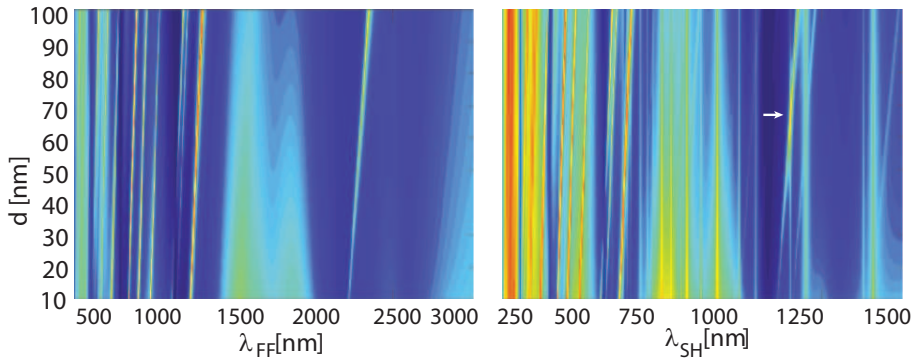

Fig. 7.6: Absorption cross section for a hexagonal cavity made of Au cylinders with fixed radius $R = 1500$ nm and varying separation distance d. The multipole excitation is considered to have $m_0 = 3$. The white arrow indicates the crossing point between a WGM and a multipole mode.

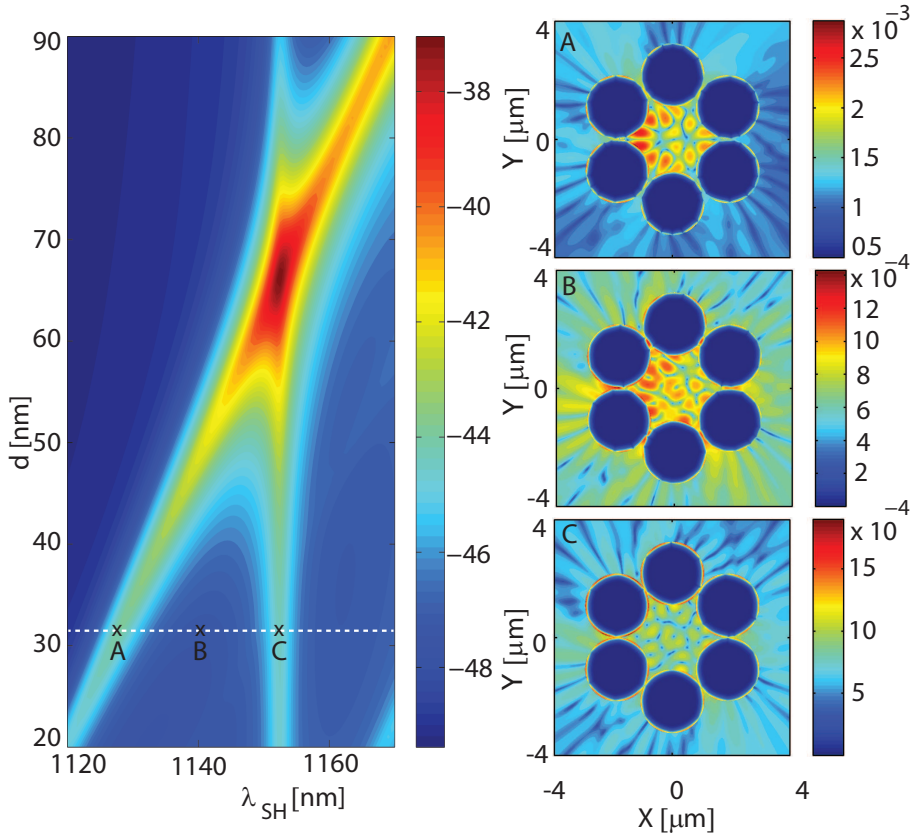

Fig. 7.7: Left panel shows absorption cross section at the SH for a hexagonal cavity with $R = 1500$ nm. The colour bar gives the natural logarithm of the physical values. Right panels show magnetic field profiles for the same cavity with $d = 32$ nm for incoming wavelengths $\lambda = 2257$ nm (A), $\lambda = 2281$ nm (B) and $\lambda = 2305$ nm(C). The multipole excitation has $m_0 = 3$ and field profiles are plotted as a second order square root of the physical values.

magnetic field H_z is shown as this particular quantity is useful in identifying the presence of multipole modes (see Chapter 6). The separation distance in all three cases is kept fixed at $d = 32\ \mathrm{nm}$. When the incoming wavelength is taken to be $\lambda = 2257\ \mathrm{nm}$, the cavity couples with a WGM at the FF which induces a non-linear mode at the SH. However, when the incoming wavelength becomes $\lambda = 2305\ \mathrm{nm}$, such that the cavity is excited at the multipole resonance frequency, the field profiles show the formation of sixth order multipole modes on the surface of the cylinders. Consequently, at a point for which $\lambda = 2281\ \mathrm{nm}$, lying between the two resonant wavelengths, neither of the two modes is excited, which is illustrated by the magnetic field profile.

Whispering gallery modes can also occur in more complex geometries, namely cavities which have a central cylindrical inclusion. As will be discussed in the next chapter, this type of cavity supports modes with a higher degree of localisation and thus allows for smaller cavity sizes. In the example illustrated in Fig. 7.8, the radius of the cylinders is $R = 800\ \mathrm{nm}$ (the radius of the inner cylinder being $R_i = 210\ \mathrm{nm}$), but the WGM occurs at a wavelength similar to that in the cases discussed in this section, specifically, $\lambda_{FF} = 700\ \mathrm{nm}$. The profiles demonstrate the formation of a whispering gallery mode at both the FF and the SH. The main conclusion pertaining to the WGMs of this type of cavity is that there is a very strong connection between the geometrical factors and the properties of the mode. This high degree of tuneability can be exploited toward designing non-linear optical devices for specific applications.

Cavity type	$m_0 = 3$	$m_0 = 9$
HEX FF	$Q = 524.2$	$Q = 554.1$
HEX SH	$Q = 525.2$	$Q = 1305$
INC FF	$Q = 145.3$	$Q = 103.1$
INC SH	$Q = 235$	$Q = 49.54$

Table 7.1: Q factors of WGMs for the hexagonal cavity (HEX) at $\lambda = 863\ \mathrm{nm}$ and the hexagonal cavity with a cylindrical inclusion (INC) at $\lambda = 700\ \mathrm{nm}$ at the FF and SH.

Finally, as previously discussed, an important property of cavity modes is their Q-factor. The Q-factors for the hexagonal cavity at $\lambda = 863\ \mathrm{nm}$ and the hexagonal cavity with a cylindrical inclusion at $\lambda = 700\ \mathrm{nm}$ were calculated. The Q-factors where found by using a Lorentzian fit of the absorption cross section peaks and using the definition $Q = \omega_0/\delta\omega$, where ω_0 is the resonance frequency of the mode and $\delta\omega$ is the width of the resonance. The results are given in Table 7.1. The results validate our conclusions that WGMs can only couple with multipole excitations with certain values of m_0. As a result, the highest Q-factors are given here, for both geometries, when $m_0 = 3$ and $m_0 = 9$, which shows the same pattern of distribution of the scattering coefficients. The dominant mode in the case of the hexagonal cavity has $Q = 1305$, which is an order of magnitude higher than the highest Q-factor of the cavity with a cylindrical in-

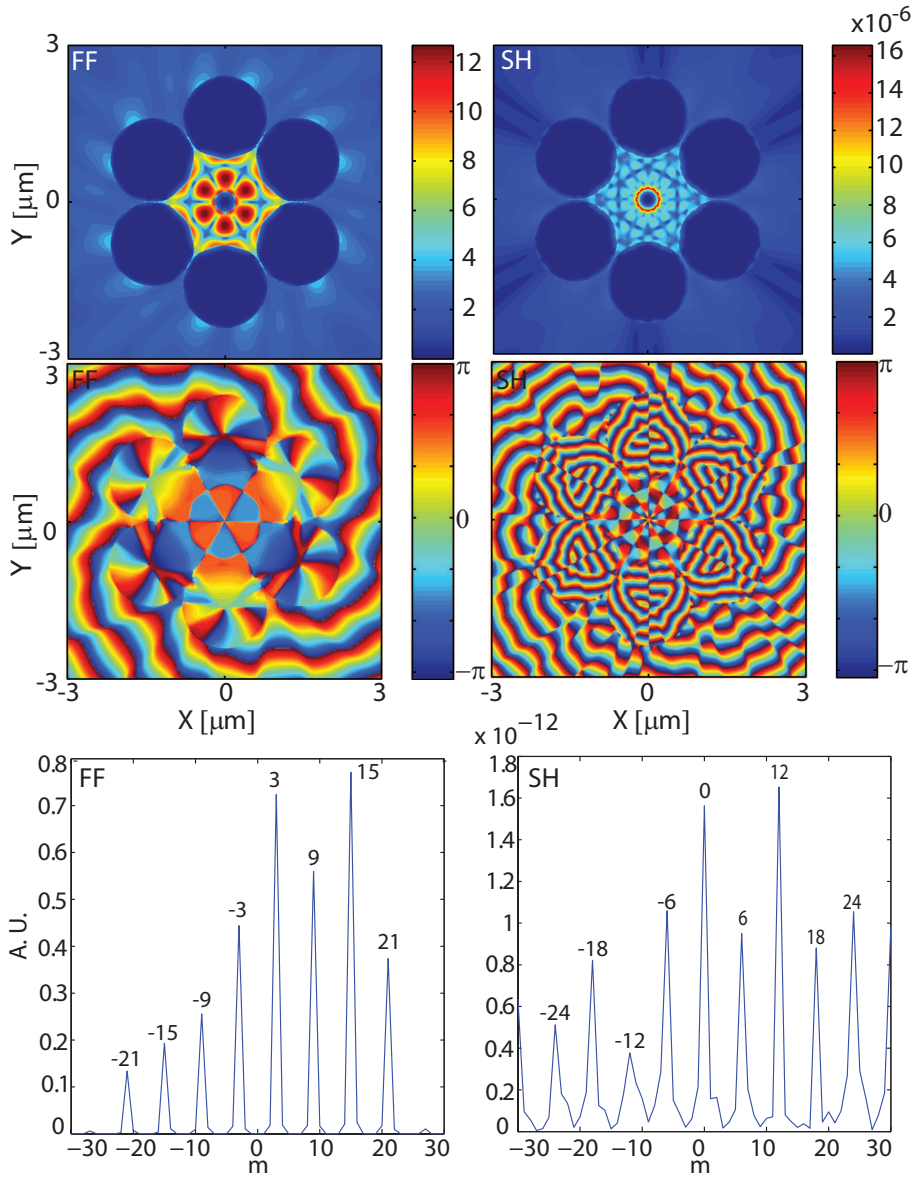

Fig. 7.8: Spatial distribution of the second order square root of the total electric field (top panels) and the phase of the magnetic field component H_z (middle panels) for $m_0 = 3$. The field profiles are calculated at $\lambda_{FF} = 863$ nm. Bottom panels show the dependence of the scattering field coefficients at the FF and the SH on the order m. The geometry consists of a hexagonal cavity of cylinders with $R = 800$ nm and a central cylindrical inclusion with $R_i = 210$ nm. The profiles are show for $\lambda_{FF} = 700$ nm.

clusion. Consequently, while the latter geometry allows for smaller devices, the former gives higher quality factors. It is thus possible to see the importance of being able to tailor the structure to obtain the best possible design for each specific application. It is important to note that no effort has been made here to tailor the non-linear plasmon cavity design and thus, whispering gallery modes with much higher Q-factors could be achievable. The absorption losses which are tied to the presence of metallic structures in this design significantly reduce the maximum achievable Q factor compared to, for example, dielectric resonators. Nevertheless, the effects of plasmon surface resonances

on the tight field confinement and enhancement in metallic cavities means that our design has significant advantages in enhancing the non-linear properties of whispering gallery modes. Also, as will be discussed in a later chapter, the presence of surface plasmons could allow for the direct control of the WGMs in such structures

7.4 Conclusions

In conclusion, in this chapter it was shown that whispering gallery modes carrying angular momentum can be coupled in non-linear plasmonic cavities made of metallic cylindrical scatterers. Similar to cavity modes, WGMs are strongly affected by the geometry of the scatterers allowing for a great deal of tuneability in the choice of design. In addition, the distributions of the scattering coefficients of the electromagnetic field in both the linear and non-linear case was examined. The results demonstrate that a direct connection can be found between the pattern of the dominant coefficients and the mode profile. Thus, WGMs can only be coupled when the distribution of the dominant scattering coefficients has the same symmetries as the mode. A similar connection can be found between the coefficient distribution and the symmetries of the cavity itself.

The quality factors of two whispering gallery modes were analysed and Q-factors of up to 1305 were found. The results suggest several possible applications for this type of cavity in optical trapping, optical manipulation and lasing. Also, as the non-linear cavity modes discussed here are a direct result of the field distribution at the fundamental frequency, it may be possible to use the magnetisation induced second harmonic generation effect to externally control the properties of the WGMs through the use of a magnetic field. This can have important applications in actively controlled optical devices. Further work can lead to a better understanding of the complex interplay between the properties of the incoming beam, those of the cavity and the WGMs which can be coupled in such structures. It is thus clear that plasmon induced, non-linear, whispering gallery modes can open up further possibilities for new applications in optics and beyond.

Bibliography

[1] A. B. Matsko and V. S. Ilchenko. Optical resonators with whispering-gallery modes-part I: basics. *IEEE J. Sel. Top. Quant.*, 12(1):3–14, January 2006.

[2] W.-H. Guo, Y.-Z. Huang, Q.-Y. Lu, and L.-J. Yu. Whispering-gallery-like modes in square resonators. *IEEE J. Sel. Top. Quant.*, 39(9):1106–1110, September 2003.

[3] L. L. Martín, P. Haro-González, I. R. Martín, D. Navarro-Urrios, D. Alonso, C. Pérez-Rodríguez, D. Jaque, and N. E. Capuj. Whispering-gallery modes in glass microspheres: optimization of pumping in a modified confocal microscope. *Opt. Lett.*, 36(5):615–617, March 2011.

[4] R. Cole, Y. Sugawara, J. Baumberg, S. Mahajan, M. Abdelsalam, and P. Bartlett. Easily Coupled Whispering Gallery Plasmons in Dielectric Nanospheres Embedded in Gold Films. *Phys. Rev. Lett.*, 97(13):137401, September 2006.

[5] E. J. R. Vesseur, F. J. García de Abajo, and A. Polman. Modal decomposition of surface-plasmon whispering gallery resonators. *Nano Lett.*, 9(9):3147–3150, September 2009.

[6] G. Kozyreff, J. L. Dominguez Juarez, and J. Martorell. Whispering-gallery-mode phase matching for surface second-order nonlinear optical processes in spherical microresonators. *Phys. Rev. A*, 77(4):043817, April 2008.

[7] H.-Y. Ryu, M. Notomi, G.-H. Kim, and Y.-H. Lee. High quality-factor whispering-gallery mode in the photonic crystal hexagonal disk cavity. *Opt. Express*, 12(8):1708–1719, April 2004.

[8] R. Chen, T. T. D. Tran, K. W. Ng, W. S. Ko, L. C. Chuang, F. G. Sedgwick, and C. Chang-Hasnain. Nanolasers grown on silicon. *Nature Photon.*, 5(3):170–175, 2011.

[9] S. L. McCall, A. F. J. Levi, R. E. Slusher, S. J. Pearton, and R. A. Logan. Whispering-gallery mode microdisk lasers. *Appl. Phys. Lett.*, 60(3):289–291, 1992.

[10] B. Min, E. Ostby, V. Sorger, E. Ulin-Avila, L. Yang, X. Zhang, and K. Vahala. High-Q surface-plasmon-polariton whispering-gallery microcavity. *Nature*, 457(7228):455–458, January 2009.

[11] K. Kieu and M. Mansuripur. Fiber laser using a microsphere resonator as a feedback element. *Opt. Lett.*, 32(3):244–246, March 2007.

[12] V. S. Ilchenko and A. B. Matsko. Optical resonators with whispering-gallery modes-part II: applications. *IEEE J. Sel. Top. Quant.*, 12(1):15–32, January 2006.

[13] K. Totsuka, N. Kobayashi, and M. Tomita. Slow Light in Coupled-Resonator-Induced Transparency. *Phys. Rev. Lett.*, 98(21):213904, May 2007.

[14] D. G. Grier. A revolution in optical manipulation. *Nature*, 424(6950):810–816, August 2003.

[15] E. Lidorikis, M. M. Sigalas, E. N. Economou, and C. M. Soukoulis. Tight-Binding Parametrization for Photonic Band Gap Materials. *Phys. Rev. Lett.*, 81(7):1405–1408, August 1998.

[16] T. Mukaiyama, K. Takeda, H. Miyazaki, Y. Jimba, and M. Kuwata-Gonokami. Tight-Binding Photonic Molecule Modes of Resonant Bispheres. *Phys. Rev. Lett.*, 82(23):4623–4626, June 1999.

[17] J. D. Jackson. *Classical Electrodynamics*. John Wiley & Sons, Hoboken, 3rd edition, 1999.

[18] C. G. Biris and N. C. Panoiu. Multi-color Whispering Gallery Modes in Plasmonic Cavities. *(to be submitted)*.

[19] V. Garces-Chavez, J. Arlt, K. Dholakia, K. Volke-Sepulveda, and S. Chavez-Cerda. Orbital angular momentum of a high order Bessel light beam. *J. Opt. B-Quantum S. O.*, 4:82–89, 2002.

Chapter 8

Applications of Plasmonic Cavities to Sensing

8.1 Introduction

The use of SPP resonances for sensing applications has been investigated for nearly three decades [1]. In particular, devices based on SPP resonances provide efficient, noninvasive, low-power and low-volume sensing. Recent work in this area has led to the development of several designs with various detection capabilities. Common detection limits (DL) for plasmon based sensing devices range from 10^{-6} refractive index units (RIU) for prism coupling and optical fiber designs to 10^{-5} RIU for waveguide designs [2]. While such detection limits are considered suitable for most sensing applications, the designs mentioned above range in size from several hundred microns to several millimeters. A submicron sensor design possessing similar detection capabilities would therefore prove to be a significant advancement in device integration. Such a design could be employed for sensing small amounts of target substances or on-chip parallel sensing.

In this chapter, we introduce and describe an ultra-compact plasmonic sensor design, which combines the advantages provided by the tight field confinement of localized SPPs and the non-linearly enhanced field induced by non-linear optical processes at metal surfaces. The design employs cavity-shaped assemblies of metallic nanowires whose optical modes are excited *via* local dipoles induced by the surface SHG process. Unlike the optical coupling to far-field radiation, these electric dipoles can excite dark (subradiant) plasmonic cavity modes that do not couple to the radiation continuum [3, 4]. As a result, the radiative losses are suppressed, the Q-factor of such dark plasmonic cavity modes being more than an order of magnitude larger than that of metallic nanoparticles [5]. This unique property of dark cavity modes can be used effectively to measure extremely small changes in the index of refraction, which can be induced, for example, by minute concentrations of trace molecules or thermal varia-

tions of the surrounding environment. To be more specific, this chapter will show that this novel approach to plasmonic sensing allows one to readily achieve detection limits of 10^{-6} refractive index units (RIU), for a detector resolution of 0.01 nm [6].

8.2 Optical Properties of Plasmonic Cavity Modes

The plasmonic cavity considered in this chapter is schematically illustrated in Fig. 8.1. It consists of a cavity-shaped distribution of parallel metallic cylinders with radius R, which are assumed to be made of Au. As it will be shown in what follows, additional functionality can be achieved by placing at the center of the plasmonic cavity a metallic cylinder, whose radius is R_i. In addition, the plasmonic nanowires forming the cavity are separated by a distance d. The plasmonic structure is excited by normally incident monochromatic plane waves with carrier frequency ω, the electric field of the incident light being perpendicular to the axis of the nanowires (TE polarisation). Under these conditions, at the FF, the optical response of the plasmonic structure is fully determined by the spatial distribution of the dielectric constant. Thus, the ensemble of plasmonic nanowires is assumed to be embedded in a background optical medium with index of refraction $n_b = \sqrt{\epsilon_b}$, where ϵ_b is the relative dielectric constant. In addition, the dielectric constant of the metallic nanowires is described by the Lorentz-Drude model given by Eq. (2.26). The simulations use the numerical values of the parameters corresponding to Au, which can be found in Appendix E.

The MSM method provides considerable flexibility in choosing the geometry and system parameters. In this chapter, three different designs of plasmonic cavities are considered. In the first two cases the plasmonic cavity consists of an assembly of six and eight identical metallic nanowires, whereas in the third case a hexagonal cavity, which contains at its center an additional metallic nanowire whose radius is different from that of those forming the boundary of the cavity (see Fig. 8.1), is considered. One efficient approach to find optical modes of plasmonic cavities is to search for resonances in the scattering and absorption cross-section spectra. However, utilizing absorption cross-section spectra provides a distinct advantage, namely, it allows one to find dark plasmon modes, as previously discussed. Moreover, we have used in our analysis of the optical response of plasmonic cavities the absorption cross-section spectra at the SH rather than those at the FF, for two main reasons. First, this choice eliminates the contribution to the total absorption of the incoming plane wave, thus increasing the accuracy of the analysis. Second, the generation of non-linear surface dipoles at the SH provides a convenient mechanism to excite dark plasmonic cavity modes, which plays a central role in enhancing the sensitivity of plasmonic sensors based on this design.

Figure 8.2 summarises the findings pertaining to the light scattering from the three plasmonic cavities investigated. One important result illustrated by this figure is the

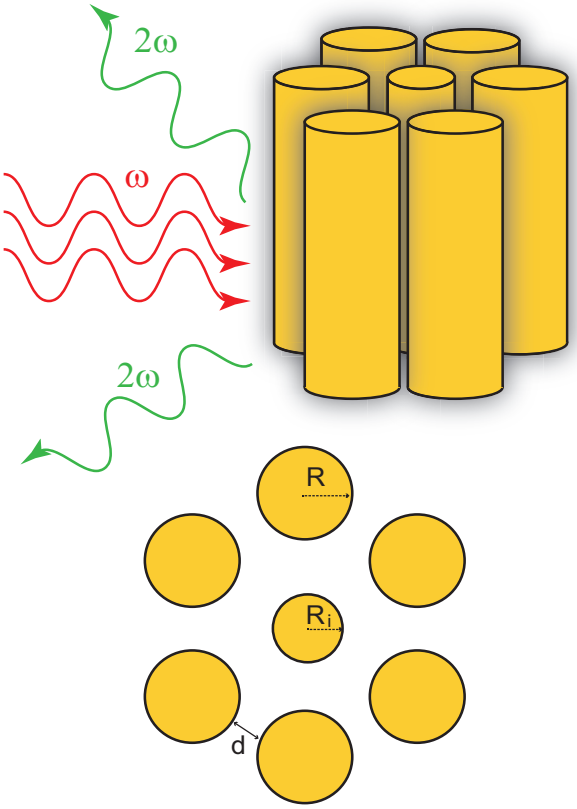

Fig. 8.1: Schematics of a plasmonic system consisting of a hexagonal cavity which contains a cylindrical inclusion at its center. All cylinders are made of Au.

presence of resonance peaks in the absorption cross section spectra, $\Sigma_a(\Omega)$, which are attributable to the excitation of plasmonic modes. There are two types of such plasmonic modes, namely, multipole modes excited on single cylinders and plasmonic cavity modes, which are the result of the coherent response of all nanowires in the plasmonic nanostructure (the electric field profiles at the SH, determined for each type of cavity for the corresponding resonance wavelength of the cavity modes, clearly confirm this conclusion). The resonance wavelength of the former modes ($\lambda_{\mathrm{SH}} = 663\ \mathrm{nm}$ and $\lambda_{\mathrm{SH}} = 937\ \mathrm{nm}$) does not depend on the geometry of the plasmonic nanostructures and therefore it cannot be tuned by modifying the geometry of the cavity. As a result these multipole plasmonic modes will not be analysed further as they have already been covered in chapter 6. By contrast, as illustrated in Fig. 8.2, the resonance wavelength of the plasmonic cavity modes is strongly dependent on the system parameters. The spectra in Fig. 8.2 also reveal several important characteristics of the plasmonic modes excited in the cavity. Thus, they clearly show that the geometry of the cavity has a strong influence on the field distribution of the cavity modes. Equally important, the scattering cross section spectra at the SH show no resonance peaks at the wavelength of the resonances in the spectra of the absorption cross-section. This important result indicates that the corresponding modes are dark plasmonic cavity modes, which are decoupled from the radiation continuum and thus cannot scatter light into the far-field. As a re-

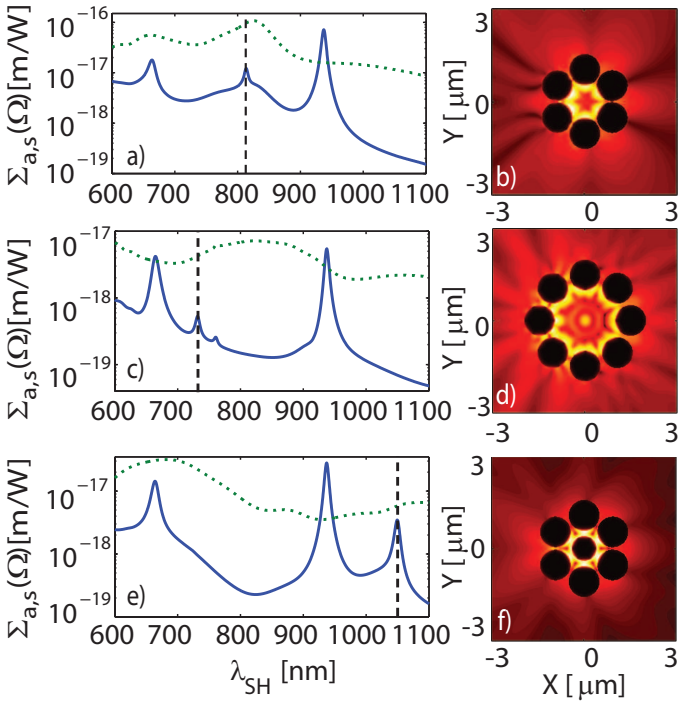

Fig. 8.2: Left panels show logarithmic spectra of the absorption (solid line) and scattering (dashed line) cross sections for (a) a six cylinder cavity; (c) eight cylinder cavity; and (e) six cylinder cavity with a cylindrical inclusion. Right panels show the field profiles of the plasmonic cavity modes, which correspond to the vertical dashed lines in the left panels. The geometric parameters are: separation distance $d = 20$ nm, $d = 130$ nm *and* $d = 70$ nm *for (a), (c) and (e), respectively, radius of the boundary cylinders* $R = 500$ nm *and radius of the cylinder at the centre* $R_i = 400$ nm.

sult, at the corresponding resonance wavelength, the plasmonic cavity is very efficient in trapping the non-linear field generated by the induced surface dipoles and therefore experiences reduced optical losses.

In order to gain a deeper insight into the physical properties of the plasmonic cavity modes a detailed study of the dependence on the system geometry of the resonance wavelength of the modes was performed. This analysis is particularly relevant for assessing the sensitivity of plasmonic sensors based on such cavities. One effective tool for performing this investigation is the dispersion map of the resonance wavelength of the plasmonic cavity modes. These maps, calculated for all three cavities, are presented in Fig. 8.3.

The dispersion maps corresponding to the three cavities clearly illustrate the strong variation of the resonance wavelength of the cavity modes with the change in the geometrical parameters defining the cavity. In the case of the six and eight cylinder cavities, an almost linear increase of the resonance wavelength of the cavity modes with the separation distance between the plasmonic nanowires can be observed. This dependence can be easily explained by the fact that the size of the cavity increases with the separation distance and, consequently, the resonance wavelength of the cavity modes is

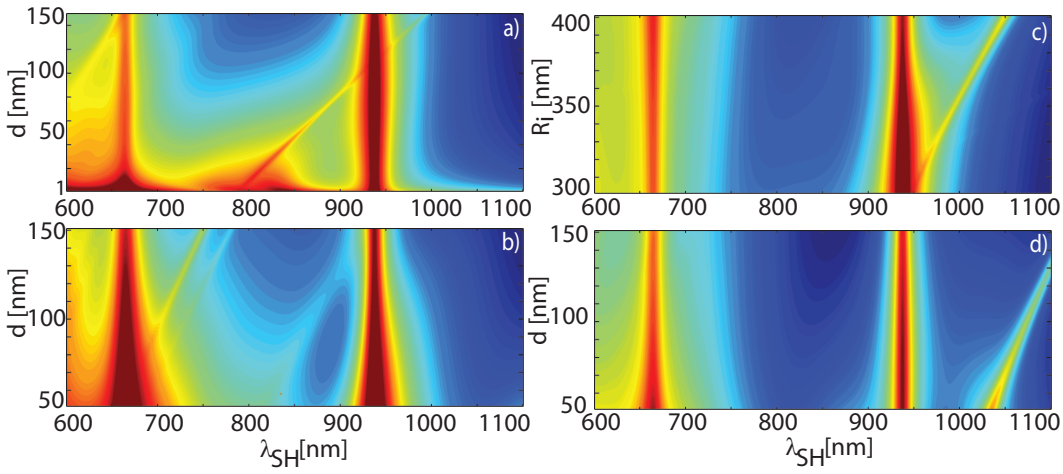

Fig. 8.3: Dispersion maps of absorption cross section, calculated for (a) a six cylinder cavity; (b) eight cylinder cavity; and (c) and (d), a six cylinder cavity with a cylindrical inclusion. Fixed geometric parameters are $d = 70$ nm *for (c) and* $R_i = 400$ nm *for (d). In all cases* $R = 500$ nm.

red-shifted. It can also be seen that the resonance wavelength shows a steeper increase with the separation distance in the case of the hexagonal cavity as compared to the case of the octagonal one. Moreover, the spectral width of the resonance is somewhat smaller in the case of the hexagonal cavity whereas in both cases the width of resonance peaks decreases with d. These findings are explained by the field distribution of the cavity modes. Thus, simulations show that the field enhancement at the surface of the metal, and consequently the optical loss, is larger in the case of the octagonal cavity and in both cases it decreases with d. More specifically, as d increases the cavities are less effective in confining the optical field and as such the electric field at the surface of the plasmonic nanowires decreases.

The modal field profiles also explain some of the effects observed when the structure of the cavity is modified, namely, when a plasmonic nanowire is placed at the center of the cavity. As shown in Fig. 8.3, the hexagonal cavity has a plasmonic mode even when a nanowire is added at its center; however, the resonance wavelength is affected by this structural change. On the other hand, simulations show that the cavity mode no longer exists in the case of the octagonal cavity. The field profiles in Fig. 8.2 clearly explain this phenomenon. The field amplitude of the plasmonic mode of the hexagonal cavity has a minimum at the center of the cavity and therefore it is only slightly perturbed by the added nanowire. By contrast, the mode of the octagonal cavity has a maximum at the center of the cavity, so that by adding a nanowire the cavity mode is suppressed. It should be also noted that in all cases the resonance wavelength of the plasmonic cavity modes depends linearly on the geometrical parameters of the cavity (d and R_i).

The resonance wavelength of the plasmonic cavity modes is also strongly affected

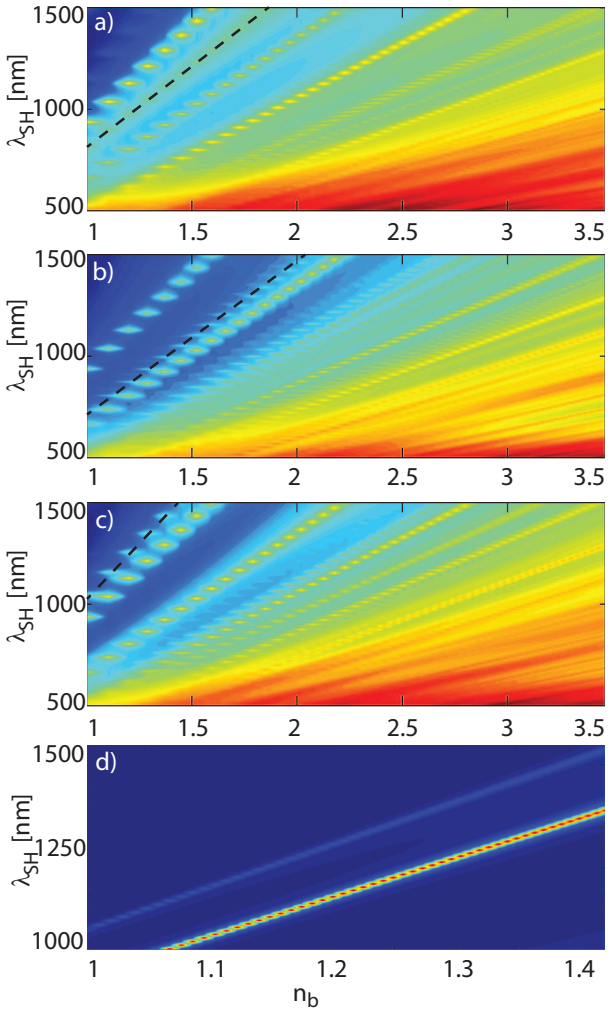

Fig. 8.4: Dependence of the absorption cross section spectra on the background refractive index, n_b, calculated for (a) a six cylinder cavity; (b) an eight cylinder cavity; and (c), (d) a six cylinder cavity with a cylindrical inclusion. The geometric parameters are $d = 20$ nm, $d = 130$ nm and $d = 70$ nm for (a), (b) and (c), respectively, and $R_i = 400$ nm for (c) and (d). In all cases $R = 500$ nm. The dashed lines mark the spectral location of the plasmonic cavity modes.

by the change in the index of refraction of the background medium, n_b. This effect has important implications when sensing applications are considered. In order to better understand this dependence, consider the three types of cavities, described by parameters $R = 500$ nm and $d = 20$ nm, $d = 130$ nm, and $d = 70$ nm for the six cylinder, eight cylinder, and the six cylinder with central inclusion cavities, respectively, the radius of the central cylinder being $R_i = 400$ nm. In all cases the resonance wavelength of the cavity modes for a background refractive index varying from $n_b = 1$ to $n_b = 3.5$ was calculated. The results of the simulations are summarized in Fig. 8.4. The dispersion maps presented in this figure, depicting the variation of the absorption cross-section spectra with the background index of refraction, demonstrate that the resonance wavelength of the cavity modes increases linearly with n_b. However, the rate at which the resonance wavelength varies with n_b is dependent on the specific plasmonic mode and

the structure of the cavity. As expected, the smaller the volume of the cavity mode, the steeper the increase of the resonance wavelength with n_b [see also Fig. 8.2]. We also remark here that the mode lines in Fig. 8.4 show an apparent discontinuity of the mode. This effect however is a result of the discretisation of λ_{SH} and n, needed to obtain the data. To further clarify this issue, we plot in Fig. 8.4d a zoomed in area of the absorption spectra in Fig. 8.4c, which has been obtained with a finer refractive index step size. Thus, it becomes clear that the modes in question are indeed continuous and that the discontinuities apparent in the spectra are simply the result of the numerical interpolation used to generate the plots. Figure 8.4 also illustrates the dispersion properties of the multipole plasmonic modes, which appear as a series of spectral bands that are more closely spaced at increasing value of the background index of refraction. These resonances have a low Q factor and as such are less effective in sensing applications; therefore, they are not discussed in what follows.

8.3 Applications to Plasmonic Sensors

Having established the main physical properties of the plasmonic cavity modes supported by the plasmonic cavities described in the previous section, we now discuss their potential for applications to plasmonic sensing. The dependence of the resonance wavelength on the background index of refraction allows one to calculate a quantity that plays a central role in characterizing the performance of plasmonic sensors, namely, the refractive index sensitivity of the sensor. The sensor sensitivity is defined as the variation of the resonance wavelength per unit change of the background index of refraction. Mathematically, it is expressed as $S = d\lambda/dn_b$, and can be determined by calculating the slope of the dispersion curves of the plasmonic cavity modes. Another important quantity characterising a detector is the detection limit, DL, which is defined as the ratio between the wavelength resolution of the detector, σ, and the detector sensitivity, S, *i.e.*, $DL = \sigma/S$. In what follows σ is measured in nanometres whereas DL is measured in refractive index units, RIU.

Figure 8.5a presents the dependence on the background refractive index of the resonance wavelength of the plasmonic cavity mode of the hexagonal cavity that contains a plasmonic nanowire at its center. The dispersion curves have been calculated for several values of the radius of the central nanowire, ranging from $R_i = 350$ nm to $R_i = 400$ nm. It can be seen that the slope of the dispersion curve increases with the radius R_i, which again is explained by the fact that the mode volume decreases with R_i. Consequently, the sensitivity of the plasmonic cavity increases with R_i. This conclusion is confirmed by the data plotted in Fig. 8.5b, which shows the dependence of the sensitivity of the plasmonic modes on the parameters defining the cavities, determined for each of the three cavities. Indeed, it can be seen that the sensitivity of the

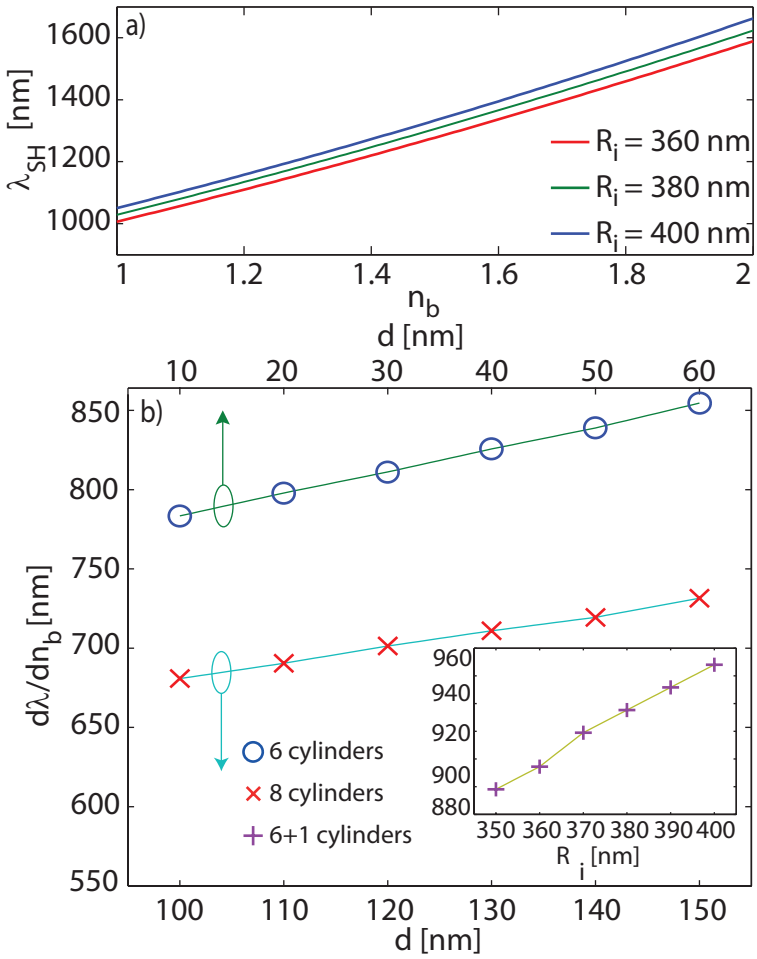

Fig. 8.5: (a) Resonance wavelength of the plasmonic cavity mode of a six cylinder cavity with a cylindrical inclusion vs. the background refractive index. (b) Sensitivity of the plasmonic cavity vs. d and R_i. The markers correspond to a six cylinder cavity ($\circ$), an eight cylinder cavity ($\times$) and a six cylinder cavity with a cylindrical inclusion (+); solid lines serve as a guide to the eye. The separation distance is $d = 70$ nm in the case of the six cylinder cavity with a cylindrical inclusion.

cavity increases with R_i, with $S = 944\ \mathrm{nm/RIU}$ for $R_i = 400$ nm. Similar large values of the sensitivity of sensors based on plasmonic perfect absorbers have been recently reported [7]. Importantly, of the three designs investigated the hexagonal cavity with a central inclusion presents the largest sensitivity, whereas the octagonal one has the lowest S. This result further proves that generally cavities with larger mode volume have lower sensitivity. For a specific cavity, however, the dependence of the sensitivity on the cavity shape can be more intricate. Thus, Fig. 8.5b shows that the sensitivity of the hexagonal and octagonal cavities increases with the separation distance d, which means that the sensitivity is determined not only by the volume of the cavity mode but also by its particular field distribution.

Utilising the results discussed above the detection limit of the devices can be calculated. The actual value of the DL depends on the wavelength resolution of the detector employed, σ. In what follows it is assumed that $\sigma = 0.01$ nm, in order to make

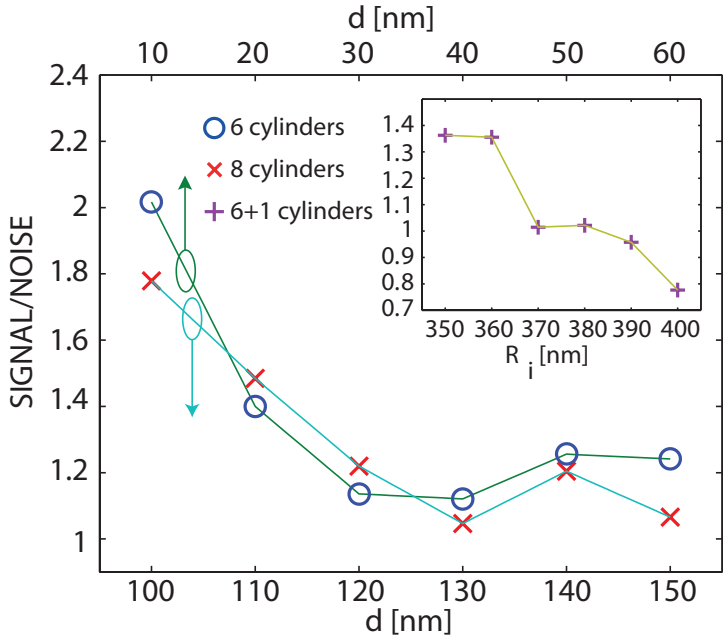

Fig. 8.6: Signal to noise ratio of the plasmonic cavity modes. The markers correspond to a six cylinder cavity (∘), an eight cylinder cavity (×) and a six cylinder cavity with a cylindrical inclusion (+); solid lines serve as a guide to the eye. The separation distance is $d = 70$ nm *in the case of the six cylinder cavity with a cylindrical inclusion.*

a quantitative comparison between these findings and several recent results pertaining to plasmonic sensors [8–10]. With this assumption, the values for the detection limit of the hexagonal cavity design varies from 1.27×10^{-5} RIU to 1.17×10^{-5} RIU when d changes from 10 nm to 60 nm, respectively. Similarly, the hexagonal cavity design with a cylindrical inclusion has a DL ranging from 1.1×10^{-5} RIU to 1.05×10^{-5} RIU when R_i increase from 350 nm to 400 nm. It is important to stress that not attempt was made to optimize the sensitivity of the plasmonic cavities and therefore further improvement of the device performance is possible. Although one can achieve lower detection limits by using millimeter-sized plasmonic sensors, my design provides the unique advantage of submicron sensing volume. This functionality makes the design easily integratable in on-chip plasmonic sensing systems.

Another important characteristic of sensing devices is the detection accuracy, or signal to noise ratio (SNR). The SNR represents a convenient means for comparing the level of the detection signal to that of the background noise. In spectral sensing characterization it is defined as $\mathrm{SNR} = \delta\lambda/w$, where $\delta\lambda$ is the shift in the resonance wavelength for a given and w is the spectral full width at half maximum of the resonance. The SNR for all three cavity designs, for different values of their geometric parameters, has been calculated. In all calculations it was assumed that $\delta n_b = 0.01$ and $n_b = 1.4142$. The results are shown in Fig. 8.6. The curves for the six and eight cylinder cavities show a similar trend, with the SNR values for the hexagonal cavity varying from 2.049 to 1.2414 as d varies from 10 to 60 nm. It should be noted that the dependence of the SNR on the separation distance (SNR decreases with d) is opposite to that of the sensitivity of the devices, within the same parameter range. This is due to the broadening of the absorption peaks as the separation distances increase. The same conclusion holds for the six cylinder cavity with a central inclusion. In this case, the SNR varies from 1.263 to 0.6764 as R_i increases from 350 to 400 nm. Unlike the case of the sensitivity of the devices, of the three designs, the six cylinder cavity with a central inclusion has the lowest SNR. This result shows that there is a complex interplay between the geometrical characteristics of the plasmonic cavities and the main parameters that characterize their sensing performance. The SNR values of the proposed plasmonic devices are within the typical range achievable with waveguide based plasmonic sensors [11, 12].

8.4 Conclusions

To summarise, we have seen that cavity-shaped assemblies of metallic nanowires support dark plasmonic cavity modes whose resonance wavelength is strongly dependent on the geometry of the cavity and the properties of the background medium. In addition, the suppression of the radiation losses of these plasmonic cavity modes leads to a significant increase of their quality factor, a property that has important practical applications to plasmonic sensors. Our theoretical analysis has revealed that these dark plasmonic modes can be effectively excited by electric dipoles induced at the surface of the metal by the SHG process, thus making them extremely sensitive to changes in the surface properties of metals and variations of the dielectric environment generated by thermal effects or chemical processes. In particular, we have demonstrated that this phenomenon can be utilised to design plasmonic sensors with enhanced sensitivity to changes in the index of refraction of the environment. This study has shown that detection limits as low as 10^{-5} RIU can be readily achieved with submicron-sized plasmonic sensors. These theoretical findings can lead to new experimental research in non-linear plasmonics and exciting applications to active plasmonic nanodevices.

Bibliography

[1] B. Liedberg, C. Nylander, and I. Lunström. Surface plasmon resonance for gas detection and biosensing. *Sensor. Actuator.*, 4:299 – 304, 1983.

[2] X. D. Fan, I. M. White, S. I. Shopova, H. Zhu, J. D. Suter, and Y. Sun. Sensitive optical biosensors for unlabeled targets: a review. *Anal. Chim. Acta*, 620(1-2):8–26, July 2008.

[3] V. A. Fedotov, M. Rose, S. L. Prosvirnin, N. Papasimakis, and N. I. Zheludev. Sharp Trapped-Mode Resonances in Planar Metamaterials with a Broken Structural Symmetry. *Physical Review Letters*, 99(14):147401, October 2007.

[4] M. Liu, T.-W. Lee, S. Gray, P. Guyot-Sionnest, and M. Pelton. Excitation of Dark Plasmons in Metal Nanoparticles by a Localized Emitter. *Phys. Rev. Lett.*, 102(10):107401, March 2009.

[5] C. G. Biris and N. C. Panoiu. Nonlinear pulsed excitation of high-Q optical modes of plasmonic nanocavities. *Opt. Express*, 18(16):17165–17179, August 2010.

[6] C. G. Biris and N. C. Panoiu. Excitation of dark plasmonic cavity modes via nonlinearly induced dipoles: applications to near-infrared plasmonic sensing. *Nanotechnology*, 22(23):235502, April 2011.

[7] N. Liu, M. Mesch, T. Weiss, M. Hentschel, and H. Giessen. Infrared Perfect Absorber and Its Application As Plasmonic Sensor. *Nano letters*, 10(7):2342–2348, June 2010.

[8] A. Suzuki, J. Kondoh, and Y. Matsui. Development of novel optical waveguide surface plasmon resonance (SPR) sensor with dual light emitting diodes. *Sensor. Actuator. B-Chem.*, 106(1):383–387, April 2005.

[9] D. Monzón-Hernández and J. Villatoro. High-resolution refractive index sensing by means of a multiple-peak surface plasmon resonance optical fiber sensor. *Sensor. Actuator. B-Chem.*, 115(1):227–231, May 2006.

[10] F. C. Chien, C. Y. Lin, J. N. Yih, K. L. Lee, C. W. Chang, P. K. Wei, C-C Sun, and S-J Chen. Coupled waveguide-surface plasmon resonance biosensor with subwavelength grating. *Biosens. Bioelectron.*, 22(11):2737–2742, May 2007.

[11] A. K. Sharma and B. D. Gupta. On the sensitivity and signal to noise ratio of a step-index fiber optic surface plasmon resonance sensor with bimetallic layers. *Opt. Commun*, 245(1-6):159–169, January 2005.

[12] A. K. Sharma and B. D. Gupta. Comparison of Performance Parameters of Conventional and Nano-plasmonic Fiber Optic Sensors. *Plasmonics*, 2(2):51–54, May 2007.

Chapter 9

Theoretical Investigations of Tuneable Plasmonic Metasurfaces

9.1 Introduction

Several recent studies have theoretically predicted that one can tailor the properties of LSPs formed in a 2D array of asymmetric apertures in metallic films so that the mid-infrared optical transmittance of the corresponding plasmonic metasurface becomes strongly dependent on the polarisation of the incoming field [1, 2] or the shape and distribution of the apertures [3]. In this chapter we will present an in-depth theoretical and numerical analysis of this effect, as well as a comparison to recent experimental results. In particular, a simple design for an *asymmetric* aperture whose properties can be conveniently tuned, namely, a Swiss cross with asymmetric arms is used. The plasmonic response of arrays of *symmetric* cruciform apertures has been extensively studied both theoretically and experimentally [4–8]. The LSP resonances of such symmetric apertures, however, consists of two degenerate modes orthogonally polarized with respect to each other and therefore the optical transmission of the corresponding plasmonic metasurfaces is polarisation insensitive. In this chapter we show that by introducing structural asymmetry in the design of the cruciform aperture, the optical transmission and reflectance of a uniform, periodic array of asymmetric apertures show enhanced optical anisotropy. In particular, the maximum of the transmission spectra, which corresponds to the resonant excitation of a LSP in the array of asymmetric cruciform apertures, can be tuned by almost 50% by simply rotating the plane of polarisation of the incident wave [9]. Moreover, by using Babinet's principle, the ideas presented in this chapter can be readily extended to the complementary geometry of metallic crosses placed on a dielectric substrate [10, 11].

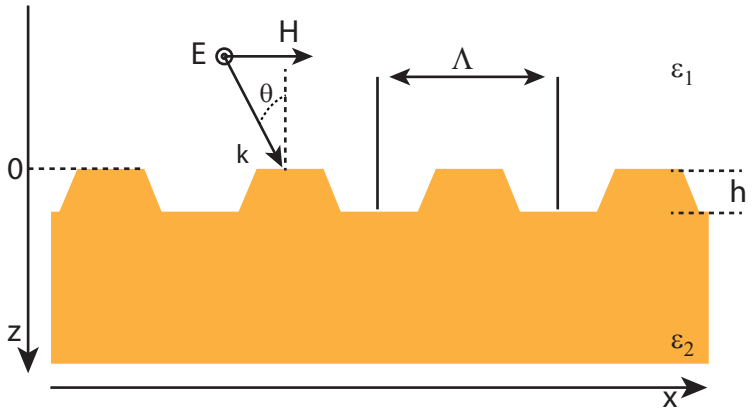

Fig. 9.1: Schematic of a 2D grating which can be numerically investigated using the rigorous coupled wave analysis method.

9.2 The Rigorous Coupled Wave Analysis Method

The numerical simulations described in this chapter are used to find the transmission coefficient, reflection coefficient, absorption and the field distribution inside metallic gratings. While there are several formalisms which can be employed for this task, this work relies on a numerical algorithm specifically designed for this type of problems, namely, the *rigorous coupled wave analysis* (RCWA) algorithm [12, 13].

Figure 9.1 illustrates a typical grating structure which can be analysed using the RCWA method. Note that RCWA can also be used in 3D structures but, for the sake of simplicity of this presentation, the discussion in this section will be limited to a 2D grating. The first step of the RCWA method consists of splitting the simulation in three domains: the area above the grating characterised by a permittivity ϵ_1, the substrate below the grating with ϵ_2, and the grating region itself. The electromagnetic field in each of these regions is treated separately.

Assuming for simplicity an incident plane wave normal to the grating surface and with component $\mathbf{E}$ perpendicular to the (x, z) plane, the field reflected by the grating into the area with dielectric constant ϵ_1 can be expanded as (if harmonic time dependence $e^{i\omega t}$ is assumed) [12]:

$$E_1 = \sum_{m=-\infty}^{\infty} R_m e^{-i(k_{x,m}x - k_{1z,m}z)}, \tag{9.1}$$

where R_m are the reflected field coefficients and $k_{1z,m} = \sqrt{k_0^2\epsilon_1 - k_{x,m}^2}$. The periodicity of the grating structure determines the expression of $k_{x,m}$ as $k_{x,m} = k_x - mK$, where $K = 2\pi/\Lambda$ and $k_x = k_0\sqrt{\epsilon_1}\sin\theta$. Here and above, k_0 and θ are the free-space wave vector and incidence angle of the incoming wave, respectively. Note that in this region, the total field also includes the incoming wave, which is assumed to be known. In the substrate region, underneath the grating, the transmitted field can be expanded

as:

$$E_2 = \sum_{m=-\infty}^{\infty} T_m e^{-i[k_{x,m}x + k_{2z,m}(z-h)]}, \tag{9.2}$$

where T_m are the transmitted field coefficients, h is the height of the grating layer and $k_{2z,m} = \sqrt{k_0^2\epsilon_2 - k_{x,m}^2}$.

Inside the region of the grating itself, the permittivity ϵ_g becomes a function of both z and x, $\epsilon_g = \epsilon_g(x,z)$. This function can be expanded into a Fourier series owing to the periodicity of the grating. Thus, $\epsilon_g(x,z)$ becomes:

$$\epsilon_g(x,z) = \epsilon_g(x+\Lambda,z) = \sum_n \epsilon_{g,n}(z) e^{in(2\pi/\Lambda)x}, \tag{9.3}$$

where Λ is the period of the grating. The electric field inside the grating can also be expanded as:

$$E_g = \sum_{m=-\infty}^{\infty} G_m(z) e^{-i(k_{x,m}x + k_{gz,0}z)}, \tag{9.4}$$

where $G_m(z)$ are the space-harmonic field expansion coefficients and $k_{gz,0} = k_0\sqrt{\epsilon_1}\cos\theta$.

To solve the electromagnetic problem, the coefficients $G_m(z)$ need to be determined first. In the grating region, the field satisfies the wave equation:

$$\nabla^2 E_g + k_0^2 \epsilon_g(x,z) E_g = 0. \tag{9.5}$$

Combining this Helmholtz equation with Eqs. (9.3) and (9.4) yields the following infinite set of second-order coupled differential equations:

$$\frac{d^2G_m(z)}{dz^2} - 2ik_{gz,0}\frac{dG_m(z)}{dz} = (k_{x,m}^2 + k_x^2)G_m(z) - k_0^2\sum_n \epsilon_n(z)G_{m-n}(z). \tag{9.6}$$

Once Eqs. (9.6) are solved and the space harmonic coefficients $G_m(z)$ are known, both the reflected and transmitted wave coefficients, R_m and T_m, respectively, can be determined by imposing the boundary conditions between the three regions. As such, at the interface between the top region with ϵ_1 and the grating, the boundary conditions require that:

$$E_1 = E_g, \qquad H_1 = H_g, \tag{9.7}$$

where the H field is parallel to the x axis (see Fig. 9.1). In the substrate region, the boundary conditions require that:

$$E_2 = E_g, \qquad H_2 = H_g. \tag{9.8}$$

Equations (9.7) and (9.8), coupled with the solution of Eqs. (9.6) thus completely determine the field distribution in the entire simulation region.

In the technical implementation of the RCWA, Eqs. (9.6) are usually solved using a state-variables method employed in linear system analysis [14]. Common to many numerical methods, the infinite sum in Eqs. (9.6) is truncated to a finite sum, with the accuracy of the results being determined by, amongst others, the number of terms one keeps. To this end, an important numerical parameter required by the RCWA method is *the number of harmonics* used. The number of harmonics (diffraction orders) N is defined as $N = (M-1)/2$ where M is the total number of expansion terms considered. A typical value for the number of harmonics used in our simulation is $N = 16$. For complex gratings, such as the one in Fig. 9.1, where the z-dependence of $\epsilon_g(x, z)$ needs to be considered, the grating region is "sliced" into a series of layers perpendicular to the z-axis, which are numerically treated as having $\epsilon_g = \epsilon_g(x)$. Also, appropriate boundary conditions are imposed at the interface between each adjacent layer. Due to the periodicity of the layer, the simulation domain is limited to the unit cell on the x-axis (or x- and y-axes in the case of 3D gratings). On the z-axis the domain is considered to be infinite in both directions with the wave propagating according to Eqs. (9.1) and (9.2).

The RCWA method is an efficient numerical solver for the problem of light diffraction on gratings, with several commercial and freely available implementations being widely used. In the remaining of this chapter, as well as Chapter 10, the RCWA method will be used to investigate the electromagnetic response of plasmonic metasurfaces with asymmetric features.

9.3 Sample Fabrication and Experimental Measurements

In this section, we briefly describe the fabrication process of the grating being investigated theoretically. Thus, the cruciform aperture arrays were fabricated using the focused ion beam (FIB) technique. The device structure and a fabricated array are shown in Fig. 9.2. Each array has 15×15 unit cells and a periodicity in both the x and y directions of $\Lambda = 2\ \mu\mathrm{m}$; thus the array has dimensions $30 \times 30\ \mu\mathrm{m}^2$. The size of the arrays is large enough so that size-dependent array effects are negligible [15]. A similar array of symmetric cruciform apertures was fabricated as a control sample. This array had the same periodicity and same number of unit cells as the arrays of asymmetric apertures.

The transmission spectra of the arrays were measured using Fourier-transform infrared (FTIR) microscopy. The transmission spectra were normalized to the bare $\mathrm{CaF_2}$ substrate while the reflection spectra were normalized to the unpatterned gold surface.

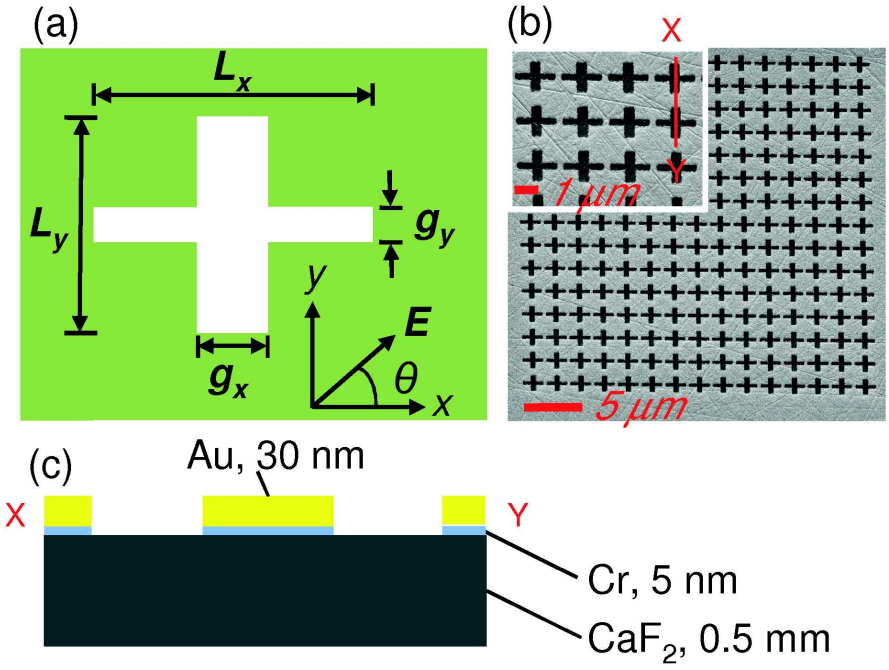

Fig. 9.2: (a) Schematic of the unit cell also showing the definition of the in-plane electric-field polarisation angle, θ. (b) Scanning electron micrograph of an array with the inset showing magnified detail. (c) Schematic cross-section through the XY*-segment, as shown in (b). The devices were fabricated at the London Center for Nanotechnology by P. Thompson and E. Osley. For more details see Ref. [9]*

Data were obtained for incident in-plane polarisation angles (as defined in Fig. 9.2a) between $\theta = 0$ and $\theta = 90°$ in $15°$ increments.

The resulting experimentally measured transmission spectra for the asymmetric cruciform array, presented in Fig. 9.3a, show two distinct peaks, A and B, the positions of which, to within the accuracy of the measurement, are invariant with respect to the polarisation angle. As the polarisation angle is changed from $\theta = 0$ to $\theta = 90°$, the amplitude of peak A decreases from its maximum value reached at $\theta = 0$ and eventually decays to below the noise level, while the peak B begins to emerge and increases in amplitude to reach its maximum at $\theta = 90°$. The spectra in Fig. 9.3a show another intriguing spectral point, I (at λ=4.46μm), at which transmission is independent of polarisation. Drawing from an analogy from molecular spectroscopy, this point is termed an isosbestic point [1]. By comparison, the spectra for the control array of symmetric cruciform apertures show a single peak (see Fig. 9.3g) and, within the inherent variations introduced by the fabrication process, the transmission is insensitive to the polarisation of the electric field. In addition, a transmission minimum is seen at $\lambda = 3.3$ μm, for arrays of both asymmetric and symmetric apertures. This minimum corresponds to the Wood's anomaly of the periodic array and is predicted to occur at $\lambda_W = n_d\Lambda/\sqrt{i^2 + j^2}$ [15–17], where n_d is the index of refraction of the dielectric medium and i and j are mode indices. In the case of square arrays the largest wave-

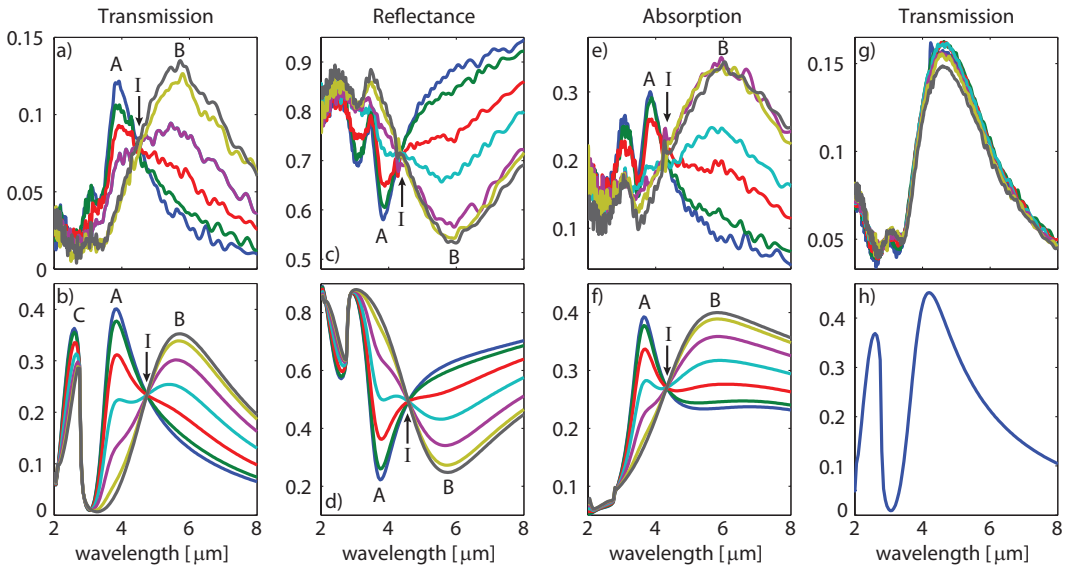

Fig. 9.3: (a), (c), and (e) Measured FTIR transmission, reflection and absorption spectra (respectively) for an array of asymmetric cruciform apertures with $L_x = 1675$ nm, $L_y = 1003$ nm, $g_x = 418$ nm *and* $g_y = 165$ nm. *These spectra show polarisation angles varying from* $\theta = 0$ *(blue) to* $\theta = 90°$ *(brown) in increments of* $15°$. *(b), (d), and (f) Simulation of FTIR transmission, reflection and absorption spectra for asymmetric cruciform apertures with the above dimensions. (g) and (h) Measured transmission and simulation spectra for the control array of symmetric cruciform apertures with dimensions* $L_x = L_y = 1264$ nm *and* $g_x = g_y = 368$ nm. *Experimental measurements were performed at the London Center for Nanotechnology by P. Thompson and E. Osley.*

length at which the Wood's anomaly occurs corresponds to $i = 1$ and $j = 0$. As such, for an array with $\Lambda = 2$ μm the wavelength of the Wood's anomaly corresponding to Au-air ($n_d = 1$) and Au-CaF_2 ($n_d = 1.4$) is $\lambda_W = 2$ μm and $\lambda_W = 2.8$ μm, respectively. The measured reflection spectra (Fig. 9.3c) are qualitatively anti-correlated with the transmission spectra, with clear reflection minima at the wavelengths of the transmission peaks A and B. Remarkably, for both the reflection and absorption spectra (Fig. 9.3e) there is an isosbestic point, its wavelength being blue-shifted with respect to that of the isosbestic point in the transmission spectra (the isosbestic point of the reflection and absorption spectra is at the wavelength $\lambda_r = 4.36$ μm and $\lambda_a = 4.32$ μm, respectively).

In order to investigate theoretically the optical properties of the fabricated arrays, it was necessary to know the fabricated dimensions of the arrays, as defined in Fig. 9.2a. Owing to fabrication process variability, the dimensions of each aperture vary. Therefore, measurements were taken of 10 fabricated apertures in each array using scanning electron microscopy and the dimensions averaged. For the array of asymmetric cruciform apertures the lengths of the arms of the cruciform were found to be $L_x = 1675$ nm and $L_y = 1003$ nm, whereas their width was $g_x = 418$ nm and $g_y = 165$ nm. Note also that for the array of symmetric cruciform apertures fabrication tolerances led to a small degree of asymmetry, the corresponding mean values being $L_x = 1270$ nm,

$L_y = 1258$ nm, $g_x = 362$ nm, and $g_y = 373$ nm. Therefore, in this case the values of L_x and L_y were averaged to arrive at a single mean value: $L_x = L_y = 1264$ nm. Similarly, the values of the width of the arms, g_x and g_y, were averaged to the mean value $g_x = g_y = 368$ nm.

Device simulations were carried out using commercially available software, RSoft's DiffractMOD [18], which implements the RCWA method. Simulated spectra for the arrays of asymmetric and symmetric cruciform apertures are shown in Fig. 9.3. In the simulations, numerical convergence was reached when $N = 17$ harmonics were included for each transverse dimension, which amounts to a total of $N^2 = 289$ Fourier expansion terms. Furthermore, it was assumed that the frequency-dependent dielectric constant of Au is described by the Drude model (Eq. (2.14)). In the case of Au, $\omega_p = 13.72 \times 10^{15}$ rad/s and $\gamma = 4.05 \times 10^{13}$ s^{-1} [19]. Note that since the devices operate in the mid-infrared frequency domain the contribution to the dielectric constant of inter-band effects can be neglected. In order to achieve a good agreement between the experimental data and the numerical results however, the damping frequency had to be increased to $\gamma \rightarrow 1.5\gamma = 6.08 \times 10^{13}$ s^{-1}. This fact is not surprising since it is well known that due to electron scattering into surface states the dielectric constant of metallic nanostructures depends on their size when the corresponding characteristic size is comparable to the skin depth. For metallic films, the bulk damping frequency is replaced by $\gamma_{\text{film}} = \gamma_{\text{bulk}} + \alpha v_F/d$, where α is a theory-dependent quantity on the order of 1, v_F is the Fermi velocity, and d is the thickness of the film [20]. Interestingly enough, at optical frequencies the corresponding scaling factor was found to be equal to 3 [21].

The two transmission maxima and their polarisation-dependence, as well as the spectral location of the isosbestic point and the Wood's anomaly in the experimentally-measured spectra are well reproduced in the simulated spectra for the asymmetric apertures. An additional peak, labeled C ($\lambda = 2.6$ μm), is however observed in the simulation, which in the experimental data appears to be only slightly above the noise level. Likewise for the array of symmetric apertures, the simulation reproduces the single peak of the experimental data at $\lambda = 4.6$ μm, but also predicts the existence of an additional peak C at shorter wavelength. This additional peak is at the same wavelength as for the asymmetric apertures. The insensitivity of the position of peak C to the detailed geometry of the unit cell suggests that it is due to extended surface plasmon polariton (SPP) resonances. Indeed, the wavelength of SPPs is given by the relation $\lambda_{\text{SPP}} = (\Lambda/\sqrt{i^2 + j^2})\text{Re}\sqrt{\epsilon_d \epsilon_{\text{Au}}/(\epsilon_d + \epsilon_{\text{Au}})}$ [15–17], which implies that for Au-air and Au-CaF_2 interfaces the SPP wavelength is $\lambda_{\text{SPP}} = 2.005$ μm and $\lambda_{\text{SPP}} = 2.807$ μm, respectively. Since $|\epsilon_{\text{Au}}| \gg \epsilon_d$, λ_{SPP} is only slightly larger than λ_{W}. The extended SPP resonances are significantly weaker in the experimental measure-

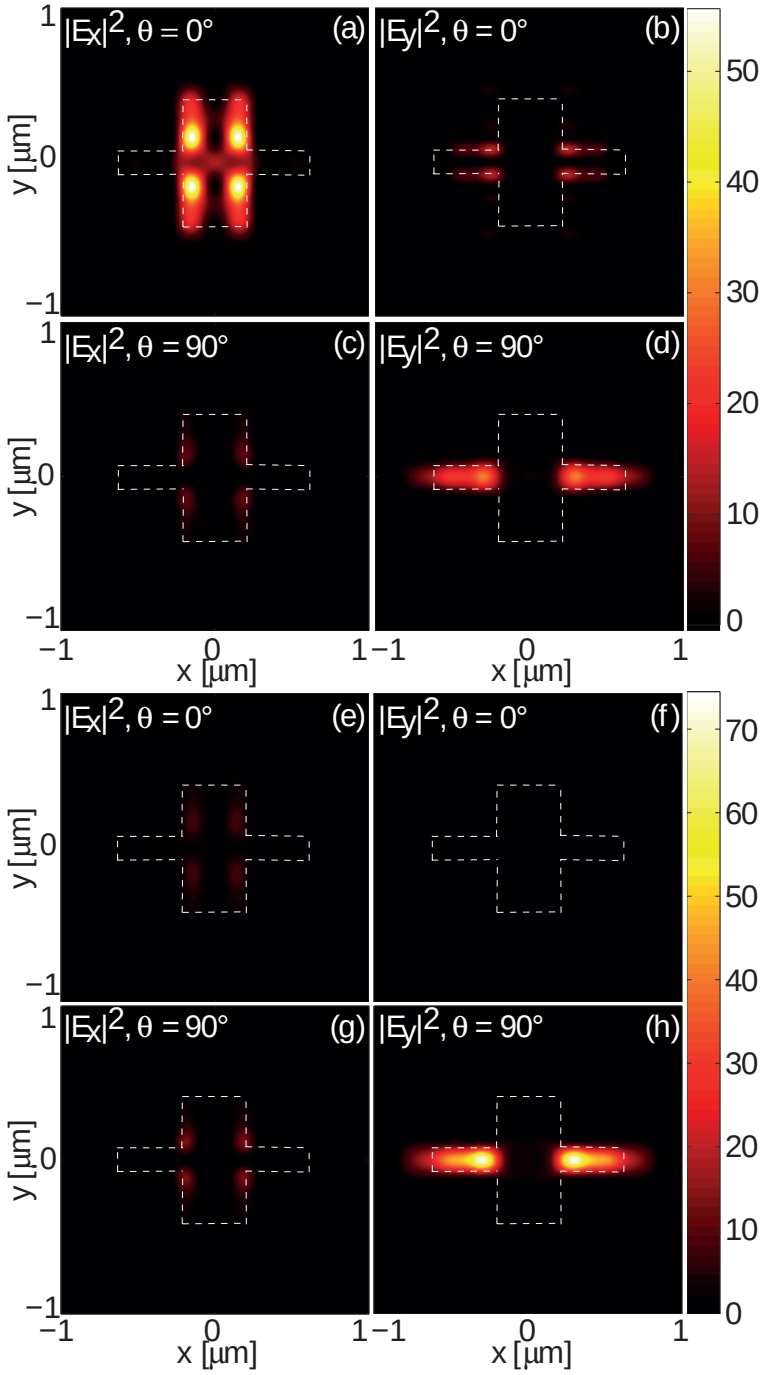

Fig. 9.4: Simulated spatial profiles of the electric field for $\theta = 0$ and $\theta = 90°$. Panels a, b, c, and d show the field profiles at a wavelength of $3.9\ \mu\mathrm{m}$ (corresponding to peak A in Fig. 9.3b), while panels e, f, g, and h show the field profiles at a wavelength of $5.75\ \mu\mathrm{m}$ (corresponding to peak B in Fig. 9.3b). The electric field is normalized to the amplitude of the incident plane wave.

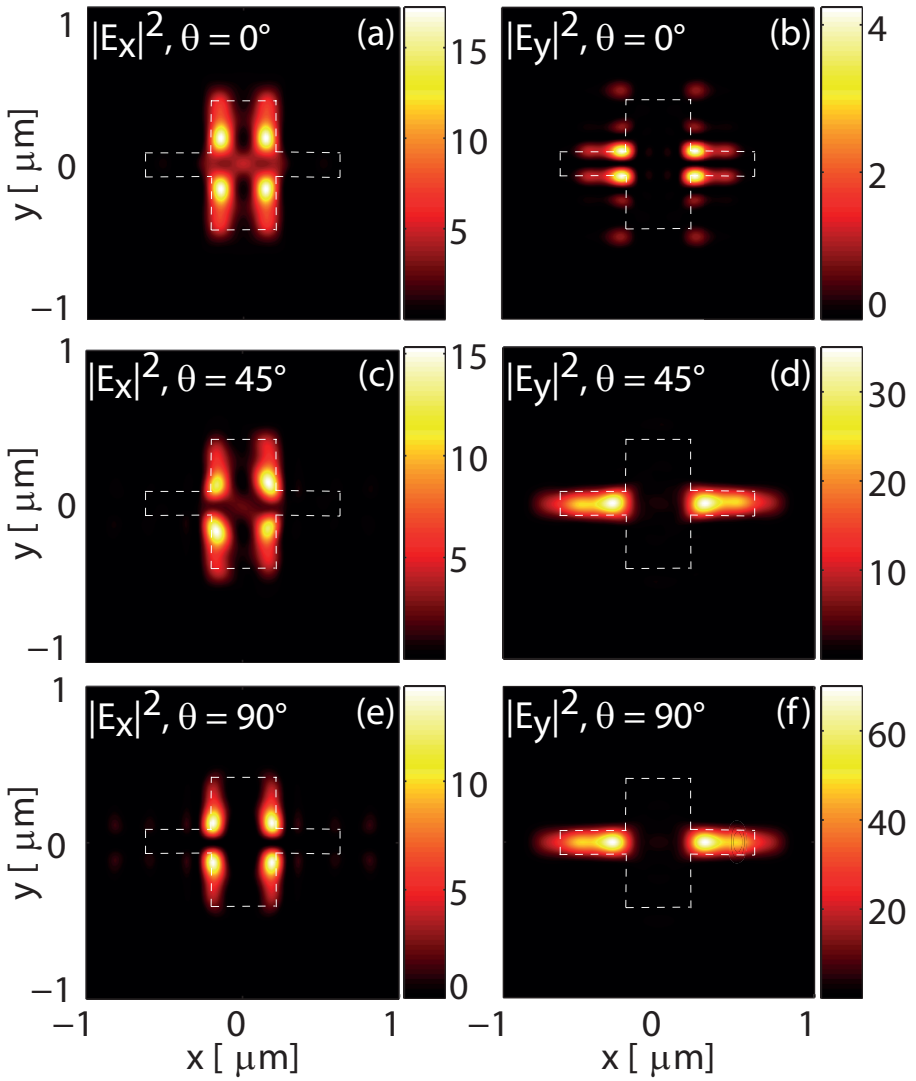

Fig. 9.5: Simulated spatial profiles of the electric field at the isosbestic point ($\lambda = 4.75\ \mu$m, corresponding to point I in Fig. 9.3b) for $\theta = 0$, $\theta = 45°$, and $\theta = 90°$. The electric field is normalized to the amplitude of the incident plane wave.

ments, as compared to those in simulations, presumably due to losses resulting from the surface roughness of the evaporated metal film [22] and low signal-to-noise ratio of the detector in the lower-wavelength spectral domain.

In contrast, peaks A and B result from local surface plasmon resonances in the shorter and longer arms of the asymmetric aperture, respectively. More specifically, they correspond to the cut-off wavelength of the waveguide modes supported by the cruciform apertures. This interpretation is further supported by the fact that the simulated spectra for the symmetric apertures are polarisation-independent as in this case the two modes are degenerate. Importantly, since the properties of these modes are defined entirely by the shape of the apertures, the corresponding transmission depends only on the optical coupling between these modes and the incoming plane wave and as such it is not affected by the roughness of the top surface of the metallic film. The amplitudes of

the measured LSP transmission peaks A and B are suppressed by comparison with the simulated peaks due to similar loss processes which suppress the extended SPP modes as described above. Structural variations introduced by the fabrication process may also play a role.

Figures 9.4 and 9.5 show the simulated field distributions within the apertures which help confirm that the interpertration of peaks A and B corresponding to LSP resonances is correct. The field profiles correspond to a depth of half of the thickness of the Au film. Figure 9.4 shows the field distributions at polarisation angles of $\theta = 0$ and $\theta = 90^\circ$ at the two transmission peaks in Fig. 9.3b. The field profiles in panels (a)–(d) in Fig. 9.4 illustrate the in-plane electric-field components at $\lambda = 3.9\ \mu\mathrm{m}$ (corresponding to peak A), while panels (e)–(h) in this same figure show the field profiles at $\lambda = 5.75\ \mu\mathrm{m}$ (corresponding to peak B). From these simulations it is clear that peak A occurs due to the resonant excitation of a waveguide mode that is primarily polarised transverse to the shorter, y-oriented arm of the aperture (as shown in 9.4a). Similarly, peak B corresponds to the cut-off wavelength of a waveguide mode with polarisation primarily transverse to the longer, x-oriented arm (as shown in 9.4h). Switching between these two modes is accomplished by changing the polarisation of the incident plane wave. It should be noted that these LSP resonances do not correspond to the cut-off modes of the separate arms of the cruciform apertures, as in this case the cut-off wavelength would obey the relation $\lambda_c < 2\mathrm{max}(L_x, L_y)$. Importantly, this result suggests that the wavelength of the transmission peaks can be readily tuned over a wide spectral range by simply changing the shape of the apertures.

Figure 9.5 shows the in-plane electric field distributions at the transmissive isosbestic point in the simulations (Fig. 9.3b), $\lambda = 4.75\ \mu\mathrm{m}$, at polarisation angles of $\theta = 0$, $\theta = 45^\circ$, and $\theta = 90^\circ$. Unlike the fields corresponding to transmission maxima, the fields calculated at the isosbestic point do not have a predominant polarisation state. This phenomenon also explains why such an isosbestic point exists. Thus, if $T_x(\lambda)$ and $T_y(\lambda)$ denote the transmission spectra corresponding to an incident plane wave polarized along the x- and y-axis, respectively, and it is assumed that there is a wavelength, λ_0, for which $T_x(\lambda_0) = T_y(\lambda_0)$, then, at $\lambda = \lambda_0$, the total transmission corresponding to the polarisation angle θ is $T(\lambda_0) = T_x(\lambda_0)\cos^2\theta + T_y(\lambda_0)\sin^2\theta$, *i.e.*, it is independent of the polarisation angle θ. In other words, despite the fact that the plasmonic metasurface is anisotropic, at $\lambda = \lambda_0$ it is optically isotropic. A similar argument holds for the isosbestic points in the reflection and absorption spectra, although the wavelength at which the reflectivity coefficients, $R_x(\lambda)$ and $R_y(\lambda)$, and the absorption components, $A_x(\lambda)$ and $A_y(\lambda)$, are mutually equal would differ in the three cases. This is an expected result as the total transmission and reflection coefficients and, implicitly, the total absorption, depend in a intricate way on the reflection and transmission coefficients at the

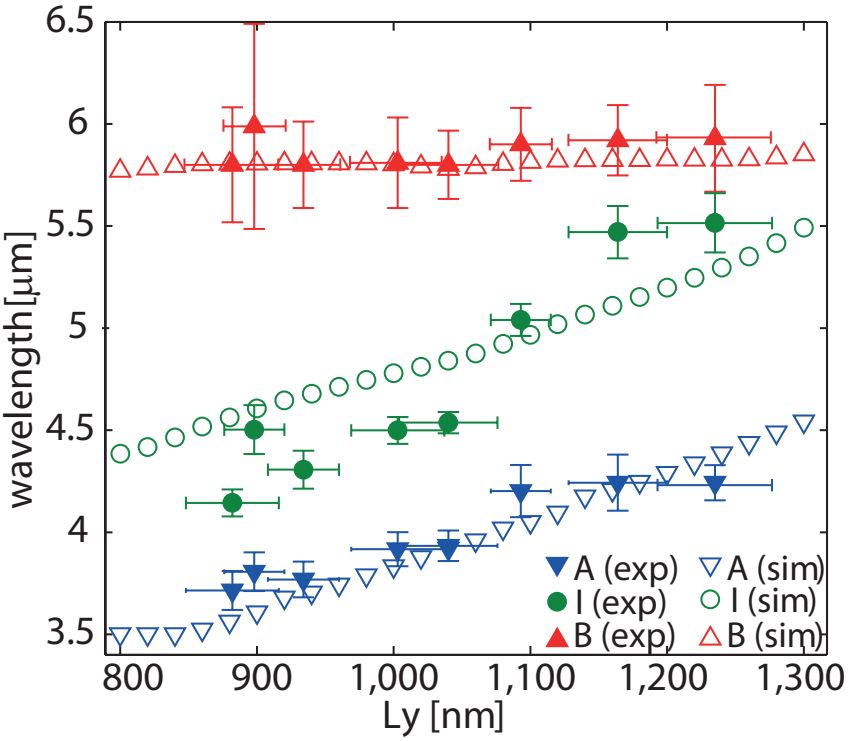

Fig. 9.6: L_y-dependence of the wavelength of the LSP transmission resonances A (blue) and B (red), and the isosbestic point I (green). Filled points are experimental data; unfilled points are data from simulations. Error bars in L_y correspond to the standard deviation of the fabricated device dimensions. Experimental measurements were performed at the London Center for Nanotechnology by P. Thompson.

top and bottom facets of the metal film as well as the coupling coefficients between the LSPs excited in the cruciform apertures and the incoming/outgoing plane waves [15]. Going back to the analogy with physical chemistry, the plasmonic metasurface can be viewed as a 2D distribution of meta-molecules whose polarizability, at the isosbestic point, is independent on polarisation.

In order to further validate the interpretation of the physical origin of the resonant peaks, the spectral location of the resonant peaks A and B, as well as that of the isosbestic point I for several values of L_y are plotted in Fig. 9.6. As expected, peak A (the shorter wavelength peak) shifts to longer wavelengths as the length, L_y, of the shorter arm increases, whereas peak B (the longer wavelength peak) is invariant with L_y. Also, as the length of L_y increases, the cruciform apertures tend toward symmetry in L_x and L_y. Thus peaks A and B, and the isosbestic point I, tend to converge toward a single peak with the amplitude of peak A increasing (due to an increasing area of the optical mode) and the amplitude of peak B decreasing. Also plotted in Fig. 9.6 are the results of the simulations for varying L_y. The values of L_x, g_x, and g_y used in the simulations are given by the mean of all these values across all the arrays, as measured by SEM. The results of the numerical simulations agree well with the experimental data, using a single value of the damping frequency $\gamma = 6.08 \times 10^{13}\ \mathrm{s}^{-1}$. This confirms the physical

interpretation of the features observed in the experimental spectra.

These findings suggest that the functionality of the proposed plasmonic nanostructures can be greatly enhanced by interspersing arrays whose unit cell consist of cruciform apertures with different sizes or, more generally, apertures with different other shapes. Since the transmission maxima of the arrays and their optical reflectivity are determined solely by the frequency of the corresponding LSP resonances, the spectral optical response of these plasmonic nanostructures can be tailored for specific applications, allowing one to explore new designs of frequency-agile metasurfaces with enhanced functionality. One such potential application is to broadband negative index metamaterials. Specifically, it has been demonstrated that by layering 2D plasmonic arrays of symmetric crosses and dielectric thin-film spacers one obtains metamaterials with a negative index of refraction [6]. In this connection, the study present in this chapter suggests that employing plasmonic arrays made of asymmetric crosses opens up the possibility of achieving negative index of refraction over a broad frequency domain. Moreover, the frequency of LSP resonances changes significantly with the index of refraction of a chemical substance filling the apertures, an effect that can be used to develop new plasmonic-based nanodevices for parallel, on-chip sensing for chemical and biomedical applications. In particular, it has been recently demonstrated [23] that molecules deposited on an optically thick metallic film perforated by a periodic array of holes can dramatically affect the transmission spectra, at wavelengths at which they are strongly absorbent, an effect called absorption induced transparency. In this connection, it can be readily understood that these plasmonic structures can be used as tunable surface filters for chemical or biological analysis.

9.4 Using Plasmon Resonances to Enhance Absorption in Metasurfaces

Another important application of the high field enhancement achievable in nanopatterned plasmonic metasurfaces is the ability to increase the total absorption of such structures. As it is well known, the absorbed electromagnetic power in a material is directly proportional to the square amplitude of the electric field in that material [24] (also see appendix D). Consequently, our plasmonic metasurfaces can be used to both enhance and control the amount of absorption in such structures. This has major practical implications in developing new metamaterials with enhanced absorption such as, for example, new photovoltaic devices [25, 26].

To investigate this effect, a new set of devices was fabricated. Thus, the metasurfaces shown in Fig. 9.2 were covered with a 100 nm thick layer of poly(methyl methacrylate) (PMMA). The covering process employed the spin coating method to

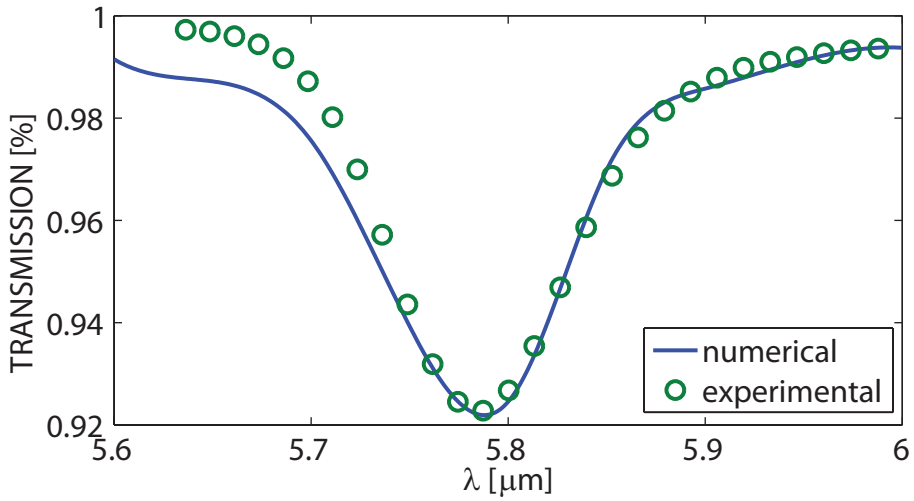

Fig. 9.7: Experimentally measured (circles) and simulated (solid line) transmission through a 100 nm thick slab of PMMA. The experimental data was obtained at the London Centre for Nanotechnology by E. Osley.

ensure that the PMMA layer is uniformly distributed on top of the Au layer while completely filling the cruciform apertures. These samples were then analysed using FTIR microscopy, as before. The fabrication and experimental analysis of the PMMA devices were carried out at the London Centre for Nanotechnology by E. Osley.

Due to its molecular structure, PMMA shows an absorption peak at $5.783\ \mu\mathrm{m}$, which corresponds to the resonant absorption of the carbon-oxygen double bond [27]. It was already shown in Fig. 9.6 that the spectral position of the transmission peaks in cruciform apertures can be easily tailored throughout the infrared spectrum. At the same time, Fig. 9.4 indicates that the peak in transmission is due to a strong field enhancement inside the apertures, caused by the excitation of localised plasmon resonances. By combining these two phenomena it can thus be possible to control, as well as enhance, the absorption, transmission and reflection characteristics of PMMA coated metasurfaces.

In order to find the appropriate geometrical parameters for the new devices, one of the two spectral peaks of a cruciform array needs to be matched to the absorption peak of PMMA. Numerical simulations based on the RCWA were performed in order to determine the proper parameters required for the new apertures. In order to accurately model the absorption of the carbon-oxygen double bond, the transmission of a $100\ \mathrm{nm}$ thick PMMA slab was experimentally determined. Transmission through the same structure was then numerically calculated. The imaginary part of the refractive index of PMMA was modelled using the Lorentzian function:

$$\mathrm{Im}[n_{PMMA}(\lambda)] = \frac{2A}{\pi}\left[\frac{\gamma}{(\lambda-\lambda_0)^2+\gamma^2}\right]. \tag{9.9}$$

By tuning the parameters of Eq. (9.9) it was possible to obtain a very good fit of the

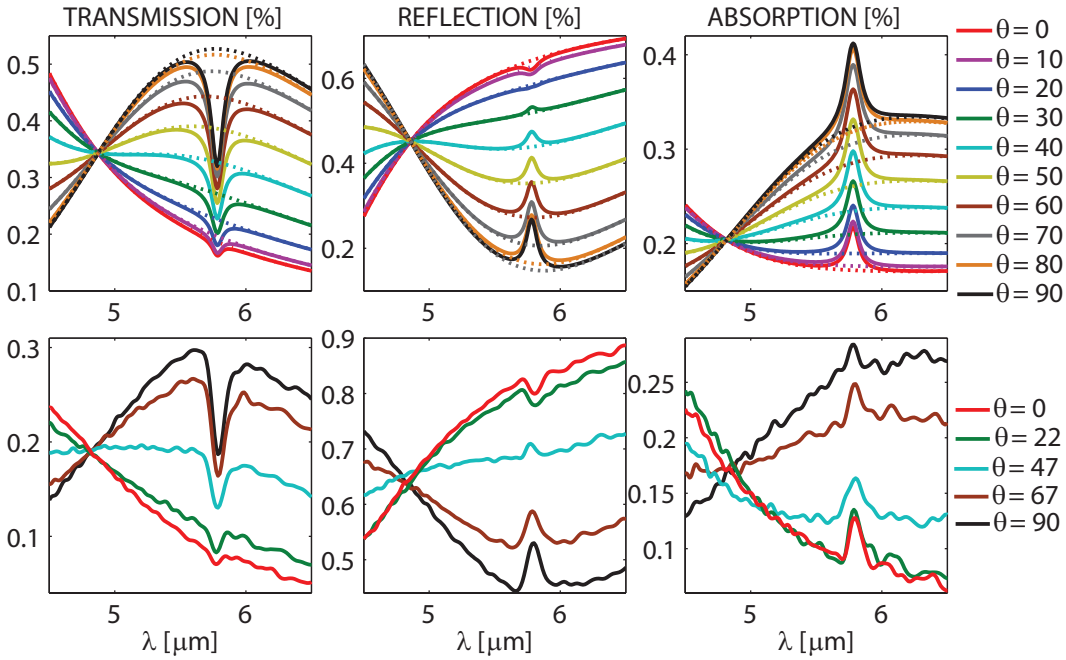

Fig. 9.8: Top panels show numerical results for transmission, reflection and absorption of a PMMA coated cruciform apertures (solid lines) and an identical aperture with PMMA treated as a non-absorbing dielectric (dashed lines). Bottom panels show the experimentally measured values for a PMMA coated structure with the same geometry. Experimental data was obtained at the London Centre for Nanotechnology by E. Osley.

experimentally measured transmission spectra for $A = 21.6$ nm, $\gamma = 46.5$ nm and $\lambda_0 = 5.783$ μm. Figure 9.7 summarises our results.

Using this accurate model of the absorption in the PMMA, it is possible to numerically find the transmission, reflection and absorption spectra of PMMA coated cruciform apertures. The numerical results showed that for an asymmetric cross with geometrical parameters $L_x = 1.731$ μm, $L_y = 1.185$ μm, $g_x = 0.471$ μm and $g_y = 0.265$ μm, the wavelength of the transmission peak B exactly matches the wavelength of the PMMA C=O bond absorption peak. A sample with these geometrical parameters was then fabricated and analysed using FTIR.

Figure 9.8 shows the results of the numerical and experimental investigations. The presence of the PMMA layer has a significant effect on the spectral shape of the plasmon resonance. The transmission through the apertures decreases due to the PMMA coating and is also strongly influenced by the intensity of the field, as expected. Thus, for $\theta = 90°$ polarisation, for which the uncoated structure has a maximum transmission at this wavelength, the transmission is decreased by almost 15%. However, for the $\theta = 0$ polarisation, the decrease in transmission is only about 1%. In the case of the reflection coefficient, the decrease in transmission is accompanied, as expected, by an increase in reflection. Remarkably, however, at a polarisation angle of $\theta \approx 20°$, the trend reverses and the reflection decreases compared to the reflection of an uncoated aperture. This effect has an interesting consequence. Close to the $\theta = 20°$ polarisation,

the reflection spectra of the PMMA coated structures becomes identical to the reference spectra of the apertures with no PMMA absorption.

The third plot in Fig. 9.8 shows that the PMMA coating has a large effect on the absorption as well. As the polarisation angle approaches $\theta = 90^{\circ}$, the relative absorption increases. This agrees well with the original assumption that the stronger field enhancement at the resonant wavelength and polarisation angle will lead to a higher absorption in this structure. It is worth mentioning here that these results were obtained for a single structure that was designed so that the second resonant peak of the cruciform aperture would be located at the same wavelength as the PMMA absorption peak. With further tailoring and more complex geometries it can be possible to build new designs with an even higher increase in absorption as well as the ability for fine tuning of the absorption, the reflection and transmission by simply changing the polarisation of the incoming light. Finally, it is important to note that Fig. 9.8 also shows a very good agreement between the numerical and experimental data.

9.5 Conclusions

In summary, in this chapter, a comprehensive theoretical and experimental study of optical properties of plasmonic metasurfaces characterized by strong form-anisotropy of the unit cell was presented. In particular, it has been demonstrated that the excitation of LSP resonances strongly affects the transmission spectra of the plasmonic nanostructure by providing polarisation-dependent transmission channels. This feature allows the transmission properties of the plasmonic arrays to be readily tuned by properly engineering the shape and size of the unit cell of the array. These findings can foster exciting new applications in nanophotonics and plasmonics, including frequency-agile surfaces, polarisation-selective absorbers, strongly anisotropic metamaterials, plasmonic-based sensors for chemical and biomedical applications, and broadband negative index metamaterials.

At the same time, it was shown that PMMA coated plasmonic metasurfaces can further enhance the resonant effects in anisotropic surface gratings, leading to increased absorption. As such, this property could be employed in applications where high field concentration and high absorption are required such as, for example, new plasmon based photovoltaic devices. It also becomes clear that these designs could potentially be employed in non-linear optical devices either by relying on surface second harmonic generation or by using a bulk non-linear material. Such efforts could lead to new physical insight into the properties of metasurfaces, including the design of metasurfaces with externally tuneable effective non-linear properties.

Bibliography

[1] R. M. Roth, N. C. Panoiu, M. M. Adams, J. I. Dadap, and R. M. Osgood. Polarization-tunable plasmon-enhanced extraordinary transmission through metallic films using asymmetric cruciform apertures. *Opt. Lett.*, 32(23):3414–3416, 2007.

[2] C. Menzel, C. Helgert, C. Rockstuhl, E.-B. Kley, A. Tünnermann, T. Pertsch, and F. Lederer. Asymmetric Transmission of Linearly Polarized Light at Optical Metamaterials. *Phys. Rev. Lett.*, 104(25):253902, June 2010.

[3] X. M. Goh, L. Lin, and A. Roberts. Plasmonic lenses for wavefront control applications using two-dimensional nanometric cross-shaped aperture arrays. *J. Opt. Soc. Am. B*, 28(3):547–553, 2011.

[4] X. Liu, T. Starr, A. F. Starr, and W. J. Padilla. Infrared Spatial and Frequency Selective Metamaterial with Near-Unity Absorbance. *Phys. Rev. Lett.*, 104(20):207403, May 2010.

[5] R. Qiang, J. Chen, T. Zhao, S. Wang, P. Ruchhoeft, and M. Morgan. Modelling of infrared bandpass filters using three-dimensional FDTD method. *Electron. Lett.*, 41(16):914–915, 2005.

[6] C. Imhof and R. Zengerle. Pairs of metallic crosses as a left-handed metamaterial with improved polarization properties. *Opt. Express*, 14(18):8257–8262, September 2006.

[7] L. Lin, L. B. Hande, and a. Roberts. Resonant nanometric cross-shaped apertures: Single apertures versus periodic arrays. *Appl. Phys. Lett.*, 95(20):201116, 2009.

[8] L. Lin and A. Roberts. Angle-robust resonances in cross-shaped aperture arrays. *Appl. Phys. Lett.*, 97(6):061109, 2010.

[9] P. G. Thompson, C. G. Biris, E. J. Osley, O. Gaathon, R. M. Osgood, N. C. Panoiu, and P. A. Warburton. Polarization-induced tunability of localized surface plasmon resonances in arrays of sub-wavelength cruciform appertures. *Opt. Express*, xx(xxxx):(to be submitted), 2011.

[10] T. Zentgraf, T. P. Meyrath, A. Seidel, S. Kaiser, H. Giessen, C. Rockstuhl, and F. Lederer. Babinets principle for optical frequency metamaterials and nanoantennas. *Phys. Rev. B.*, 76(3):033407, July 2007.

[11] C. Rockstuhl, T. Zentgraf, T. P. Meyrath, H. Giessen, and F. Lederer. Resonances in complementary metamaterials and nanoapertures. *Opt. Express*, 16(3):2080–2090, February 2008.

[12] M. G. Moharam and T. K. Gaylord. Rigorous coupled-wave analysis of metallic surface-relief gratings. *J. Opt. Soc. Am. A*, 3(11):1780–1787, November 1986.

[13] L. Li. New formulation of the Fourier modal method for crossed surface-relief gratings. *J. Opt. Soc. Am. A*, 14(10):2758, October 1997.

[14] L. C. Liu and J. W. S. Liu. *Linear Systems Analysis*. McGraw-Hill, New York, 1975.

[15] F. J. Garcia-Vidal, T. W. Ebbesen, and L. Kuipers. Light passing through subwavelength apertures. *Rev. Mod. Phys.*, 82(1):729–787, March 2010.

[16] I. I. Smolyaninov, A. V. Zayats, A. Gungor, and C. C. Davis. Single-Photon Tunneling via Localized Surface Plasmons. *Phys. Rev. Lett.*, 88(18):187402, 2002.

[17] S. A. Maier. *Plasmonics: Fundamentals and Applications*. Springer-Verlag, New York, 2007.

[18] RSoft Design Group. `http://www.rsoftdesign.com/`.

[19] M. A. Ordal, R. J. Bell, R. W. Alexander, L. L. Long, and M. R. Querry. Optical properties of fourteen metals in the infrared and far infrared: Al, Co, Cu, Au, Fe, Pb, Mo, Ni, Pd, Pt, Ag, Ti, V, and W. *Appl. Optics*, 24(24):4493–4499, December 1985.

[20] U. Kreibig and M. Vollmer. *Optical Properties of Metal Clusters*. Springer-Verlag, Berlin, 1995.

[21] S. Zhang, W. Fan, B. K. Minhas, A. Frauenglass, K. J. Malloy, and S. R. J. Brueck. Midinfrared Resonant Magnetic Nanostructures Exhibiting a Negative Permeability. *Phys. Rev. Lett.*, 94(3):037402, January 2005.

[22] H. Raether. *Surface Plasmons on Smooth and Rough Surfaces and on Gratings*. Springer-Verlag, Berlin, 1986.

[23] J. A. Hutchison, D. M. O'Carroll, T. Schwartz, C. Genet, and T. W. Ebbesen. Absorption-induced transparency. *Angew. Chem. Int. Ed.*, 50(9):2085–9, February 2011.

[24] J. D. Jackson. *Classical Electrodynamics*. John Wiley & Sons, Hoboken, 3rd edition, 1999.

[25] N. C. Panoiu and R. M. Osgood. Enhanced optical absorption for photovoltaics via excitation of waveguide and plasmon-polariton modes. *Opt. Lett.*, 32(19):2825–2827, October 2007.

[26] H. A. Atwater and A. Polman. Plasmonics for improved photovoltaic devices. *Nature Mater.*, 9(3):205–213, 2010.

[27] B. H. Stuart. *Infrared spectroscopy: fundamentals and applications*. John Wiley & Sons, Hoboken, 2004.

Chapter 10

Second Harmonic Generation in Plasmonic Metasurfaces

10.1 Introduction

As discussed in Chapter 2, there is a high degree of interest in non-linear effects in nano-patterned metasurfaces and their technological applications. In this chapter, a theoretical and numerical study of second harmonic generation in chiral metasurfaces will be presented and the results compared to experimental findings. The first part of the chapter will present the results of a computational analysis of the spatial distribution of the local field enhancement at the fundamental frequency. The numerical maps of the local field enhancement at the fundamental frequency will be shown to match the experimental mapping of SHG sources. Consequently, this analysis proves that the origin of the SHG can unambiguously be attributed to maxima of the surface charge density, which in turn depend on the geometry of the structures. These results suggest that SHG microscopy can be used efficiently for mapping the local field enhancement in nanostructured metamaterials [1].

In the second part of the chapter an example of how SHG microscopy can be used to investigate complex electromagnetic phenomena in metasurfaces, at the nanoscale, will be given. Specifically, it will be demonstrated how numerical simulations confirm that surface non-linear effects can be studied using the magnetisation-induced second harmonic generation (MSHG) microscopy. Thus, it will be shown, through a mix of numerical results validated by experiment, that surface plasmons can create asymmetries in the rotational dependence of the MSHG signal, which can reveal the direction of the magnetization in nanostructures made of nickel [2].

10.2 The Origin of Second Harmonic Generation in Chiral Optical Metamaterials

To understand the origin of SHG in metallic gratings we need to consider the polarisation at the second harmonic. As previously mentioned, this polarisation ca be written as the sum of two contributions:

$$P_i(2\omega) \propto P_i^s(2\omega) + P_i^b(2\omega) = \epsilon_0 \chi_{ijk}^{(2)} : E_j(\omega) E_k(\omega) + \epsilon_0 \chi_{ijkl}^{(3)} \vdots E_j(\omega) \nabla_k E_l(\omega), \quad (10.1)$$

where $\chi_{ijk}^{(2)}$ and $\chi_{ijkl}^{(3)}$ are second- and third-rank susceptibility tensors, respectively, while i, j and k represent any of the Cartesian coordinates x, y and z. The first polarisation term in Eq. (10.1) is the *surface-specific* electric dipole contribution, indicated by the index s. The second polarisation term in Eq. (10.1) includes the *bulk-specific* electric quadrupole and magnetic dipole contributions, indicated by the index b. In isotropic media, the latter takes the following form [3]:

$$\begin{aligned} \mathbf{P}^b(2\omega) = {} & \epsilon_0(\chi_{xxxx} - \chi_{xyyx} - \chi_{xxxy} - \chi_{xyxy}) \sum_i \hat{e}_i E_i(\omega) \nabla_i E_i(\omega) \quad (10.2) \\ & + \epsilon_0 \frac{\chi_{xyxy}}{2} \nabla[\mathbf{E}(\omega) \cdot \mathbf{E}(\omega)] + \epsilon_0 \chi_{xyyx} [\mathbf{E}(\omega) \cdot \nabla] \mathbf{E}(\omega) + \epsilon_0 \chi_{xxyy} \mathbf{E}(\omega) [\nabla \cdot \mathbf{E}(\omega)]. \end{aligned}$$

If metals are considered, this relation can be written as [4]:

$$\mathbf{P}^b(2\omega) \propto \chi_{xyyx} [\mathbf{E}(\omega) \cdot \nabla] \mathbf{E}(\omega) + \chi_{xxyy} \mathbf{E}(\omega) [\nabla \cdot \mathbf{E}(\omega)]. \quad (10.3)$$

If we assume that $\mathbf{E}_{local}(\omega) = L(\omega)\mathbf{E}(\omega)$, where $L(\omega)$ represents the local field factors for the fundamental frequency [3], it then follows that, for the dipolar contributions:

$$P_{i,local}^s \propto L(2\omega) \chi_{ijk}^{(2)} : E_{j,local}(\omega) E_{k,local}(\omega) \propto L(2\omega) L^2(\omega) P_i^s(2\omega), \quad (10.4)$$

where $L(2\omega)$ represents the local field factors at the SH. The local field factors $L(\omega)$ and $L(2\omega)$ contain the contributions from plasmonic excitations, such as those observed in our nanostructures. Furthermore, for the quadrupolar contributions:

$$\begin{aligned} \mathbf{P}_{local}^b(2\omega) \propto {} & L(2\omega) \chi_{xyyx} [L(\omega)\mathbf{E}(\omega) \cdot \nabla] L(\omega)\mathbf{E}(\omega) \\ & + L(2\omega) \chi_{xxyy} L(\omega)\mathbf{E}(\omega) [\nabla \cdot L(\omega)\mathbf{E}(\omega)]. \quad (10.5) \end{aligned}$$

Combining Eqs. (10.4) and (10.5), we obtain:

$$\mathbf{P}_{local}(2\omega) = L(2\omega) L^2(\omega) \mathbf{P}(2\omega). \quad (10.6)$$

And henceforth, the intensity at the second harmonic can be expressed as:

$$I(2\omega) \propto |L(2\omega)L^2(\omega)\mathbf{P}(2\omega)|^2. \tag{10.7}$$

This relationship implies that, in metal nanostructures, we expect a correspondence between the distribution of local field enhancement at the fundamental frequency and the SHG sources.

One of the main difficulties in characterizing the SHG from metallic nanoparticles stems from the fact that the SHG can be the result of several competing contributions, such as electric dipoles, magnetic dipoles and electric quadrupoles, as well as higher-order effects. In centrosymmetric materials, the (local) bulk electric dipole contribution to the SHG cancels and, therefore, the leading-order sources of the SHG are surface electric dipoles and the (nonlocal) contributions from bulk magnetic dipoles and electric quadrupoles. In metallic nanostructures, the local field enhancement and the corresponding large spatial variation of the field distribution increase the contribution to the SHG of both the surface and bulk components. Large multipolar contributions have thus been observed in plasmonic *L*-shaped [5] and *G*-shaped [6] metal nanostructures. Contributions from octupoles to the SHG signal of gold nanoparticles with size of $\approx 100\ \mathrm{nm}$ have also been reported [7]. In this connection, a theoretical model that attributes most SHG to the bulk sources, thus explaining the enhancement of multipolar contribution to the SHG, has been proposed [8]. However, this same issue of surface versus bulk contribution to the SHG in nanostructured metal films has been previously investigated, the conclusion of this study being that the surface contribution dominates [9]. While the distribution of the local field enhancement at the fundamental frequency undoubtedly plays a role in the SHG response, both these studies lack an experimental mapping of the near-field distribution at the second harmonic.

The relationship between the local field enhancement at the fundamental frequency and the SHG in chiral metamaterials has not been unambiguously demonstrated yet. Because of the large dielectric constant of most metals, the near-field distribution in metallic nanostructures is extremely inhomogeneous. In previous theoretical studies the local field enhancement and spatial field inhomogeneity have been taken into account, for instance, when calculating the SHG response of spherical particles [10]. Numerical simulations based on the multiple scattering approach, for example, can rigorously provide the spatial variation of the fundamental frequency and the second harmonic fields at nanoscale although, in some cases, they can be time consuming and computationally demanding. To validate these numerical algorithms, however, it is essential to develop alternative, experimental techniques, which then are to be used in conjunction with numerical methods to explore nonlinear optical effects at the nanoscale.

10.3 Numerical Simulations and Experimental SHG Microscopy

The plasmonic structures being investigated are shown in Fig. 10.1. In Fig. 10.1a and Fig. 10.1b, the geometry of the G-shaped and mirror-G-shaped nanostructures, respectively, can be seen. The substrate consists of a single crystalline Si layer toped by a $100\ \mathrm{nm}$ thick SiO_2 layer. The Au structures have a thickness of $25\ \mathrm{nm}$ and are grown on top of the silica. A $3\ \mathrm{nm}$ thick layer of Ti assures adhesion between the Au and the substrate. The transverse profile of the structures is illustrated in Fig. 10.1c. The samples were fabricated and experimentally investigated at the Katholieke Universiteit Leuven. The experimental SHG field distribution was achieved using a confocal scanning microscope with a fundamental excitation wavelength of 800 nm.

Numerical characterisation of the chiral metasurfaces was performed using two complementary approaches. The first one maps the distribution of fundamental surface currents in the structures and employs the MAGMAS solver. MAGMAS is a numerical software tool, originally developed at the Katholieke Universiteit Leuven, for electromagnetic problems in the microwave and millimeter wave frequency bands [11, 12].

In the second approach, the near-field distribution at the fundamental frequency was investigated using RSoft's DiffractMOD [13] which is based on the RCWA. In the simulations numerical convergence has been reached when $N = 17$ diffraction orders were used [see Sec. 9.2] for each transverse dimension, which amounts to $M = (2N + 1)^2 = 1225$ Fourier modes. Moreover, it was assumed that the dielectric constant of gold is described by the Lorentz-Drude model. The simulations have shown that the Ti adhesion layer does not affect the field distribution at the surface of the metallic structures although, as expected, it leads to larger overall absorption in the structure. This increase can be explained by the presence of the thin metallic layer of Ti which, coupled with the resonant surface plasmon modes, leads to increased metallic absorption. Figure 10.2 illustrates this result.

For these structures, under the influence of linearly polarized light, SHG microscopy reveals four hotspots that are positioned along the diagonals in Fig. 10.3c

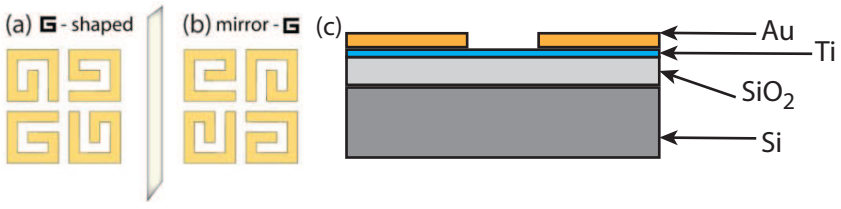

Fig. 10.1: Four-fold simmetry chiral (G-shaped) metasurfaces. Panels (a) and (b) show the surface pattern. Panel (c) gives a depth profile. The samples were prepared at the Katholieke Universiteit Leuven by V. Valev et al. For more details, see Ref. [1].

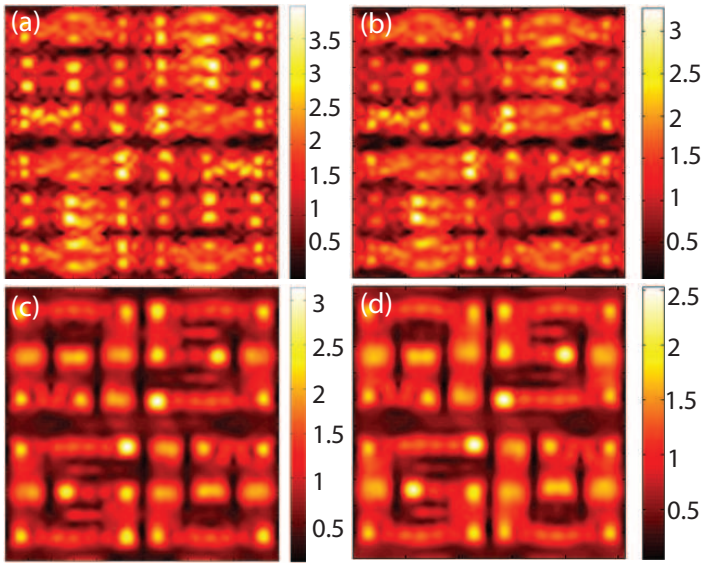

Fig. 10.2: Electric and magnetic field profile distributions at the surface of the G-shaped nanostructures. In (a) and (b), electric field profile without and with the Ti adession layer, respectively. In (c) and (d), the same but for the magnetic field.

and Fig. 10.3d. This result has already been reported, though the precise location of the hotspot on the structures was not clear [14].

Figure 10.3e and Fig. 10.3f show the numerical maps of the current distribution at the surface of the nanostructures, calculated using MAGMAS. In each case, the strongest field enhancements are situated in four regions that correspond to the SHG hotspots. Because these simulations do not take into account the dielectric, the substrate, and the Ti adhesion layer, their agreement with the SHG results demonstrates that the electromagnetic behavior of the gold nanostructures is the main cause for the SHG signal. Moreover, numerical simulations of the electric fields at the fundamental frequency in Fig. 10.3g and Fig. 10.3h are in remarkable agreement with both MAGMAS simulations and the SHG microscopy. For better comparison with the SHG, the DiffractMOD results show the squared electric fields at the surface of the nanostructures. The agreement between the experimental results at the second harmonic and both simulations at the fundamental frequency can also be observed for right-hand circularly polarized light, Fig. 10.3i to Fig. 10.3n, as well as for left-hand circularly polarized light, Fig. 10.3o to Fig. 10.3t. It should be noted that for circularly polarized light, there is a large circular dichroism effect both in the SHG and in the simulations. In fact, this effect regarding SHG has previously been reported, though, as with linearly polarized light, the location and origin of the hotspot patterns was ambiguous.

It should be noted that both the MAGMAS and the DiffractMOD simulations were performed with a linearly polarized light and did not take into account the tight beam focusing of the beam. More specifically, the incident beam was assumed to be a plane wave. In the case of the simulations performed using DiffractMOD, field profiles for

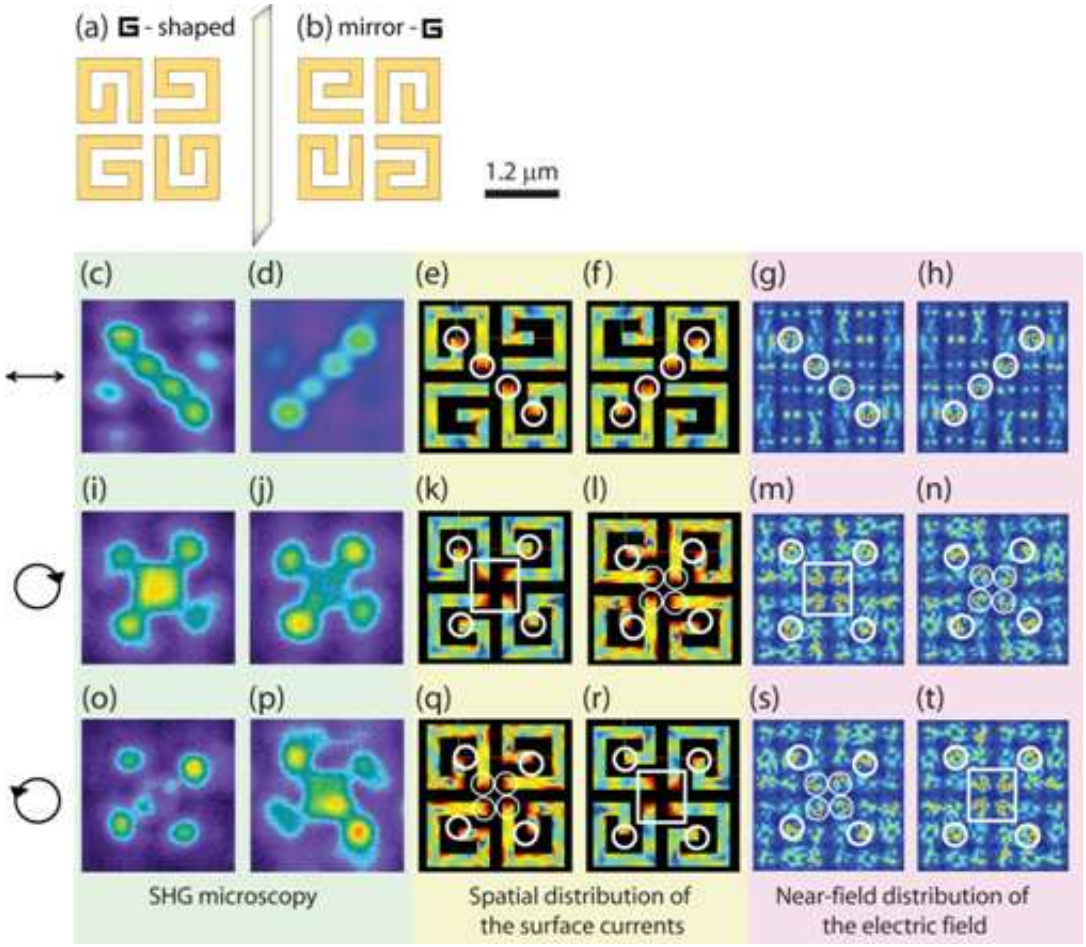

Fig. 10.3: Mapping of the SHG sources matches the mapping of surface field enhancements at the fundamental frequency. In (a) and (b), the geometry of the two sample configurations that were used for the gold nanostructures. Experiments and calculations were performed for linearly, right-hand and left-hand circularly polarized light as indicated on the left side. The images are organized columnwise according to the sample. The images (c), (i), (o), (e), (k), (q), (g), (m), (s) and (d), (j), (p), (f), (l), (r), (h), (n), (t) refer to G-shaped and mirror-G, respectively. The first two columns of the images are obtained with SHG microscopy. The third and fourth columns are calculated with the MAGMAS software. The first four columns were obtained at the Katholieke Universiteit Leuven by V. K. Valev et. al.. The fifth and sixth columns are obtained with the DiffractMOD software.

the circular polarisation were obtained by combining the results of two independent simulations with x and y linear polarisation, respectively. Thus, the field amplitude in the case of circularly polarised light can be written [15]:

$$U_j^{circular} = U_j^{(x)} \pm iU_j^{(y)}, \tag{10.8}$$

where U is either of the electric or magnetic fields,j is one of the three Cartesian coordinates x, y or z and the superscripts x and y denote the direction of linear polarisation. The choice of plus or minus in Eq. (10.8) correspond to left or right circular polarisation, respectively, when looking into the beam. The agreement between simulations

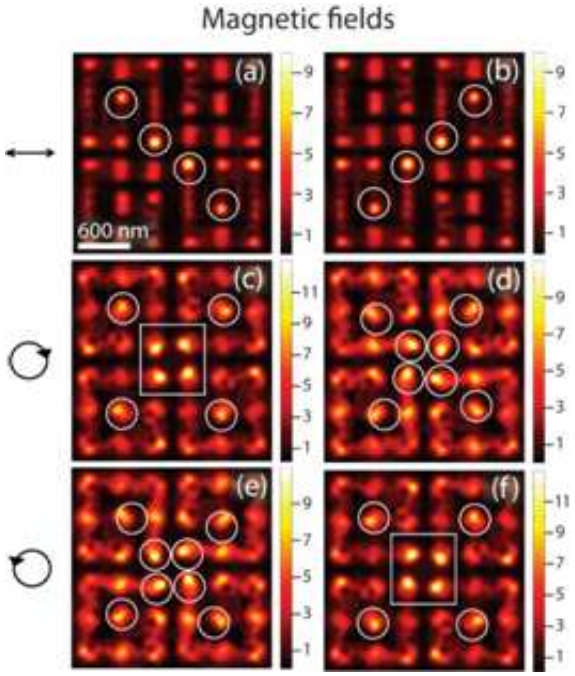

Fig. 10.4: Magnetic fields at the surface of the gold nanostructures also match the distribution of SHG sources. In (a), (c) and (e), magnetic field intensity in G-shaped nanostructures, for linearly, right-hand circularly and left-hand circularly polarized light, respectively. In (b), (d) and (f), magnetic field intensity in mirror-G-shaped nanostructures, for linearly, right-hand circularly and left-hand circularly polarized light, respectively. The white lines are guides to the eye, highlighting the correspondence to the SHG microscopy patterns.

and experimental results clearly demonstrates that the tight focusing does not represent a crucial factor, which is explained by the fact that the hotspot formation is chiefly a near-field effect. The simulations results in Fig. 10.3 pinpoint the exact location of the hotspots on the structures and establish a clear relationship between the location of the second harmonic sources and local field enhancements of the electrical currents and field, at the fundamental frequency.

In optical metamaterials, it was suggested that larger SHG signals could be detected when magnetic-dipole resonances are excited, as compared with purely electric-dipole resonances [39]. In order to investigate the magnetic fields at the fundamental optical frequency in the G-shaped nanostructures, DiffractMOD simulations were performed and the resulting maps are shown in Fig. 10.4. Starting with the G-shaped nanostructures, as it can be seen for linearly, right-hand circularly and left-hand circularly polarized light in Fig. 10.4a, Fig. 10.4b, and Fig. 10.4c, respectively, the maxima of the magnetic field intensities correspond to the SHG microscopy patterns, indicated with white lines. This same correspondence is also observed with the mirror-G-shaped nanostructures, in Fig. 10.4d, Fig. 10.4e, and Fig. 10.4f.

These results demonstrate that the sources of SHG in these structures coincide with the locations of large local field enhancements at the fundamental frequency. From a practical point of view, this data demonstrate that SHG microscopy constitutes an

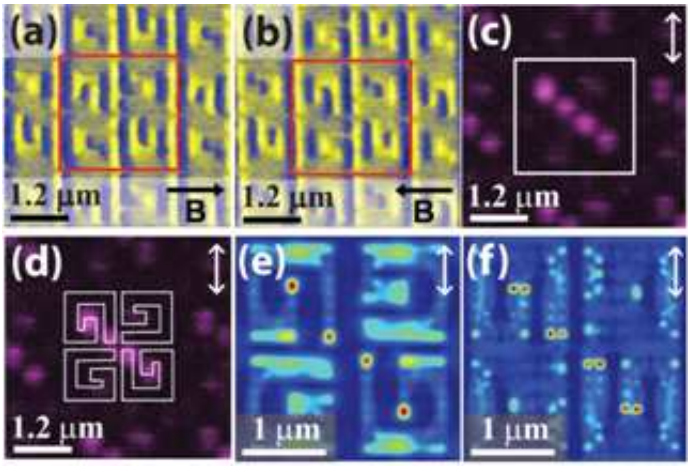

Fig. 10.5: Magnetization-induced second harmonic generation is measured in four-fold symmetric magnetic, plasmonic nanostructures. (a) and (b) are magnetic force microscope images of the sample structures. The yellow-blue contrast reveals typical in-plane magnetization for B=+25 mT and B=-25 mT, respectively. In (c), second harmonic microscopy shows plasmonic local field enhancements at 800 nm. The direction of polarization is indicated with an arrow. In (d), the geometrical structures of the unit cell is superimposed on the SHG micrograph in order to illustrate the origin of the SHG hotspots. In (e) and (f), spatial distribution of the intensity of the magnetic and electric fields, respectively, upon excitation of the sample with 800 nm light. SHG microscopy results were obtained at the Katholieke Universiteit Leuven by V. K. Valev et al.

effective imaging method for mapping local field enhancements in metamaterials. This new visualisation tool is important because it can be instrumental in exploring the novel properties of chiral optical metamaterials.

10.4 Second Harmonic Generation in Nickel Chiral Metasurfaces

A similar structure to the one described in the previous section was also investigated using numerical techniques and SHG microscopy. In this case, the Au surface features were replaced by structures made of nickel. Nickel is known to be a good plasmonic material [16, 17] and, unlike the noble metals, also exhibits strong magnetisation. In these samples, the presence of plasmons is directly evidenced by means of SHG microscopy images. These images are collected using an identical process to the one described in Sec. 10.3.

The field profile shows four hotspots within the unit cell of four Gs. While this unit cell is indicated with a red rectangle in Fig. 10.5a and Fig. 10.5b, it is indicated with a white rectangle in Fig. 10.5c. For clarity, in Fig. 10.5d the geometry of the unit cell is reproduced over the SHG micrograph. In this manner, the origin of the hotspots is revealed. The hotspots themselves are due to localised field enhancements that result in localised SHG sources. The field enhancements are a consequence of localized plasmons in the Ni nanostructures, in agreement with numerical simulations

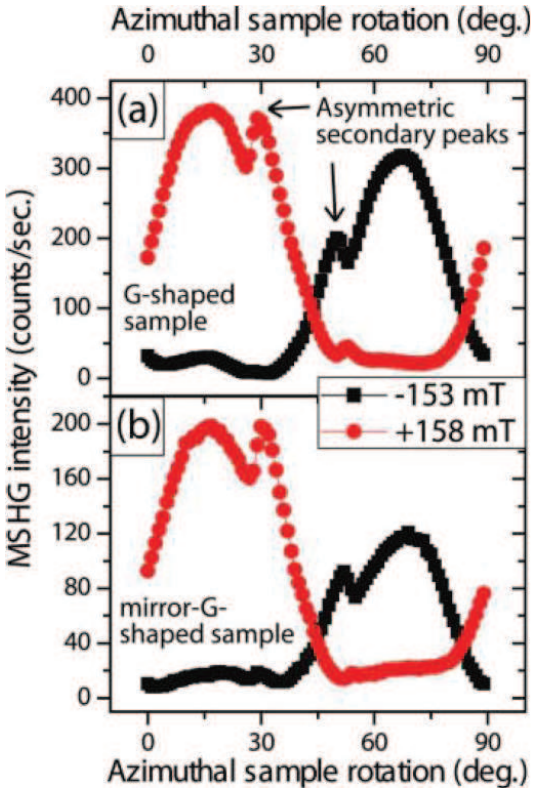

Fig. 10.6: MSHG intensity as a function of the azimuthal sample rotation angle for G-shaped (a) and mirror G-shaped (b) metasurfaces. The samples are placed in an external magnetic field which is switched between $-153\ \mathrm{mT}$ *(black) and* $+158\ \mathrm{mT}$ *(red). The measurements were performed at the Katholieke Universiteit Leuven by V. K. Valev et al.*

of both the optical frequency magnetic (Fig. 10.5e) and electric (Fig. 10.5f) fields. The simulations are performed using RSoft DiffractMod, numerical convergence being reached if $N = 18$ diffraction orders are used for each transverse dimension. The dielectric constant of Ni is described by the Lorentz-Drude model, with the interband effects being characterized by a superposition of four Lorentzians.

The samples were placed in an external magnetic field $\mathbf{B}$ which was applied in the plane of optical incidence. The samples were then rotated around the z axis (azimuthal rotation). According to Eq. 2.72 the orientation of the magnetic field will directly affect the second harmonic field intensity due to MSHG. This effect is shown in Fig. 10.6 wherein $\mathbf{B}$ is switched from $-153\ \mathrm{mT}$ to $+158\ \mathrm{mT}$. The MHSG intensity shows a corresponding switch between the two case, as theoretically predicted. Furthermore, it can be seen in Fig. 10.6 that the position of the resonant peaks is dependent on the sample rotation angle. This can be explained by the fact that in our samples, light waves couple to plasmon modes that depend on the geometry of the nanostructures. Rotating the samples changes the orientation of the structures with respect to the direction of optical polarisation. Consequently, the total MSHG intensity can exhibit local maxima depending on whether or not plasmon modes are addressed along that particular location. Thus, it can be said that MSHG can be used to reveal the direction of magneti-

sation in asymmetric metasurfaces made of nickel, as a direct result of the excitation of surface plasmon modes.

10.5 Conclusions

In conclusion, numerical simulations were used to show that the local field enhancement at the fundamental frequency matches the distribution of hot-spots in SHG from metallic metasurfaces. Consequently, it was shown that SHG microscopy can accurately map the SHG sources of a nanostructure. These results are also in good agreement with the existing theoretical framework for SHG enhancement from local field factors. The numerical simulations presented here could be extended to the second harmonic response in order to reproduce the overall SHG intensity for different polarisation cases.

Also, it was shown that the MSHG effect leads to a change in the intensity of the second harmonic wave in metasurfaces made of nickel. This change is also strongly affected by the coupling of surface plasmon modes and, as a result, MSHG can be employed to determine the the direction of magnetisation in magnetic nanostructures. This result suggests that it is possible to build nano-patterned metasurfaces wherein the effective linear and non-linear properties can be externally controlled using the magneto-optic effect.

Bibliography

[1] V. K. Valev, X. Zheng, C. G. Biris, A. V. Silhanek, V. Volskiy, B. De Clercq, O. A. Aktsipetrov, M. Ameloot, N. C. Panoiu, and G. A. E. Vandenbosch. The origin of second harmonic generation hotspots in chiral optical metamaterials. *Opt. Mater. Express*, 1(1):36–45, 2011.

[2] V. K. Valev, A. V. Silhanek, W. Gillijns, Y. Jeyaram, H. Paddubrouskaya, A. Volodin, C. G. Biris, N. C. Panoiu, B. De Clercq, M. Ameloot, O. A. Aktsipetrov, V. V. Moshchalkov, and T. Verbiest. Plasmons reveal the direction of magnetization in nickel nanostructures. *ACS Nano*, 5(1):91–6, January 2011.

[3] N. Bloembergen, R. K. Chang, S. S. Jha, and C. H. Lee. Optical second-harmonic generation in reflection from media with inversion symmetry. *Phys. Rev.*, 174(3):813–822, 1968.

[4] C. K. Chen, A. R. B. De Castro, and Y. R. Shen. Surface-enhanced second-harmonic generation. *Phys. Rev. Lett.*, 46(2):145–148, 1981.

[5] S. Kujala, B. K. Canfield, M. Kauranen, Y. Svirko, and J. Turunen. Multipole Interference in the Second-Harmonic Optical Radiation from Gold Nanoparticles. *Phys. Rev. Lett.*, 98(16):167403, April 2007.

[6] V. K. Valev, A. V. Silhanek, N. Verellen, W. Gillijns, P. Van Dorpe, O. A. Aktsipetrov, G. A. E. Vandenbosch, V. V. Moshchalkov, and T. Verbiest. Asymmetric Optical Second-Harmonic Generation from Chiral G-Shaped Gold Nanostructures. *Phys. Rev. Lett.*, 104(12):127401, March 2010.

[7] J. Butet, G. Bachelier, I. Russier-Antoine, C. Jonin, E. Benichou, and P.-F. Brevet. Interference between Selected Dipoles and Octupoles in the Optical Second-Harmonic Generation from Spherical Gold Nanoparticles. *Phys. Rev. Lett.*, 105(7):077401, August 2010.

[8] Y. Zeng, W. Hoyer, J. Liu, S. W. Koch, and J. V. Moloney. Classical theory for second-harmonic generation from metallic nanoparticles. *Phys. Rev. B.*, 79(23):235109, June 2009.

[9] F. Xiang Wang, F. J. Rodríguez, W. M. Albers, R. Ahorinta, J. E. Sipe, and M. Kauranen. Surface and bulk contributions to the second-order nonlinear optical response of a gold film. *Phys. Rev. B.*, 80(23):4–7, December 2009.

[10] J. I. Dadap, J. Shan, K. B. Eisenthal, and T. F. Heinz. Second-Harmonic Rayleigh Scattering from a Sphere of Centrosymmetric Material. *Phys. Rev. Lett.*, 83(20):4045–4048, November 1999.

[11] Y. Schols and G. A. E. Vandenbosch. Separation of Horizontal and Vertical Dependencies in a Surface/Volume Integral Equation Approach to Model Quasi 3-D Structures in Multilayered Media. *IEEE Trans. Antennas Propag.*, 55(4):1086–1094, April 2007.

[12] M. Vrancken and G. A. E. Vandenbosch. Hybrid dyadic-mixed potential integral equation analysis of 3-D planar circuits and antennas. *IEE Proc. Microw. Antennas Propag.*, 149(5-6):265–270, 2002.

[13] RSoft Design Group. `http://www.rsoftdesign.com/`.

[14] V. K. Valev, N. Smisdom, A. V. Silhanek, B. De Clercq, W. Gillijns, M. Ameloot, V. V. Moshchalkov, and T. Verbiest. Plasmonic ratchet wheels: switching circular dichroism by arranging chiral nanostructures. *Nano Lett.*, 9(11):3945–3948, November 2009.

[15] J. D. Jackson. *Classical Electrodynamics*. John Wiley & Sons, Hoboken, 3rd edition, 1999.

[16] V. V. Temnov, G. Armelles, U. Woggon, D. Guzatov, A. Cebollada, A. Garcia-Martin, J. M. Garcia-Martin, Ti. Thomay, A. Leitenstorfer, and R. Bratschitsch. Active magneto-plasmonics in hybrid metalferromagnet structures. *Nature Photon.*, 4(2):107–111, 2010.

[17] A. Kirilyuk and Th. Rasing. Magnetization-induced-second-harmonic generation from surfaces and interfaces. *J. Opt. Soc. Am. B*, 22(1):148–167, 2005.

Chapter 11

Zero-$\bar{n}$ Bandgaps in Photonic Supperlatices containing Negative Refractive Index Materials

11.1 Introduction

One important type of photonic crystal can be obtained by cascading alternating layers of NIMs and positive index materials (PIMs) [1–3]. This photonic structure (example shown in Fig. 11.3) has unique optical properties, including complete photonic bandgaps [4] and phase-invariant field for cloaking applications [5]. Moreover, these binary photonic structures have an omnidirectional bandgap that is insensitive to wave polarization, incidence angle, structure periodicity, and structural disorder [6]. The existence of such a gap is because the path-averaged refractive index is equal to zero within a frequency band [1–3]. Specifically, at this frequency the Bragg condition, $k\Lambda = (\bar{n}\omega/c)\Lambda = m\pi$, is satisfied for $m = 0$, irrespective of the period Λ of the superlattice; here, k and ω are the wavevector and frequency respectively, and $\bar{n}$ is the averaged refractive index. Because of this property this photonic bandgap is called *zero-*$\bar{n}$, or *zero-order bandgap* [3].

Near-zero index materials have a series of exciting potential applications, such as beam self-collimation [7], extremely convergent lenses and spontaneous emission control [8], strong field enhancement [9], and cloaking devices [5]. The vanishingly small value of the refractive index of near-zero index materials and their large phase velocity can reshape electromagnetic phase fronts emitted by optical antennas [10] or, for highly-directive antennas, transfer near-field phase information into the far-field. At the near-zero index regime the electromagnetic field has an unusual dual character, i.e., it is static in the spatial domain (phase difference between arbitrary spatial locations is equal to zero) while remaining dynamic in the time domain, thus allowing energy transport. Nevertheless, perhaps the most important application of near-zero

index materials is to optical links in lumped nanophotonic circuits [11]. In particular, chip-scale optical interconnects or interferometers that can guide light over hundreds of wavelengths without introducing phase variations can be effectively used to reduce unwanted effects of frequency dispersion. This remarkable property has other exciting technological applications to photon delay lines with zero phase difference, information processing devices, and new optical phase control and measurement techniques.

Through the use of finite difference time domain (FDTD) simulations, the existence of the zero-$\bar{n}$ is verified in a PIM-NIM stacked Si waveguide. This same method will also be employed to show that the photonic bandgap is robust against structural disorder.

11.2 The Finite-Difference Time-Domain Method

There are several numerical methods widely used to study the propagation of electromagnetic waves through complex structures. Two of these methods have already been discussed, namely, the multiple scattering matrix method and the rigorous coupled-wave analysis method. One of the drawbacks of both these methods is that they solve Maxwell's equations in the frequency domain. While the MSM method can be extended to the time domain, it still relies on solving what is essentially a frequency domain problem. One of the most popular and widely used numerical algorithms in electromagnetism, which operates in the time domain is the *finite-difference time-domain method* (FDTD) [12]. Since FDTD is a time-domain algorithm, it allows one to investigate the dynamics of the electromagnetic field and, implicitly, its spectral content. FDTD simulation can cover a very wide frequency range with a single computational run by using a very narrow temporal pulse as a source. A brief overview of the FDTD formalism will be given in this section and its advantages over frequency based solvers as well as several of its limitations will also be discussed.

Finite-difference time-domain is a time-stepping algorithm that uses a leap-frog type iteration to update the values of the electric and magnetic field at different time steps and throughout the entire computational grid. To do this, in the FDTD approach, the spatial domain is split into parallelipipedic unit cells known as *Yee cells* [13]. Figure 11.1b shows the standard cartesian Yee cell. The numerical values of the electric field are calculated in the centre edges of the cell while the magnetic fields are calculated at the centre faces of the cell. It is interesting to note that in this approach, two interspersed spatial grids are actually employed. One contains the electric field components on its edges, while the other contains the components of the magnetic field. This spatial discretisation method is known as the *staggered-grid* approach.

To better understand the mathematical formalism employed in the FDTD method, consider the simple one dimensional case of a wave propagating along the x-axis in a

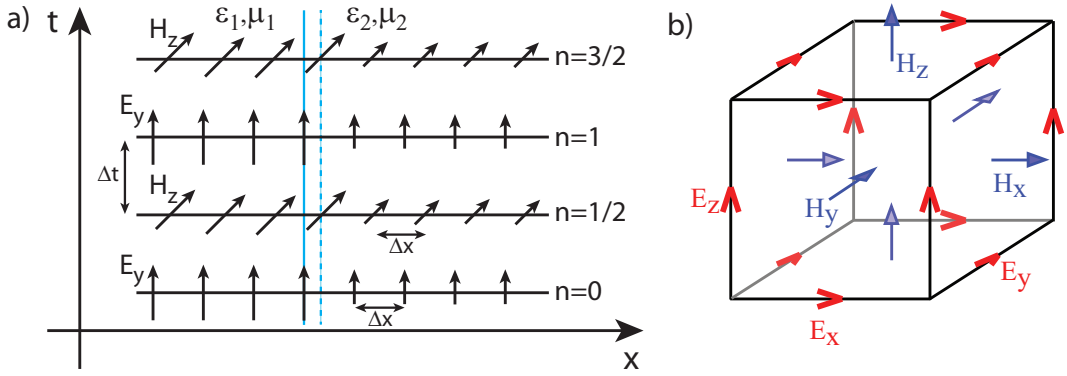

*Fig. 11.1: Standard finite-difference time-domain computational domains: a) schematic of spatial and temporal stepping in a 1D simulation; n represents the time steps. The two vertical bars denote the numerical interface (**E** field, solid line and **H** field, dashed line) between two dielectric with ϵ_1 and ϵ_2; b) the 3D Yee cell [14].*

non-dispersive dielectric medium with permittivity ϵ and permeability μ. Figure 11.1a illustrates this physical setting. Assuming an electric field polarisation along the y-axis, the one dimensional wave equation can be written:

$$\left(\frac{\partial^2}{\partial x^2} - \frac{1}{\epsilon\mu}\frac{\partial^2}{\partial t^2}\right) U = 0, \tag{11.1}$$

where U can be either E_y or H_z. Equation (11.1) can be written as two separate, first order, partial differential equations:

$$\frac{\partial E_y}{\partial x} = -\mu\frac{\partial H_z}{\partial t} \tag{11.2a}$$

$$\frac{\partial H_z}{\partial x} = -\epsilon\frac{\partial E_y}{\partial t}. \tag{11.2b}$$

By using the Yee grid in Fig. 11.1a, Eqs. (11.2) can be written as a set of discrete equations in time and space:

$$\frac{(H_z)^{n+1/2}_{m+1/2} - (H_z)^{n-1/2}_{m+1/2}}{\Delta t} = -\frac{1}{\mu}\frac{(E_y)^n_{m+1} - (E_y)^n_m}{\Delta x} \tag{11.3a}$$

$$\frac{(E_y)^{n+1}_m - (E_y)^n_m}{\Delta t} = -\frac{1}{\epsilon}\frac{(H_z)^{n+1/2}_{m+1/2} - (H_z)^{n+1/2}_{m-1/2}}{\Delta x}, \tag{11.3b}$$

where n and m are indices of the time and space steps, respectively, and Δt and Δx are the time and space step size, respectively. Equations (11.3) reveal how the FDTD iteration process works. At any given time step n, the electric field at each point in space can be calculated using the value of the field at the previous time step and the numerical *curl* of the local spatial distribution of the magnetic field which is known from the previous half-iteration. The calculation of the magnetic field occurs at time step $n+1/2$. This procedure mimics the physical process of a varying electric field giving rise to a

varying magnetic field, which in turn gives rise to a varying electric field, and so on. The start of this iterative process occurs at $t = 0$, where the spatial distribution of the electric and magnetic field components is given by the initial condition (*e.g.* the source used in the simulation).

The question now arises as to how FDTD handles inhomogeneous structures, that is to say, separate areas of space with different electromagnetic properties. Figure 11.1b gives a basic example of this case. At the interface between two media with ϵ_1, μ_1 and ϵ_2, μ_2, the linear electromagnetic boundary conditions need to be imposed. More specifically, the tangential components of the electromagnetic fields need to be continuous across the interface. In the simple 1D case, FDTD handles the continuity conditions of the two field components individually on the two separate grids. For example, in the case of the E_y component, the interface between the two media is considered to lie on the cell boundary of the grid containing the electric field components (*i.e.* the solid line in Fig. 11.1a). Because this grid interface is shared by the two regions, the continuity of the E_y component is enssured. Equation (11.3a) can now be used to find the magnetic field in the next half-iteration at the two neighbouring points of the grid. As these points lie on either side of the interface, the value of μ is well defined in both cases. The same reasoning is applied for the H_z component but in this case, the material interface is taken to lie on the cell boundary of the magnetic grid (*i.e.* the dashed line in Fig. 11.1a). The tangent component H_z is once again continuous across the interface and the values of ϵ needed for the next iteration are well defined on either side of the interface. In real applications however, it is unlikely that the actual interface will lie on the boundaries of one of the grids, in which case an averaging of the electromagnetic constants of the two media is required for some of the cells close to the interface. This method is also used, for example, when dealing with curved interfaces, such as cylinders or spheres. Because of this, for structures with very fine features, a very high spatial resolution is required. At the same time, the ability to accurately determine the field at an interface, like in the case of the multiple scattering method, is lost. This is one of the disadvantages of the FDTD method.

An important factor to consider when using the FDTD method is the type of boundary conditions imposed at the edges of the system. The FDTD method finds the values of the fields throughout the entire spatial domain at any given time step. As such, the actual domain of simulation needs to be finite and some form of boundary in the case of a propagating wave. Several solutions to this problem exist. In some cases, periodic boundary conditions can be imposed, which means the simulation is limited to the unit cell of the structure being investigated. However, in the case of finite structures, periodic boundary conditions cannot be used. One type of boundary conditions often employed in this case is the perfect metal boundary condition. In this case, the

fields at the boundary are forced to zero in the spatial step outside the boundary, which cuts off the simulation domain. Perfect metallic walls, however, still experience reflection back inside the structure, which can be undesirable. To overcome this problem, a type of boundary layer known as a *perfectly matched layer* (PML) was introduced [15]. Perfectly matched layers act as a perfect absorber with no reflection back into the simulation domain. In the case of FDTD, however, due to the discretisation of space and time, a PML will have to be large enough to fully absorb the wave and only reflect a small part of the field back into the system. In practice, a PML with about 16 unit cells reduces the reflection coefficient to less than 10^{-8} [12]. The PML boundaries must be taken far enough from the structure being investigated to prevent any unwanted interference (usually one wavelength is sufficient).

Another important factor to consider in FDTD simulations is the size of the time and spatial discretisation steps, Δt and Δx, respectively. Thus, the numerical stability of the FDTD method is governed by numerical stability is governed by the *Courant-Friedrichs-Lewy* (CFL) condition. This condition requires that, for the simulation to be stable, the time and space step sizes are related by:

$$c\Delta t \leq S\Delta x, \tag{11.4}$$

where S is known as the *Courant factor*. A well known rule for the Courant factor states that:

$$S < \frac{n_{min}}{\sqrt{N_{dim}}}, \tag{11.5}$$

where n_{min} is the minimum refractive index in the system and N_{dim} is the number of space dimensions of the simulation. The main implication of this stability condition is that when decreasing the size of the spatial step in order to obtain a higher spatial resolution, the size of the time step also needs to be decreased according to Eq. (11.4), which can lead to a large increase in the computational time, especially in the case of 3D simulations.

11.3 Negative Refractive Index in Photonic Crystals

In Chapter 2, the idea that an effective negative refractive index can occur in artificially structured media was discussed. An increasing interest in negative index metamaterials (NIMs) [16,17] has been witnessed over the last years. Metal based NIMs [18–22] have been actively studied due to their unusual physical properties and potential use in many technological applications [23–25]; however, they usually have large optical losses in their metallic components. One method of overcoming this disadvantage of metallic NIMs is to design dielectric structure with negative refraction where the optical losses would be reduced.

Fig. 11.2: Panels a) and b) show EFS diagrams (top) and refraction schematics (bottom) for the conventional case of refraction between two isotropic media and the PhC case of refraction between an isotropic medium and a PhC, respectively. Panel c) shows the photonic band structure of a PhC with a triangular lattice of air holes in a InP/GaInAs/InP slab. All panels after Ref. [27].

The reason behind the existance of media with negative refractive index stems from the definition of the refractive index:

$$n = \pm\sqrt{\epsilon\mu}, \tag{11.6}$$

where n is the index of refraction and ϵ and μ are the permittivity and permeability, respectively. When ϵ and μ are both negative, the minus sign must be taken in Eq. (11.6) and as a result, the refractive index n will be negative. Achieving negative permittivity and permeability is possible in metallic metamaterials by employing sub-wavelength resonant structures.

However, one can also define the refractive index in terms of the wave vector $\mathbf{k}$ and the group velocity $\mathbf{v}_g$ as [26]:

$$n = \mathrm{sgn}(\mathbf{v}_g \cdot \mathbf{k}) c \frac{|\mathbf{k}|}{\omega}, \tag{11.7}$$

a definition that is particularly important in the analysis of the optical properties of periodically structured media. Consequently, a structure in which $\mathbf{v}_g \cdot \mathbf{k} < 0$ will, for all purposes, have negative index of refraction even without the need for negative ϵ and μ.

Photonic crystals are an example of optical structures in which negative index of refraction can readily be achieved. Thus, PhCs have been shown to exhibit complex photonic bands as a result of their periodicity, a property that leads to negative index of refraction. To understand this concept of negative n in photonic crystals, we can employ an analysis based on *equifrequency surfaces* (EFS).

An EFS plots the contour of the wave vector $\mathbf{k}$ for a given frequency $\omega(\mathbf{k})$. For an isotropic and homogenous material, the dispersion relation $|\mathbf{k}| = n\omega/c$ implies that the EFS contours are circular [28]. This concept is illustrated in Fig. 11.2a. Here, the case of refraction between two isotropic media is plotted. The beam is assumed to be incom-

ing from Material 1 upon Material 2. The continuity of the tangential component of $\mathbf{k}$ at the interface between the two materials (illustrated in Fig. 11.2a by the dashed line) determines the properties of the refracted wave vector. As noted before, the group velocity of light is defined as $\mathbf{v}_g = \nabla_k(\omega(\mathbf{k}))$ where $\nabla_k = (\partial_{k_x}, \partial_{k_y}, \partial_{k_z})$. Consequently, the group velocity vector is always perpendicular to the EFS and oriented along the direction in which the frequency, $\omega(\mathbf{k})$ increases [27]. In Fig. 11.2a, this leads to the well known refraction case between two isotropic materials.

In the case of refraction between an isotropic medium and a PhC, the process is influenced by the presence of the photonic bands in the latter. Fig. 11.2c shows the band structure of a PhC consisting of a triangular lattice of air holes in a InP/GaInAsP/InP slab. Assuming light incident along the ΓM direction, in the frequency ranged marked by the dashed contour (*i.e.* the "working area"), the slope of the second (green) band implies that the group velocity should be oriented towards the EFS in the crystal. This effect is illustrated in Fig. 11.2b. Here, it can be seen that negative refraction occurs between the two media. Thus, it can be said that the photonic crystal has an effective refractive index n which is negative for this particular frequency range. This property of photonic crystals has been investigated theoretically [26, 28] and verified experimentally [27, 29, 30]. The mechanism of negative refraction in PhCs was also used to design a perfectly flat lens [31, 32].

Further to this, it can be proven analytically that in an infinite PhC, the sign of $\mathbf{v}_g \cdot \mathbf{k}$ is the same as the sign of $\mathbf{S} \cdot \mathbf{k}$, as $\mathbf{v}_g$ and $\mathbf{S}$ are collinear [33]. However, the Poynting vector, $\mathbf{S}$, is always oriented away from the source. As a result, if $n < 0$, which implies $\mathbf{S} \cdot \mathbf{k} < 0$ according to Eq. 11.7, the Poynting vector and the wave vector must have opposite orientation. This can only occur if energy and phase propagate in opposite directions, which is one of the defining characteristics of left-handed (negative index of refraction) media [16].

11.4 Existence, Invariance and Robustness against Structural Disorder of Zero-$\bar{\mathrm{n}}$ Bandgaps

The existence of zeron-$\bar{\mathrm{n}}$ bandgaps can be demonstrated by considering a 1D photonic crystal with periodic layers of permittivity and permeability, in the z direction, such that $\epsilon(z) = \epsilon(z + \Lambda)$ and $\mu(z) = \mu(z + \Lambda)$, where Λ is the period of the layers. The dispersion relation for this structures can then be determined by solving the equation for the electric field [1]:

$$-\frac{1}{\epsilon(z)}\frac{d}{dz}\left[\frac{1}{\mu(z)}\frac{dE(z)}{dz}\right] = \frac{\omega}{c}^2 E(z). \tag{11.8}$$

We now seek a solution to Eq. (11.8) with periodicity $E(z+\Lambda) = E(z)e^{i\kappa\Lambda}$, where κ is the Bloch wave vector. For a one-dimensional (1D) binary periodic lattice, the solution condition implies that the trace of the transfer matrix, T, of a primary unit cell can be expressed as [1, 3]:

$$\mathrm{Tr}[T(\omega)] = 2\cos(\kappa\Lambda) = 2\cos\left(\frac{\bar{\mathrm{n}}\omega\Lambda}{c}\right) - \left(\frac{Z_1}{Z_2} + \frac{Z_2}{Z_1} - 2\right)\sin\left(\frac{n_1\omega d_1}{c}\right)\sin\left(\frac{n_2\omega d_2}{c}\right), \tag{11.9}$$

where $n_{1(2)}$, $Z_{1(2)}$ and $d_{1(2)}$ are the refractive index, impedance and length of the first (second) layer, respectively.

In the case of impedance matching ($Z_1 = Z_2 = Z_0$), Eq. (11.9) becomes:

$$\kappa_0\Lambda = \frac{\bar{n}\omega\Lambda}{c}, \tag{11.10}$$

which is the dispersion relation of a homogenous medium with average refractive index $\bar{n} = 1/\Lambda\int_0^\Lambda n(z)dz$. When an impedance mismatch occurs ($Z_1 \neq Z_2$), the dispersion relation is given by:

$$\kappa_0\Lambda = \frac{\bar{n}\omega\Lambda}{c} = m\pi, \tag{11.11}$$

where m is an integer. This is the well known Bragg condition. It states that for any frequency ω where $n_1 d_1\omega/c$ is not an integral multiple of m, Eq. (11.9) will only have imaginary solutions in κ, which leads to a photonic bandgap.

When stacking both positive and negative index materials, there is another possibility for achieving a bandgap. Equation (11.9) implies that if the spatially averaged refractive index ($\bar{n}$) is zero, all solutions for the wave vector are imaginary as well, which signifies the presence of a spectral bandgap [1, 3]. This property also implies that the total phase accumulation upon beam propagation in the structure cancels at wavelengths corresponding to the zeron-$\bar{\mathrm{n}}$ gap [6]. Unlike the bandgaps given by the Bragg condition, this type of bandgap does not depend on the spacing of the layers (Λ) and will always occur at frequencies for which $\bar{n} = 0$.

The photonic structures examined for the presence of zero-$\bar{\mathrm{n}}$ gaps (Fig. 11.3) consist of dielectric PhC superlattices with alternating layers of negative index PhC and positive index homogeneous slabs [3]. The PhC band structure is shown in Fig. 11.4a-b, with geometrical parameters from averaged fabricated samples (hole-to-lattice constant r/a ratio of 0.283 and $a \approx 423\mathrm{nm}$). This two-dimensional (2D) hexagonal PhC has a negative index within the spectral band of 0.270 to 0.278, in normalized frequencies of $\omega a/2\pi c$, or wavelengths from 1520 nm to 1566 nm. Moreover, within this operating wavelength range (Fig. 11.4b) the PhC has two TM-like bands, one with positive re-

fractive index and the other one with negative refractive index, and an almost complete TE-like bandgap.

The numerical transmission spectra were determined by using MIT's MEEP [34], a freely available code based on the finite-difference time-domain (FDTD) method. In all numerical simulations a uniform computational grid of 40 grid points per micron was used. This ensures that a widely used rule-of-thumb for setting the size of the computational grid in FDTD simulations is satisfied, namely, that the smallest characteristic length of the system (in this case, the diameter of the holes) contains at least 10 grid points. The transmission spectra corresponding to a specific geometry of the photonic superlattice have been determined by normalising the transmission spectrum of the photonic superlattice to the transmission spectrum of the homogeneous structure that is obtained by replacing the PhC regions with homogeneous slabs. In all the FDTD-based numerical simulations a pulsed excitation source with central wavelength $\lambda_0 = 1550\ \mathrm{nm}$ and spectral full-width at half-maximum of $90\ \mathrm{nm}$ was used. A typical simulation run on 64 Intel ®Xeon processors was performed in about 7 hours.

A set of three devices of different periods Λ were fabricated, with the negative index PhC layer in the superlattice spanning 7, 9, and 11 unit cells along the z-axis, so that the thickness of this layer was $d_1 = 3.5\sqrt{3}a$ (2.564 μm), $d_1 = 4.5\sqrt{3}a$ (3.297 μm) and $d_1 = 5.5\sqrt{3}a$ (4.029 μm), respectively. The experiments span 1520 nm to 1620 nm and the negative refractive index band exists for wavelengths up to 1570 nm. The effective refractive index of the PhC region is obtained from the band diagram (Fig. 11.4a-b) and the PIM layer index is computed from the asymmetric TM slab waveguide mode effective index (for example, at 1550 nm the mode index is 2.671). To have the zero-$\bar{\mathrm{n}}$ frequency in the middle of the negative index band, the length ratio between the PIM and PhC sections of the superlattice was set to 0.78. As such, the zero-$\bar{\mathrm{n}}$ gap should occur at 1552.6 nm [6]. The corresponding PIM layer thickness is determined by requiring the average index to be zero [$\bar{n} = (n_1 d_1 + n_2 d_2)/\Lambda = 0$], while keeping the ratio d_2/d_1 unchanged for all three devices in the set. Here, n_1 and n_2 are the effective mode indices in the PhC and homogeneous layers, respectively, at the corresponding wavelengths. This leads to the following values for the superperiod (SPs): $\Lambda_{7UC} = 4.564\ \mu\mathrm{m}$, $\Lambda_{9UC} = 5.869\ \mu\mathrm{m}$ and $\Lambda_{11UC} = 7.173\ \mu\mathrm{m}$, where UC stands for unit cells. Example transmission spectra for the fabricated samples are summarized in Fig. 11.4 and show that the zero-$\bar{\mathrm{n}}$ gap is around $1557.8 \pm 1.5\ \mathrm{nm}$, very close to the theoretically-predicted values ($\Delta\lambda/\lambda < 5\%$) and numerically-computed spectra.

One of the main properties of zero-$\bar{\mathrm{n}}$ bandgaps is their remarkable robustness against effects induced by structural disorder. To study this property, we considered the optical transmission in randomly perturbed photonic superlattices. Specifically, we considered superlattices for which the PIM lengths are randomly distributed within the

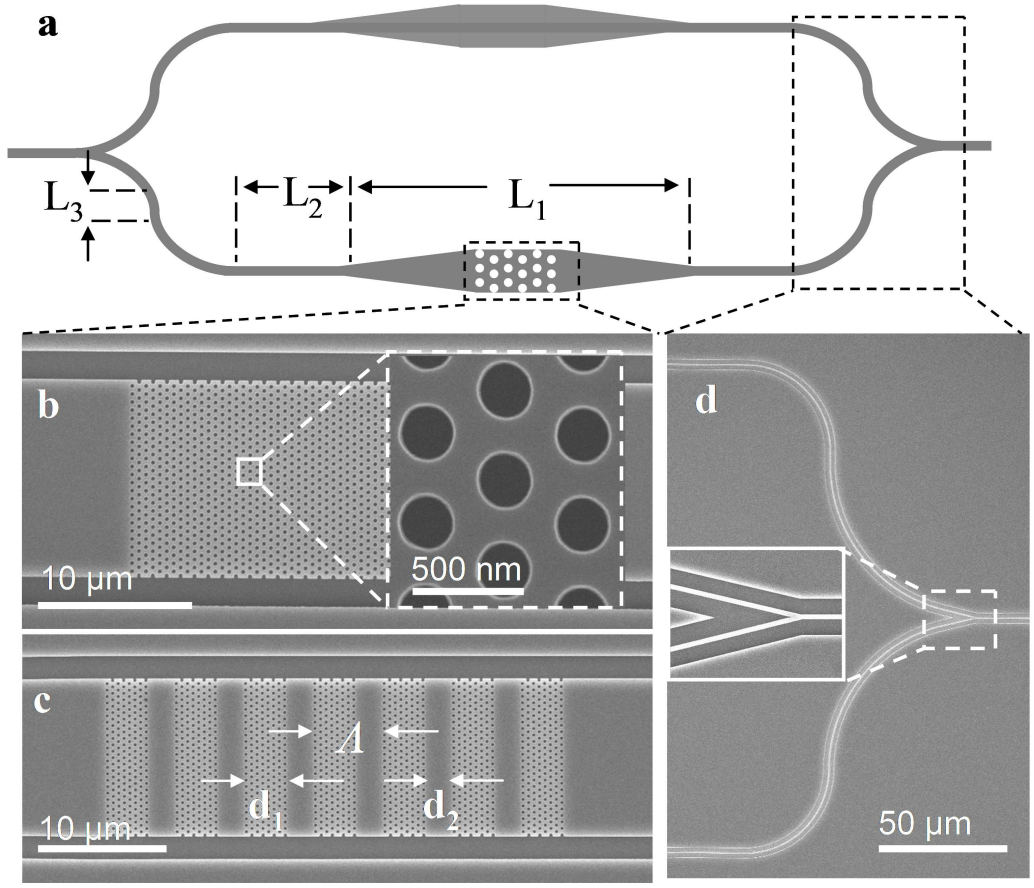

Fig. 11.3: Schematic of a Mach-Zehnder interferometer (MZI) with alternating negative and positive index regions and scanning electron microscope images of the fabricated device. The structure was designed and fabricated as part of a collaboration between Columbia University, University College London, The Institute of Microelectronics, Singapore, and the Center for Functional Nanomaterials at Brookhaven National Laboratory. The fabrication was carried out by M. S. Aras, M. B. Yu, D. L. Kwong and A. Stein. For more details, see Ref. [6].

domain ($d_2 - \Delta d_2/2$, $d_2 + \Delta d_2/2$), amounting to a random variation of the superperiod Λ. The degree of structural disorder is quantified by the parameter $\sigma = \Delta d_2/d_2$. The main results of the computational investigation are presented in Fig. 11.4d. It can be clearly seen that the zero- bandgap is preserved even when the disorder parameter is as large as $\sigma = 10\%$, i.e., a value much larger than from the fabrication processes. Note that the amplitude oscillations in the transmission spectra are Fabry-Perot resonances in the superlattice.

In addition, the numerical simulations show that the structural disorder associated with a random perturbation of the hole radii or their location has a comparable or smaller influence on the existence of zero-$\bar{\text{n}}$ bandgaps. More exactly, the radius of the holes is set in the domain ($r - \Delta r/2$, $r + \Delta r/2$), according to a uniform random distribution whereas in the second case the location of the holes is randomly perturbed by Δl. In these models, the degree of structural disorder is characterized by a disorder parameter defined as $\sigma = \Delta r/r$ and $\sigma = \Delta l/a$, respectively. The main results of

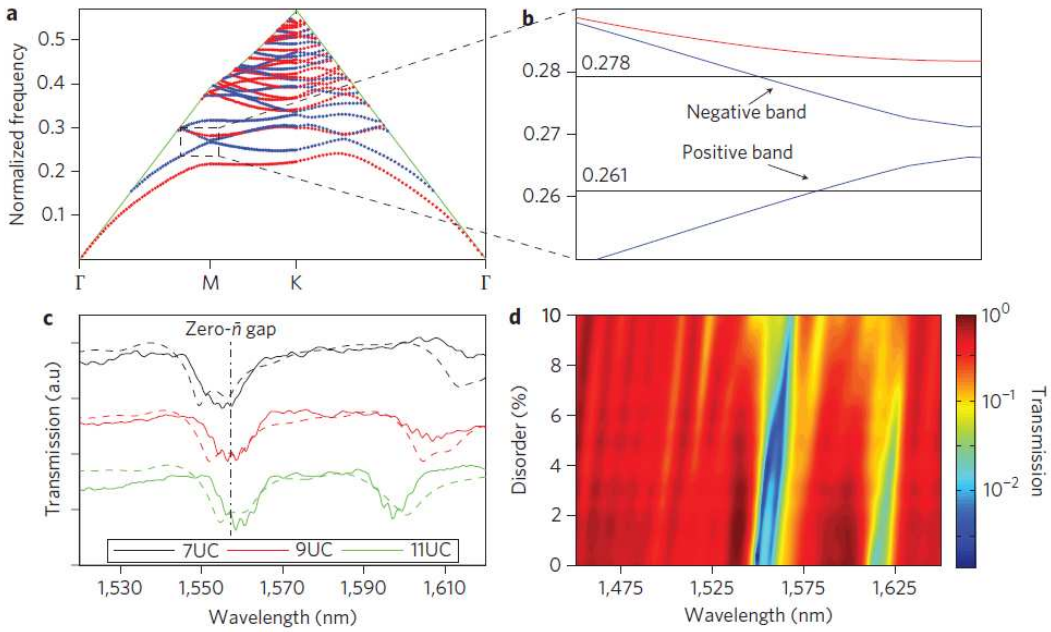

Fig. 11.4: Band diagram of the PhC, verification of period-invariant zero-$\bar{n}$ bandgaps, and influence of structural variations on transmission spectra: a) Band diagram of the PhC in Fig. 11.3 and $d_1 = 2.564\ \mu\text{m}$, $d_2 = 2\ \mu\text{m}$ and $\Lambda = 4.564\mu\text{m}$. The TM-like (TE-like) photonic bands are depicted in blue (red). The light cone is denoted by the green lines. b) A zoom-in of the spectral domain corresponding to experimental region of interest. Experiments were performed in the spectral region marked by the two horizontal lines (0.278-0.261 normalized frequency). c) Experimental verification of the zero- bandgap in superlattices with varying period ($\Lambda_{Black} = 4.56\ \mu\text{m}$, $\Lambda_{Red} = 5.87\ \mu\text{m}$, and $\Lambda_{Green} = 7.17\ \mu\text{m}$) and the same ratio, $d_2/d_1 = 0.78$, and numerically simulated transmission spectra (dashed lines). d) Influence of lattice disorder (parameter σ)on the transmission spectra. Color bar indicates the transmission scaling. The simulations in panels a) and b) and the experimental measurements in panel c) were performed by S. Kocaman at Columbia University.

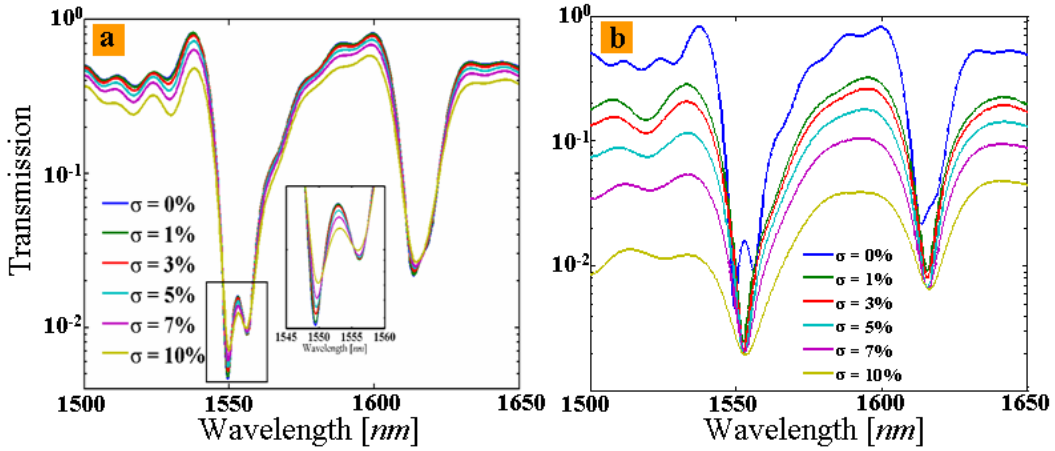

Fig. 11.5: Transmission spectra calculated for different values of the disorder parameter σ. The inset shows the expanded transmission spectra. Panel a) corresponds to structural disorder introduced by randomly changing the radius of the holes in the PhC sections of the superlattice. Panel b) shows the effects of structural disorder generated by randomly perturbing the location of the holes.

the computational investigations are summarized in Fig. 11.5. Thus, it can be seen that in the case of random perturbation of the radius of the holes the transmission spectra in the superlattice are only slightly affected, even if the disorder parameter is as large as $\sigma = 10\%$. As observed, the main effect consists of a small decrease of the zero-$\bar{n}$ superlattice transmission with increasing values of the disorder parameter σ. It is seen, however, that structural disorder induced by randomly changing the location of the holes has a much larger effect on the transmission spectra. It is important to note though that a value of $\sigma = 10\%$ corresponds to variations of tens of nanometers of the location of the holes, variations which are much larger than those measured in the fabricated devices.

11.5 Conclusions

To conclude, this chapter has shown that deterministic photonic bandgaps can be observed in alternatively stacked negative and positive index photonic crystals. The bandgaps are associated with a spatially averaged refractive index $\bar{n} = 0$. The numerical simulations of the transmission spectra fully confirmed the experimental findings. Zero-$\bar{n}$ gaps were also shown to remain invariant to geometric changes of up to $\sigma = 10\%$.

The structure numerically examined in this chapter was fabricated and used to demonstrate, for the first time, zero phase delay in negative-positive-index superlattices [6]. The engineered control of the phase delay which is possible in these near-zero refractive index superlattices can be implemented in chip-scale transmission lines and interferometers with deterministic phase array and dispersion control, and has significant technological potential in phase-insensitive image processing, phase-invariant field for electromagnetic cloaking, lumped elements in optoelectronics, information processing, and engineering of radiation wavefront to pre-designed shapes.

Bibliography

[1] J. Li, L. Zhou, C. T. Chan, and P. Sheng. Photonic Band Gap from a Stack of Positive and Negative Index Materials. *Phys. Rev. Lett.*, 90(8):083901, 2003.

[2] N. C. Panoiu, R. M. Osgood, S. Zhang, and S. R. J. Brueck. Zero-$\bar{n}$ bandgap in photonic crystal superlattices. *J. Opt. Soc. Am. B*, 23(3):506–513, 2006.

[3] S. Kocaman, R. Chatterjee, N. C. Panoiu, J. F. McMillan, M. B. Yu, R. M. Osgood, D. L. Kwong, and C. W. Wong. Observation of Zeroth-Order Band Gaps in Negative-Refraction Photonic Crystal Superlattices at Near-Infrared Frequencies. *Phys. Rev. Lett.*, 102(20):203905, 2009.

[4] I. V. Shadrivov, A. A. Sukhorukov, and Y. S. Kivshar. Complete band gaps in one-dimensional left-handed periodic structures. *Phys. Rev. Lett.*, 95(19):193903, November 2005.

[5] J. Hao, W. Yan, and M. Qiu. Super-reflection and cloaking based on zero index metamaterial. *Appl. Phys. Lett.*, 96(10):101109, 2010.

[6] S. Kocaman, M. S. Aras, P. Hsieh, J. F. McMillan, C. G. Biris, N. C. Panoiu, M. B. Yu, D. L. Kwong, A. Stein, and C. W. Wong. Zero phase delay in negative-refractive-index photonic crystal superlattices. *Nature Photon.*, 5(8):499–505, 2011.

[7] V. Mocella, S. Cabrini, A. S. P. Chang, P. Dardano, L. Moretti, I. Rendina, D. Olynick, B. Harteneck, and S. Dhuey. Self-Collimation of Light over Millimeter-Scale Distance in a Quasi-Zero-Average-Index Metamaterial. *Phys. Rev. Lett.*, 102(13):133902, April 2009.

[8] S. Enoch, G. Tayeb, P. Sabouroux, N. Guérin, and P. Vincent. A Metamaterial for Directive Emission. *Phys. Rev. Lett.*, 89(21):213902, November 2002.

[9] N. M. Litchinitser, A. I. Maimistov, I. R. Gabitov, R. Z. Sagdeev, and V. M. Shalaev. Metamaterials: electromagnetic enhancement at zero-index transition. *Opt. Lett.*, 33(20):2350–2352, October 2008.

[10] R. Ziolkowski. Propagation in and scattering from a matched metamaterial having a zero index of refraction. *Phys. Rev. E*, 70(4):046608, 2004.

[11] N. Engheta. Circuits with light at nanoscales: optical nanocircuits inspired by metamaterials. *Science*, 317(5845):1698–1702, September 2007.

[12] A. Taflove and C. S. Hagness. *Computational Electrodynamics: The Finite-Difference Time-Domain Method*. Artech House, Boston, 3rd edition, 1980.

[13] K. S. Yee. Numerical Solution of Initial Boundary Value Involving Maxwell's Equations in Isotropic Media. *IEEE Trans. Antennas Propag.*, 14(3):302–307, 1966.

[14] S. G. Johnson. Standard Yee lattice, 2006.

[15] J.-P. Berenger. A Perfectly Matched Layer for the Absorption of Electromagnetic Waves. *J. Comp. Phys.*, 114(21):185–200, 1994.

[16] V. G. Veselago. The Electrodynamics of Substances with Simultaneously Negative Values of ϵ and μ. *Phys.-Uspekhi*, 10(4):509–514, 1968.

[17] J. B. Pendry. Time reversal and negative refraction. *Science*, 322(5898):71–73, October 2008.

[18] R. A. Shelby, D. R. Smith, and S. Schultz. Experimental verification of a negative index of refraction. *Science*, 292(5514):77–79, April 2001.

[19] D. K. Gramotnev and S. I. Bozhevolnyi. Plasmonics beyond the diffraction limit. *Nature Photon.*, 4(2):83–91, 2010.

[20] N. C. Panoiu and R. M. Osgood. Influence of the dispersive properties of metals on the transmission characteristics of left-handed materials. *Phys. Rev. E*, 68(1):016611, July 2003.

[21] S. Zhang, W. Fan, N. C. Panoiu, K. J. Malloy, R. M. Osgood, and S. R. J. Brueck. Experimental Demonstration of Near-Infrared Negative-Index Metamaterials. *Phys. Rev. Lett.*, 95(13):137404, 2005.

[22] J. Valentine, S. Zhang, T. Zentgraf, E. Ulin-Avila, D. A. Genov, G. Bartal, and X. Zhang. Three-dimensional optical metamaterial with a negative refractive index. *Nature*, 455(7211):376–379, September 2008.

[23] G. Dolling, C. Enkrich, M. Wegener, C. M. Soukoulis, and S. Linden. Simultaneous negative phase and group velocity of light in a metamaterial. *Science*, 312(5775):892–894, 2006.

[24] K. L. Tsakmakidis, A. D. Boardman, and O. Hess. 'Trapped rainbow' storage of light in metamaterials. *Nature*, 450(7168):397–401, November 2007.

[25] A. J. Hoffman, L. Alekseyev, S. S. Howard, K. J. Franz, D. Wasserman, V. A. Podolskiy, E. E. Narimanov, D. L. Sivco, and C. Gmachl. Negative refraction in semiconductor metamaterials. *Nature Mater.*, 6(12):946–950, December 2007.

[26] S. Foteinopoulou and C. M. Soukoulis. Negative refraction and left-handed behavior in two-dimensional photonic crystals. *Phys. Rev. B.*, 67(23):235107, June 2003.

[27] A. Berrier, M. Mulot, M. Swillo, M. Qiu, L. Thylén, A. Talneau, and S. Anand. Negative Refraction at Infrared Wavelengths in a Two-Dimensional Photonic Crystal. *Phys. Rev. Lett.*, 93(7):073902, August 2004.

[28] M. Notomi. Theory of light propagation in strongly modulated photonic crystals: Refractionlike behavior in the vicinity of the photonic band gap. *Phys. Rev. B.*, 62(16):10696–10705, October 2000.

[29] H. Kosaka, T. Kawashima, A. Tomita, M. Notomi, T. Tamamura, T. Sato, and S. Kawakami. Superprism phenomena in photonic crystals. *Phys. Rev. B.*, 58(16):R10096–R10099, October 1998.

[30] E. Cubucku, K. Aydin, E. Ozbay, S. Foteinopoulou, and C. M. Soukoulis. Negative refraction by photonic crystals. *Nature*, 423:604–605, 2003.

[31] E. M. Mills, M. L. Banks, J. E. Sprague, and T. Finkel. Imaging by flat lens using negative refraction. *Nature*, 426:404, 2003.

[32] T. Decoopman, G. Tayeb, S. Enoch, D. Maystre, and B. Gralak. Photonic Crystal Lens: From Negative Refraction and Negative Index to Negative Permittivity and Permeability. *Phys. Rev. Lett.*, 97(7):073905, August 2006.

[33] K. Sakoda. *Optical Properties of Photonic Crystals*. Springer-Verlag, Heidelberg, 2nd edition, 2005.

[34] MIT Meep. `http://ab-initio.mit.edu/wiki/index.php/Meep`.

Chapter 12

Conclusions and Future Work

The field of photonic metamaterials has greatly advanced during the recent years. The ability to engineer new structures which can directly manipulate light has lead to the development of new metamaterials and devices, which have properties and functionalities that cannot be replicated using naturally occurring materials. It has now become crucial to be able to probe and understand the underlying physical phenomena that characterise this new class of materials. This work is part of this challenging endeavour. The ability to investigate the electromagnetic effects occurring in metamaterials, photonic crystals and plasmonic materials offered by theoretical analysis and advanced numerical simulations complements the knowledge that can be directly retrieved through experiment. At the same time, while significant progress in our understanding of the principles of photonic metamaterials has been achieved, due to advances in nanotechnology and modern nano-fabrication techniques, many aspects pertaining to these materials are largely unexplored. To this end, my work has focused on using theoretical and numerical methods to further investigate the electromagnetism of photonic metamaterials. In particular, I have endeavoured to study, within this project, non-linear phenomena pertaining to second harmonic generation in plasmonic nano-structures, their properties and applications.

I have also, throughout the course of the work, attempted to tie in these non-linear effects to other linear and non-linear phenomena occurring in metamaterials, such as plasmon coupling, excitation of cavity modes, rotating plasmon modes, structural sensitivity and magnetic effects. The results presented in this thesis have shown that photonic metamaterials possess a high degree of flexibility in their design and operation, from which their versatility and large number of potential applications are drawn. Consequently, having a powerful model of the interplay between these electromagnetic effects and the many remarkable properties of metamaterials is a crucial factor in expanding our current knowledge of this field. Many challenges posed by this research question have been successfully tackled in this thesis.

In what follows, I will discuss how my work has directly contributed to overcoming some of these research challenges and how it has managed to achieve its intended objectives. In the end, I will also elaborate on how this work can be further expanded upon so as to open up new avenues of exploration and potentially provide answers to some of the remaining research questions in this field.

12.1 Contributions of the Work

In this thesis, I have shown how theoretical analysis and numerical simulations in photonics can be used to better understand new electromagnetic phenomena, design new structures and devices with remarkable properties and how these results can be correlated with experimental work, so as to allow for new designs of active optical devices and a deeper understanding of some of the important optical effects in photonic metamaterials.

Specifically, in this thesis, I have presented a new mathematical formalism, based on multiple scattering theory, that allows one to accurately map the linear and non-linear field distributions in an array of arbitrarily distributed metallic nanowires or, more generally speaking, cylinders made of centrosymmetric materials. This formalism is unique as it includes the full contribution of surface and bulk second harmonic generation in centrosymmetric materials. I have also discussed the implementation of this formalism into a fully functional numerical software tool which, to the best of my knowledge, allows one for the first time to numerically investigate the largely unexplored area of non-linear optics in plasmonic metamaterials.

The enhanced functionality of the software tools developed as part of this project has led to a series of new results, which have been instrumental in explaining and enhancing our understanding of the complex optical phenomena in plasmonic structures. In this connection, I was able to demonstrate that plasmon coupling in metallic nanowire arrays can lead to a complex response of the linear and non-linear fields which can result in high field enhancement, light localisation and light focusing. One of the major challenges in photonics today is to employ these effects in designing new nano-scale active optical devices. In my work, I have shown that non-linear plasmonic cavities can be engineered to provide high quality factors for sub-wavelength lasing applications, to sustain whispering gallery modes, which can be employed in optical trapping and manipulation, and to be used as compact sub-wavelength on-chip sensors for biological and chemical applications.

It is also vital that the conclusions of analytical and numerical analysis be matched with experimental results and this is especially true in the field of electromagnetism. A broad array of analytical and numerical methods allows one to investigate a large number of phenomena and possible designs for new photonic devices. These devices can

then be practically implemented and studied using experimental means. Consequently, this can provide further insight into the practical applications of one's work and their practical implementation in real world devices. To this end, I have investigated how plasmons can be employed to generate second-harmonic fields in nano-patterned metasurfaces, where chirality can play an important role in the non-linear effects. I have also discussed nano-patterned metasurfaces that can be used to create polarisation agile structures where localised plasmon resonances lead to large shifts in the transmission, reflection and absorption of light in response to a change in the polarisation of incident waves. These structures also showed great promise in increasing absorption by using the strong field enhancement associated with the excitation of plasmon resonances. These results give novel insights into the properties of surface plasmon resonances in metamaterials and their connection to non-linear surface effects. Finally, I have also considered in my work the properties another type of photonic structure, specifically, photonic crystals. In this connection, I confirmed numerically experimental findings, which demonstrated that a new kind of spectral band gap can appear when layering positive and negative refractive index regions, corresponding to an effective zero refractive index medium.

12.2 Future Prospects

The work discussed in this thesis shows that, as a logical extension to the results presented within, there are several new avenues which are worth exploring. As the understanding of the fundamental physical phenomena which support the many discoveries made in the field of photonics expands, so does the need to delve even further and begin to investigate more complex systems and more advanced designs, which have the potential to lead to new scientific breakthroughs. It is my belief that further analytical, numerical and experimental work, toward this end, can prove to be an important source of new science. As such, this section will cover the several steps which can be taken to further extend the work carried out thus far.

The OPTIMET software has, as shown throughout the bulk of this work, proven to be an efficient and robust tool for investigating linear and non-linear effects in nanowire arrays. OPTIMET in its current form can be employed for a wide range of studies, some of which being discussed here. Nevertheless, there is great potential for further exploration using the current code implementation. There are several new designs which I believe will offer new results and greatly extend the work done so far. For example, it is possible to use OPTIMET to investigate nanowire arrays containing only dielectric or combinations of both metallic and dielectric scatterers. In this case, new optical phenomena could be investigated; large arrays of dielectric nanowires can be used to observe, for example, the diffraction of light by cylindrical scatterers with radii much

smaller than the wavelength. In effect, this would allow the use of OPTIMET to investigate media with effective electromagnetic properties. For instance, by using silicon cylinders, the surface nonlinear effects would still be present and thus it would be possible to study metamaterials with non-linear effective properties, an important step forward in developing new artificial media with complex optical response. Further, silicon scatterers can be used to build photonic crystals with defect-type cavities, which could support non-linear whispering gallery modes similar to those discussed in this work. The use of dielectric components would eliminate the unwanted effects of optical absorption in metals. Finally, new geometries could allow for linear and non-linear sub-wavelength devices that possess directional field scattering, coupling and transmission of light between devices, strong beam focusing and many others. These efforts can also be aided by implementing, within OPTIMET, new types of incoming waves, such as waves with a Gaussian spatial distribution.

At the same time, OPTIMET can be extended in numerous ways to develop a more powerful software package. One of the possible extensions is the incorporation of the effects of external magnetic fields, which can lead to both magnetisation induced second harmonic generation as well as the possibility to externally control the SHG in nanowire arrays. For example, it could be possible to tune the properties of whispering gallery modes in non-linear plasmonic cavities by changing the direction and intensity of the external magnetic field. In addition, using the current code base it is possible to extended OPTIMET's capabilities by allowing for periodic boundary conditions. With this feature implemented, several new structures could be designed and investigated, including structures with practically an infinite number of unit cells, which would allow one to study the near-field phenomena in non-linear metamaterials. Further to this, adding support for scatterers with arbitrary shape would allow for new devices, such as elliptical scatterers, bow-tie antennas and many others. It is worth noting here that although this design would require a spatial grid to find the boundary conditions around the scatterers, this does not limit the advantages offered by the multiple scattering matrix method because even in this case, the field can be readily found at any point in the geometry.

Perhaps the most important feature that can be added to OPTIMET at this point, however, is the ability to simulate 3D structures. This would open up a large number of possible new designs which could be investigated. The current 2D version of the numerical method relies on the expansion of the fields in cylindrical Fourier-Bessel series. For 3D structures, this expansion will have to be carried out using spherical Fourier-Bessel functions and spherical harmonics. To this end, there are known algorithms and numerical libraries which have this capability and which could be readily integrated in the OPTIMET package. At the same time, 3D structures would no longer offer the

possibility of using pure TE or TM modes, which would further increase the computational complexity of the software, so care will have to be taken to make sure that the software implementation of the numerical method is fully optimised. The use of mixed modes would mean that the bulk component of the non-linear polarisation would contribute directly to the second harmonic generation, which could open up new avenues of exploration.

The technical implementation of OPTIMET is currently robust but with the possibilities of expanding to 3D there are areas where improvements can be made. Parallelisation will have to be achieved at a deeper level and the use of a hybrid OpenMP and MPI method is one possibility. Also, the output system while efficient for the work carried out so far will need to be extended to allow for faster parallel output using specialised libraries, such as HDF5 or NetCFD. At the same time, while the input system in the current stable version is sufficient, it would be possible to extend it further and increase its user friendliness. One method of doing this is to include a full scripting language as an input system, most likely by including an established language and wrapping it to OPTIMET's application programming interface. Of course, it would also be possible to extend OPTIMET by developing a fully fledged graphical user interface for it.

With the improvements to OPTIMET I just outlined, it would be possible to extend its capabilities to encompass some of the more complex structures presented in this work, such as metasurfaces and photonic crystals or combine its results with other numerical methods. As a result, further investigations of metasurfaces and PhCs could lead to new and more advanced designs with enhanced functionality. For example, replacing the PMMA coating in the cruciform structures with GaAs can lead to strong, polarisation tuneable, non-linear effects. Specifically, the strong linear field enhancement effect could be used to increase the second harmonic generation in GaAs. At the same time, GaAs coated chiral metasurfaces could give rise to chiral non-linear effects and, for geometry sizes much smaller than the wavelength, metasurfaces with effective non-linear properties not readily available in nature. Non-linear optical effects could also be further investigated in dielectric based photonic crystals were the high absorption in metals can be overcome, however, at the cost of no longer being able to excite surface plasmon resonances.

Thus, it is clear that there is great potential for future development in the field. With photonics offering the possibility of tackling some of the challenges of today's world, and having an impact on a global scale, this potential should not be overlooked. The scientific quest to understand the behaviour of our natural environment has led to countless incredible breakthroughs. Yet even with the vast amount of scientific knowledge available today, many questions still remain. This work has proposed an answer to

some of those questions, specifically related to non-linear effects in photonic metamaterials. The contributions of this thesis to the research field can, in my opinion, provide a good foundation for future development, both theoretical and practical, and promises to allow us to design and develop new active optical devices with remarkable functionality. Still, many challenges lie ahead, both in the particular case of this project, as well as photonics in general. A well known quote, sometimes attributed to Lord Kelvin, says that “There is nothing new to be discovered in physics now. All that remains is more and more precise measurement”. Yet in the very year this claim was made, Max Planck was developing his theory of the black body radiation. Perhaps in a similar way, it has taken well over a century for us to fully exploit the potential of Maxwell’s equations and the electromagnetic field. And with what may be called an “optical revolution” on the horizon, the future of photonics and metamaterials looks bright indeed.

Appendix A

Non-linear Boundary Conditions at a Metal-Dielectric Interface

The non-linear boundary conditions of the electromagnetic field at the interface between two media can be found by starting from Maxwell's equations with sources [1]:

$$\nabla \cdot \mathbf{D} = -\nabla \cdot \mathbf{P}^{nl} \tag{A.1a}$$

$$\nabla \times \mathbf{E} + \frac{\partial \mathbf{B}}{\partial t} = 0 \tag{A.1b}$$

$$\nabla \cdot \mathbf{B} = 0 \tag{A.1c}$$

$$\nabla \times \mathbf{H} - \frac{\partial \mathbf{D}}{\partial t} = \frac{\partial \mathbf{P}^{nl}}{\partial t}, \tag{A.1d}$$

where $\mathbf{P}^{nl}$ is the non-linear polarisation with $\mathbf{P}^{nl} = \mathbf{P}^{s} + \mathbf{P}^{b}$ being the surface and bulk contributions, respectively. The surface contribution is defined as $\mathbf{P}^{s} = \boldsymbol{\mathcal{P}}^{s}(x, y)\delta(z)$. The geometry in question and the integration domains used to drive the boundary conditions domains are depicted in figure A.1. Thus, let us consider two semi-infinite media with ϵ_1 and ϵ_2, separated by a slab of vanishingly small thickness with permittivity ϵ'. Because of the infinitesimally small thickness of the slab, $D_z + P_z^{nl}$, $\mathbf{E}_t$, B_z and $\mathbf{H}_t$ must vanish across it, because of the linear boundary conditions and so:

$$\int_{0^-}^{0^+} (D_z + P_z^{nl})dz = \int_{0^-}^{0^+} \mathbf{E}_t dz = \int_{0^-}^{0^+} B_z dz = \int_{0^-}^{0^+} \mathbf{H}_t dz = 0, \tag{A.2}$$

where the tangential and normal components have the indices t and z respectively. Thus, at is well known, in a polarised slab of infinitesimally small thickness, the normal component of the electric induction becomes singular. This condition leads to:

$$\int_{0^-}^{0^+} (D_z + P_z^{nl})dz = \int_{0^-}^{0^+} (D_z + P_z^{b} + P_z^{s})dz, \tag{A.3}$$

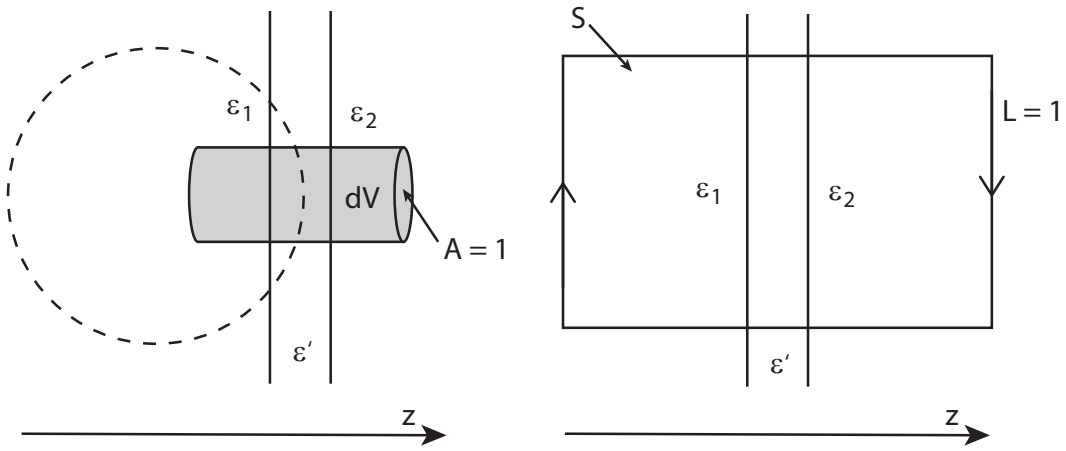

Fig. A.1: Integration domains for the non-linear boundary conditions at the interface between two media. The thickness of the slab of permitivitty ϵ' is considered to be infinitesimally small.

where P_z^b is the bulk contribution to the non-linear polarisation and P_z^s the surface contribution. P_z^b and D_z must vanish across a thin slab, thus:

$$\int_{0^-}^{0^+} (D_z + P_z^b + P_z^s)dz = -\int_{0^-}^{0^+} P_z^s dz = -\int_{0^-}^{0^+} \mathcal{P}_z^s \delta(z)dz = -\mathcal{P}_z^s. \tag{A.4}$$

When integrating over the volume V, (A.1c) becomes:

$$\int_V \nabla \cdot \mathbf{B} dV = 0, \tag{A.5}$$

and from the divergence theorem:

$$\int_{\partial V} \mathbf{B} \cdot d\mathbf{A} = 0, \tag{A.6}$$

which implies:

$$B_{z,1} - B_{z,2} = 0, \tag{A.7}$$

which is the boundary condition for the B_z component.

Integrating (A.1d) over the area S of contour l with sides $L = 1$, in the direction shown in Fig. A.1 leads to:

$$\int_S \left(\nabla \times \mathbf{H} - \frac{\partial \mathbf{D}}{\partial t} \right) d\mathbf{S} = \int_S \left(\frac{\partial \mathbf{P}^{nl}}{\partial t} \right) d\mathbf{S}, \tag{A.8}$$

and from Stokes' theorem:

$$\oint_{\partial S} \mathbf{H} \cdot d\mathbf{l} = \int_S \frac{\partial \mathbf{D}}{\partial t} \cdot d\mathbf{S} + \int_S \frac{\partial \mathbf{P}^{nl}}{\partial t} \cdot d\mathbf{S}. \tag{A.9}$$

Here, the first integral in the r.h.s. vanishes as the integration is taken in opposing

directions on the two sides of the interface. Therefore, the tangential component of $\mathbf{H}$ must obey the boundary condition:

$$\Delta \mathbf{H}_t = \frac{\partial \boldsymbol{\mathcal{P}}^s}{\partial t} \times \hat{\mathbf{z}}. \tag{A.10}$$

For the D_z component, the integral over the volume V of (A.1a) is:

$$\int_V \nabla \cdot \mathbf{D} dV = -\int_V \nabla \cdot \mathbf{P}^{nl} dV, \tag{A.11}$$

which combined with the divergence theorem becomes:

$$\int_{\partial V} \mathbf{D} \cdot d\mathbf{A} = -\int_V \nabla \cdot [\boldsymbol{\mathcal{P}}^s(x,y)\delta(z) + \mathbf{P}^b] dV. \tag{A.12}$$

As before, $\mathbf{P}^b$ vanishes across the slab and so the boundary condition for D_z becomes:

$$\Delta D_z = -\nabla_t \cdot \boldsymbol{\mathcal{P}}^s(x,y), \tag{A.13}$$

where $\nabla_t = \hat{x}(\partial/\partial x) + \hat{y}(\partial/\partial y)$ is the gradient operator in the tangent plane.

Finally, following the same procedure as for the $\mathbf{H}_t$ component, Eq. (A.1b) implies:

$$\oint_{\partial S} \mathbf{E} \cdot d\mathbf{l} = 0. \tag{A.14}$$

Since $D_z = \epsilon' E_z$ and $\int_{0^-}^{0^+} (D_z + P_z^b) dz = -\mathcal{P}_z^s$, it follows that:

$$\Delta \mathbf{E}_t = -\frac{1}{\epsilon'}(\nabla_t \mathcal{P}_z^s - \mathbf{P}_t^b). \tag{A.15}$$

In conclusion, the boundary conditions for electromagnetic radiation at the interface between a medium with surface and bulk non-linear polarisations and free space are:

$$\Delta B_z = 0 \tag{A.16a}$$

$$\Delta \mathbf{H}_t = \frac{\partial \boldsymbol{\mathcal{P}}^s}{\partial t} \times \hat{z} \tag{A.16b}$$

$$\Delta D_z = -\nabla_t \cdot \boldsymbol{\mathcal{P}}^s(x,y) \tag{A.16c}$$

$$\Delta \mathbf{E}_t = -\frac{1}{\epsilon'}(\nabla_t \mathcal{P}_z^s - \mathbf{P}_t^b). \tag{A.16d}$$

One final question is the nature of ϵ'. In the mathematical formalism presented above, ϵ' is a "boundary" value between ϵ_1 and ϵ_2. In most studies of surface non-linear optics, ϵ' is usually set to be equal to the permittivity of the polarised medium.

Appendix B

Calculation of the Local Scattering Matrix Coefficients in the Multiple Scattering Matrix Formalism

At the fundamental frequency, the total field outside a cylinder j at a point P and calculated in a system of coordinates with origin in the centre of the cylinder, O_j, can be written in the MSM formalism as [see Chap. 3 and Fig. B.1 for more details]:

$$U_{z,j}^{\mathrm{tot}}(P) = \sum_{m=-\infty}^{\infty} \left[d_{mj} J_m(\kappa_b r_P^j) + b_{mj} H_m^{(2)}(\kappa_b r_P^j) \right] e^{im\varphi_P^j}. \tag{B.1}$$

In the case of TE polarisation which will be assumed in what follows, $U_{z,j}^{tot} = H_{z,j}^{tot}$. Inside the cylinder, the magnetic field becomes:

$$H_{z,j}^{\mathrm{int}}(P) = \sum_{m=-\infty}^{\infty} c_{mj} J_m(\kappa_j r_P^j) e^{im\varphi_P^j}. \tag{B.2}$$

The azimuthal component of the electric field is related to the magnetic field by:

$$E_{\varphi,j} = \frac{1}{\kappa^2} \mu_0 \omega \frac{\partial H_{z,j}}{\partial r}. \tag{B.3}$$

From eq. (B.3), the total electric field outside the cylinder, $E_{\varphi,j}^{\mathrm{tot}}$ and the electric field inside the cylinder, $E_{\varphi,j}^{\mathrm{int}}$ become:

$$E_{\varphi,j}^{\mathrm{tot}} = \frac{1}{\kappa_b} \omega \mu_0 \sum_{m=-\infty}^{\infty} \left[d_{mj} J'_m(\kappa_b r_P^j) + b_{mj} H_m^{(2)\prime}(\kappa_b r_P^j) \right] e^{im\varphi_P^j}, \tag{B.4a}$$

$$E_{\varphi,j}^{\mathrm{int}} = \frac{1}{\kappa_j} \omega \mu_0 \sum_{m=-\infty}^{\infty} c_{mj} J'_m(\kappa_j r_P^j) e^{im\varphi_P^j}. \tag{B.4b}$$

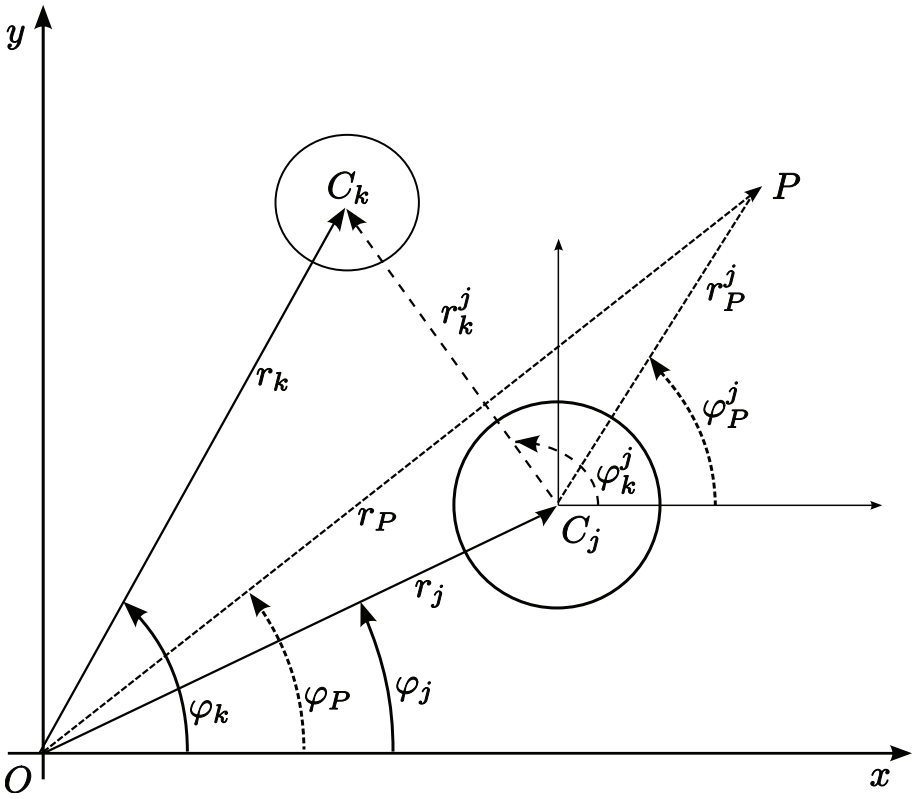

Fig. B.1: Schematic of the system geometry [see Chap. 3 for more details].

The linear boundary conditions at the interface between the cylinder and the background ($r_P^j = R_j$, with R_j the radius of the cylinder) are:

$$H_{z,j}^{\text{ext}}(R_j, \varphi) = H_{z,j}^{\text{int}}(R_j, \varphi), \tag{B.5a}$$

$$E_{\varphi,j}^{\text{ext}}(R_j, \varphi) = E_{\varphi,j}^{\text{int}}(R_j, \varphi). \tag{B.5b}$$

Imposing the boundary conditions to both the electric and the magnetic fields yields a set of equations for the external expansion coefficients c_{mj}:

$$c_{mj} = \frac{d_{mj} J_m(\kappa_b R_j) + b_{mj} H_m^{(2)}(\kappa_b R_j)}{J_m(\kappa_b R_j)} \tag{B.6a}$$

$$c_{mj} = \frac{\kappa_j}{\kappa_b} \frac{d_{mj} J_m'(\kappa_b R_j) + b_{mj} H_m^{(2)\prime}(\kappa_b R_j)}{J_m'(\kappa_b R_j)}. \tag{B.6b}$$

Eliminating the c_{mj} between the two equations above gives the relation between the coefficients d_{mj} and b_{mj}:

$$\frac{b_{mj}}{d_{mj}} = \frac{\beta_j J_m'(\kappa_b R_j) J_m(\kappa_j R_j) - J_m(\kappa_b R_j) J_m'(\kappa_j R_j)}{H_m^{(2)}(\kappa_b R_j) J_m'(\kappa_j R_j) - \beta_j H_m^{(2)\prime}(\kappa_b R_j) J_m(\kappa_j R_j)}. \tag{B.7}$$

This equation defines the local scattering matrix $\mathbf{S}_j$ of cylinder j, as the components of the scattering matrix are defined as $S_{j,mn} = (b_{mj}/d_{mj})\delta_{mn}$.

In the TM case, the z component of the electromagnetic field will be E_z. The procedure outlined above still holds for this case with the provision that the electromagnetic boundary conditions at $r_P^j = R_j$ now read:

$$E_{z,j}^{\mathrm{ext}}(R_j, \varphi) = E_{z,j}^{\mathrm{int}}(R_j, \varphi), \tag{B.8a}$$

$$H_{\varphi,j}^{\mathrm{ext}}(R_j, \varphi) = H_{\varphi,j}^{\mathrm{int}}(R_j, \varphi). \tag{B.8b}$$

Thus, the relation between the d_{mj} and b_{mj} coefficients for TM polarisation can be written as:

$$\frac{b_{mj}}{d_{mj}} = \frac{\alpha_j J'_m(\kappa_b R_j) J_m(\kappa_j R_j) - J_m(\kappa_b R_j) J'_m(\kappa_j R_j)}{H_m^{(2)}(\kappa_b R_j) J'_m(\kappa_j R_j) - \alpha_j H_m^{(2)\prime}(\kappa_b R_j) J_m(\kappa_j R_j)}, \tag{B.9}$$

where $\alpha_j = (\epsilon_b \kappa_j)/(\epsilon_j \kappa_b)$.

At the second harmonic, the same scattering matrix is used as for the fundamental field but care must be taken when using the wave vector, $k(\omega) \to k(2\omega)$.

Appendix C

Components of the Non-linear Polarisation expressed in Cylindrical Coordinates

The non-linear source term which contains both the surface and bulk contributions to the second harmonic generation from a cylinder j and embedded in a homogeneous background medium can be written, using the notations introduced in Chapter 3 [also see Fig. B.1], as:

$$a_{\Omega,mj} = -\frac{\omega}{2}\int_{\Gamma} H_m^{(2)}(\kappa_b r_j(P)) e^{im\varphi_j(P)} [\nabla_{r'} \times \mathbf{P}_m(\mathbf{r}' - \mathbf{r}_j)]\mathbf{e}_z dr', \qquad \text{(C.1)}$$

where $r_j(P) = |\mathbf{r}' - \mathbf{r}_j|$ and Γ is the boundary between the medium and the cylinder j. In what follows, to simplify the notations, the index m for the polarisation $\mathbf{P}$ has been dropped.

The surface contribution to the source term can be written as:

$$(\nabla_{r'} \times \mathbf{P}^s)\mathbf{e}_z = \frac{1}{r}\left(\frac{\partial P_\varphi^s}{\partial r} r + P_\varphi - \frac{\partial P_r^s}{\partial \varphi}\right). \qquad \text{(C.2)}$$

Here, $P_\varphi^s = 2\epsilon_0 \chi^{(2)}_{\varphi\varphi r} E_r E_\varphi = 2\epsilon_0 \chi^{(2)}_{|||_\perp} E_r E_\varphi$ and $P_r^s = \epsilon_0 \chi^{(2)}_{rrr} E_r^2 = \epsilon_0 \chi^{(2)}_{\perp\perp\perp} E_r^2$ and the components of the electric field are taken at the fundamental frequency ω.

The bulk contribution in Eq. (C.1) is $(\nabla_{r'} \times \mathbf{P}^b)\mathbf{e}_z$, where:

$$\mathbf{P}^b(2\omega) = \alpha[\mathbf{E}(\omega)\cdot\nabla]\mathbf{E}(\omega) + \beta\mathbf{E}(\omega)[\nabla\cdot\mathbf{E}(\omega)] + \gamma\nabla[\mathbf{E}(\omega)\cdot\mathbf{E}(\omega)]. \qquad \text{(C.3)}$$

Because in the case of TE polarisation considered here, $E_z = 0$ and the source term is part of the scalar product with $\mathbf{e}_z$, the only relevant components of the $\mathbf{P}^b(2\omega)$ polari-

sation vector are P_φ^b and P_r^b:

$$P_\varphi^b = P_\varphi^{b(\alpha)} + P_\varphi^{b(\beta)} + P_\varphi^{b(\gamma)} \tag{C.4a}$$

$$P_r^b = P_r^{b(\alpha)} + P_r^{b(\beta)} + P_r^{b(\gamma)}. \tag{C.4b}$$

The six terms in Eqs. (C.4) can be determined from Eq. (C.3) and are:

$$P_\varphi^{b(\alpha)} = \alpha \left(E_r \frac{\partial E_\varphi}{\partial r} + E_\varphi \frac{1}{r} \frac{\partial E_\varphi}{\partial \varphi} \right) \tag{C.5a}$$

$$P_\varphi^{b(\beta)} = \beta E_\varphi \left(\frac{1}{r} E_r + \frac{\partial E_r}{\partial r} + \frac{1}{r} \frac{\partial E_\varphi}{\partial \varphi} \right) \tag{C.5b}$$

$$P_\varphi^{b(\gamma)} = \gamma \frac{1}{r} \left(2 \frac{\partial E_\varphi}{\varphi} E_\varphi + 2 \frac{\partial E_r}{\partial \varphi} E_r \right) \tag{C.5c}$$

$$P_r^{b(\alpha)} = \alpha \left(E_r \frac{\partial E_r}{\partial r} + E_\varphi \frac{1}{r} \frac{\partial E_r}{\partial \varphi} \right) \tag{C.5d}$$

$$P_r^{b(\beta)} = \beta E_r \left(\frac{1}{r} E_r + \frac{\partial E_r}{\partial r} + \frac{1}{r} \frac{\partial E_\varphi}{\partial \varphi} \right) \tag{C.5e}$$

$$P_r^{b(\gamma)} = 2\gamma \left(\frac{\partial E_\varphi}{r} E_\varphi + \frac{\partial E_r}{r} E_r \right). \tag{C.5f}$$

Here, as before, the electric field components are calculated at the fundamental frequency ω.

The two electric field components in Eqs. (C.5) and their derivatives are given by:

$$E_{\varphi,m} = \frac{i}{\kappa_j} \mu_0 \omega c_m J'_m(\kappa_j r) e^{im\varphi} \tag{C.6a}$$

$$E_{r,m} = \frac{1}{\kappa_j^2} m \mu_0 \omega c_m \frac{1}{r} J_m(\kappa_j r) e^{im\varphi} \tag{C.6b}$$

$$\frac{\partial E_{\varphi,m}}{\partial r} = i \mu_0 \omega c_m J''_m(\kappa_j r) e^{im\varphi} \tag{C.6c}$$

$$\frac{\partial E_{r,m}}{\partial r} = \frac{1}{\kappa_j} m \mu_0 \omega c_m \frac{1}{r} J'_m(\kappa_j r) e^{im\varphi} \tag{C.6d}$$

$$\frac{\partial E_{\varphi,m}}{\partial \varphi} = -\frac{1}{\kappa_j} m \mu_0 \omega c_m J'_m(\kappa_j r) e^{im\varphi} \tag{C.6e}$$

$$\frac{\partial E_{r,m}}{\partial \varphi} = \frac{i}{\kappa_j^2} m^2 \mu_0 \omega c_m \frac{1}{r} J_m(\kappa_j r) e^{im\varphi}. \tag{C.6f}$$

Here the internal field expansions coefficients c_m have been used as the non-linear bulk contribution only occurs inside the cylinders.

It is worth noting here that three of the non-linear source components, P_φ^s, P_r^s and P_r^b, also enter in the non-linear boundary conditions at the interface between the cylinders and the background [see Eqs. (3.54)].

Appendix D

Calculation of the Total, Scattered and Absorbed Power in Assemblies of Cylinders

The asymptotic form of the Bessel and Hankel functions and their derivatives, as $x \to \infty$ are:

$$J_m(x) = \sqrt{\frac{2}{\pi x}} cos\left(x - \frac{m\pi}{2} - \frac{\pi}{4}\right) \tag{D.1a}$$

$$J'_m(x) = -\sqrt{\frac{2}{\pi x}} sin\left(x - \frac{m\pi}{2} - \frac{\pi}{4}\right) \tag{D.1b}$$

$$H_m^{(2)}(x) = \sqrt{\frac{2}{\pi x}} e^{-i\left(x - \frac{m\pi}{2} - \frac{\pi}{4}\right)} \tag{D.1c}$$

$$H_m^{(2)\prime}(x) = -i\sqrt{\frac{2}{\pi x}} e^{-i\left(x - \frac{m\pi}{2} - \frac{\pi}{4}\right)}. \tag{D.1d}$$

The total power in the system is defined as:

$$P = P_{abs} + P_{scat}, \tag{D.2}$$

or the sum of the absorbed and scattered power. From Eq. (3.72), and assuming that all scattering coefficients are defined relative to the origin O and account for all cylinders (i.e. $b_m \equiv \tilde{b}_m$), Eq. (D.2) becomes [see Chapter 3 for the definition of the fields and scattering coefficients]:

$$P = -\frac{1}{2}\int_0^{2\pi} \mathrm{Re}(E_{s\varphi} \cdot H_{iz}^* + E_{i\varphi} \cdot H_{sz}^*) r d\varphi. \tag{D.3}$$

The Fourier-Bessel expansions of the four field components in Eq. (D.3) are:

$$H_{iz} = \sum_m a_m J_m kr e^{im\varphi} \tag{D.4a}$$

$$H_{sz} = \sum_m b_m H_m^{(2)}(kr) e^{im\varphi} \tag{D.4b}$$

$$E_{i\varphi} = \frac{i}{k}\mu_b\omega \sum_m a_m J_m'(kr) e^{im\varphi} \tag{D.4c}$$

$$E_{s\varphi} = \frac{i}{k}\mu_b\omega \sum_m b_m H_m^{(2)}(kr) e^{im\varphi}, \tag{D.4d}$$

where the sumation is taken over the integer numbers. Inserting these expression into Eq. (D.3) and moving the integral inside the sum yields two separate integrals. The first integral can be written:

$$\begin{aligned}\int_0^{2\pi} E_{s\varphi} \cdot H_{iz}^* d\varphi = \frac{2\mu_b\omega}{\pi k^2 r} \int_0^{2\pi} \left(\sum_m b_m e^{-i\left(kr - \frac{m\pi}{2} - \frac{\pi}{4}\right)} e^{im\varphi} \right) \\ \times \left(\sum_n a_{in}^* cos\left(kr - \frac{n\pi}{2} - \frac{\pi}{4}\right) e^{-in\varphi} \right) d\varphi.\end{aligned} \tag{D.5}$$

Taking into account that:

$$\int_0^{2\pi} e^{im\varphi} e^{-in\varphi} d\varphi = 2\pi\delta_{mn}, \tag{D.6}$$

equation (D.5) becomes:

$$\int_0^{2\pi} E_{s\varphi} \cdot H_{iz}^* d\varphi = -\frac{4\mu_b\omega}{k^2 r} \sum_m a_m b_m^* \times e^{i\left(kr - \frac{m\pi}{2} - \frac{\pi}{4}\right)} \cdot i \sin\left(kr - \frac{m\pi}{2} - \frac{\pi}{4}\right). \tag{D.7}$$

A similar expression can be derived for the second integral in Eq. (D.3). The total power can then be written:

$$P = -\frac{2\mu_b\omega}{k^2} Re\left[\sum_m (C_m \cos(\alpha_m) - C_m^* i \sin(\alpha_m) \right], \tag{D.8}$$

where:

$$\alpha_m = kr - \frac{m\pi}{2} - \frac{\pi}{2} \tag{D.9a}$$

$$C_m = a_m^* b_m e^{i\alpha_m}. \tag{D.9b}$$

Here, a_m are the incoming field expansion coefficients [see Eqs. (3.23)].

Equation (D.8) can, after some elementary algebra, be expressed as:

$$\begin{aligned} P &= -\frac{2\mu_b\omega}{k^2} Re\{\sum_m |C_m| \left[\cos(\phi_m + \alpha_m) + i\sin(\phi_m - \alpha_m)\right]\} \\ &= -\frac{2\mu_b\omega}{k^2} \sum_m |C_m| cos(\phi + \alpha_m), \end{aligned} \tag{D.10}$$

where ϕ_m is the phase of C_m, $C_m = |C_m|e^{i\phi_m}$. From the definition of C_m, it can be written as:

$$C_m = \frac{1}{Z_b}|b_m|e^{i\left(\arg(b_m) - m\frac{\pi}{2} + m\varphi_0 - \alpha_m\right)}, \tag{D.11}$$

which implies that:

$$\phi_m = \arg(b_m) - m\frac{\pi}{2} + m\varphi_0 - \alpha_m \tag{D.12a}$$

$$|C_m| = \frac{|b_m|}{Z_b}, \tag{D.12b}$$

where $Z_b = \sqrt{\mu_b/\epsilon_b}$ is the impedance of the background.

Finally, the total power in the system now becomes:

$$P = -\frac{2\mu_b\omega}{k^2}\frac{1}{Z_b}\left[\sum_m |b_m| \cos\left(\arg(b_m) - m\frac{\pi}{2} + m\varphi_0\right)\right]. \tag{D.13}$$

The scattered power can also be determined using the expression of the Poynting vector. According to Eq. (3.66) the scattered power is:

$$P_{sca} = \frac{1}{2}\int_0^{2\pi} Re[E_{s\varphi} \cdot H_{sz}^*] r d\varphi. \tag{D.14}$$

Using the asymptotic expressions (D.1) and an approach similar to that used to calculate the total power, it can be shown that P_{sca} becomes:

$$P_{sca} = \frac{\mu_b\omega}{\pi k^2}\int_0^{2\pi} |\sum_m b_m e^{im\varphi}|^2 d\varphi = 2\frac{\mu_b\omega}{k^2}\sum_m |b_m|^2. \tag{D.15}$$

Expressions (D.13) and (D.15) show that the total and scattered powers depend on the scattering coefficients b_m and known parameters of the system. Consequently, once the scattering problem is solved (the scattering coefficients b_m are determined), the two powers can be calculated. Then, using Eq. (D.2), one can determine the absorbed power. It is worth noting here that for the non-linear case, the total power cannot be found using this approach as there is no incident field. The total power, however, can be calculated numerically by finding the Joule losses in the system as is discussed in Sec. 3.3.5.

Appendix E

Linear and Non-linear Optical Constants of Gold and Silver

Coefficient	Au	Ag
$\lambda_p[\mathrm{nm}]$	137.3041	137.6089
f_0	0.76	0.845
$\Gamma_0[\mathrm{nm}]$	23394	25830.33
f_1	0.024	0.065
$\Gamma_1[\mathrm{nm}]$	5144.6	319.05
$\lambda_1[\mathrm{nm}]$	2987.6	1519.43
f_2	0.01	0.124
$\Gamma_2[\mathrm{nm}]$	3593.8	2743.04
$\lambda_2[\mathrm{nm}]$	1493.8	276.69
f_3	0.071	0.065
$\Gamma_3[\mathrm{nm}]$	1425.1	19075.7
$\lambda_3[\mathrm{nm}]$	417.6	151.47
f_4	0.601	0.84
$\Gamma_4[\mathrm{nm}]$	497.13	1353.55
$\lambda_4[\mathrm{nm}]$	288.07	136.5
f_5	4.384	5.646
$\Gamma_5[\mathrm{nm}]$	560	512.54
$\lambda_5[\mathrm{nm}]$	93.08	61.106

Table E.1: Lorentz-Drude model coefficients for Au and Ag [see Eq. 2.26] [2].

	Au	Ag
$\chi^2_{\parallel\parallel\perp}[\mathrm{m}^2/\mathrm{V}]$	4.6286×10^{-20}	3.98×10^{-20}
$\chi^2_{\perp\perp\perp}[\mathrm{m}^2/\mathrm{V}]$	1.5903×10^{-18}	2.79×10^{-18}

Table E.2: Non-linear susceptibilities of Au and Ag [3].

Bibliography

[1] T. F. Heinz. Second-order nonlinear optical effects at surfaces and interfaces. In *Nonlinear Surface Electromagnetic Phenomena*, chapter 5, pages 353–416. Elsevier, 1991.

[2] A D Rakic, A B Djurisic, J M Elazar, and M L Majewski. Optical properties of metallic films for vertical-cavity optoelectronic devices. *Applied optics*, 37(22):5271–83, August 1998.

[3] D. Krause, C. W. Teplin, and C. T. Rogers. Optical surface second harmonic measurements of isotropic thin-film metals: Gold, silver, copper, aluminum, and tantalum. *J. Appl. Phys.*, 96(7):3626–3634, 2004.